



**Investigation into covalent triazine frameworks for high  
efficiency visible-light driven water splitting**

*Dan Kong*

2018

*A thesis submitted for the partial fulfilment of the requirements for the degree of  
Doctor of Philosophy at University College London*

*Department of Chemical Engineering,*

*University College London,*

*Torrington Place,*

*London,*

*WC1E 7J*

## Declaration

I, Dan Kong, confirm that the work presented in this thesis is my own. Where information has been derived from other sources, I confirm that this has been indicated in the thesis.

.....

Signature

.....

Date

# Main Contents

I.	ACKNOWLEDGEMENTS.....	4
II.	ABSTRACT.....	5
III.	PUBLICATIONS & CONFERENCES.....	8
IV.	CONTENTS.....	10
V.	LIST OF FIGURES.....	14
VI.	LIST OF TABLES.....	19
VII.	LIST OF EQUATIONS.....	20
VIII.	NOMENCLATURE.....	21

## I. Acknowledgements

I would like to express my sincere gratitude to everyone who has provided constructive comments and discussions on my project. Firstly, I would like to thank my supervisor, Professor Junwang Tang for his excellent guidance, expertise and insight throughout the entire project. I would also like to thank my secondary supervisor, Prof Zheng-xiao Guo, for many beneficial discussions, and for being very supportive in difficult times. I also appreciate any support from our collaborators (Dr Stephen A. Shevlin, Dr Srinivas Gadipelli & Mr Kaipei Qiu). Great thanks to all the material characterizing technicians in UCL including Mr Martin Vickers, Mr Mark Turmaine, Dr Robert Palgrave, Mr Steve Firth, Dr Abil E Aliev, and Mr John Cowley for their tutoring the operation of XRD, SEM, XPS, EDX, NMR, and Glassblower, respectively. I thank all people (Dr Wenjun Luo, Dr Savio Moniz, Dr Xu Liu, Dr Mustafa, Mr Chaoran Jiang, Dr Chiching Lao, Mr Yiou wang, Mr Yaoming Li, Mr Jijia Xie, Mr Qiushi Ruan, Mr Ayoola Shoneye, Miss Tina Miao, Miss Huiwang, Mr Qingning Yang) in the solar energy and advanced materials group at UCL for discussion of experiment set ups and result analysis. At last, I want to acknowledge the financial support from UCL (Dean's Prize) and the China Scholarship Council (CSC File No.201406320165). More importantly, I would greatly appreciate the psychological support from my love Mr Tian Jiang and my family; Mum, Dad, Sisters, Nans and Grandads- you literally kept me going and I will never forget the sacrifices you made.

## II. Abstract

Efficient utilisation of solar energy could alleviate major energy and the related environmental issues. The conversion of solar energy into chemical fuels by artificial photosynthesis has thus received much attention, e.g. production of renewable hydrogen from water. Since the first photoelectrode titanium dioxide was found for photoelectrochemical water splitting in 1972, substantial progress on semiconducting materials for photocatalytic water splitting has been made. Specifically, to utilise sunlight efficiently, developing visible-light-responsive photocatalysts is indispensable to realise the application of solar-to-chemical energy conversion in practice. Considering few overall water splitting systems reported, investigation on the oxidative and the reductive half reactions separately is significant for fundamental understanding, optimisations and finally complete water-splitting cycles.

Among these photocatalysts, inorganic photocatalysts have been widely explored for the hydrogen evolution reaction. However, most of them are either only active under UV light irradiation or their efficiency is moderate, due to either large band gap energy or fast charge recombination. In the past few years, the increasing interest in a class of metal-free organic photocatalysts for water splitting has been raised, as these organic polymers feature two-dimensional (2D) conjugated structures, high chemical stability, ease of modification to achieve suitable thermodynamical potentials to overall water splitting. The most common metal-free organic photocatalyst is melon-based graphitic carbon nitride (for simplicity, usually denoted g-C<sub>3</sub>N<sub>4</sub>). Moreover, a series of covalent triazine frameworks (CTFs) were synthesised recently. These materials were formed by the ionothermal trimerization of aromatic nitriles in molten ZnCl<sub>2</sub> and built up by alternating triazine and phenyl building blocks. Because of the covalent triazine-based structure, CTFs possess excellent thermal and chemical stability, beneficial as new

catalysts in liquid phase reactions. CTFs with the  $\pi$ -stacked aromatic units would also be expected to promote exciton separation and charge transportation, promising for photocatalytic light-driven water splitting.

As such, the research project targets on visible light-driven CTF photocatalysts for pure water splitting. Firstly, the photooxidation of water using oxygen doped CTF-1(OCT) was investigated. The OCT was created by a simple dynamic trimerization reaction of the precursor 1,4-dicyanobenzene in ionothermal conditions, that is, in molten zinc chloride at high temperature. It was found that due to the oxygen-containing reaction atmosphere, some oxygen was doped in the crystals to modify the structure, optical, and electrical properties of the materials, resulting in the much better operation window (from UV to NIR) than the benchmark photooxidation catalyst  $\text{BiVO}_4$  (only active from UV to 500 nm). The external quantum efficiency of OCT was determined to be 2.6% at the wavelength of 400 nm, 1.5% at 500 nm, even  $\sim 0.2\%$  at wavelength as long as 800 nm. Structure optimization, thermodynamic calculation and electronic structure analysis of OCT calculated by density functional theory (DFT) were carried out to illustrate the mechanism of the increasing photooxidation yield successfully, which could be applied to improve other semiconductors.

Furthermore, hydrogen and oxygen evolutions from water were carried out by another polymer photocatalyst CTF-0, which is one member of the CTFs group and based on 1,3,5-tricyanobenzene as monomer under ionothermal conditions. Compared with OCT, CTF-0 crystals have higher nitrogen ratio and smaller pore size. Herein, two different synthesis ways of a novel photocatalyst covalent triazine framework CTF-0 were utilised and tested for photocatalytic  $\text{H}_2$  and  $\text{O}_2$  evolution under visible light irradiation. The CTF-0- $\text{M}_2$  produced by a microwave method shows an almost 7 times higher photocatalytic activity of hydrogen evolution (up to 701  $\mu\text{mol/h}$ ) than

the CTF-0-I produced by an ionothermal trimerization method under similar photocatalytic conditions, which leads to an extremely high turnover number (TON) of 726 over a platinum cocatalyst after seven circles. This can be attributed to the narrow band gap and the rapid photogenerated charge separation and transportation. Whereas, CTF-0-I has produced rough 6 times higher oxygen of 22.6  $\mu\text{mol}$  in the first hour than CTF-0-M<sub>2</sub> under the same experimental condition. A high apparent quantum efficiency (AQY) of 7.2% at 420 nm for oxygen production was obtained from aqueous  $\text{AgNO}_3$  solution without any cocatalysts, exceeding most of the reported CTFs, due to the large driving force of water oxidation and the large number of active sites.

Finally, considering that the CTF-0 has a wide bandgap, which could produce both hydrogen and oxygen theoretically, decorating the different co-catalysts on the CTF-0 was explored for the entire water splitting to produce hydrogen and oxygen. The presence of the cocatalyst Pt and  $\text{Co}_3\text{O}_4$  promotes the  $\text{H}_2$  and  $\text{O}_2$  evolution on the surface of the photocatalysts simultaneously, due to enhanced separation of photogenerated charge carriers, more active sites for catalytic  $\text{H}_2$  and  $\text{O}_2$  evolution and the improved stability by suppressing photo-corrosion. Loading different ratio of cobalt cocatalysts on CTF-0 has been explored for overall water splitting. And it is found that water splitting rates are influenced by the concentration of the cocatalyst. 6 wt%  $\text{Co}_3\text{O}_4$  and 3wt% Pt-deposited CTF-0 shows the best photocatalytic performances of 0.82  $\mu\text{mol/h}$   $\text{H}_2$  and 0.42  $\mu\text{mol/h}$   $\text{O}_2$ , nearly close to the stoichiometric  $\text{H}_2/\text{O}_2$  ratio of 2:1. Whereas, the system didn't work under the visible light but UV light irradiation, which might be because of the limitation of light absorption range and the efficiency of the charged carriers. Further work is required to confirm the factors and mechanism of the pure water splitting of CTF-0s.

### III. Impact statement

Abundant energy is necessary for the developments in the modern world. However, the energy resource from fossil-fuels is finite. Another drawback is that the exhaust after the consumption of these fuels is potential for environmental pollution and impulses the climate change, especially increasing the greenhouse effect. This situation urges the society to discover renewable energy sources as sustainable alternatives to the limited fossil-fuels. Given the abundance of water and sunlight in nature, artificial photocatalytic splitting of water might be applied to produce hydrogen sustainably, which can be used as an alternative clean-fuel and become a part-solution to satisfy the increasing global energy demands. Despite more than four decades of intensive researches in photocatalytic water splitting, an efficient photocatalyst, possessing long-lived charge carriers, proper energy level offsets, stability against irradiation and wide-window absorption, is still highly desirable for the development to achieve a practical solar to fuel efficiency.

In this research, I have successfully synthesised a series of polymeric photocatalysts utilised in the water splitting into H<sub>2</sub> and O<sub>2</sub> separately. Firstly, OCT synthesised by an ionothermal method can produce oxygen efficiently at a wide operation window from UV, visible, and even to NIR with an unprecedented external quantum efficiency even at 600 nm and 800 nm. Furthermore, it remains active for H<sub>2</sub> production. The simulation and experimental results illustrated that a controlled small amount of oxygen in the ionothermal reaction could not only narrow the band gap but also causes appropriate band-edge shifts. Secondly, the photocatalysts of higher performance of water reduction and oxidation, CTF-0, were synthesised by two methods. The covalent triazine framework CTF-0-M<sub>2</sub> produced by the microwave method shows the best

photocatalytic hydrogen evolution under both UV and visible light irradiation. CTF-0-I synthesised by ionothermal method with the highest amount of benzene units exhibits the best photocatalytic water oxidation performance under the same light irradiation condition. Furthermore, such kind of tunable bandgap materials can be explored and applied in the photocatalytic water splitting and photocatalysis. It is also beneficial for the fundamental research of the modification of other framework photocatalysts by different reaction conditions or precursors, and their influence on the structure and physical and chemical properties.

In the end, pure overall water splitting into hydrogen and oxygen was achieved on CTF-0 after loading both Pt and  $\text{Co}_3\text{O}_4$  as cocatalysts. My research provides novel methods for polymers synthesis with controlled dopants to tune their band structure and new catalysts to realise overall water splitting. Furthermore, my project results offer alternative directions for utilising polymeric photocatalysts in sustainably producing of  $\text{H}_2$  fuel and partially to prevent environmental pollutions.

## IV. Publications & Conferences

### Publications

1. **D Kong**, Y Zheng, M Kobielski, YO Wang, W Macyk, XC Wang, JW Tang\*, "Recent advances in visible light-driven water oxidation and reduction in suspension systems", *Materials Today*, 2018, 21 (8), 897-924.
2. **D Kong**, SA Shevlin, ZX Guo, JW Tang\*, "An oxygenated covalent triazine 2-D photocatalyst works efficiently from UV to IR for water oxidation", *Energy & Environmental Science*, in 2<sup>nd</sup> revision.
3. **D Kong**, XY Han, QS Ruan, S Gadipelli, ZX Guo, JW Tang\*, "Tunable covalent triazine-based frameworks CTF-0 for visible light-driven efficient hydrogen and oxygen generation", submitted to *ACS Catal.*
4. **D Kong**, ZX Guo, JW Tang\*, "Stable overall water splitting on the selected CTF-0 polymers", submitted to *Angew. Chem. Int. Ed.*
5. JF de Lima, MH Harunsani, DJ Martin, **D Kong**, PW Dunne, D Gianolio, RJ Kashtiban, J. Sloan, OA Serra, JW Tang\*, RI Walton\*, "Control of chemical state of cerium in doped anatase TiO<sub>2</sub> by solvothermal synthesis and its application in photocatalytic water reduction", *Journal of Materials Chemistry A*, (2015), 3, 9890-9898.
6. YO Wang, H Suzuki, JJ Xie, O Tomita, DJ Martin, M Higashi, **D Kong**, R Abe, and JW Tang, "Mimicking Natural Photosynthesis: Solar to Renewable H<sub>2</sub> Fuel Synthesis by Z-Scheme Water Splitting Systems", *Chemical Reviews*, (2018), April 20.

## Conferences

1. "Organic semiconductor for both oxygen and hydrogen evolution from water", 16th International Congress on Catalysis, Beijing, China, July 2016.
2. "Oxygen Doped CT-1 for Oxygen and Hydrogen Evolution from Water", 7th UK - Japan Symposium on Fundamental Research Advances in Carbon Nanomaterials, London, UK, June 2016.
3. "Organic semiconductor for both oxygen and hydrogen evolution after water", 4<sup>th</sup> UK Solar Fuels Symposium, January 2016.

## V. Contents

I. Acknowledgements .....	4
II. Abstract .....	5
III. Impact statement .....	8
IV. Publications & Conferences.....	10
Publications.....	10
Conferences.....	11
V. Contents .....	12
VI. List of Figures .....	18
VII. List of Tables.....	27
VIII. List of Equations .....	28
IX. Nomenclature.....	30
Acronyms & initialisms.....	30
Roman symbols .....	32
Greek symbols .....	32
1. Chapter 1.....	33
Introduction .....	33
1.1 Background.....	33
1.2 Motivation.....	33

1.3 Objectives .....	35
1.4 Outline .....	37
<b>2. Chapter 2.....</b>	<b>38</b>
Literature review .....	38
2.1 Principle of photocatalytic water splitting .....	38
2.2 Key factors influencing the photocatalytic performance of semiconductor photocatalysts	40
2.2.1 Band gap changes by doping .....	40
2.2.2 Architecture parameters.....	41
2.2.3 Cocatalysts .....	43
2.2.4 The solution pH.....	46
2.2.5 Sacrificial and mediator reagents.....	47
2.3 Material development on photocatalytic water reduction and oxidation in a suspension system .....	49
2.3.1 Inorganic semiconductors.....	50
2.3.2 Metal-free photocatalysts.....	66
2.3.3 The development of CTFs.....	77
<b>3 Chapter 3.....</b>	<b>82</b>
Methodology.....	82
3.1 Material characterizations.....	82
3.1.1 BET .....	82

3.1.2 UV-visible spectroscopy.....	85
3.1.3 Attenuated total reflectance Fourier transform infrared (ATR-FTIR) spectroscopy .....	87
3.1.4 Raman spectroscopy .....	89
3.1.4 Powder X-ray diffraction (PXRD).....	91
3.1.5 X-ray photoelectron spectroscopy (XPS) .....	93
3.1.6. Nuclear magnetic resonance (NMR) spectroscopy .....	95
3.1.7 Scanning and transmission electron microscopy (SEM and TEM) .....	96
3.1.8 Elemental Analysis (EA) .....	100
3.2 Material performance test.....	100
3.2.1 Gas chromatography setup.....	101
3.2.2 Particle suspension reactors .....	106
3.2.3 Light source.....	108
3.2.4 Efficiency calculations .....	109
<b>4 Chapter 4.....</b>	<b>113</b>
Modified OCT for water oxidation across UV to full visible spectrum .....	113
4.1 Introduction.....	114
4.2 Methodology.....	116
4.1.1 Synthesis techniques.....	116
4.1.2 General characterization .....	117
4.1.3 Photocatalytic activity evolution .....	118

4.1.4 Computational simulations .....	119
4.2 Results and discussion .....	120
4.2.1 General strategy and structural analysis of OCT .....	120
4.2.2 Photocatalytic and optical properties of 6.68 at% OCT .....	130
4.2.3 Discussion of prospective structure optical properties .....	136
4.2.4 Effect of oxygen content on water oxidation and optical and electrical properties ....	138
4.3 Conclusions.....	141
<b>5 Chapter 5.....</b>	<b>142</b>
New CTF-0 for both visible light-driven efficient hydrogen and oxygen generation from water .....	142
5.1 Introduction .....	143
5.2 Methodology.....	144
5.2.1 Chemicals .....	144
5.2.2 Synthesis of CTF-0-I.....	144
5.2.3 Synthesis of CTF-0-Ms.....	145
5.2.4 Characterization .....	145
5.2.5 Theoretical Calculations.....	146
5.2.6 Photocatalytic measurements.....	147
5.2.7 Photoelectrochemical Measurements.....	147
5.3 Results and Discussion.....	148

5.3.1 General Characterisations.....	148
5.3.2 Optical properties and the proposed band gap structure diagram .....	155
5.3.3 Photocatalytic performance and stability .....	161
5.3.4 Understanding the electronic characteristics and the photocatalytic kinetics .....	166
5.3 Conclusions.....	170
<b>6 Chapter 6.....</b>	<b>172</b>
Overall water splitting on the selected CTF-0 polymers.....	172
6.1 Introduction.....	172
6.2 Methodology.....	174
6.6.1 Materials and Synthesis of samples.....	174
6.2.2 Characterizations .....	174
6.2.3 Cocatalysts depositions .....	174
6.2.4 Photocatalytic activity tests .....	175
6.2.5 Photoelectrochemical measurements .....	176
6.3 Results and discussion .....	176
6.3.1 Structural characterizations.....	176
6.3.2 Photocatalytic activity .....	185
6.3.3 Mechanism discussion.....	187
6.4 Conclusion .....	190
<b>7 Overall conclusions .....</b>	<b>192</b>

<b>8 Future Work .....</b>	<b>195</b>
<b>9. Bibliography .....</b>	<b>197</b>

## VI. List of Figures

Figure 1. Solar irradiance spectrums above atmosphere and at surface. Extreme UV and X-rays are produced (at left of wavelength range shown) but comprise very small amounts of the Sun's total output power. ....	34
Figure 2. The main processes and the principle of photocatalytic water splitting on semiconductor photocatalysts. ....	36
Figure 3. Formation of new valence and conduction bands by electron donor and acceptor atoms, enabling a UV-active material to respond to visible light. ....	41
Figure 4. Schematic illustration of the growth mode of Cu <sub>2</sub> O (a) Octahedra and (b) Cubes. The ammonia solution with a certain concentration may favour the preferential crystal growth along the <100> direction and make it far exceed that of <111>, thus {100} faces shrink <sup>31</sup> . ....	43
Figure 5. Mechanism of highly efficient photocatalytic water splitting over NiO/NaTaO <sub>3</sub> :La photocatalysts. The small particle size and the ordered surface nanostep structure created by the lanthanum doping contributed to the suppression of recombination between the photogenerated electrons and holes and the separation of active sites to avoid the back reaction, resulting in the highly efficient water splitting into H <sub>2</sub> and O <sub>2</sub> <sup>33</sup> . ....	45
Figure 6. Schematic of the principles of Z-scheme water splitting system. ....	49
Figure 7. Principal cation components of semiconductor photocatalysts for water splitting. The red and green colour elements are the typical metal cations with filled d orbitals having a d <sup>0</sup> and d <sup>10</sup> electronic configuration, respectively, widely used as active photocatalysts for water splitting. The blue colour elements are the transition-metal cations with partly filled d electrons (i.e., d <sup>n</sup>	

electronic configuration:  $0 < n < 10$ ), usually functioning as cocatalysts in the photocatalytic water splitting systems.....51

Figure 8. Photoinduced reactions in  $\text{TiO}_2$  photocatalysis and the corresponding time scales<sup>72</sup>...54

Figure 9. Crystal structures of perovskites and layered perovskite compounds (red spheres: oxygen; dark blue spheres: B-site element; green and light blue spheres: A-site element)<sup>85</sup>.....56

Figure 10. Schematic diagram of a perfect graphitic carbon nitride sheet constructed from melem units.....68

Figure 11. (a) TEM image of the NGO-QDs, (b) HRTEM image of a NGO-QD, (c) a conceptual schematic of the NGO-QD structure and (d) the p-n type photochemical diode in NGO-QDs<sup>154</sup>.  
.....71

Figure 12. (a) A tunable triphenylarene platform for photocatalytic hydrogen evolution. Replacement of 'C-H' by 'nitrogen atoms' at the green dots changes the angle between central aryl and peripheral phenyl rings, which leads to varied planarity in the platform. (b) Synthesis of  $\text{N}_x$ -COFs from  $\text{N}_x$ -aldehydes and hydrazine<sup>165</sup>.....74

Figure 13. (a) The puckered structure of a few layer BP sheet. (b) Top view of monolayer BP. The x and z axes are along zigzag and armchair directions, respectively<sup>176</sup>.....75

Figure 14. Schematic illustration of the trimerization reaction to synthesise CTF-0 (a), CTF-1 (b) and CTF-2 (c), respectively. ....78

Figure 15. Schematic representation of an ATR-FTIR system<sup>212</sup>. ....88

Figure 16. Energy-level diagram showing the states involved in Raman spectra.....90

Figure 17. The Schematic diagram of a gas chromatograph.....101

Figure 18. Photograph of the gas chromatograph system used during photocatalysis experiments. .....	102
Figure 19. Photograph of the gastight syringe used during photocatalysis experiments. ....	102
Figure 20. An example of the chromatograph. The hydrogen peak is at 2.36 min, the oxygen peak is at 4.29 min and the nitrogen peak is at 7.68 min. ....	104
Figure 21. Schematic of the GC/MS system. The chromatograph of TCD detects the retention times and response areas, and the MS reveals the kind of molecules in the mixture by the peak positions. ....	106
Figure 22. Mass spectrum of water.....	106
Figure 23. Borosilicate reactor for water redox batch reactions. Light is irradiated on the side window and two side outlets are used for purging and taking the gas products. ....	107
Figure 24. The lamp system is used to supply the irradiation light. ....	109
Figure 25. Reaction Mechanism of OCT starting from 1,4-dicyanobenzene to the extended 2D OCT. Red dots are oxygen atoms, olive-green ones are carbon atoms and grey ones are nitrogen atoms.....	117
Figure 26. Schematic of formation process of pure CTF-1 (a and d), OCT(i) (b and e), OCT(ii) (b and f) and OCT(iii) (c and g) structures. . Carbon is represented by brown sphere, nitrogen grey, hydrogen light pink, and oxygen red. (h) The band alignments of CTF-1 and proposed OCT structures. The dots represent the VBEs and the squares and triangles represent the unoccupied defect states and CBEs, respectively. The dash lines are the $H^+/H_2$ (up) and $O_2/H_2O$ (down) redox levels. All the energy is calculated with reference to the vacuum level. ....	121

Figure 27. The periodic structures of pure CTF-1 (a), OCT(i) (b), OCT(ii) (c) and OCT(iii) (d). The solid lines represent the unit cell. ....	122
Figure 28. Powder XRD spectra of 6.68 at% OCT. The peaks (100), (110), (200) and (001) indicates that crystalline triazine-based frameworks have been formed. ....	124
Figure 29. The Spatial distribution of the valence band maximum (VBM) (a, c, e, g) and the conduction band minimum (CBM) (b, d, f, h) of the structure pure CTF-1, OCT(i), OCT(ii) and OCT(iii), respectively. All the isosurfaces were set to $0.005 e/a_0^3$ , where $a_0$ is the Bohr radii. ....	125
Figure 30. FTIR spectroscopy of 6.68 at% OCT. The peaks at 796 and 1020 $\text{cm}^{-1}$ match well with the C-H in-plane bending vibrations of the benzene rings, and the C=C bending of benzene units, respectively. The characteristic bonds for the triazine unit were found at 1508 $\text{cm}^{-1}$ (C-N stretching mode) and 1354 $\text{cm}^{-1}$ (in-plane ring stretching vibrations), confirming the successful formation of triazine rings in these experiments. ....	126
Figure 31. (a) $^{13}\text{C}$ cross-polarization magic angle spinning solid-state NMR and (b) XPS survey spectrum after etching to 150 nm thickness of the 6.68 at% OCT. The light blue dots are carbon atoms, the dark blue ones are nitrogen atoms, and the red one is oxygen atom. ....	128
Figure 32. The C1s (a) and O1s (b) XPS spectra for the 6.68 at% OCT. (Charge referenced to adventitious C1s peak at 284.8 eV). ....	128
Figure 33. Carbon(a), nitrogen(b) and oxygen(c) K-edge region of the electron energy loss spectroscopy (EELS) from averaging three different spectra taken from the intensity line profiles from the region in ADF-STEM image (d) of 6.68 at% OCT. ....	129

Figure 34. Time courses of 6.68 at% OCT for oxygen (a) and hydrogen (b) production from water under full-arc irradiation and visible light illumination ( $\lambda > 420$ nm) in the presence of relevant scavengers. ....	131
Figure 35. (a) AQY for O <sub>2</sub> generation at 400, 420, 500, 600 and 800 nm (left-hand axis) with optical absorption spectrum plotted (right-hand side) and (b) band positions and the pathways for water redox of 6.68 at% OCT, where the CBE is the original conduction band in the unmodified CTF-1 and the unoccupied defect state is the lowered CB in the OCT. ....	131
Figure 36. O <sub>2</sub> evolution of 0. 1 g BiVO <sub>4</sub> under visible light ( $\lambda > 420$ nm) in the presence of the electron scavenger of 1 g AgNO <sub>3</sub> . ....	133
Figure 37. The typical time courses of (a) O <sub>2</sub> production from water containing 1 g AgNO <sub>3</sub> as a hole scavenger and (b) H <sub>2</sub> production from water containing 10 vol% TEOA as an electron donor and 3 wt% Pt (H <sub>2</sub> PtCl <sub>6</sub> ) as a cocatalyst, under full arc and visible light (of wavelength longer than 420 nm) by 6.68 at% OCT. The reaction of O <sub>2</sub> evolution was run for 24 h, with evacuation every 8 h (dashed line). The reaction of H <sub>2</sub> evolution was run for 18 h, with evacuation every 6 h (dashed line).....	134
Figure 38. FTIR spectra(a) and <sup>13</sup> C cross-polarization magic angle spinning ssNMR spectra(b) of 6.68 at% OCT before and after water oxidation reaction. The light blue dots are carbon atoms, the dark blue ones are nitrogen atoms, and the red one is oxygen atom. ....	135
Figure 39. Gas Chromatography mass spectra of oxygen obtained under full arc irradiation in the 95% <sup>18</sup> O-labelled-water photocatalytic system at reaction time points of (a) 0 h and (b) 2 h.....	135
Figure 40. The density of states (DOS) of the structure for pure CTF-1 (a), OCT(i) (b), OCT(ii) (c) and OCT(iii) (d). The Fermi levels were adjusted to zero. ....	138

Figure 41. Oxygen evolution amount for different amount of oxygen doped in OCT (a) and the corresponding Tauc Plots calculated based on the UV-vis spectra(b). .....	140
Figure 42. The equilibrium structures and its density of states for pure CTF-1 (a and d), 3.33 at% OCT(ii) (b and e) and 6.68 at% OCT(ii) (c and f), respectively and the band alignment calculations in PBE level of OCT(ii) for different oxygen doping levels (g). The bottom ones (solid circles) are the position of the VBs and the solid squares and triangle represent the CBs and the unoccupied defect state.....	140
Figure 43. (a) C1s and (b) O1s XPS spectra for the 7.71 at% OCT. (Charge referenced to adventitious C1s peak at 284.8 eV).....	141
Figure 44. PXRD patterns of CTF-0-I prepared by the ionothermal method, and CTF-0-M <sub>1</sub> , CTF-0-M <sub>2</sub> and CTF-0-M <sub>3</sub> prepared by the microwave method. ....	150
Figure 45. Transmission electron microscopy (TEM) image of CTF-0-M <sub>2</sub> .....	150
Figure 46. Nitrogen sorption measurements of CTF-0-I prepared by the ionothermal method, and CTF-0-M <sub>1</sub> , CTF-0-M <sub>2</sub> and CTF-0-M <sub>3</sub> prepared by the microwave method. ....	151
Figure 47. Solid-state <sup>13</sup> C NMR spectra of CTF-0-I prepared by the ionothermal method, and CTF-0-M <sub>1</sub> , CTF-0-M <sub>2</sub> and CTF-0-M <sub>3</sub> prepared by the microwave method.....	153
Figure 48. XPS survey spectra of CTF-0-I, CTF-0-M <sub>1</sub> , CTF-0-M <sub>2</sub> and CTF-0-M <sub>3</sub> .....	153
Figure 49. FTIR spectra of CTF-0-I prepared by the ionothermal method, and CTF-0-M <sub>1</sub> , CTF-0-M <sub>2</sub> and CTF-0-M <sub>3</sub> prepared by the microwave method. ....	155
Figure 50. Photoluminescence spectrum of CTF-0-I, CTF-0-M <sub>1</sub> , CTF-0-M <sub>2</sub> and CTF-0-M <sub>3</sub> .....	156
Figure 51. UV/Vis absorption spectra and optical energy band gap estimated by the method proposed by wood and Tauc <sup>278</sup> of CTF-0-I, CTF-0-M <sub>1</sub> , CTF-0-M <sub>2</sub> and CTF-0-M <sub>3</sub> .....	157

Figure 52. Valence-band XPS spectra of CTF-0-I, CTF-0-M <sub>1</sub> , CTF-0-M <sub>2</sub> and CTF-0-M <sub>3</sub> .....	159
Figure 53. Mott-Schottky plots of the CTF-0-I (a), CTF-0-M <sub>2</sub> (b), CTF-0-M <sub>1</sub> (c) and CTF-0-M <sub>3</sub> (d) electrode in 0.1 M Na <sub>2</sub> SO <sub>4</sub> at 2k, 1k and 0.5k Hz under the dark condition. ....	159
Figure 54. Band structure diagram of CTF-0-I, CTF-0-M <sub>1</sub> , CTF-0-M <sub>2</sub> and CTF-0-M <sub>3</sub> .....	160
Figure 55. The time course of the H <sub>2</sub> production for CTF-0-I and CTF-0-Ms polymers under (a) full arc and (b) under visible light irradiation ( $\lambda > 420$ nm). ....	161
Figure 56. The time course of the O <sub>2</sub> evolution production for CTF-0-I and CTF-0-Ms polymers under (a) full arc and (b) under visible light irradiation ( $\lambda > 420$ nm). ....	162
Figure 57. (a) Apparent quantum yield (AQY) for H <sub>2</sub> production and (b) stability test of CTF-0-M <sub>2</sub> at atmospheric pressure under nearly one sun irradiation conditions. The seven cycles were under ambient conditions ( $\lambda > 420$ nm irradiation). ....	163
Figure 58. XRD patterns (a) and FTIR spectra (b) of CTF-0-M <sub>2</sub> before and after photocatalyst reaction. ....	163
Figure 59. (a) Apparent quantum yield (AQY) for O <sub>2</sub> production and (b) stability test of CTF-0-I at atmospheric pressure under ambient conditions.....	164
Figure 60. XRD patterns (a) and FTIR spectra (b) of CTF-0-I before and after photocatalyst reaction. ....	165
Figure 61. XPS survey spectra of CTF-0-I before and after photocatalyst reaction (a) and Ag 3d XPS spectra of CTF-0-I after photocatalytic reaction. Charge referenced to adventitious C1s peak at 284.8eV. ....	166
Figure 62. The Spatial distribution of the CBM (a) and the VBM (c), and the band alignments (b) of CTF-0 estimated by DFT calculations. All the energy is calculated with reference to the vacuum	

level. Carbon, nitrogen and hydrogen in the structural models are shown as brown, baby blue and pale pink spheres, respectively. ....	168
Figure 63. The periodic on/off photocurrent response (a) and Nyquist plots (b) of CTF-0-I, CTF-0-M <sub>1</sub> , CTF-0-M <sub>2</sub> and CTF-0-M <sub>3</sub> electrodes in 0.1 M Na <sub>2</sub> SO <sub>4</sub> with 0 V bias versus Ag/AgCl. ....	169
Figure 64. XRD patterns of CTF-0 and Pt/CoO <sub>x</sub> @CTF-0.....	178
Figure 65. <sup>13</sup> C CP-MAS ssNMR spectra of CTF-0 and Pt/CoO <sub>x</sub> @CTF-0.....	178
Figure 66. <sup>15</sup> N CP-MAS ssNMR spectra of CTF-0 and Pt/CoO <sub>x</sub> @CTF-0. ....	179
Figure 67. FTIR spectra of CTF-0 and Pt/CoO <sub>x</sub> @CTF-0. ....	179
Figure 68. The XPS survey spectra of CTF-0 and Pt/CoO <sub>x</sub> @CTF-0. ....	181
Figure 69. The Co 2p XPS spectra of Pt/CoO <sub>x</sub> @CTF-0. ....	182
Figure 70. The O 1s XPS spectra of Pt/CoO <sub>x</sub> @CTF-0.....	182
Figure 71. The Pt 4f XPS spectra of Pt/CoO <sub>x</sub> @CTF-0.....	183
Figure 72. TEM(a) and HRTEM (b) images of Pt/CoO <sub>x</sub> @CTF-0.....	183
Figure 73. Elemental mapping images (a-d) of Pt/CoO <sub>x</sub> @CTF-0.....	184
Figure 74. Schematic description of the role of CTF-0 catalyst in Pt and Co <sub>3</sub> O <sub>4</sub> generations, separately. E <sub>a1</sub> and E <sub>a2</sub> are the activation energy without and with CTF-0 catalysts in the reaction, respectively. ΔG is the standard free energy for the reaction, E is the minimum energy required for Pt or Co <sub>3</sub> O <sub>4</sub> generation. CTF-0 catalysts can largely decrease the activation energy of the Pt and Co <sub>3</sub> O <sub>4</sub> generation, separately. ....	184
Figure 75. (a) H <sub>2</sub> half reaction of pure and Pt-deposited CTF-0 with TEOA as the sacrificial agent, (b) O <sub>2</sub> half reaction of pure, Co <sub>3</sub> O <sub>4</sub> -deposited CTF-0 with AgNO <sub>3</sub> as the sacrificial agent, (c)	

Photocatalytic overall water splitting of different amounts of Co-loaded on CTF-0 with 3 wt% Pt as co-catalyst except for the blank one, (d)Cyclic runs of H<sub>2</sub> and O<sub>2</sub> production from pure water by 6 wt% Co<sub>3</sub>O<sub>4</sub> and 3 wt% Pt-deposited CTF-0. All the experiments were under full arc irradiation of a 300 W Xe lamp..... 187

Figure 76. The FTIR spectra of Pt/Co<sub>3</sub>O<sub>4</sub>@CTF-0 before and after photocatalytic reaction..... 187

Figure 77. Diffuse reflectance UV-vis absorption spectra and Tauc plots (right top side corner) of CTF-0, Pt@CTF-0, Co<sub>3</sub>O<sub>4</sub>@CTF-0 and Pt/Co<sub>3</sub>O<sub>4</sub>@CTF-0. .... 189

Figure 78. Electrochemical impedance spectroscopy Nyquist plots (a), transient photocurrent response (b) of CTF-0 and Pt/Co<sub>3</sub>O<sub>4</sub>@CTF-0, and proposed schematic of the photocatalytic overall water splitting reaction mechanism on Pt/Co<sub>3</sub>O<sub>4</sub>@CTF-0 (c)..... 190

## VII. List of Tables

Table 1. Summary of TiO <sub>2</sub> modification approaches for photocatalytic applications, except dye sensitisations <sup>52</sup> . .....	53
Table 2. Gases and corresponding thermal conductivity at STP <sup>221</sup> . .....	103
Table 3. Elemental analysis of different ratio OCTs and the corresponding mole ratio of O <sub>2</sub> /1,4-dicyanobenzene during the synthesis. ....	129
Table 4. The reaction energy of each structure of pure CTF-1 and OCTs. ....	136
Table 5. Elemental analysis data of the polymers CTF-0-I, CTF-0-M <sub>1</sub> , CTF-0-M <sub>2</sub> and CTF-0-M <sub>3</sub> . .....	154

## VIII. List of Equations

Equation 1. The absorbed light wavelength is directly related to the band gap size.....	38
Equation 2. ....	49
Equation 3. ....	49
Equation 4. The BET equation.....	83
Equation 5. The BET constant C.....	83
Equation 6. ....	84
Equation 7. ....	84
Equation 8. BET SSA equation .....	84
Equation 9. Transmission-reflectance-absorption relation .....	85
Equation 10. Absorbance conversion .....	85
Equation 11. Kubelka-Mulk relation .....	86
Equation 12. Tauc relation .....	86
Equation 13. Planck relation (nm).....	87
Equation 14. The depth of penetration.....	88
Equation 15. Scherrer's equation .....	92
Equation 16. Conservation of binding energy .....	93
Equation 17. Signals emitted from different parts of the interaction volume. ....	99
Equation 18. Apparent Quantum Yield .....	110

Equation 19. Turnover Number.....	111
Equation 20. STH% .....	112

## IX. Nomenclature

### Acronyms & initialisms

<b>0D</b>	Zero dimensional
<b>1D</b>	One dimensional
<b>2D</b>	Two dimensional
<b>AC</b>	Activated carbon
<b>ADF-STEM</b>	Dark field scanning transmission electron microscopy
<b>AQY</b>	Apparent quantum efficiency
<b>ATR-FTIR</b>	Attenuated total reflectance Fourier transform infrared spectroscopy
<b>BET</b>	Brunauer-Emmett-Teller
<b>BP</b>	Phosphorous
<b>CB</b>	Conduction band
<b>CBE</b>	Conduction band edge
<b>CBM</b>	Conduction band minimum
<b>CMP</b>	Conjugated microporous polymer
<b>CNNS</b>	Graphitic carbon nitride nanosheet
<b>COF</b>	Covalent organic framework
<b>CQD</b>	Carbon quantum dots
<b>CTF</b>	Covalent triazine framework
<b>CTF-0</b>	The CTF synthesised by the trimerization of 1,3,5-tricyanobenzene
<b>CTF-0-I</b>	CTF-0 synthesised by the ionothermal method
<b>CTF-0-M</b>	CTF-0 synthesised by the microwave method
<b>CTF-1</b>	The CTF synthesised by the trimerization of 1,4-dicyanobenzene
<b>CTF-2</b>	The CTF synthesised by the trimerization of 2,6-dicyanonaphthalene
<b>DFT</b>	Density functional theory
<b>DOS</b>	Density of state
<b>EA</b>	Elemental analysis
<b>EDS, EDX</b>	Energy-dispersive X-ray spectroscopy
<b>EDTA</b>	Ethylenediaminetetraacetic acid
<b>EELS</b>	Electron energy loss spectroscopy
<b>EIS</b>	Electrochemical impedance spectra
<b>FTIR</b>	Fourier transform infrared spectroscopy
<b>FTO</b>	Fluorine doped Tin oxide
<b>GC</b>	Gas chromatograph

<b>GC-MS</b>	Gas chromatograph-mass spectrometer
<b>GO</b>	Graphene
<b>HOMO</b>	Highest occupied molecular orbital
<b>HRTEM</b>	High-resolution transmission electron microscopy
<b>IR</b>	Infrared
<b>LUMO</b>	Lowest unoccupied molecular orbital
<b>MeOH</b>	Methanol
<b>MOF</b>	Metal-organic framework
<b>NGO-QD</b>	Nitrogen-doped graphene oxide quantum dot
<b>NHE</b>	Normal hydrogen electrode
<b>NIR</b>	Near-infrared
<b>NMR</b>	Nuclear magnetic resonance
<b>OCT</b>	Oxygen-doped CTF-1
<b>PCP</b>	Porous coordination polymer
<b>PL</b>	photoluminescence
<b>PRC</b>	Proton reduction catalyst
<b>PXRD</b>	Powder X-ray diffraction
<b>RT</b>	Retention time
<b>SAC</b>	Single-atom catalyst
<b>SEM</b>	Scanning electron microscopy
<b>SSR</b>	Solid-state reaction
<b>STH</b>	Solar-to-hydrogen conversion
<b>TAS</b>	Time-resolved absorption spectroscopy
<b>TCB</b>	1,3,5-tricyanobenzene
<b>TCD</b>	Thermal conductivity detector
<b>TEM</b>	Transmission electron microscopy
<b>TEOA, TEA</b>	Triethanolamine
<b>TFMS</b>	Trifluoromethanesulfonic acid
<b>TFPT</b>	1,3,5-tris-(4-formyl-phoenyl) triazine
<b>TOF</b>	Turnover frequency
<b>TON</b>	Turnover number
<b>UPS</b>	Ultraviolet photoelectron spectroscopy
<b>UV/vis</b>	Ultraviolet-visible
<b>VB</b>	Valence band
<b>VBE</b>	Valence band edge
<b>VBM</b>	Valence band maximum
<b>XAFS</b>	X-ray absorption fine structure
<b>XPS</b>	X-ray photoelectron spectroscopy

XRD X-ray diffraction

### Roman symbols

<b>a</b>	Mass of the powdered absorbents
<b>A</b>	Absorbance (%)
<b>A<sub>T</sub></b>	Constant based on effective masses of electrons and holes
<b>C</b>	BET constant
<b>dp</b>	Depth of penetration
<b>e<sup>-</sup></b>	Electron
<b>E<sub>BG</sub></b>	Band gap (eV)
<b>h</b>	Planck's constant
<b>h<sup>+</sup></b>	Hole
<b>K</b>	Shape factor
<b>n</b>	Direct/indirect band gap transition variable, usually takes the values of 0.5, 2
<b>n<sub>1</sub></b>	Indices of refraction of the ATR crystal
<b>n<sub>2</sub></b>	Indices of refraction of the sample being probed
<b>N<sub>A</sub></b>	Avogadro's number
<b>P</b>	Partial vapour of adsorbate gas
<b>P<sub>0</sub></b>	Saturated pressure of adsorbate gas
<b>R</b>	Reflectance (%)
<b>S</b>	Absorption cross section of the powder
<b>T</b>	Transmission (%)
<b>V</b>	Molar volume of gas
<b>V<sub>a</sub></b>	Volume of gas absorbed at standard temperature and pressure
<b>V<sub>m</sub></b>	Volume of gas absorbed at standard temperature and pressure to produce an apparent monolayer
<b>ΔE<sub>H</sub></b>	Adjustment energy of each structure

### Greek symbols

<b>∅</b>	Work function dependent on both the spectrometer and the material
<b>α</b>	Absorption coefficient
<b>β</b>	Line broadening at the half the maximum intensity
<b>θ</b>	Angle of incidence
<b>ι</b>	Mean size of the ordered crystalline domains
<b>λ</b>	Wavelength of the incident light
<b>λ<sub>BG</sub></b>	Band gap wavelength
<b>ν</b>	Light frequency

# 1. Chapter 1

## Introduction

### 1.1 Background

It has been predicted that fossil fuels (including oil, coal and gas) will deplete in 2042, 2112 and 2046, respectively, calculated by the modified Klass model<sup>1</sup>. The consumption of fossil fuels also has brought out the large amount of greenhouse gas, which will lead to catastrophic climate change<sup>2</sup>. Therefore, it is very urgent for us to discover alternative sources of energy which is sustainable, clean and abundant<sup>3-4</sup>. Among all renewable energy sources, sunlight is the most abundant one in the world. Moreover, solar energy is clean and environmentally friendly. Therefore, finding a method to convert and store solar energy for the subsequent use is the primary goal for researchers in the field today. Brilliantly, plants show us how to utilise sunlight, which can oxidise water into O<sub>2</sub> and reduce CO<sub>2</sub> into glucose in the photosynthesis. Following the similar mechanism, an artificial system can be designed not only to oxidise the water by a light driven process to produce O<sub>2</sub> but also to drive the reduction of protons to yield hydrogen. Hydrogen has the highest energy density by weight as well as its combustion product is only water. At the same time, producing O<sub>2</sub> is the rate-determining and most energy-intensive step in the overall water splitting process. Due to these considerations, hydrogen and oxygen generation by visible-light-driven water splitting have been widely investigated.

### 1.2 Motivation

Since the first report about photocatalysis of TiO<sub>2</sub> to produce H<sub>2</sub> and O<sub>2</sub> in a photoelectrochemical cell<sup>5</sup>, numerous semiconductor photocatalysts<sup>6-7</sup> have been reported in the last four decades.

Considering that the intense irradiance of sunlight is mainly in the visible region as shown in Fig. 1, the discovery of economic and sustainable photocatalysts active and efficient under visible light irradiation is a key target but very challenging. Spectacular advances have been made on inorganic nanomaterials<sup>8-10</sup>, however, most of them are either only active under the UV light irradiation or their efficiency was very moderate, due to either wide band gaps or fast charge recombination<sup>11-13</sup>. Very recently conjugated polymers<sup>8</sup> attracted particular interests they are much closer to biological systems in composition and their electronic structure can be tuned readily. In particular, these organic photocatalysts are able to overcome the weakness of inorganic materials, namely heavily metals with significant toxicity<sup>14</sup> and limited concentration of active sites<sup>15</sup>. Until right now, in spite of the wide application of conducting polymers in the photovoltaics<sup>16</sup>, the influence of these polymers on water splitting technology remains minor.

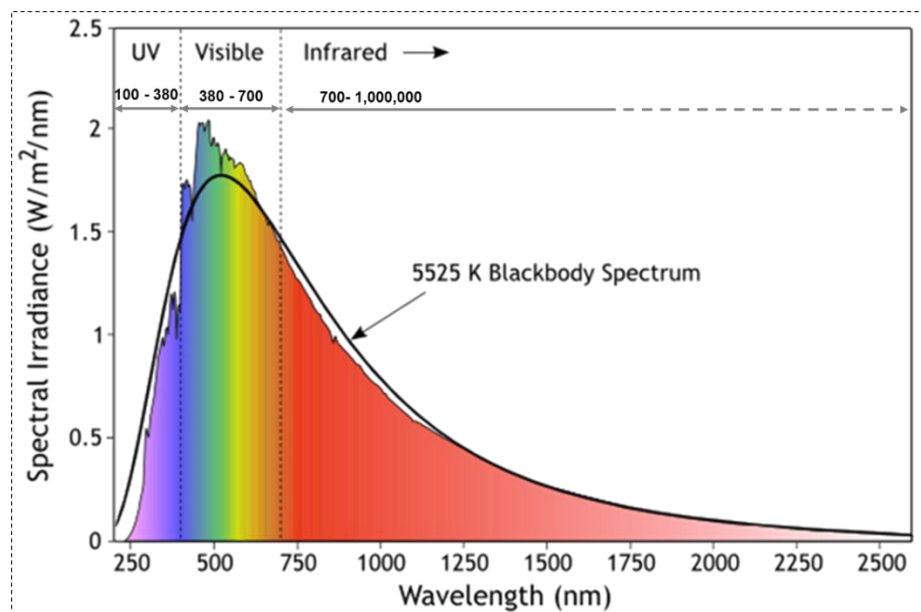


Figure 1. Solar irradiance spectrums above atmosphere and at surface. Extreme UV and X-rays are produced (at left of wavelength range shown) but comprise very small amounts of the Sun's total output power.

Recent advances in synthetic chemistry have shown the success of fabricating the 2D organic CTFs. These porous polymers can change the parameters flexibly, such as C/N/H ratio, pore size and surface area. Moreover, there are two potentials that result into the possibility of organic photocatalysts for water splitting. Firstly, CTFs have the similar structure and chemical properties to the graphitic carbon nitride (g-C<sub>3</sub>N<sub>4</sub>), which has been studied since 2006<sup>17</sup> and is suitable for the photocatalytic application on visible-light-driven water splitting but with a relatively large band gap of 2.7 eV<sup>8</sup>. Secondly, these thermalised triazine frameworks are porous and their band gaps can be modified to match to the solar spectrum.

### 1.3 Objectives

Here, the aim of the project is to realise the overall water splitting on polymer semiconductors under visible light irradiation which has hardly been reported. The most important aspect of realising the overall water splitting by a polymer semiconductor is the design of the suitable z-scheme system composed of two suitable photocatalysts with matching electronic structure or a single photocatalyst with the suitable co-catalysts. Basically, suitable photocatalysts available in the water splitting system under visible light irradiation has to satisfy the following three requirements, as shown in Fig. 2<sup>18-19</sup>: (i) The photocatalyst must have a relatively narrow band gap to absorb visible light as much as possible; meanwhile, the bottom of its conduction band has to be more negative than the reduction potential of water to produce H<sub>2</sub> or the top of its valance band has to be more positive than the oxidation potential of water to produce O<sub>2</sub>. (ii) It's essential to make sure the photogenerated charge carriers can separate efficiently and move to the surface reaction sites simultaneously. (iii) The photocatalysts have low overpotential for water reduction or oxidation reactions.

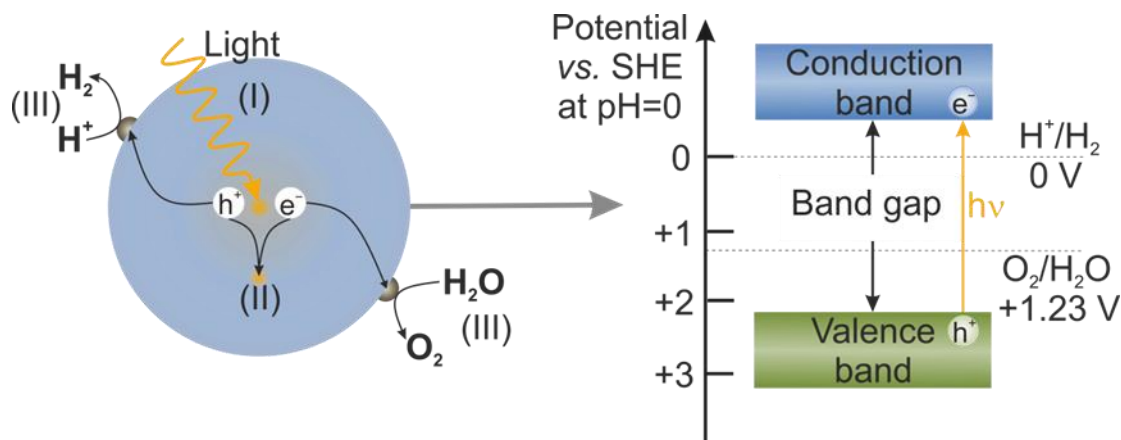


Figure 2. The main processes and the principle of photocatalytic water splitting on semiconductor photocatalysts.

However, there are always conflicts appearing on these requirements in practice and thus some compromises have to be made. Therefore, the ultimate target of this project is to design a cost-effective, highly efficient and stable polymer photocatalytic system for overall water splitting in a suspension system driven by visible light. In details, the objectives of this project can be summarised as below:

- (1) Design the efficient and stable photocatalysts for  $O_2$  evolution based on CTFs, e.g. CTF-0, CTF-1 and CTF-2 as well as the modified CTFs.
- (2) Design the efficient polymer photocatalysts for  $H_2$  evolution, e.g. CTF-0, CTF-1 and CTF-2
- (3) Maximise photocatalytic performance by optimizing the reaction conditions, such as pH, the concentration of the scavengers, and the different efficient cocatalysts;
- (4) Exploring the mechanism of charge transfer in polymer photocatalysts. Some assumption of the mechanism will be verified by using density functional theory (DFT) to probe the electronic structures and optical properties of prospective modified structures;
- (5) Realizing the overall water splitting on a single photocatalyst.

## 1.4 Outline

This project will focus on developing an efficient polymer photocatalyst based on CTFs to produce H<sub>2</sub> and O<sub>2</sub> from water under visible light irradiation, in which the only feedstocks are sunlight and water. In the first chapter, the background of energy source and motivation to convert solar energy into chemical fuels via solar-driven water redox route is discussed. The fundamental principle of water redox (i.e. photo induced charge carriers' generation, charge carriers transfer mechanisms on the surface of the photocatalysts in a suspension system and surface kinetics for water oxidation or reduction reaction), key factors for solar water redox, strategy for an optimised photocatalyst active under visible light in a suspension system, and the materials development for photocatalysis will be introduced in Chapter 2. The methodology used for material synthesis, characterization and performance test will be described in Chapter 3. In Chapter 4, oxygen-doped covalent triazine polymers (OCT) will be investigated as a photocatalyst for oxygen and hydrogen evolution. The recent work on CTF-0 as a photocatalyst will be discussed in the Chapter 5. The overall water splitting on CTF-0 decorated by the cocatalysts will be explored in the Chapter 6. The conclusion on strategies to optimise CTFs to realise the entire water splitting into hydrogen and oxygen, and the mechanism and the factor influencing the activity will finally be summarised in Chapter 7. Ultimately, the further requirement for detailed mechanism, the application of CTFs on the commercial scale and the factors affecting pure water splitting efficiency will be discussed in Chapter 8.

## 2. Chapter 2

### Literature review

#### 2.1 Principle of photocatalytic water splitting

In Chapter 1.3, Fig. 2 shows the major three steps of photocatalytic water splitting. The first step is the absorption of photons to generate pairs of electron and holes (I). Afterwards these charges will separate and migrate to the reaction sites or recombine together (II). Finally, electrons or holes react with water molecules to evolve O<sub>2</sub> or H<sub>2</sub>, respectively (III).

The key of the first step is that the energy of incident light should be larger than the band gap of the irradiated photocatalyst, resulting in the excitation of the electrons from the valence band (VB) to the conduction band (CB), and holes left in the VB. Numerous oxide photocatalysts were found to be active in the visible region<sup>20,21</sup>, which means their band gap is narrower than 2.95 eV corresponding to the wavelength of 420 nm based on the equation 1. At the same time, the bottom level of the CB should be more negative than the reduction potential of H<sub>2</sub>O/H<sub>2</sub> (0 eV vs. Normal Hydrogen Electrode (NHE), pH=0), while the top level of the VB should be more positive than the oxidation potential of O<sub>2</sub>/H<sub>2</sub>O (+1.23 eV vs. NHE, pH=0). Therefore, the theoretical minimum band gap for water splitting is 1.23 eV that corresponds to light about 1100 nm based on the equation 1. In short, the width of the band gap and the levels of the CB and VB are extremely important for semiconductor photocatalysts, which is the footstone for the second and the third step.

*Equation 1. The absorbed light wavelength is directly related to the band gap size*

$$\text{band gap (eV)} = \frac{1240}{\lambda} \text{ (nm)}$$

Dynamically, the charge generation is at picosecond timescale and these electrons and holes will be separated and transferred to active sites on the surface of photocatalyst powders at nano- to microsecond timescale while surface reaction for water splitting is extremely slow at microsecond to second timescale due to the slow rate determine step of O<sub>2</sub> production in the third step<sup>22-23</sup>. Thus, it needs much longer life time electron-hole pairs to realise efficient water redox reactions on the surface. However, the recombination of charger carriers competes with the last step<sup>22, 24</sup>. As a result, it is challenging to keep the life time of electrons and holes long enough against the recombination of electrons and holes. Here, a cocatalyst can solve this problem as enhancing the charge separation by forming a Schottky junction with semiconductors<sup>25</sup>. For the half reactions of water splitting, appropriate sacrificial reagents can also prevent the recombination of electrons and holes efficiently by extracting one type of charge carriers, leaving the other carrier to react with water and to produce hydrogen or oxygen<sup>25</sup>, as explained in chapter 2.2.5.

The reaction rate of the last step is important for the whole photocatalytic process. The reason is not only that the competition of the recombination of charge pairs will reduce the concentration of reacted charges, but also that the desorption rate of the created H<sub>2</sub> or O<sub>2</sub> molecules is much slower, limiting the surface reaction dynamically<sup>23</sup>. In addition, water redox will take place when the practical potential meets the energetic requirements, which has to be much higher than the minimum required to overcome overpotential and other system losses<sup>26</sup>. Therefore, the slowdown of charge recombination is the most important step and improving the surface chemical reactions is highly important in the research field, which has a great meaning for the improvement of the conversion efficiency from solar energy to chemical fuels.

## **2.2 Key factors influencing the photocatalytic performance of semiconductor photocatalysts**

According to the main process in photocatalytic water redox, there are a few key factors that influence the photocatalytic performance of semiconductor photocatalysts, including doping, architecture parameters, cocatalysts, the solution pH and sacrificial and mediator reagents as explained in the following.

### **2.2.1 Band gap changes by doping**

As shown in Fig. 2, when light of high enough energy is irradiating on the surface of the photocatalysts, electrons are promoted from the VB to the CB, and the concomitant oxidation and reduction process take place. The materials, who have band gaps wider than 3.10 eV as mentioned in chapter 2.1, are not active under visible light irradiation, especially for TiO<sub>2</sub>, which is among the semiconductors of highest photocatalytic activity but requires irradiation with light of wavelength shorter than the absorption band onset (~400 nm)<sup>27-28</sup>. Thus, metal doping or doping with no-metallic elements have become an intense forefront aimed at expanding the photoresponse of the materials with wide bandgaps to the visible region. Doping anions (e.g. N, C and P) or cations (e.g. Cr, Ni, Ta, Sb and Fe) in the UV-active photocatalysts can provide new VB or CB positions between the original VB and CB positions, thus reducing the band gap and increasing the range of light responsiveness as shown in Fig. 3<sup>29</sup>. To a short sum up, doping is an efficient method for extending the light-absorption range of the individual photocatalysts to achieve activity under visible light as well as UV light irradiation.

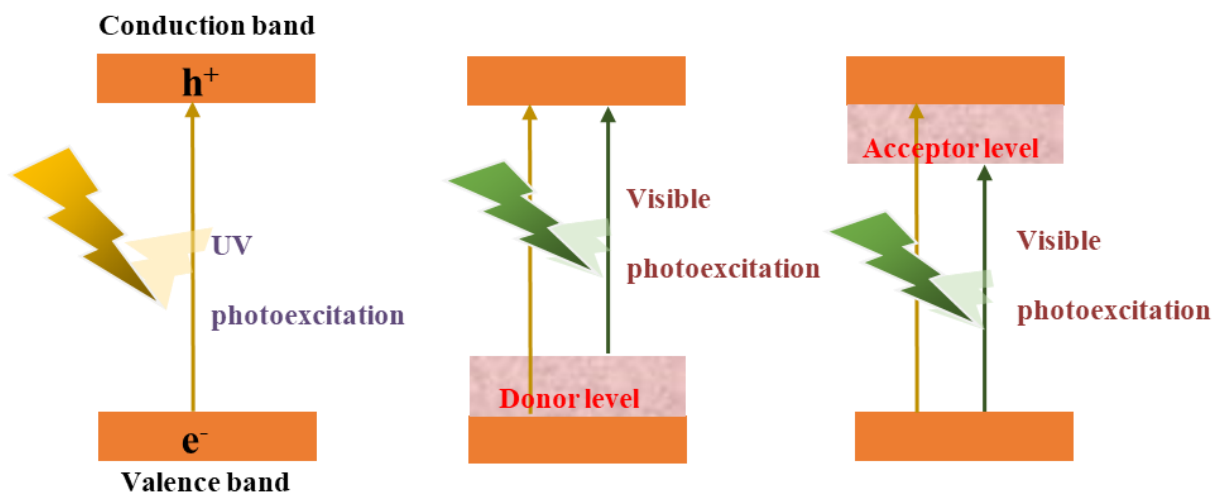


Figure 3. Formation of new valence and conduction bands by electron donor and acceptor atoms, enabling a UV-active material to respond to visible light.

### 2.2.2 Architecture parameters

The separation and migration of photogenerated electrons and holes and the surface chemical reaction of H<sub>2</sub> or O<sub>2</sub> evolution are also affected by their architectures, such as morphology, the crystal structure, particle size and surface area<sup>28, 30</sup>. The improvements on the morphology of the photocatalysts can increase the reflection and scattering of incident light among its constituent nanoparticles<sup>28</sup>. For example, Cu<sub>2</sub>O with different morphologies, such as spherical particles, porous spherical particles, cubes and octahedral could be obtained via adjusting the concentration of NH<sub>3</sub> solution during the synthesis<sup>31</sup>. The edge lengths of octahedral could be easily tuned from 130 to 600 nm via adjusting the NaOH concentration. As a result, the octahedral Cu<sub>2</sub>O particles showed the better absorption ability and photocatalytic activity than the cubic particles as shown in Fig. 4<sup>31</sup>. Usually, changing the morphology can also adjust the particle size and crystallinity. Photogenerated charges are extremely easy to be trapped and recombine at

boundaries and defects. Thus, if the crystallinity is much better, the defects and boundaries will become less, which will improve the photocatalytic activity. Normally, the crystallinity can be improved by calcination in the suitable temperature, which can change the crystal structure and surface area as well<sup>32</sup>. Generally, the specific surface area (as determined by BET measurements) is relevant to the particle size. Experimentally, it was reported that the smaller particle size and the higher crystallinity of the NiO/NaTaO<sub>3</sub>:La photocatalyst powder (0.1-0.7 $\mu$ m)<sup>33</sup> showed the higher efficiency of water splitting into H<sub>2</sub> and O<sub>2</sub> than the nondoped NaTiO<sub>3</sub> crystal (2-3 $\mu$ m), and the reason was that the small particle size with a high crystallinity was advantageous to an increase in the probability of the reaction of photogenerated electrons and holes with water molecules against the recombination. The small particle size to some extent brings about the quantum size effect especially in colloidal system, resulting in widening a band gap and blueshift in the absorption spectrum, which increases driving force and also leads to higher activity<sup>18</sup>. In conclusion, optimising the practical hydrogen or oxygen evolution rate is based on the balance of the various parameters of the architecture mentioned above.

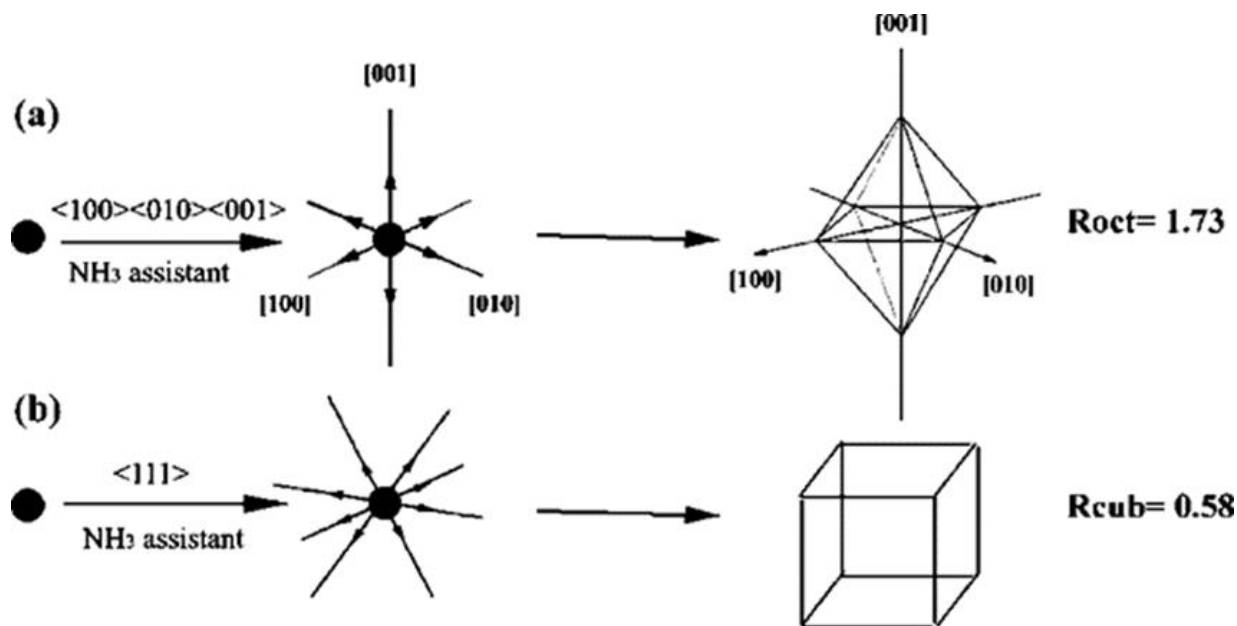


Figure 4. Schematic illustration of the growth mode of  $\text{Cu}_2\text{O}$  (a) Octahedra and (b) Cubes. The ammonia solution with a certain concentration may favour the preferential crystal growth along the  $\langle 100 \rangle$  direction and make it far exceed that of  $\langle 111 \rangle$ , thus  $\{100\}$  faces shrink<sup>31</sup>.

### 2.2.3 Cocatalysts

The CB levels of many oxide photocatalysts are not negative enough to overcome the overpotential and provide the driving force dynamically for hydrogen evolution. Co-catalysts such as  $\text{Pt}$ <sup>34</sup>,  $\text{RuO}_2$ <sup>35</sup>,  $\text{Ni}/\text{NiO}$ <sup>36</sup> usually require a small overpotential and also provide more active sites for the photocatalysis. At the same time, these cocatalysts can form the Schottky junctions with semiconductors and enhance charge separation on the photocatalysts. Not only water reduction but also the water oxidation can be enhanced by cocatalysts. The most common cocatalysts for oxygen production in the half water oxidation reaction are  $\text{PtO}_x$ <sup>37-38</sup>,  $\text{IrO}_x$ <sup>39</sup> and  $\text{CoO}_x$ <sup>40-42</sup>. However, it is not crucial for photocatalytic  $\text{O}_2$  evolution to load co-catalysts on oxide photocatalysts, because their VBs are usually much more positive than the redox potential of  $\text{O}_2/\text{H}_2\text{O}$  (+1.23 V vs. NHE). But one molecular  $\text{O}_2$  is formed by oxidising water by four holes,

which is kinetically more challenging than the two-electron reduction of  $\text{H}_2\text{O}$  into one molecular  $\text{H}_2$ <sup>43</sup>, so active sites on cocatalysts for four-hole oxidation of water are very helpful to enhance the  $\text{O}_2$  evolution rate. For example, in the NiO loaded  $\text{NaTaO}_3$  doped with lanthanum system<sup>33</sup>,  $\text{H}_2$  was produced on the ultrafine NiO particles while the  $\text{O}_2$  evolution proceeded on the groove of  $\text{NaTaO}_3\text{:La}$  nanostep structure (Fig. 5), which contributed to the highly efficient water splitting into  $\text{H}_2$  and  $\text{O}_2$  stoichiometrically.

Furthermore, the catalytic performance of cocatalysts can be significantly influenced by their physical and chemical properties, such as particle size and valence states. Usually the more active sites on the photocatalysts, the better performance the photocatalysts will have. But in most cases, the more active sites induced by cocatalysts would lead to the lowered light absorption of the photocatalysts due to a shielding effect. Therefore, optimising the loading amount of the cocatalysts should be considered to obtain the maximum activity of water splitting under light irradiation. Because the low-coordinated metal atoms often function as the catalytically active sites, the specific activity per metal atom usually increases with decreasing size of the metal particles. The ultimate small size for metal particles is the single-atom catalyst (SAC), which contains isolated metal atoms singly dispersed on the surface of the photocatalysts. SACs maximise the efficiency of metal atom use. Moreover, with well-defined and uniform single-atom dispersion, SACs often great potential for achieving high activity and selectivity<sup>44-49</sup>. For example, isolated metal atoms (Pt, Pd, Rh or Ru) stably by anchoring on  $\text{TiO}_2$  by a facile one-step method led to a 6-13-fold increase in photocatalytic activity over the metal clusters loaded on  $\text{TiO}_2$  by the traditional method, as well as enhancing the stability of the photocatalysts<sup>46</sup>. Both measurements and first-principle calculations illustrated that introducing the single-atom Pt could optimise the performance of  $\text{TiO}_2$  catalyst in photocatalytic  $\text{H}_2$  evolution. Moreover, the

catalytic activity of the isolated Pt atoms could be even better than that of the metallic Pt deposited on  $\text{TiO}_2$ , owing to the decreased  $\text{H}^\ddagger$  adsorption energy on Pt and increased exposing reaction sites, which is closer to the optimum thermodynamically<sup>46</sup>.

Cocatalysts, by definition, should lower the activation energy of the reaction taking place at their surfaces. In photocatalysis, the ‘cocatalyst’ term is often incorrectly used for any surface decoration which improves the charge separation and therefore decreases the recombination rate but cannot reduce the activation energy. Although such effect is in general desired, it has nothing to do with a real catalytic process.

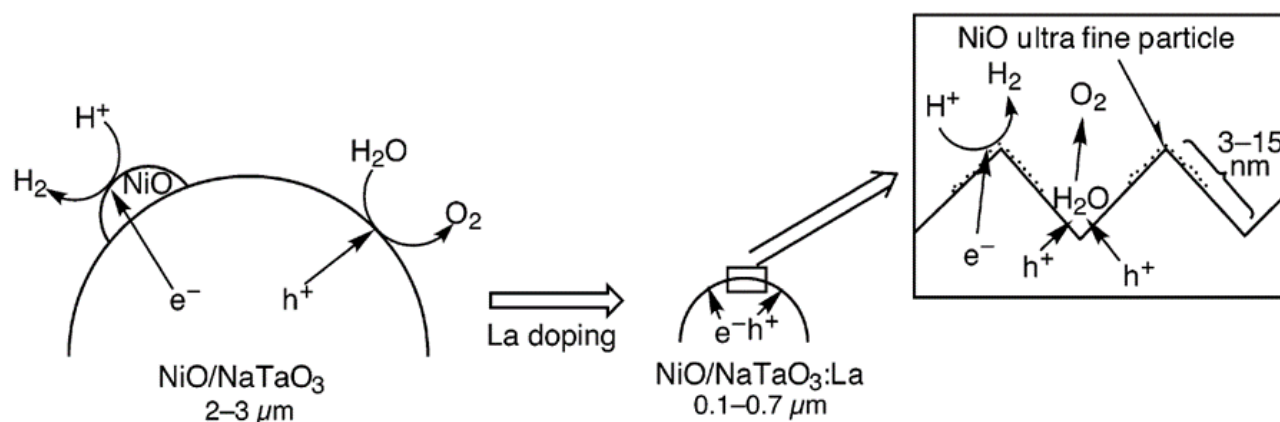


Figure 5. Mechanism of highly efficient photocatalytic water splitting over  $\text{NiO}/\text{NaTaO}_3:\text{La}$  photocatalysts. The small particle size and the ordered surface nanostep structure created by the lanthanum doping contributed to the suppression of recombination between the photogenerated electrons and holes and the separation of active sites to avoid the back reaction, resulting in the highly efficient water splitting into  $\text{H}_2$  and  $\text{O}_2$ <sup>33</sup>.

## 2.2.4 The solution pH

Because the different pH can change the band edge levels, surface chemistry and the states of compounds in a suspension system, the solution pH is one of the key factors influencing the semiconductor photocatalysis, especially in a Z-scheme water splitting system. The suitable pH in an  $\text{Fe}^{3+}/\text{Fe}^{2+}$  redox system is limited to the acidic condition because iron ions undergo precipitation to give iron hydroxide in neutral and basic conditions. On the other hand, it is possible to perform a reaction in a wide range of pH when an  $\text{IO}_3^-/\text{I}^-$  couple is employed. One comprehensive study illustrated these aspects, in which a Pt-TiO<sub>2</sub>-anatase/TiO<sub>2</sub>-rutile system was fabricated<sup>50</sup>. It was found the basic pH condition was favourable for the overall water splitting with the presence of  $\text{IO}_3^-/\text{I}^-$ . The reason was that the main oxidative product over Pt-TiO<sub>2</sub> anatase was  $\text{I}_3^-$  at the acidic conditions, which caused a light loss due to the strong absorption of the  $\text{I}_3^-$  anion around 350 nm. On the contrary, the basic condition was more favourable for efficient water splitting because the redox cycle of  $\text{IO}_3^-/\text{I}^-$  mainly took place in this condition. This research also discussed the different pH led the different thermodynamic standpoint of the reactions. The oxidation of water was a thermodynamically less favourable reaction compared with the oxidation of  $\text{I}^-$ , and preferentially proceeded over TiO<sub>2</sub>-rutile than TiO<sub>2</sub>-anatase even in the presence of  $\text{I}^-$ . However, in a Pt-SrTiO<sub>3</sub>:Cr/Ta and Pt-WO<sub>3</sub> system, the water splitting reaction would be carried out in a neutral condition around pH=7 with the presence of  $\text{IO}_3^-/\text{I}^-$  pairs because WO<sub>3</sub> was unstable in basic conditions. This paper comprehensively indicates the pH condition is a crucial factor to be considered in the water redox especially Z-scheme water splitting system.

On the other side, adjusting the suitable pH value could also improve the stability of the photocatalysts and reactant species. For example, the photocatalytic performance of RuO<sub>2</sub>-loaded

GaN:ZnO<sup>51</sup> was found to be strongly dependent on the pH value of the aqueous solution. The activity increased as the pH decreased from pH=7, passing through a maximum at pH=3, and then decreased. The reason was that (oxy)nitride materials usually had an inherent instability in basic media but were stable in acidic media, resulting in the highest activity at pH=3.

The above studies all indicate that adjusting the proper pH in a suspension system can improve the hydrogen or oxygen evolution rate due to acquiring better reaction environments including the stability of reactants, the chemical states of sacrificial reagents, the absorption intensity at the certain wavelength and the thermodynamic states of reactants.

### **2.2.5 Sacrificial and mediator reagents**

The half reaction of water reduction into H<sub>2</sub>, in particular oxidation into O<sub>2</sub> is very inefficient due to rapid recombination of the excited holes and electrons on the surface of the photocatalyst. But the higher gas production can be achieved by the addition of a suitable sacrificial reagent (a hole or electron scavenger). In principle, the sacrificial reagent tends to react with one type of charge carrier while the other type of carrier reacts with water to produce hydrogen or oxygen. A hole scavenger (an electron donor) can consume the generated holes on the surface of the photocatalyst and the left electrons are used for water reduction reaction. On the opposite side, an electron scavenger (an electron acceptor) can react with the generated electrons and the left holes are consumed in the water oxidation reaction. Theoretically, the hole scavengers must have stronger power to capture photoexcited holes than water due to their less positive potential, while the electron scavengers must be more readily reduced than water by photoexcited electrons<sup>19</sup>. Methanol<sup>52</sup>, ethanol<sup>53</sup>, ethylenediaminetetraacetic acid (EDTA)<sup>54</sup>, triethanolamine (TEA or TEOA)<sup>55</sup> and an aqueous solution of K<sub>2</sub>SO<sub>3</sub> + Na<sub>2</sub>S<sup>56</sup> or Na<sub>2</sub>SO<sub>3</sub> + NaS<sup>57</sup> are widely acknowledged

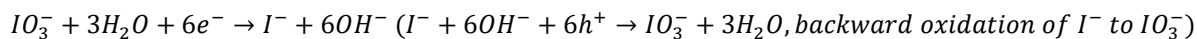
as good electron donors for the photocatalytic hydrogen evolution, whereas the metal salts such as  $\text{AgNO}_3$ <sup>58</sup>,  $\text{Na}_2\text{S}_2\text{O}_8$ <sup>59</sup>,  $\text{KIO}_3$ <sup>60</sup> and  $\text{NaIO}_3$ <sup>61</sup> are usually used as electron scavengers.

Different from sacrificial reagents, redox mediators take the necessary roles in the Z-scheme system or a dual system (Fig. 6). The mediator shuttles usually have two different molecules, so that they can capture the electrons from one semiconductor as well as the holes from the other semiconductor. At the same time, these two molecules take the redox reactions, so that they can return to their original chemical states. More importantly, it needs two different photocatalysts, in which one can provide the excited holes to recombine with one mediator molecule and the left excited electrons for  $\text{H}_2$  evolution, and the other can provide the excited electrons to recombine with hole mediators and the left excited holes for  $\text{O}_2$  evolution in the water splitting system as shown in Fig. 6. The most popular mediators are  $\text{IO}_3^-/\text{I}^-$ <sup>38</sup>,  $\text{I}_3^-/\text{I}^-$ <sup>37, 43</sup> and  $\text{Fe}^{3+}/\text{Fe}^{2+}$ <sup>37, 43</sup>. The use of these mediator molecules is, however, not free of some serious drawbacks. For example, the pairs of  $\text{IO}_3^-/\text{I}^-$  require the exchange of six electrons<sup>50</sup>, as shown in equation 2, and proceed in neutral or basic media. This process is often a very slow step and requires an effective cocatalyst, such as Pt or  $\text{PtO}_x$ . Moreover, an unwanted side reaction (competing with water splitting) leading to the  $\text{I}_3^-$  production takes place at low pH as shown in equation 3.  $\text{I}_3^-$  ions absorb efficiently UV and visible light and play the role of a light shield<sup>50</sup>. Similarly, the  $\text{Fe}^{3+}/\text{Fe}^{2+}$  redox pairs appear reversible only at pH lower than 2, since at higher pH precipitation of  $\text{Fe}(\text{OH})_3$  takes place<sup>62</sup>.

Non-sacrificial Z-scheme water splitting is the eventual goal for the artificial conversion of solar energy into renewable chemical fuels<sup>43</sup>. Especially, the all-solid-state Z-scheme photocatalytic systems without redox mediators have been recently reported in water splitting, as it can avoid the undesirable backward reactions and shorten the path of Z-scheme electron transfer<sup>63</sup>. However, the non-sacrificial Z-scheme system has some drawbacks compared to the one-step

system, such as a higher complexity and double photons are needed for producing the same amount of charges reacted<sup>63</sup>.

Equation 2.



Equation 3.

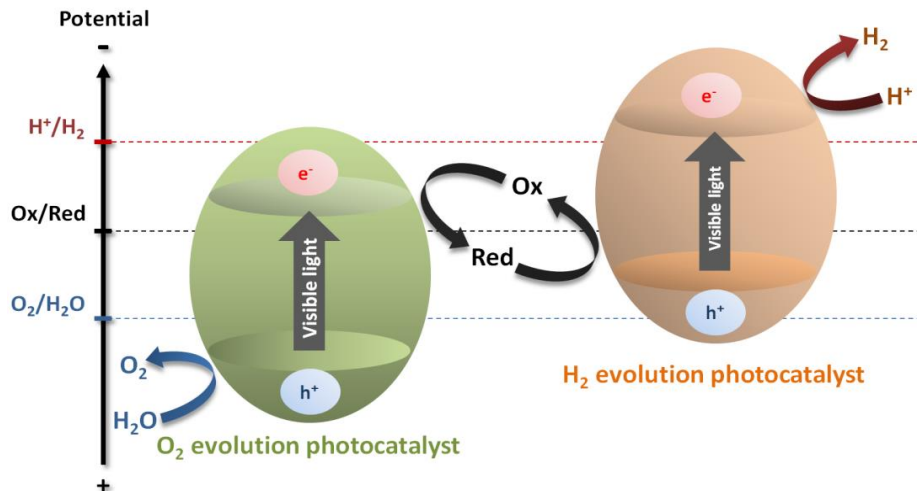


Figure 6. Schematic of the principles of Z-scheme water splitting system.

### 2.3 Material development on photocatalytic water reduction and oxidation in a suspension system

In order to highlight recent developments and to identify promising directions in the increasingly complex research area of photocatalytic water reduction and oxidation in a suspension system, this section summarises the known inorganic and organic photocatalysts and discusses property-activity relationships with a focus on structural features.

### 2.3.1 Inorganic semiconductors

This project mainly focuses on the research of organic materials, due to their facile synthesis, appealing electronic band structure, high physicochemical stability and 'earth-abundant' nature. But before introducing the organic materials, vast of inorganic materials have been explored as visible-light-responsive photocatalysts, which is illustrated below as a footstone in the history of the light-responsive photocatalysts. The inorganic photocatalysts are usually composed of active metal cations and organic elements (oxygen, sulphur, nitrogen). Fig. 7 illustrated the common transition-metal and main-group-metal cations that act as active cation components in a water splitting photocatalyst. The typical metal cations with filled d orbitals (red and green colour) that can form suitable band-gap structures of the corresponding oxide materials, which have been successfully applied as photocatalysts for water splitting<sup>64</sup>. The transition-metal cations with partly filled d electrons are widely used as the cocatalysts to promote the performance of the photocatalysts<sup>65</sup>. This section will mainly focus on the typical and most common photocatalysts, starting with the TiO<sub>2</sub>, perovskites, metal(oxy)nitrides, metal sulphides, metal phosphides, WO<sub>3</sub>, BiVO<sub>4</sub>, Ag<sub>3</sub>PO<sub>4</sub>, metal-organic frameworks, *etc.*.

1	2	3	4	5	6	7	8	9	10	11	12	13	14	15	16	17	18
H																	He
Li	Be											B	C	N	O	F	Ne
Na	Mg											Al	Si	P	S	Cl	Ar
K	Ca	Sc	Ti	V	Cr	Mn	Fe	Co	Ni	Cu	Zn	Ga	Ge	As	Se	Br	Kr
Rb	Sr	Y	Zr	Nb	Mo	Tc	Ru	Rh	Pd	Ag	Cd	In	Sn	Sb	Te	I	Xe
Cs	Ba	Ln	Hf	Ta	W	Re	Os	Ir	Pt	Au	Hg	Tl	Pb	Bi	Po	At	Rn
Fr	Ra	An	Rf	Db	Sg	Bh	Hs	Mt	Ds	Rg	Cn	Uut	Uuq	Uup	Uuh	Uus	Uuo
	Ln:	La	Ce	Pr	Nd	Pm	Sm	Eu	Gd	Tb	Dy	Ho	Er	Tm	Yb	Lu	
	An:	Ac	Th	Pa	U	Np	Pu	Am	Cm	Bk	Cf	Es	Fm	Md	No	Lr	

Figure 7. Principal cation components of semiconductor photocatalysts for water splitting. The red and green colour elements are the typical metal cations with filled d orbitals having a  $d^0$  and  $d^{10}$  electronic configuration, respectively, widely used as active photocatalysts for water splitting. The blue colour elements are the transition-metal cations with partly filled d electrons (i.e.,  $d^n$  electronic configuration:  $0 < n < 10$ ), usually functioning as cocatalysts in the photocatalytic water splitting systems.

## TiO<sub>2</sub>

Titania (TiO<sub>2</sub>) was the first material applied as a photochemical water-splitting catalyst successfully by Fujishima and Honda<sup>5</sup>. They found that the photolysis of water into H<sub>2</sub> and O<sub>2</sub> was greatly affected by the nature of surface defects. However, the wide band gap of TiO<sub>2</sub> results in the only UV-active photocatalytic performance, limiting its application in the visible light range. It crystallises in three structure types: rutile, anatase and brookite. TiO<sub>2</sub> (anatase, rutile and brookite) and lepidocrocite-type titanate are constructed of basic TiO<sub>6</sub> octahedral structure unites. Their band gaps are slightly different (3.0 eV for rutile, 3.2 eV for anatase and 3.3 eV for brookite)<sup>66</sup>.

Due to the nontoxicity, abundance (inexpensiveness), thermal/chemical stability, and high redox potential of TiO<sub>2</sub>, the extensive efforts have been made to improve its photocatalytic activity under both UV and visible light irradiation, mainly from the surface area, particle size, ratio of polymorphs, type of dopants, defect concentration and phase purity<sup>67-71</sup>. As a summary, Table 1 shows the main features of the different procedures for the development of TiO<sub>2</sub> photocatalyst. The chemical synthesis methods used for the doping of trace impurities into TiO<sub>2</sub> usually include high temperature sintering in different atmospheres, wet chemical methods such as sol-gel processes, hydrothermal treatment, spray pyrolysis and supercritical methods. Besides the chemical doping methods, physical doping methods, including transition metal ion-implantation techniques, also effectively incorporated anions or transition metal ions into TiO<sub>2</sub> to prepare visible light-responsive TiO<sub>2</sub> photocatalysts<sup>72</sup>. Especially, Pd nanoparticles anchored on the tetrahedrally coordinated Ti oxide moiety within the zeolite frameworks had contributed to the high reactivity of the electron-hole pair excited in the Ti-oxide sites by investigations employing various molecular spectroscopies such as XAFS and TEM<sup>73</sup>. The photocatalytic reactions on such single site oxide catalysts have subsequently been investigated by various research groups<sup>45, 47, 49, 74-76</sup>. Recently, the sensitizing effect of the surface plasmon resonance absorption by metal nanoparticles has been considered to also be a promising approach for the development of visible light-responsive TiO<sub>2</sub> photocatalysts<sup>72</sup>. Furthermore, a new class of inorganic-organic materials called metal-organic frameworks (MOFs) or porous coordination polymers (PCPs) has emerged, and attention has been focused on their photocatalytic properties under visible light irradiation<sup>77</sup>. Especially, the recent milestone to improve visible and infrared optical adsorption was engineering the disorder of nanophase TiO<sub>2</sub> with simultaneous dopant incorporations<sup>52</sup>. In its simplest form, a disorder in the surface layers of nanophase TiO<sub>2</sub> was introduced by hydrogenation. The disorder-engineered black TiO<sub>2</sub> nanocrystals obtained 24% of the quantum

efficiency for hydrogen production. It could more efficiently harvest the infrared photons for photocatalysis than bulk anatase, presumably due to the localization of both photoexcited electrons and holes preventing fast recombination as suggested by authors<sup>52</sup>.

Table 1. Summary of TiO<sub>2</sub> modification approaches for photocatalytic applications, except dye sensitisations<sup>52</sup>.

doping elements		TiO <sub>2</sub> based Junction
<b>Main elements and compounds used</b>	Non-metal dopants and co-dopants: N, C, S, F;  Metal dopants: transition metals (Cu, Fe, Mn, Ni, V, Zn, Zr, etc.); noble metals (Ag, Au, Os, Pd, Pt, Ru, Rh, IR, etc.); rare earth metals (Sc, Y, La, etc.).	CdS, Fe <sub>2</sub> O <sub>3</sub> , CdSe, ZnO, SnO <sub>2</sub> , WO <sub>3</sub> , or V <sub>2</sub> O <sub>5</sub> , Bi <sub>2</sub> S <sub>3</sub> .
<b>Objectives</b>	To enhance the photocatalyst response to visible light  To promote the separation between electron-hole pairs to enhance photocatalytic activity	
<b>Drawbacks</b>	Metal ions may also serve as recombination centres for electron-hole pairs, thus reducing the overall photocatalytic activity	Possible aggregation/dissolution during the photocatalytic reaction

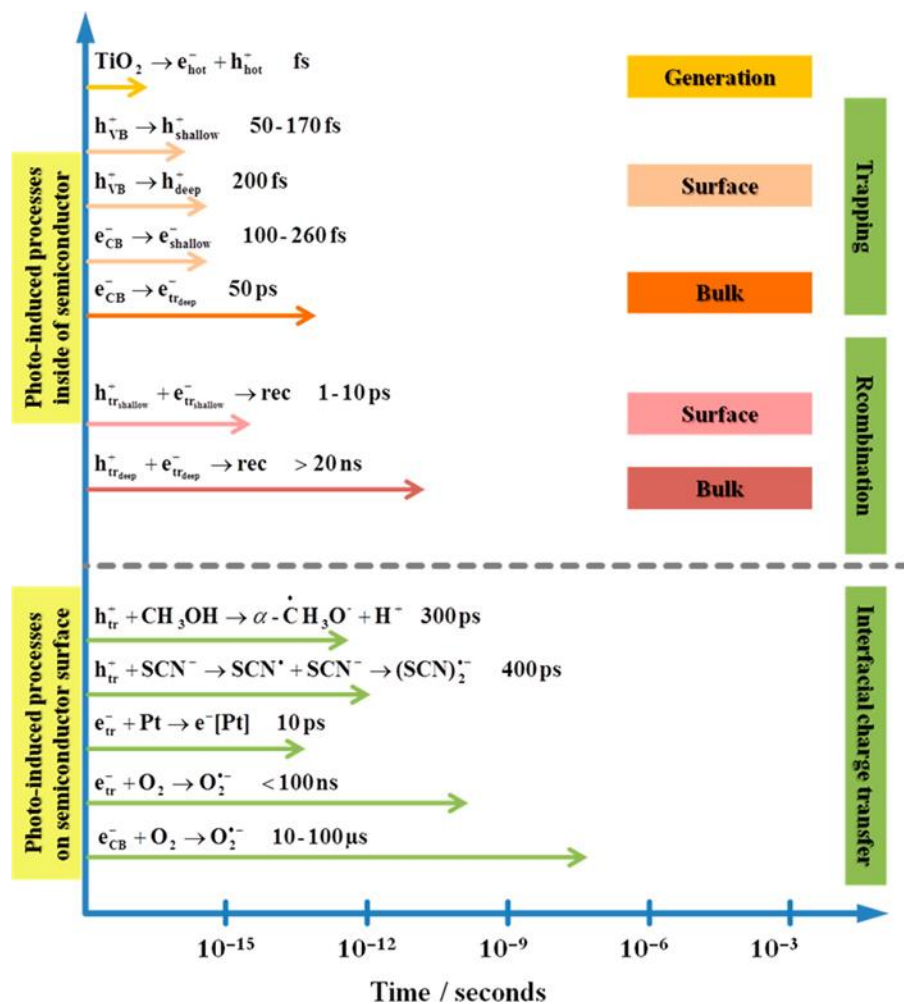


Figure 8. Photoinduced reactions in  $\text{TiO}_2$  photocatalysis and the corresponding time scales<sup>72</sup>.

For a better design of the photocatalytic systems, it is important to understand the photocatalytic reaction mechanism. Thus, various fundamental studies concerning the initial and very fast photocatalytic process, induced by the absorption of a photon, the energy of which exceeds the bandgap energy of the photocatalyst, inside and at the surface of the semiconductor, have been carried out at the same time. Fig. 8 provides an overview of the possible photoinduced steps inside and on the surface of a  $\text{TiO}_2$  photocatalyst in the time scale region from femtoseconds to microseconds. The reaction dynamics of the photogenerated charge carriers in  $\text{TiO}_2$ , are usually obtained by means of time-resolved absorption spectroscopy (TAS), being a widely employed

technique to study the formation, relaxation, recombination, and transfer processes of photogenerated charge carriers in photocatalysts. The mechanism of redox processes induced in a photocatalytic system by light absorption is presented in Fig. 2, in which the absorption of a photon with an energy exceeding its bandgap energy generates an electron/hole pair (process I) that either recombines (process II) or induces two redox processes (process III), both of which take place in close vicinity on the particle's surface. However, considerable evidence has been collected that this mechanistic picture is highly oversimplified<sup>78-82</sup>. A so-called "antenna effect" has been observed by various research groups<sup>79, 83</sup>. Excitons formed through the absorption of light in one of the aggregated photocatalyst nanoparticles are likely to be transported throughout until arriving at a suitable trap site. Once one of the charge carriers has been trapped, that is, has been involved in a redox reaction with the adsorbate, the other charge carrier can continue its "journey" through the particle network until reacting itself. Obviously, the particle network replaces the individual photocatalyst particle shown in Fig. 2, thus resulting in an improved photocatalytic activity of the overall system, that is, through a cooperative effect within the network. Interestingly, a mechanism for water oxygen production that the production of one molecule of oxygen from two water molecules requires four holes has been proved under the condition of a single laser pulse, which impulses the generation of holes, contributing to almost all of the oxygen production and rarely migrating between nanoparticles<sup>22</sup>. Besides the experimental techniques described so far, such as FTIR spectroscopy and ATR-FTIR measurements, the combination of electrochemical investigations and measurements of the photocatalytic activity can provide interesting information concerning the properties of photocatalytic materials. A comparison of the results of Mott-Schottky measurements carried out on TiO<sub>2</sub> thin film electrodes with the photocatalytic activities of these films for the photocatalytic

water reduction into  $H_2$ , revealed a good correlation of both the flatband potential and the donor density with the photonic efficiencies of the photocatalytic water reduction<sup>84</sup>.

### Perovskite materials

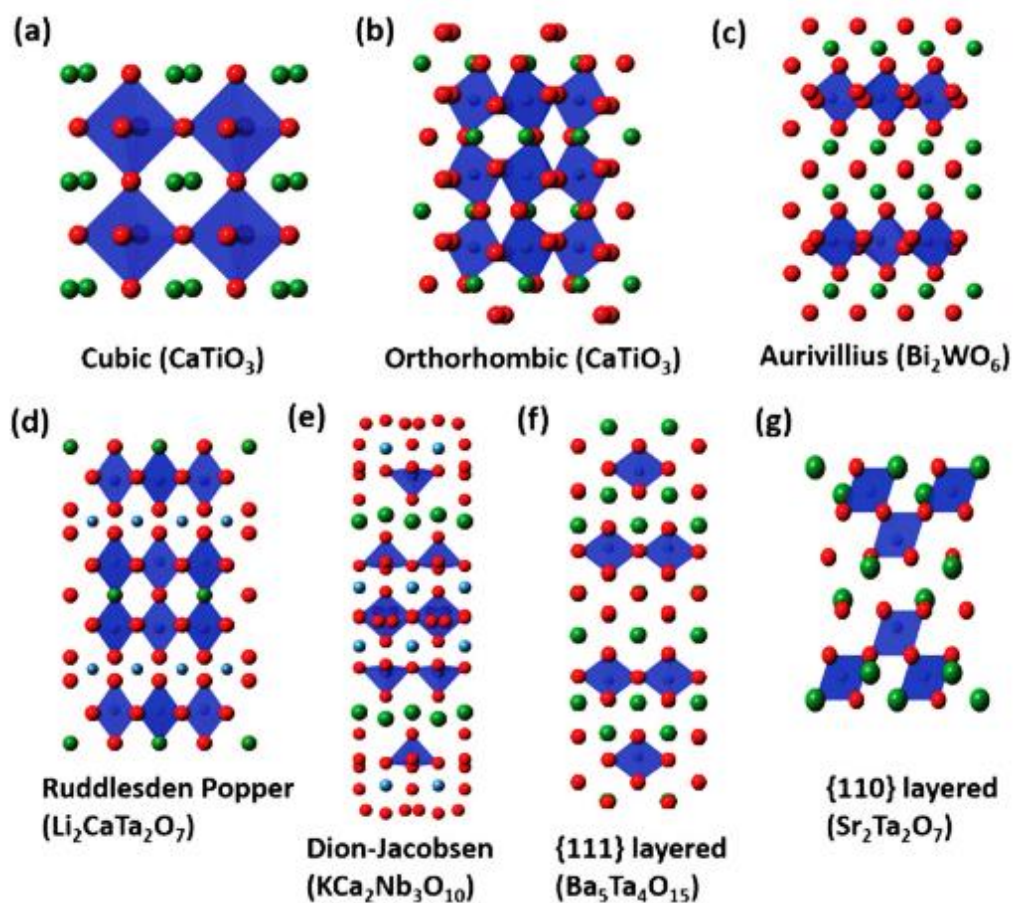


Figure 9. Crystal structures of perovskites and layered perovskite compounds (red spheres: oxygen; dark blue spheres: B-site element; green and light blue spheres: A-site element)<sup>85</sup>.

Among a large library of photocatalyst materials, perovskite oxides and their derivatives (layered perovskite oxides) comprise a large family of promising semiconductor photocatalysts because of their structural simplicity and flexibility, good stability and efficient photocatalytic performance. The ideal perovskite has a cubic structure with a general formula of  $ABO_3$ , as shown

in Fig. 9a. The A cation is normally an alkali or alkali earth metal or a rare earth element, while the B cation is typically a metallic transition metal element, which thus extends the family of perovskite oxides by rationally combining different metal ions at A and B sites<sup>86</sup>. Apart from the ideal cubic perovskite, structural distortion can be induced by multiple metal cation substitutions, which can inevitably change the physical, electronic and photocatalytic properties of pristine materials. A slightly distorted perovskite structure with orthorhombic or rhombohedral symmetry is presented in Fig. 9b. The A and B atoms can be with the same or different valences and ionic radii. Furthermore, either A or B cations can be partially substituted by the other dopants, to extend the  $ABO_3$  perovskite into a broad family of  $A_xA_{1-x}B_yB_{1-y}O_{3\pm\delta}$ . Fig. 9c-g present the general formula for the most well-known layered perovskite oxides, such as  $(Bi_2O_2)(A_{n-1}B_nO_{3n+1})$  (Aurivillius phase),  $A_{n+1}B_nO_{3n+1}$  or  $A_2'A_{n-1}B_nO_{3n+1}$  (Ruddlesden-Popper phase) and  $A'[A_{n-1}B_nO_{3n+1}]$  (Dion-Jacobson phase) for {100} series,  $(A_nB_nO_{3n+2})$  for {110} series and  $(A_{n+1}B_nO_{3n+3})$  for {111} series. In these structures, n represents the number of  $BO_6$  octahedra that span a layer, which defines the thickness of the layer. Compared with  $TiO_2$  materials, perovskite photocatalysts have their unique features in terms of tunable compositions, crystalline and electronic/energy band structures, which in some cases lead to more effective photocatalytic reduction and oxidation efficiencies.

Strontium titanate ( $SrTiO_3$ ) is a typical perovskite semiconductor belonging to the cubic phase and has shown photocatalytic activity in overall water splitting.  $SrTiO_3$  has a band gap of 3.2 eV, so responds to UV light ( $\lambda < 387$  nm). After loading of Pt and  $Co_3O_4$  dual-cocatalysts as catalytic sites,  $SrTiO_3$  single nanocrystal can easily achieve spatial charge separation for photocatalytic overall water splitting<sup>87</sup>. But this spatial separation of photo-reduction and photo-oxidation catalytic sites on  $SrTiO_3$  can only be achieved for 18-facet nanocrystals with anisotropic facets but

not for 6-facet SrTiO<sub>3</sub> with isotropic facets. And a fivefold enhancement in apparent quantum efficiency for photocatalytic water splitting could be achieved<sup>87</sup>. La<sub>2</sub>Ti<sub>2</sub>O<sub>7</sub> is a member of a family of perovskite-type layer-structured photocatalyst (similar to Sr<sub>3</sub>Ti<sub>2</sub>O<sub>7</sub> and K<sub>2</sub>La<sub>2</sub>Ti<sub>3</sub>O<sub>10</sub>)<sup>88-89</sup>. The La<sub>2</sub>Ti<sub>2</sub>O<sub>7</sub> prepared by the conventional solid-state reaction (SSR) had a band gap of 3.2 eV, narrower than that (3.87 eV) of the samples prepared by polymerised complex (PC)<sup>90</sup>. However, the quantum yield of the Ni-loaded heat-treated PC samples was 27%, much higher than that (12%) of the SSR samples for the photocatalytic decomposition of water under UV light. The reason was that the La<sub>2</sub>Ti<sub>2</sub>O<sub>7</sub> formed in the heat-treated PC sample had better crystallinity and phase purity, higher surface area, and the wider dispersed state of nickel metal.

### **Metal (oxy)nitrides**

Because the electronegativity of nitrogen is lower than that of oxygen, metal nitrides are prone to anodic photocorrosion due to the lower electronegativity of nitrogen than that of oxygen. However, in the presence of sacrificial reagent methanol, Ta<sub>3</sub>N<sub>5</sub> nanocrystals generated 135 μmol H<sub>2</sub> in 5 h under visible light irradiation ( $\lambda > 400$  nm) after the attachment of Pt cocatalyst particles<sup>91</sup>. As nitrogen and oxygen have the similar chemical, structural and electronic characteristics such as polarizability, electronegativity, coordination numbers and ionic radii, the substitution of nitrogen for oxygen in oxides, forming oxynitrides, would significantly extend the nitride family<sup>84, 92-98</sup>. Transition-metal oxynitrides are an important class of emerging materials that, in optimal cases, may combine the advantages of oxides and nitrides. Generally, oxynitride stabilities in air and moisture are greater than those of the pure nitrides, but with smaller band gaps than those comparable oxides. The reason is that nitrogen is less electronegative than oxygen so the optical gap between the anion-based valence band and the cation-based conduction band decreases as oxide is substituted by nitride. Moreover, nitrogen is more polarizable than oxygen;

the metal-ligand bond in metal oxynitride is more covalent and this increases the nephelauxetic effect (expansion of electron cloud), and then decreases the electronic repulsion and the energy of the d orbitals<sup>96</sup>, resulting the better stabilities of oxynitrides than the pure nitrides and the narrower band gap than the pure metal oxides. The valence bands of these oxynitride materials are populated by hybridizing N<sub>2p</sub> and O<sub>2p</sub> orbitals while conduction is mostly composed of the empty d orbitals of the corresponding metal ions, resulting in more negative valence band levels and smaller band gaps compared to those of conventional oxide semiconductors, allowing visible-light driven water splitting<sup>40, 91, 98-101</sup>. In this case, it is expected that the conduction band levels are not significantly affected because the cationic components are not changed. Since N<sup>3-</sup> has a similar ionic radius to that of O<sup>2-</sup>, the substitution of N<sup>3-</sup> for all or part of the O<sup>2-</sup> in the oxide is possible in some cases<sup>99</sup>. For example, β-TaON is an extensively investigated visible photocatalyst with yellow or green colour, which has a smaller band gap than Ta<sub>3</sub>N<sub>5</sub>, sufficient to absorb visible light<sup>100</sup>. Photooxidation of water on TaON proceeded very efficiently, but the photocatalytic activity for H<sub>2</sub> evolution was not satisfactory. Experimental analysis found that the bottom of the conduction band and the top of the valence band were estimated to be -0.3 and +2.2 eV vs. NHE at pH=0, respectively, suggesting that TaON had a small overpotential for reduction of H<sup>+</sup>, thus having small H<sub>2</sub> evolution rate. One of the most active oxynitride photocatalysts under visible light irradiation is a gallium-zinc oxynitride solid solution of GaN and ZnO also known as (Ga<sub>1-x</sub>Zn<sub>x</sub>)(N<sub>1-x</sub>O<sub>x</sub>), which had an absorption edge at ~500 nm and a quantum yield of 5.2% at 410 nm. The band gap of (Ga<sub>1-x</sub>Zn<sub>x</sub>)(N<sub>1-x</sub>O<sub>x</sub>) was roughly estimated to be 2.6-2.8 eV, which was substantially smaller than that for either GaN (3.4 eV) or ZnO (3.2 eV)<sup>92</sup>.

Nitridation of perovskite oxides to form oxynitride-type perovskite ABO<sub>2-x</sub>N<sub>1+x</sub> is also an effective approach to reduce the band gap of ABO<sub>3</sub> and enhance the photocatalytic performance under

visible light. Most of the  $ABO_{2-x}N_{1+x}$  materials have strong visible light absorption up to 600-650 nm. The tantalum, niobium and titanium oxynitride perovskites are promising candidates for photocatalytic water splitting under visible light illumination, due to their narrow band gap (1.5-2.5 eV)<sup>101</sup>. For example,  $LaTiO_2N$  had a band gap of 2.1 eV and exhibited both photocatalytic  $H_2$  and  $O_2$  evolution from a sacrificial aqueous system under visible light irradiation up to *ca.* 600 nm<sup>102</sup>. Niobium-based perovskite type oxynitrides,  $ANbO_{2-x}N_{1+x}$  ( $A=Ca, Sr, Ba$  and  $La$ ), have smaller band gap energies than the corresponding Ta-based analogous oxynitrides because the conduction band of Nb formed by the empty  $Nb_{4d}$  orbitals lied at a more positive potential and had the higher electronegativity than the  $Ta_{5d}$ .  $BaNbO_2N$  was of particular interest for solar energy conversion for its narrow band gap of 1.7 eV allowing light absorption up to 740 nm, and it could be activated for photocatalytic water splitting in the presence of sacrificial reagents by modifying the materials and loading appropriate co-catalysts<sup>41, 95</sup>.  $BaNbO_2N$  generated  $O_2$  of *ca.* 300  $\mu\text{mol}/(\text{hg})$  from an aqueous  $AgNO_3$  solution under visible light irradiation ( $\lambda > 410$  nm) after modification with  $CoO_x$  and was active even under illumination up to 740 nm, the longest wavelength ever reported for (oxy)nitride photocatalysts<sup>103</sup>.

### **Metal sulphides**

Although metal sulphides usually have a problem of photocorrosion, they are attractive as photochemical water splitting catalysts because of their small band gaps that allow absorption of visible light. The valence band position of  $S_{3p}$  orbitals is more negative than that of  $O_{2p}$  and thus some sulphides have narrower band gaps.  $CdS$  is probably the best studied metal sulphide photocatalysts<sup>57, 104-106</sup>, due to its relatively narrow band gap (2.4 eV) and the absorption of light wavelengths up to 510 nm. The flat-band potential of  $CdS$  (-0.87 eV vs. NHE) was sufficiently high to reduce  $H_2O$ , and the top of valence band (+1.5 eV vs. NHE) was theoretically suitable to

allow oxidation of water<sup>107</sup>. For CdS nanoparticles with the diameter of 4 nm, the lifetime of photogenerated charge carrier was on the order of 50 ps<sup>108</sup>. However, prolonged irradiation of CdS suspensions led to photocorrosion of CdS into Cd<sup>2+</sup> and S (sulfide in the presence of O<sub>2</sub>)<sup>109</sup>. This reaction could be suppressed by the addition of reducing agents to the aqueous phase, such as DETA<sup>110-111</sup>, S<sub>2</sub><sup>2-</sup>, SO<sub>3</sub><sup>2-</sup>, or S<sub>2</sub><sup>2-</sup>/HPO<sub>2</sub><sup>109</sup>. The most recent studies have focused on other forms of CdS, including CdS nanoparticles stabilised in micelles<sup>112</sup>, CdS composites with other semiconductors (TiO<sub>2</sub><sup>113</sup>, ZnS<sup>114</sup> and CdSe<sup>115</sup>, MoS<sub>2</sub><sup>105</sup>), metal cocatalysts (Pt, Pd, Rh, Ru, Ir, Fe, Ni and Co)<sup>116</sup>, hollow CdS microparticles<sup>117</sup> and Cu-doped CdS<sup>118</sup>. For example, loaded Ni<sup>119</sup> or MoS<sub>2</sub><sup>105</sup> as a cocatalyst on CdS could significantly enhance the H<sub>2</sub> production under visible light in the appropriate reagent.

ZnS is the other major metal sulphide investigated for photocatalytic water splitting, which has a wide band gap of around 3.54 eV. But after doped by Ni, Zn<sub>0.999</sub>Ni<sub>0.001</sub>S showed an energy gap of 2.3 eV<sup>20</sup>. Without cocatalyst such as Pt, the rate of H<sub>2</sub> evolution was 280 μmol/h under visible light (λ>420 nm) and the quantum yield at 420 nm was 1.3%<sup>20</sup>. Similar to CdS, ZnS underwent photocatalytic decomposition into the elemental sulphur when irradiated in the absence of electron donors. The most comprehensive study on photocatalysis of ZnS and ZnS-Pt was investigated under the consideration of the effect of catalyst preparation, electron donors, pH and the temperature<sup>120</sup>. Importantly, it was found that, in the presence of SO<sub>3</sub><sup>2-</sup>, metallic Zn was formed, which was thought to assume a role in electron transfer to water molecules. Long-time photocatalytic tests showed that no deactivation of ZnS occurred over 34 h. Doping of ZnS with variable amounts of AgInS<sub>2</sub> or CuInS<sub>2</sub> produced a series of solid solutions that crystallised in the cubic zinc blende or Wurtzite structure<sup>56, 121-122</sup>. For the Pt-loaded Ag<sub>0.22</sub>In<sub>0.22</sub>Zn<sub>1.56</sub>S<sub>2</sub> photocatalysts, a QE of 20% was measured at 420 nm under solar irradiation conditions<sup>122</sup>.

While pure InS or In<sub>2</sub>S<sub>3</sub> was inactive for photocatalytic water splitting, several ternary indium sulphides were active for that. Na<sub>14</sub>In<sub>17</sub>Cu<sub>3</sub>S<sub>35</sub>X·H<sub>2</sub>O evolved small quantities of H<sub>2</sub> under visible light irradiation in the presence of Na<sub>2</sub>S as the sacrificial, equal to QE = 3.7% at 420 nm<sup>122</sup>. Interestingly, WS<sub>2</sub> formed the MoS<sub>2</sub> structure containing layers of trigonal-prismatic WS<sub>6</sub> units, which had a 1.7 eV direct band gap and a 1.3 eV indirect band gap and could produce H<sub>2</sub> from EDTA solution under visible light irradiation<sup>123</sup>. Bi<sub>2</sub>S<sub>3</sub> containing chains of corner-shared BiS<sub>4</sub> tetrahedra in the bismuthinite structure type, could produce H<sub>2</sub> at intermediate rates from an aqueous sulphide solution. Rates declined after 100 min, but the activity was improved by 25% by platinization<sup>124</sup>. Other metal sulphides had also been tested. Of these, In<sub>2</sub>Se<sub>2</sub>, SnS<sub>2</sub>, HgS, Tl<sub>2</sub>S, PdS, EuS, CuS, FeS, CoS and Fe<sub>2</sub>S<sub>3</sub> were found to be inactive because of their narrow band gaps (< 2 eV)<sup>118</sup>.

### **Metal phosphides**

Metal phosphides demonstrate different characteristics according to the metal species, M/P ratios, and crystallographic structure. Generally, most metal-rich phosphides, such as Ni<sub>2</sub>P, Ni<sub>12</sub>P<sub>5</sub>, Co<sub>2</sub>P, CoP and Cu<sub>3</sub>P, have comparable properties to metals and ceramics. They not only possess excellent heat and electrical conductivity, but also have good thermal and chemical stability. The chemical states of the metals and phosphorus were usually measured by XPS<sup>125</sup>. The measurement results showed nearly all mentioned metals and phosphorus band binding energies close to that of the zero-valent state. The related metals had very small positive charges and the phosphorus possessed a rather small negative charge in comparison with elemental metals and phosphorus. At the same time, the metal-P bond possessed charge-transfer characteristics. Thus, numerous transition-metal phosphides have been reported as highly efficient, stable and low cost cocatalysts and are even comparable with some classical noble metals, such as Pt and Pd. For

example, Ni<sub>2</sub>P highly improved the efficiency and durability for photogeneration of hydrogen in water as a cocatalyst to form a well-designed integrated photocatalyst with one-dimensional semiconductor CdS nanorods<sup>126</sup>. The highest rate for hydrogen production reached ~1200 μmol h<sup>-1</sup> mg<sup>-1</sup> based on the photocatalyst. The turnover number (TON) reached ~3 270 000 in 90 hours with a turnover frequency (TOF) of 36 400 for Ni<sub>2</sub>P, and the apparent quantum yield was ~41% at 450 nm.

### WO<sub>3</sub>

Developing visible-light-sensitive materials with the alternative ability to evolve H<sub>2</sub> or O<sub>2</sub> is significant for the wide application of the semiconductors with narrow band gaps to treat water splitting reaction in terms of two coupled half reactions<sup>127-129</sup>. As water oxidation is found to be more challenging than hydrogen generation because the formation of one molecular oxygen involves the transportation and reaction of four electrons or holes<sup>22, 130-132</sup>, exploring a relatively cheap, robust and efficient water oxidation photocatalyst is widely accepted to be key to solar driving fuel synthesis, if it is to be commercially viable.

In terms of native oxide photocatalysts, WO<sub>3</sub> is well-known for oxygen production from water in the presence of an electron scavenger such as Ag<sup>+</sup>. This compound is an n-type semiconductor with a band gap of 2.7 eV and is capable of harvesting the blue part of solar spectrum. WO<sub>3</sub> modified with two different cocatalysts together, PtO<sub>x</sub> and RuO<sub>2</sub>, led to excellent activity for water oxidation in an aqueous NaIO<sub>3</sub> solution, giving an apparent quantum yield of 14.4% at 420 nm<sup>133</sup>. Electrochemical analyses suggested that PtO<sub>x</sub> and RuO<sub>2</sub> loaded on WO<sub>3</sub> collected photogenerated electrons and holes, reducing IO<sub>3</sub><sup>-</sup> ions and oxidizing water, respectively.

## **BiVO<sub>4</sub>**

Another excellent semiconductor for photocatalytic oxygen evolution from water is BiVO<sub>4</sub>, with a 2.3 eV band gap. In 1998, BiVO<sub>4</sub> was synthesised and firstly used in photocatalyzing water oxidation to produce O<sub>2</sub> in an aqueous solutions containing Ag<sup>+</sup> as an electron scavenger under visible light, leading to a quantum yield of 0.5% at 450 nm<sup>134</sup>. Recently, experimental results revealed spatial separation of the photogenerated electrons and holes between {010} and {110} facets of BiVO<sub>4</sub>, which were mainly owing to the different energy levels of these facets<sup>135</sup>. When the reduction cocatalyst Pt was selectively photo-deposited on the electron-accumulated {010} facet while the oxidation cocatalyst MnO<sub>x</sub> on hole-concentrated {110} facet of BiVO<sub>4</sub>, the photocatalytic activity of water oxidation could be greatly enhanced.

## **Ag<sub>3</sub>PO<sub>4</sub>**

Ag<sub>3</sub>PO<sub>4</sub> is regarded as a significant breakthrough in the field of visible light responsive photocatalysts for water oxidation, with a quantum yield of nearly 90% for visible light driven photocatalytic water oxidation<sup>136</sup>. Under the same reaction conditions, Ag<sub>3</sub>PO<sub>4</sub> produced O<sub>2</sub> of 636 μmol·h<sup>-1</sup> from aqueous AgNO<sub>3</sub> solution under illumination ( $\lambda > 400$  nm), while BiVO<sub>4</sub> and WO<sub>3</sub> produced O<sub>2</sub> of 246 and 72 μmol·h<sup>-1</sup>, respectively. Given the fact that most photocatalysts show a relatively poor quantum yield as low as 20%, the exceptionally high efficiency of Ag<sub>3</sub>PO<sub>4</sub> is intriguing. The energy-band dispersion and density of states of Ag<sub>3</sub>PO<sub>4</sub> was calculated using CASTEP by Ray L. Withers *et al.*<sup>136</sup>, which illustrated that the bottoms of the conduction bands of the materials were mainly composed of hybridised Ag 5s5p as well as a small quantity of P 3s orbitals, whereas the tops of the valence bands were composed of hybridised Ag 4d and O 2p orbitals. Both the highly dispersive VBs and CBs should be beneficial for the transport of

photoexcited electrons and holes, which in turn was likely to suppress the recombination of electron-hole pairs and thus account for the high photooxidation activity.

But the most serious drawback of unwanted and uncontrolled photocorrosion would inevitably become a main obstacle for  $\text{Ag}_3\text{PO}_4$ <sup>136-137</sup>. This is mainly due to its slight solubility in solution and its own characteristic of energy-band structure<sup>136-137</sup>. The CB energy of  $\text{Ag}_3\text{PO}_4$  is +0.45 eV vs. NHE, which is higher than the reduced potential of  $\text{H}_2\text{O}/\text{H}_2$  (0.0 eV vs. NHE), resulting the reduction of  $\text{Ag}^+$  and then the deposition of  $\text{Ag}^0$  on the surface, subsequently reducing the light absorption efficiency<sup>136-137</sup>. Thus, many efforts have been devoted recently to further improve and optimise the photocatalytic activity and stability of  $\text{Ag}_3\text{PO}_4$ , such as morphology control<sup>138</sup>, doping<sup>139</sup>, cocatalyst decoration<sup>140-141</sup>, conjunction with other materials<sup>142-143</sup>, optimising the photocatalytic system<sup>137</sup>. For example, as the theoretical calculations predicted that the {111} facet of  $\text{Ag}_3\text{PO}_4$  crystal possessed considerably higher surface energy than either {110} or {100}, the tetrahedral  $\text{Ag}_3\text{PO}_4$  crystals, composed of {111} facets, were successfully synthesised, which showed an extremely high activity for water photooxidation, with an initial oxygen evolution rate exceeding  $6 \text{ mmol} \cdot (\text{hg})^{-1}$ , 10 times higher than either {110} or {100}<sup>138</sup>. It was the first time that the internal quantum yield for water photooxidation was almost unity at 400 nm, and greater than 80% from 365 to 500 nm, achieved by {111} terminated tetrahedrons. This was due to the differences in the effective masses of holes and electrons, which were directionally sensitive to the crystal structure. The hole mass along [111] was much smaller compared to other directions in  $\text{Ag}_3\text{PO}_4$  crystals, indicating the hole migration towards {111} facets was greatly encouraged, since hole mobility was increased, which favored the fast and efficient transport of holes to the surface for oxidation reactions. Furthermore, the over-abundance of dangling phosphorus-oxygen bonds resulted the high surface energy of the {111}, which provided more oxidation sites.

## Metal-organic frameworks

Metal-organic frameworks (MOFs) are a new class of highly porous materials, found in 1995 by Hailian Li *et al.*<sup>144</sup>, which are formed by linking organic and inorganic moieties through covalent coordination linkages, in part through H-bonding,  $\pi$ - $\pi$  stacking and van der Waals forces. The sunlight absorption capability (band gap), the number of active sites and the charge separation/transfer efficiency of a MOF-based material will strongly influence the photocatalytic efficiency for water splitting. The band gap energy of MOFs can be tailored by changing the metal-oxo clusters and bridging organic linkers. The incorporation of active sites, such as Pt nanoparticles<sup>145</sup>, into MOFs was found to dramatically enhance the photocatalytic activity. Post-synthetic functionalization by organic dyes could also improve the light harvesting and the charge transfer<sup>146-147</sup>. For example, a stable photoactive MOF UiO-66(Zr) sensitised by absorbed or directly added rhodamine B dye enhanced the photocatalytic activity to 30 and 26 times in the presence of Pt as a cocatalyst than that of Pt@UiO-66(Zr) and the bare UiO-66(Zr)<sup>146</sup>. The probable mechanism was that a large energy band offset would form between RhB\* and UiO-66(Zr) when visible-light irradiates on RhB sensitised Pt@UiO-66(Zr), resulting the excited electrons transferring to the LUMO of UiO-66(Zr) composed of empty metal orbitals, afterwards, the trapped electrons subsequently transferred to Pt nanoparticles due to the higher work function of Pt than UiO-66(Zr), thus restraining the recombination process and the promoting electron transfer and photocatalytic hydrogen generation.

### 2.3.2 Metal-free photocatalysts

The metal-free photocatalysts, such as graphitic carbon nitride (g-C<sub>3</sub>N<sub>4</sub>), graphene, covalent organic frameworks, and phosphorene, containing earth-abundant non-metallic elements (C, N, H, O, *etc.*), have emerged as alternative catalysts for water splitting. The activities of these

materials for either H<sub>2</sub> or O<sub>2</sub> generation are limited without modification, but they will have comparable or even better performances than metal-containing photocatalysts after doping with heteroatoms, engineering defects, and/or forming composites among them. This section will discuss and summarise the latest developments of metal-free photocatalysts for water splitting.

### **g-C<sub>3</sub>N<sub>4</sub> and the hybrids**

In 2009, g-C<sub>3</sub>N<sub>4</sub>, a polymeric semiconductor with tri-s-triazine (melem) as the basic building unit connected by planar amino groups (Fig. 10), has been reported as an organic photocatalyst for hydrogen evolution under visible light<sup>8</sup>. It has a graphite like sp<sup>2</sup>-bonded C-N structure and behaves like a π-conjugated semiconductor. The band gap of g-C<sub>3</sub>N<sub>4</sub> was measured to be 2.7 eV with the CB and VB positions located energetically possible for water splitting<sup>127</sup>. Theoretically, the electronic structure calculated by density functional theory (DFT) reveals that the carbon and nitrogen atoms could be preferred sites for proton reduction and water oxidation, respectively. However, the relatively large band gap of pristine g-C<sub>3</sub>N<sub>4</sub> limits its visible light absorption and the nature of covalent bonding in g-C<sub>3</sub>N<sub>4</sub> leads to low proton reduction and water oxidation efficiencies on its surface. Great efforts have been made by many groups to improve such properties of g-C<sub>3</sub>N<sub>4</sub> to improve its photocatalytic performance, such as the combination with other carbonaceous materials.

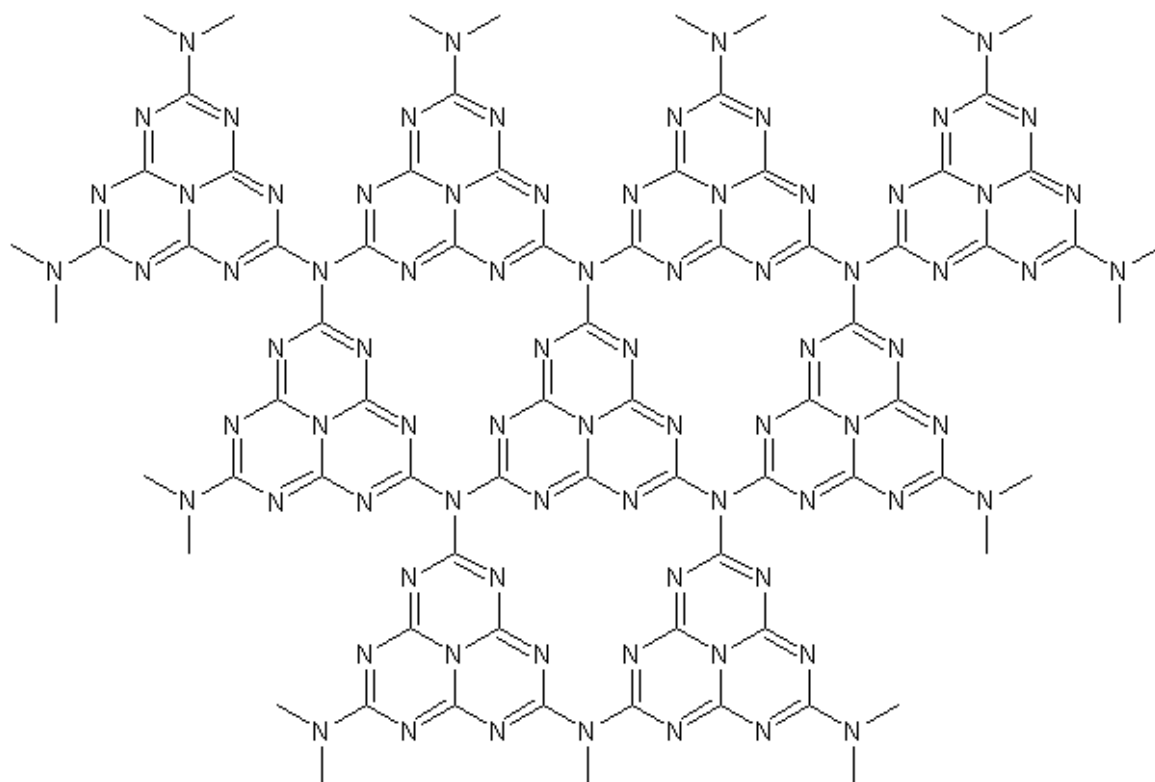


Figure 10. Schematic diagram of a perfect graphitic carbon nitride sheet constructed from melem units.

For example, loading a small amount of carbon dots (0.0016 wt%) in the matrix of g-C<sub>3</sub>N<sub>4</sub> could lead to stable overall water splitting into H<sub>2</sub> and O<sub>2</sub> in a stoichiometric ratio under visible light for at least 200 days<sup>148</sup>. Remarkably, the quantum efficiencies was achieved, such as 16% at wavelength  $\lambda = 420 \pm 20$  nm, 6.29% at  $\lambda = 580 \pm 15$  nm, and 4.42% at  $\lambda = 600 \pm 10$  nm, and determined an overall solar energy conversion efficiency of 2.0 % when loading 0.48 wt% carbon dots (CDots), which was not far away from the target set by the U.S. Department of Energy-for a reasonable production cost of H<sub>2</sub> by photocatalytic systems. Different to the conventional one-step four-electron reaction, CDots-C<sub>3</sub>N<sub>4</sub> catalysed water splitting to hydrogen and oxygen via the stepwise two-electron/two-step pathway under visible light irradiation. C<sub>3</sub>N<sub>4</sub> was responsible for the first step to photocatalyse the water into H<sub>2</sub>O<sub>2</sub>, and CDots were responsible for the second step to decompose H<sub>2</sub>O<sub>2</sub> to O<sub>2</sub>, however it was challenging to reproduce such a breakthrough<sup>149</sup>.

Interestingly, carbon quantum dots (CQDs) was integrated with exfoliated g-C<sub>3</sub>N<sub>4</sub> nanosheets (CNNSs) as a hetero-photocatalyst via a brief one-step hydrothermal method, which largely improved the H<sub>2</sub> evolution rates of CNNS in both under UV and visible light irradiation, and for the first time, near-infrared (NIR) light from an 808 nm laser beam induced H<sub>2</sub> generation with a rate of 6.76 μmol·(hg)<sup>-1</sup> without any cocatalysts<sup>150</sup>. This was mainly attributed to the excellent light absorption from UV to NIR of the narrow gap sp<sup>2</sup> carbon clusters embedded in CQDs and the decreased apparent band gaps by forming subband energy levels in the band gap of CNNS/CQDs<sup>148</sup>.

### **Graphene and related materials**

Graphene is a relatively new member of the carbon family as it was experimentally discovered in 2004<sup>151</sup>, which is a single-atom-thick planar sheet of sp<sup>2</sup> hybridised carbons that are densely bound in a hexagonal lattice. Furthermore, graphene is the mother block of all graphitic forms, and it can build a variety of graphitic materials including 0D fullerene, 1D carbon nanotubes, 3D graphite, and even other 3D carbon architectures. In general, pristine graphene holds a symmetric band structure and is regarded either as a conductor or a zero band-gap semiconductor, which means almost no photocatalytic activities. Fortunately, opening its band gap is feasible by extensive functionalization and modification strategies due to its unique structure properties, and thus improves its reactivity for photocatalytic applications. Firstly, one of most promising options is to incorporate heteroatoms (*e.g.* N, S, B, P) into the graphene frameworks, which could disrupt the sp<sup>2</sup> network and cause sp<sup>3</sup> defects in the graphene lattice, leading to the change in the electronic density within the graphene sheet. Secondly, chemical modified graphene materials (*e.g.* GO and reduced GO), possess abundant structural defects and residual functional groups, which feature the various electronic properties and conductivities based on the type and quantity

of functionalities introduced. Thirdly, optimising the size and morphology of graphene materials is also an alternative strategy to tune their properties.

Among the modified graphene materials, GO has a wider bandgap by introducing oxygen functional groups into the surface of graphene and thus exhibits p-type characteristics due to that the electronegativity of oxygen atoms is larger than that of carbon atoms, which makes GO a potential candidate for a metal-free photocatalyst. For example, GO was utilised as a photocatalyst for H<sub>2</sub> production from an aqueous methanol solution, which revealed the photocatalytic activity of H<sub>2</sub> evolution was related to the oxidation levels during synthesis<sup>152</sup>. The GO semiconductor showed a bandgap energy of 2.4 ~ 4.3 eV based on the controlled oxidation, which was sufficient to overcome the energy barrier for the water splitting reaction but hinder the O<sub>2</sub> evolution due to the p-type conductivity of GO impeding the photogenerated hole transfer to the surface of the photocatalyst due to downward band bending. But engineering the composition of its oxygenated groups and the oxidation level could change the type of conductivity of GO. For instance, treating GO with NH<sub>3</sub> gas at room temperature introduced the amino and amide groups into its surface, thus transforming GO into an n-type semiconductor and change the electronic structure<sup>153</sup>. The resulting n-type N-containing GO realised the photocatalytic oxygen evolution by effectively promoting the transfer of photogenerated holes. Further exploration of nitrogen-doped quantum dots (NGO-QDs) derived from GO sheets achieved the stoichiometrically water splitting into H<sub>2</sub> and O<sub>2</sub> under visible light irradiation<sup>154</sup>. The NGO-QDs consisted of N-doped graphene sheets stacked into crystals with oxygenated groups on the crystal surface (Fig. 11a-c). The N atoms in the graphene lattice functioned for the n-conductivity and the oxygenated groups on the surface resulted in the p-conductivity, leading to the formation of p-n type photochemical diodes in the structure (Fig. 11d). Therefore, tuning

the parameters of the oxidation degree, size, morphology and composition of GO is expected to improve its photocatalytic performance for the water splitting reaction.

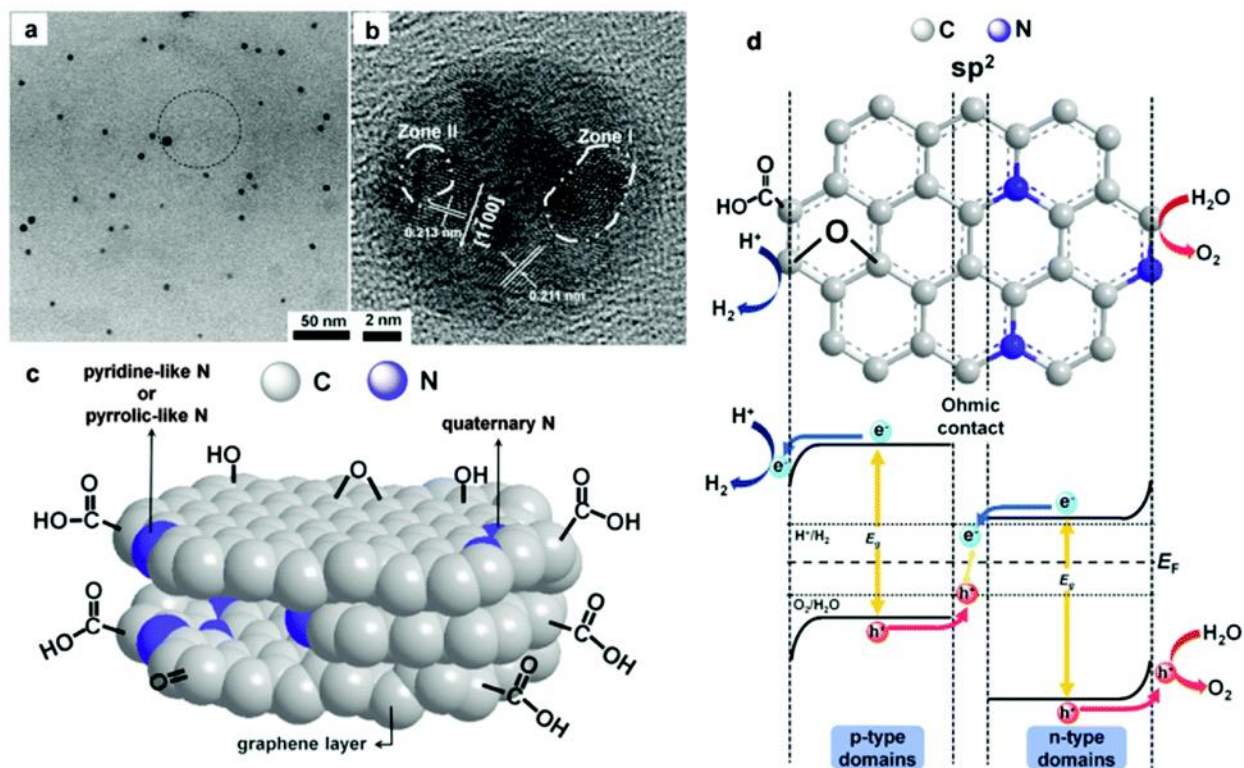


Figure 11. (a) TEM image of the NGO-QDs, (b) HRTEM image of a NGO-QD, (c) a conceptual schematic of the NGO-QD structure and (d) the p-n type photochemical diode in NGO-QDs<sup>154</sup>.

Heteroatom (e.g. N, B) doped graphene is another alternative of graphene-based metal-free photocatalyst for water splitting reactions. Recent theoretical DFT calculations revealed that the band gap of the heteroatom doped graphene should be increased with the doping content<sup>155</sup>. Different from the conductor nature of pristine graphene, N-doped graphene behaves as a semiconductor with a quasi neutral absorption and exhibits high efficiency for the photocatalytic generation of  $H_2$  from water/methanol mixtures in the absence of a metal cocatalyst under both UV and visible light. Another featured example is the P-doped graphene photocatalyst, whose

optical band gap and the photocatalytic performance of P-doped graphene increased with the P content<sup>156</sup>. The optimal P-doped graphene photocatalyst exhibited an activity for H<sub>2</sub> generation about 9 times higher than that of GO under UV light irradiation from water/methanol mixtures and was also active under visible-light illumination. Besides N and P, a series of halogen atom (*e.g.* F, Cl, Br, I) doped graphene materials could also improve the efficiency of the photocatalytic H<sub>2</sub> evolution from water in the presence of methanol<sup>157</sup>. On these basis, more highly efficient heteroatom doped graphene materials are still waiting for the exploration through control of the type and content of dopants and their bonding configurations in the graphene framework.

### **Covalent organic frameworks (COFs)**

Other than g-C<sub>3</sub>N<sub>4</sub> that is invariably composed of heptazine or triazine units, and, thus, offers only limited chemical variety and not very susceptible to systematic post-modification, a closely related class of organic polymers, dubbed covalent organic frameworks (COFs), are apt to overcome these inherent weakness of carbon nitrides by combining chemical versatility and modularity with potentially high crystallinity and porosity<sup>158-162</sup>. COFs are crystalline porous materials constructed from a variety of rigid organic building units solely from light elements (H, B, C, N and O) and with different structural configurations, which are connected via robust covalent bonds. The designed synthesis of COFs results in the low density, large surface area, tunable pore size and structure, facily-tailored functionality, versatile covalent-combination of building units, and so on, which provides the COFs with high potentials in further applications for gas storage, adsorption, optoelectricity, catalysis and as functional devices. As the optical and electronic properties of the resulting framework materials can readily be tuned by tailoring the organic precursors<sup>163-165</sup>, photofunctional COFs present an interesting area of research with the application of the photocatalytic water splitting. For example, the first COF was achieved for the

visible light driven hydrogen evolution in the presence of Pt as the proton reduction catalyst (PRC)<sup>166</sup>. This hydrazone-based COF was constructed from 1,3,5-tris-(4-formyl-phenyl) triazine (TFPT), featuring mesopores of 3.8 nm in diameter and the extremely high surface area of 1603 m<sup>2</sup>/g. Using a 10 vol% aqueous triethanolamine (TEOA) solution as a sacrificial donor, the maximum quantum efficiency (QE) for H<sub>2</sub> production was 2.2% at 400 nm. The triazine moieties in the TFPT-COF may point to an active role in the photocatalytic process. Another two-dimensional (2D) azine-linked COFs were synthesised by using a series of triphenylaldehydes with the central aryl ring containing 0 - 3 nitrogen atoms as building blocks as shown in Fig. 12<sup>167</sup>. The best photocatalytic performance for hydrogen evolution from water was 1703 μmol/(hg) produced by the N<sub>3</sub>-COF. The corresponding photonic efficiency (PE) was highest of 0.44% at 450 nm. Interestingly, a highly stable COF (TpPa-2) functioned as a support matrix for anchoring Cd nanoparticles, which significantly enhanced the photocatalytic H<sub>2</sub> evolution rate up to 3678 μmol·(hg)<sup>-1</sup> as compared to the bulk CdS (124 μmol·(hg)<sup>-1</sup>)<sup>168</sup>. The presence of a π-conjugated backbone, high surface area, and occurrence of abundant 2D hetero-interface was possibly beneficial for the efficient charge transfer, the nanoparticles stability and suppressing the recombination of the photogenerated electron-hole pairs on the photocatalyst surface, thereby resulting in a high photocatalytic activity.

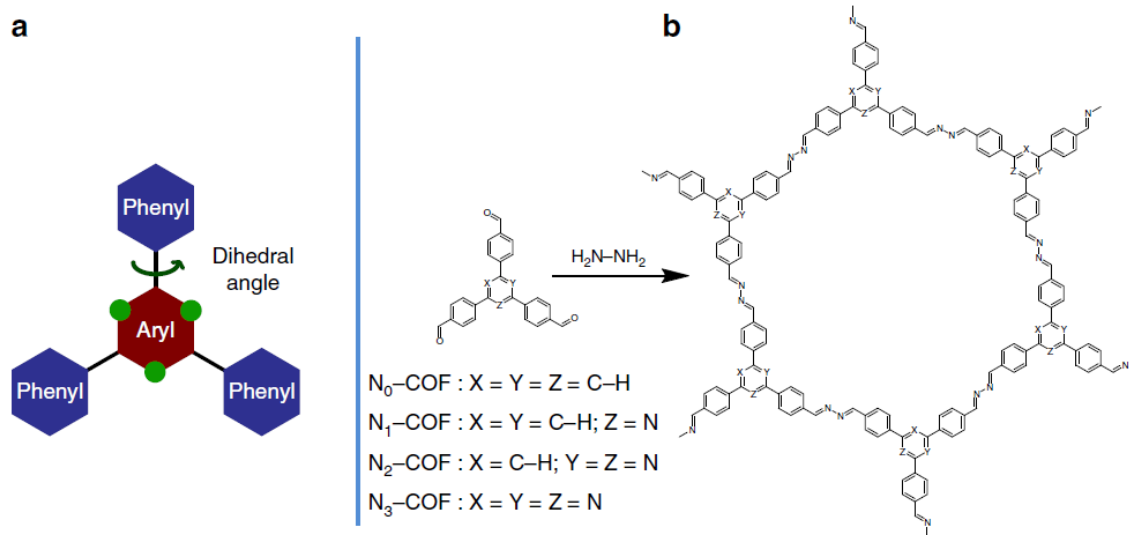


Figure 12. (a) A tunable triphenylarene platform for photocatalytic hydrogen evolution. Replacement of 'C-H' by 'nitrogen atoms' at the green dots changes the angle between central aryl and peripheral phenyl rings, which leads to varied planarity in the platform. (b) Synthesis of  $N_x$ -COFs from  $N_x$ -aldehydes and hydrazine<sup>165</sup>.

## Phosphorene

In 2014, a monolayer of black phosphorous (BP) was synthesised using the same sticky-tape technique as for graphene, named as 'phosphorene'<sup>169</sup>. BP has an orthorhombic, simple cubic and rhombohedral crystalline structure with five valence electrons in its outer shell<sup>170</sup>. Each P atom becomes saturated by making a covalent bond – two of which exist on the same plane, whilst another is on a neighbouring plan via 3p orbitals leaving a hole-electron pair, which leads to a quadrangular pyramid structure that resembles a puckered honeycomb structure as shown in Fig. 13. It results a highly asymmetric band structure and unique in-plane anisotropic properties<sup>171-172</sup>: (i) quantum confinement in the direction perpendicular to the 2D plane, which results in noble electronic and optical properties; (ii) no lattice mismatch issues for constructing a vertical heterostructure with other 2D materials; (iii) natural surface passivation without any dangling bond ( a suppressed charge carrier recombination is expected); (iv) large lateral size

with ultra-high specific surface area and high ratio of exposed surface atoms; and (v) strong interaction with light<sup>173-174</sup>, which are all considered highly desirable in photocatalysis applications. For example, a water stable phosphorene synthesised via liquid exfoliation was applied successfully in photocatalytic oxygen generation and methyl-orange decomposition<sup>175</sup>. The liquid exfoliated phosphorene nanosheets had a greater number of active sites for surface atoms, reduced electron-hole recombination rate and faster charge carrier mobility than bulk BP, which illustrated the characteristics as a good photocatalyst. However, the ultrathin BP nanosheets would be degrade with prolonged exposure to light, which needed to be resolved before large-scale commercial applications.

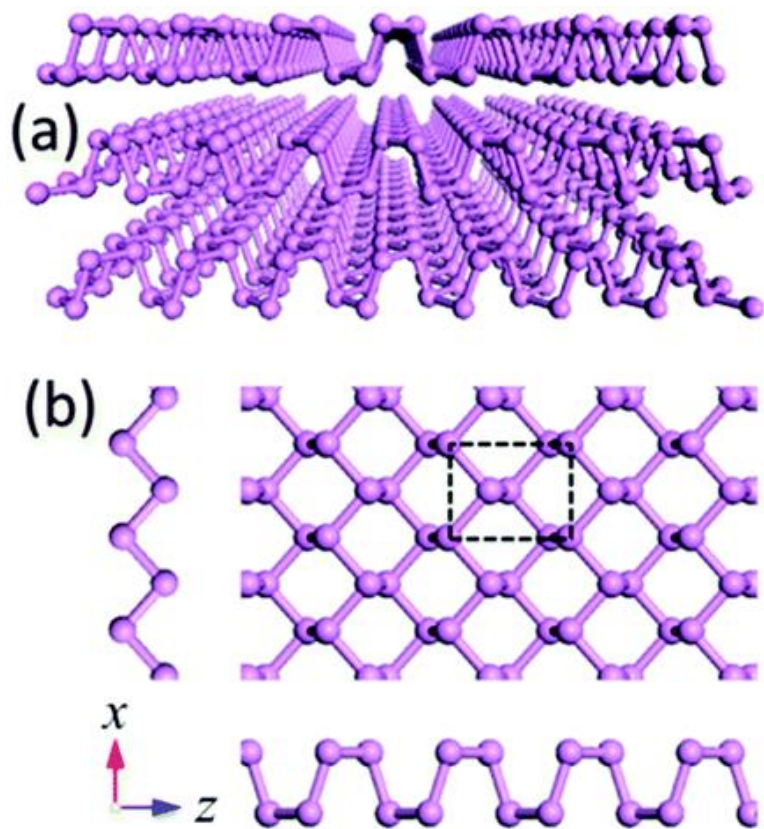


Figure 13. (a) The puckered structure of a few layer BP sheet. (b) Top view of monolayer BP. The  $x$  and  $z$  axes are along zigzag and armchair directions, respectively<sup>176</sup>.

## Porous organic polymers

An important development made recently is the construction of (nano)porous organic polymers, such as hypercrosslinked polymers<sup>177</sup>, polymers of intrinsic microporosity (PIMs)<sup>178</sup>, conjugated microporous polymers (CMPs)<sup>164</sup>, and so on<sup>179-180</sup>. Considering that the copolymers can be produced over a continuous range of monomer compositions, thus achieving systematic control over physical properties. A series of pyrene-based conjugated microporous polymers (CMPs) were used to tune the optical gap over a broad range (1.94-2.95 eV) by varying monomer composition<sup>164</sup>. Unlike most inorganic hydrogen-production photocatalysts, certain copolymers were active under visible light, but UV light contributed little to the photocatalytic activity, possibly because higher-energy excited states were diverted into pathways that were not suitable for hydrogen evolution. Another unique point was that these polymers did not require the deposition of an additional metal cocatalyst but still could produce hydrogen. Another series of conjugated phenylene oligomers (SM1-SM5) were fused by the introduction of a methylene bridge, or other bridging functionality, which lowered the phenylene-phenylene torsion angle and increased rigidity<sup>181</sup>. These planarised conjugated co-polymers strongly enhanced the hydrogen evolution from water in the presence of a mixed sacrificial electron donor (methanol and trimethylamine) both under visible and UV light irradiation. Here planarization and rigidification might be a general strategy for improving photocatalytic water splitting activity in organic polymers where the optical gap could be tuned by composition<sup>181</sup>. Interestingly, a light harvesting microporous organic network (VH-MON) was prepared based on Knoevena gel condensation between triformylarene and bicyanomethylarene species<sup>182</sup>. The VH-MON/TiO<sub>2</sub>-Pt system showed promising activity with 50  $\mu\text{mol}$  hydrogen production in the first 5 hours and kept stable in the next four rounds of 5 hours, which might be attributed to the electronic push and pull organic building blocks.

### 2.3.3 The development of CTFs

Classic polymers are primarily built up by one-dimensional chains, whereas porous organic polymers (POPs) exhibit two or three-dimensional structures which create and stabilise the pores in the materials. Among great varieties of POPs, covalent organic frameworks (COFs) are the only crystalline polymers. Here, CTFs are very often referred as a subclass of COFs since the CTF-0<sup>183</sup>, CTF-1<sup>184</sup> and CTF-2<sup>185</sup> are crystalline porous frameworks. This project mainly focuses on the crystalline CTFs, one of which was prepared in 2008 when the dicyanobenzene was melt with ZnCl<sub>2</sub> in 400 °C for 40 h<sup>184</sup>. The material showed the excellent surface areas up to 2475 m<sup>2</sup>g<sup>-1</sup> with high thermal and chemical stabilities. Most of preparation requires high temperatures<sup>186-187</sup> which sometimes could be up to 700 °C<sup>188</sup>. On the other hand, researchers also found that microwave assisted synthesis could produce CTFs at very low temperature by using trifluoromethanesulfonic acid (CF<sub>3</sub>SO<sub>3</sub>H) as a catalyst<sup>189</sup>. Obvious difference compared with previous works is that the CTFs are of pale yellow to brown. Their solid-state UV-vis spectra showed relatively broad absorption, and some had the peaks at visible light region. A schematic illustration to synthesise CTF-0, CTF-1 and CTF-2 are shown in Fig. 14<sup>190</sup>.

CTFs with high surface areas are promising materials for gas storage such as hydrogen<sup>184, 191-193</sup>, carbon dioxide<sup>183, 189, 191-192, 194-196</sup> and methane capture<sup>191-192</sup>. CTFs can also adsorb organic dyes in good quantities<sup>197-198</sup>, such as the pollutant 4,4'-(propane-2,2-diyl)diphenol<sup>199</sup>. Another popular application of CTFs is as matrices for catalysis due to their properties of easy recyclability and high stability<sup>200-202</sup>. Due to the presence of N-heterocyclic moieties in the frameworks, the stability of Pd nanoparticles decorated on these frameworks was improved during the liquid glycerol oxidation<sup>200</sup>. Similarly, Pd on the CTF was more stable in recycling than Pd on activated carbon (AC) and less sensitive than Pd on AC to the decrease of reactant concentration, resulting into the

higher selectivity to benzaldehyde (98%) with a considerable activity (turnover frequency 1453 h<sup>-1</sup>)<sup>201</sup>. Another popular metal cooperating with CTFs for gas oxidation is platinum which was reported for the oxidation of a carbon-hydrogen bond of methane to produce methyl esters as Pt complexes<sup>202</sup>. In recent years, due to the terephthalonitrile-driven nitrogen-rich network, CTF-1 also can be used as supercapacitor<sup>203</sup> or energy storage devices<sup>204</sup> in the rechargeable energy storage technology as it exhibited exceptionally high specific power, long cycle life and good energy storage efficiency.

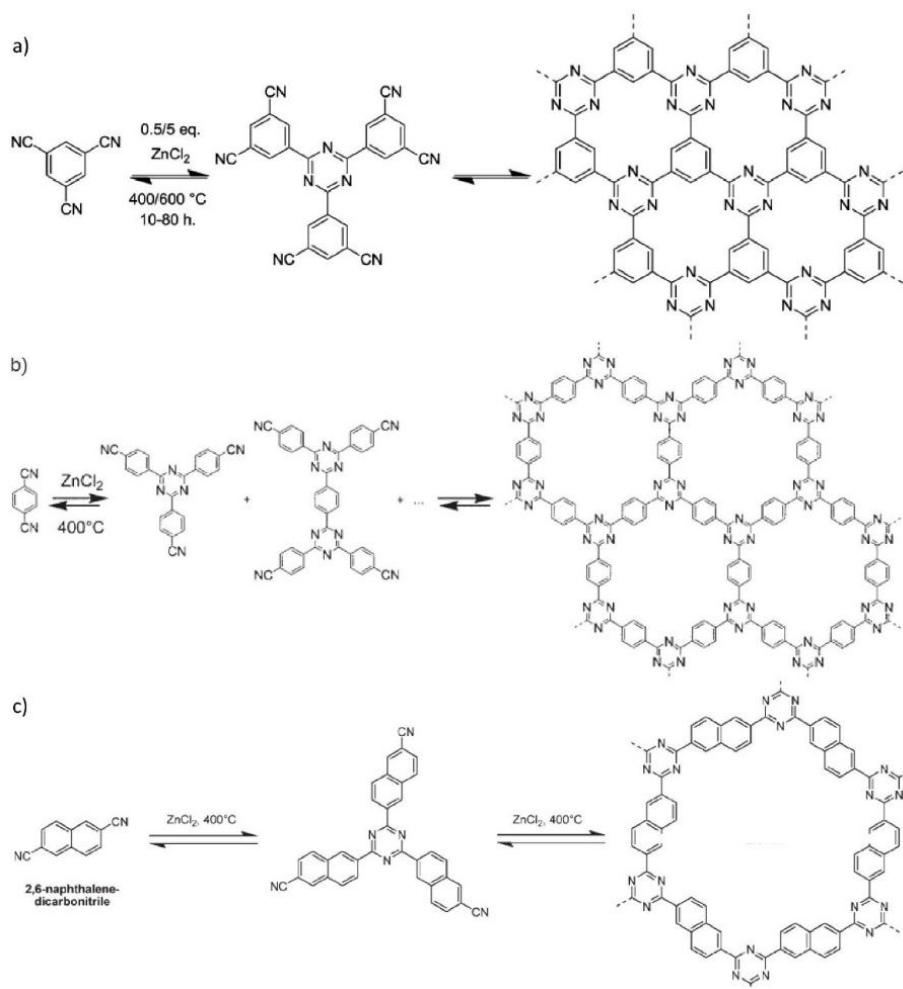


Figure 14. Schematic illustration of the trimerization reaction to synthesise CTF-0 (a), CTF-1 (b) and CTF-2 (c), respectively.

Such colored compounds might be capable of light-induced hydrogen/oxygen evolution as the recent experimental and theoretical results delineated the structural and photophysical properties of CTF-1-type materials, which obtained through the trimerization of 1,4-dicyanobenzene, producing them as potentially suitable semiconductor photocatalysts<sup>189, 205</sup>. Usually, ionothermal method is the efficient way to form triazine ( $C_3N_3$ ) ring at the high temperature and using long reaction time. In order to shorten the reaction time and lower the reaction temperature, microwave-assisted polymerisation was a preferable method by using trifluoromethanesulfonic acid (TFMS) as the catalyst at lower temperatures<sup>189</sup>.

As described above, the incorporation of triazine units into polymeric systems has shown correlation with hydrogen evolution rates as the triazine nitrogen may act as the active site<sup>135</sup>. Covalent triazine-based frameworks (CTFs) as a typical COFs are composed of  $\pi$ -stacked aromatic units, which are expected to promote exciton separation and charged transport and thus prefer for photocatalysis. CTF-Ts with a graphene-like layered morphology, indicating the excellent photocatalytic activity in water reduction under visible light irradiation ( $\lambda \geq 420$  nm)<sup>206</sup>. The hydrogen evolution rate of CTF-T1 was preliminarily proved very moderate at around 20  $\mu\text{mol/h}$  (80mg photocatalysts) and the photocatalyst was relatively stable for five circles. After loading  $\text{RuO}_2$ , CTF-T1 could also produce  $\text{O}_2$  although the activity was very low, around 0.7  $\mu\text{mol/h}$  (80mg photocatalysts) from water under visible light irradiation. Electrochemical measurement and the theoretical calculations revealed the HOMO and LUMO energy levels of CTF-T1 had the suitable band position with respect to the oxidation and reduction levels of  $\text{H}_2\text{O}$ . Importantly, it was anticipated that more efficient CTF-based photocatalysts could be expected via facilely tuning the frameworks. Thereupon, a series of oligomers of CTF-1, with different length and connectivity, were synthesized by a lower reaction temperature than pure CTF-1 during

ionothermal trimerization synthesis<sup>207</sup>. These oligomers showed the hydrogen evolution performance with an average rate of 10.8 ( $\pm$ 2.8)  $\mu\text{mol/h}$  (10 mg photocatalysts) under simulated sunlight irradiation, whereas little hydrogen was observed for the CTF-1 polymer. The reason for the much lower activity of CTF-1 might be a reduced thermodynamic driving force for hydrogen evolution or the incipient carbonization at its synthesis temperature of 400 °C, where light absorption by carbon prevented photon absorption by the framework, thus rendering hydrogen evolution. For these oligomers, it seems like that the increased photocatalytic activity correlates with an increased amount of nitrile moieties and improved  $\pi$ -stacking.

Subtle differences between the experimental optical absorption spectra and the fluorescence spectra of CTFs prepared using different synthesis routes illustrated that different synthesis routes could influence bandgap engineering<sup>205</sup>. Moreover, based on first principles calculation, it was predicted that certain CTFs should be promising visible-light photocatalysts according to the suitable band gap (e.g CTF-1, 2.42 eV) and the position of its band potentials which were dependent on the nitrogen content in the CTFs, the number of ring systems, and the extent of interactions<sup>208</sup>. This kind of 2D metal-free organic materials combine the unique advantages of high surface area, low cost, chemical and thermal stability in aqueous solution, easy fabrication, and mechanical flexibility. From these, I believe that the charge transfer kinetics can be tuned by controlling the polymerization progress of CTFs. Although there are a few studies on CTF-1 for H<sub>2</sub> production, water oxidation by the CTFs is very challenging with few successful reports given it is the rate determining step in water splitting. Furthermore, there are fewer reports on other CTF polymer photocatalysts and less mechanistic studies were taken to understand the correlation between the structure of the CTFs and their physical and photocatalytic properties. Herein, this project will mainly concentrate on a group of CTFs to achieve efficient photocatalytic

water oxidation and in parallel reduction under visible light irradiation. Finally, pure water splitting will also be targeted, and the fundamental understanding is another topic.

## 3 Chapter 3

### Methodology

This session describes the general characterisation methods and the essential parts of the photocatalytic performance test system in details.

#### 3.1 Material characterizations

It is essential to characterise the compounds of the materials correctly when either engineering a new material or modifying existing photocatalysts. A various characterization methods are presented in this section, which not only help to confirm the composition of the materials, but also aid in understanding the water splitting mechanism for the photocatalytic system.

##### 3.1.1 BET

Specific surface area was measured via the Brunauer-Emmett-Teller (BET) method, using N<sub>2</sub> adsorption by a Micromeritics® Tristar 3000. As one example, powdered samples were placed in a borosilicate vial with a weight to surface area ratio of 1 g to 30 m<sup>2</sup> in order to acquire suitable data. The volume of gas adsorbed to the surface of the particles by Van de Waals forces was measured at the boiling point of nitrogen (-196 °C). The amount of adsorbed gas was correlated to the total surface area of the particles including pores in the surface. The calculation was based on the BET theory. Traditionally nitrogen was used as adsorbate gas. Gas adsorption also enabled the determination of size and volume distribution of micropores (0.35-2.0 nm).

The data were treated according to the Brunauer, Emmett and Teller (BET) adsorption isotherm equation:

*Equation 4. The BET equation*

$$\frac{1}{V_a \left( \frac{P_0}{P} - 1 \right)} = \frac{C-1}{V_m C} \times \frac{P}{P_0} + \frac{1}{V_m C}$$

In the equation, P is the partial vapour pressure of adsorbate gas in equilibrium with the surface at 77.4 K (b.p. of liquid nitrogen) in pascals; P<sub>0</sub> is the saturated pressure of adsorbate gas in pascals; V<sub>a</sub> is the volume of gas adsorbed at standard temperature and pressure (STP) [273.15 K and atmospheric pressure (1.013\*10<sup>5</sup> pa)] in millilitres; V<sub>m</sub> is the volume of gas adsorbed at STP to produce an apparent monolayer on the sample surface in millilitres; C is the dimensionless constant that is related to the enthalpy of adsorption of the adsorbate gas on the powder sample.

*Equation 5. The BET constant C*

$$C = e^{\frac{(E_1 - E_L)}{RT}}$$

Where E<sub>1</sub> is the first layer's heat of adsorption, and E<sub>L</sub> is the corresponding heat of absorption for n layers > 1.

Equation 4 can be simplified as a 'y = mx + c' graph, and the result is termed as a 'BET plot'. The ordinate term is  $\frac{1}{V_a \left( \frac{P_0}{P} - 1 \right)}$ , whilst  $\frac{P}{P_0}$  can be plotted on the abscissa. Linearity is found at approximately  $0.01 \leq \frac{P}{P_0} \leq 0.3$  and thus extrapolating from this point using the gradient A<sub>0</sub> to y-intercept I<sub>0</sub> gives V<sub>m</sub> and C according to the equation:

Equation 6.

$$V_m = \frac{1}{A_0 + I_0}$$

Equation 7.

$$C = 1 + \frac{A_0}{I_0}$$

The BET specific surface area (SSA) is then given by:

Equation 8. BET SSA equation

$$S_{BET} = a \left( \frac{V_m N_A S}{V} \right)$$

Where  $a$  is the mass of the powdered adsorbents,  $N_A$  is Avogadro's number,  $S$  is the adsorption cross section of the powder, and  $V$  is the molar volume of gas.

From the practical point of view, it is much simpler to obtain a value of specific surface area, since the surface area analyser can calculate all the above automatically. All needed is a precise measurement of the mass of the sample, and to correctly pick the point of the linearity (a line of the best fit). The linearity can be improved by a constant trial and error process which minimises the correlation coefficient (R-factor), so that the value is as close to 1 as possible (acceptable values are normally  $\geq 0.999$ ).

### 3.1.2 UV-visible spectroscopy

Absorbance, reflectance and transmission spectra were collected from a Shimadzu UV-2550 spectrophotometer fitted with an integrating sphere. The reflectance is related to the absorption by the following equations:

*Equation 9. Transmission-reflectance-absorption relation*

$$1 = T + R + A$$

where T, R and A is the transmission, reflectance and absorbance in %, respectively.

The UV-visible spectrophotometers measures the intensity of light passing through a sample ( $I$ ), and compares it to the intensity of refence light ( $I_0$ ). The ratio  $I/I_0$  is called the transmittance (T%).

The absorbance, A, is based on the transmittance:

*Equation 10. Absorbance conversion*

$$A = -\log\left(\frac{T\%}{100\%}\right)$$

The UV-visible spectrophotometer can also be configured to measure reflectance. In this case, the spectrophotometer measures the intensity of light reflected from a sample ( $I$ ), and compares it to the intensity of refence light ( $I_0$ ) (such as barium sulfate slice). The ratio  $I/I_0$  is called the refectance (R%). The reflection could be directly converted to absorption coefficient ( $a$ ) by the Kubelka-Munk transformation:

Equation 11. Kubelka-Mulk relation

$$\alpha = \frac{(1 - R)^2}{2R}$$

Typically, data of the electromagnetic spectrum would be collected by UV-visible spectrophotometers from ultraviolet (250 nm) through to the visible range (800 nm), with an optimum slit width of 2 nm. This reduces noise whilst not compromising the accuracy of the data. The frequency of the data was 0.5 nm, as this was more than adequate enough to determine precise spectra. Molecules often undergo electron transitions at these frequencies, since semiconductors have discrete energy levels corresponding to allowed electron states<sup>29</sup>. Therefore, one can determine the size and the type of band gap (direct or indirect). This is done using a Tauc plot, often used in thin films<sup>209</sup>:

Equation 12. Tauc relation

$$(\alpha h\nu) = A_T(h\nu - E_{BG})^n$$

Where  $h$  is Planck's constant,  $\nu$  is the light frequency,  $h\nu$  is the energy of incident radiation,  $A_T$  is the constant which is based on effective masses of electrons and holes, and  $n$  can take the values of 0.5 and 2, for a direct and indirect band gap transition. The band gap ( $E_{BG}$ ) of semiconductor is approximately equal to the absorption edge, which can be also obtained from extrapolating towards the x-axis on a plot of wavelength (x-axis) versus absorption. Then using the following relation, calculate the band gap:

Equation 13. Planck relation (nm)

$$E_{BG} = h\nu = \frac{hc}{\lambda} = \frac{1240}{\lambda}$$

The absorption edge can be blue shifted by decreasing the particle size and is often attributed to either a quantum size or a direct charge-transfer transition. If the band gap region possess a long tail, and appears to be red shifted, then this would conclude that there are additional sub band gap exists between the band gap<sup>210</sup>.

### **3.1.3 Attenuated total reflectance Fourier transform infrared (ATR-FTIR) spectroscopy**

ATR-FTIR is a fast infrared spectroscopic technique for probing in situ single or multiple layers of absorbed/deposited species at a solid/liquid interface<sup>211</sup>. Using ATR-FTIR, we have been able to detect fingerprints of covalent bonds or triazine bonds, which is beneficial for both characterisation and analysis of impurities/contaminants on the surface of the photocatalysts. In the project, organic photocatalysts or impurities are intrinsically molecularly complex, and thus will easily be detectable using IR spectroscopy. In FTIR, a broadband/polychromatic light source (all frequencies to be measured) is used to illuminate the sample. The beam first passes through a Michelson interferometer, a beam polariser device which causes a deliberate path length shift, subsequently hitting the sample with a mixed interference beam of all wavelengths and finally collected by the detector. Beam polariser is caused by a moving mirror within the interferometer, which has real units of length. Therefore, the detector produces an interferogram; a fixed set of polarise values and a corresponding set of intensities. A Fast Fourier Transform (FFT) is automatically applied by the instrument, converting time/space to frequency. The resultant FTIR

spectrum is a set of inverse lengths ( $\text{cm}^{-1}$  is often used) versus intensity. Thus, bonds can be assigned to intensities at certain wavenumbers (energies).

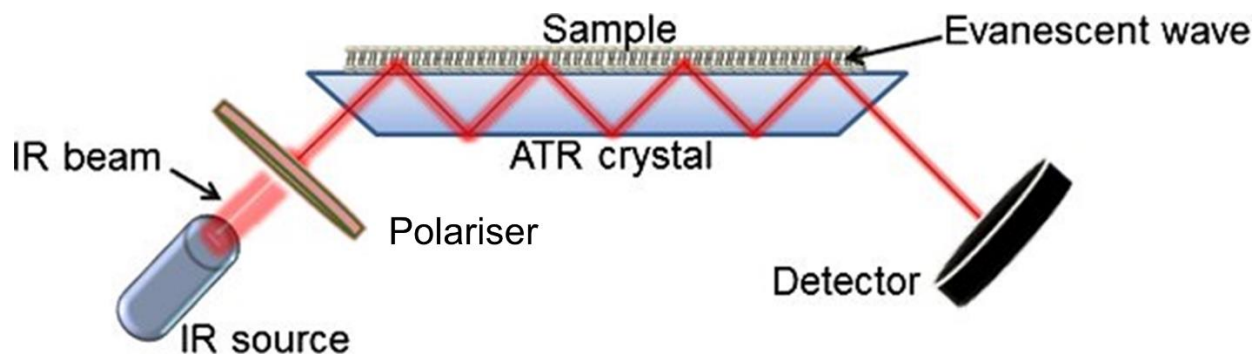


Figure 15. Schematic representation of an ATR-FTIR system<sup>212</sup>.

Fig. 15 illustrated a typical and simplified ATR-FTIR set up. A beam of infrared light is passed through the ATR crystal in such a way that it reflects at least once off the internal surface in contact with a sample. The reflection forms the evanescent wave which extends into the sample. The penetration depth into the sample determined by the wavelength of light ( $\lambda$ ), the angle of incidence ( $\theta$ ) and the indices of refraction for the ATR crystal ( $n_1$ ) and the sample being probed ( $n_2$ )<sup>213</sup>, typically between 0.5 and 3  $\mu\text{m}$ . The evanescent effect only works when the ATR base has a higher refractive index than the sample, which prevents the light is lost into the sample. The governing equation depth of penetration is shown below:

Equation 14. The depth of penetration

$$dp = \frac{\lambda}{2\pi\sqrt{n_1}} \sqrt{\sin^2(\theta) - n_2^2}$$

Compared to the transmission-IR, ATR-IR has the limited path length into the sample, avoiding the strong attenuation of the IR signal in highly absorbing media such as aqueous solutions. On

the other side, for UV-visible light, the evanescent light path is sufficiently short so that interaction with the sample is decreased with wavelength. For optical dense samples, UV-vis spectroscopy is alternative measurement to clarify the compounds of the samples. In addition, as no light path has to be established in ATR-FTIR system, single shaft probes are enough for process monitoring and are applicable in both the near and mid infrared spectrum. In the studies, ATR-FTIR spectroscopy was performed on a Perkin-Elmer 1605 FT-IR spectrometer in the wavelength range from 400-4000  $\text{cm}^{-1}$  with a resolution of 0.5  $\text{cm}^{-1}$ . Powered samples were placed on the ATR crystal, and then compressed using a flat axial screw.

#### **3.1.4 Raman spectroscopy**

Different from the ATR-FTIR spectroscopy that it can provide a compound fingerprint, Raman spectroscopy is less widely used method of vibrational, rotational or other low frequency modes in a system. In FTIR spectroscopy, a polychromatic light source is used, and detection of activated IR bonds depends on the loss of a certain frequency due to absorption. In Raman spectroscopy, a monochromatic laser beam illuminates the sample, which is in turn scattered by the sample, but not absorbed as FTIR spectroscopy. The laser light interacts with molecular vibrations, phonons or other excitations in the system, resulting in the energy of the laser photons being shifted up or down. The shift in energy gives information about the vibrational modes in the system. The Raman effect is based on the interaction between the electron cloud of a sample and external electrical field of the monochromatic light. An incident photon creates an induced dipole moment within the molecule based on its polarizability, which puts the molecule into a virtual energy state for a short time and then emits a photon and return to a vibrational state. The energy of the emitted photon is of either lower or higher than the incident photon, termed as inelastic light scattering. After the scattering event, the sample is in a different rotational or vibrational state.

For the total energy of the system to remain constant after the molecule changes to a new rovibronic state, the scattered photon will be shifted to a lower frequency (lower energy) if the final state is higher in energy than the initial state. This shift in frequency is called a Stokes shift, or downshift, as shown in Fig. 16. If the final state is lower in energy, the scattered photon will be shifted to a higher frequency, which is called an anti-Stokes shift, or upshift (Fig. 16). The intensity of the Raman scattering is proportional to this polarisability change with respect to the vibrational coordinate change corresponding to the rovibronic state change. On the other side, if the photon excites a vibrational energy state to a virtual state and subsequently returns to the same vibrational energy state, it is called Elastic/Raleigh scattering. Raleigh scattering is around  $10^6 - 10^8$  more popular than Raman scattering, which is a very weak process, and thus needs a monochromatic source. Rayleigh scattering at the wavelength corresponding to the laser line is filtered out by either a notch filter, edge pass filter, or a band pass filter, while the rest of the collected light is dispersed onto a detector.

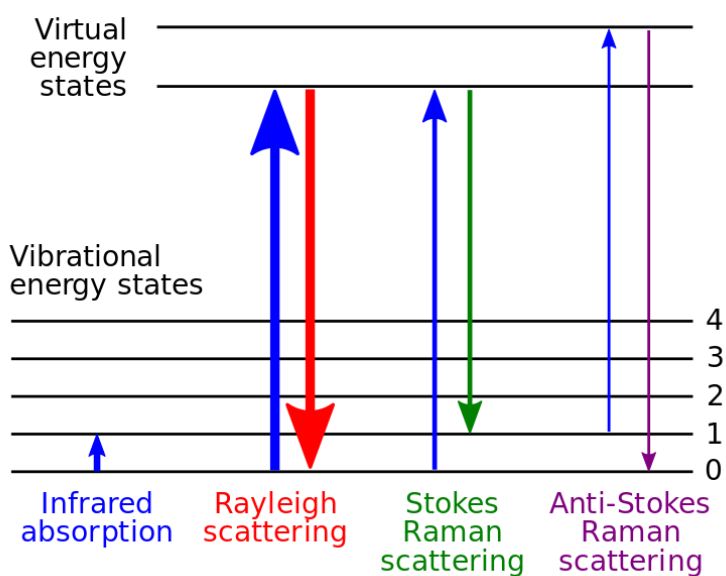


Figure 16. Energy-level diagram showing the states involved in Raman spectra.

In terms of its application in analysing semiconductor photocatalysts, Raman spectroscopy can be used to identify the molecules by characteristic phonon modes and be used to study the chemical bonding in the structure. Due to that the vibrational frequencies are specific to a molecule's chemical bonds and symmetry (the fingerprint region of organic molecules is in the wavenumber range 500 -1500  $\text{cm}^{-1}$ ), Raman spectrum provides a fingerprint to identify molecules. Simultaneously, the possible contaminants on the surface of the photocatalyst can also be detected, which often act as either recombination traps or electron/hole scavengers and prevent the photocatalytic performance. Similarly, the distortion in local structure (*i.e.* change in electron orbital overlap) can be interpreted by the change in the Raman shift at a certain wavelength, which can influence the photocatalytic activity<sup>214</sup>.

In this study, the advanced micro-Raman spectroscopy system consists of a Renishaw spectrograph system based on use of Kayser™ notch filters with a sensitive CCD detector coupled to a microscope for point-by-point analyses. The incident laser for Raman scattering and fluorescence measurements is 325 nm, and a wavenumber range from 100-200  $\text{cm}^{-1}$ . A few milligrams powered samples were placed on the glass slide and then irradiated by the incident lasers.

#### **3.1.4 Powder X-ray diffraction (PXRD)**

PXRD is a rapid analytical technique primarily used for phase identification of a crystalline material and can provide purity and composition information on unit cell dimensions. The analyzed material is finely ground, homogenised, and average bulk composition is determined. The X-rays are generated by a cathode ray tube, filtered to produce monochromatic radiation, collimated to concentrate, and directed towards the sample. The interaction of the incident rays

with the sample produces constructive interference (and a diffracted ray) when conditions satisfy Bragg's Law ( $n\lambda = 2d\sin\theta$ ), where the wavelength of electromagnetic radiation ( $\lambda$ ) is related to the diffraction angle ( $\theta$ ) and the lattice spacing in a crystalline sample ( $d$ ). After scanning the sample through a range of  $2\theta$  angles, all possible diffraction directions of the lattice should be attained due to the random orientation of the powdered material. These diffracted X-rays are then detected, processed and counted. Conversion of the diffraction peaks to d-spacings allows identification of the crystal phase because each crystal phase has a set of unique d-spacings. Typically, this is achieved by comparison of d-spacings with standard reference patterns. This technique is good for gaining insight into photocatalytic mechanisms for the photocatalysts which has multiple phases, since the change of phase and crystallinity influences the band gaps, and it is also very easy to see impurities, both of which can affect photocatalytic activity.

More specific features of compounds can be obtained by further analysis, such as crystallite size, and the average distance between molecules. The weak peak response, in conjunction with a broad width, indicates the poor crystallinity. On the other side, strong peak responses with broad features often mean the particle size is very varied. The average particle or crystallite size can be calculated using Scherrer's equation:

*Equation 15. Scherrer's equation*

$$\tau = \frac{K\lambda}{\beta \cos \theta}$$

Where K is the shape factor (near 1, but crystalline shape dependant),  $\lambda$  is the X-ray wavelength,  $\beta$  is the line broadening at half the maximum intensity,  $\theta$  is the Bragg angle, and  $\tau$  is the mean size of the ordered crystalline domains, which is approximately the grain size. The Scherrer

equation works in the condition of nano-sized particles and is limited to a grain size of 0.1  $\mu\text{m}$ . Actually, a lower bound to the particle size will be calculated by the Scherrer formula, as the width of the diffraction peak can be determined by many factors, not just crystallite size, such as inhomogeneous strain and instrumental effects<sup>215</sup>. In this case, it is more appropriate to use other particle sizing techniques (such as TEM or SEM) to identify the particle size.

In this study, Powder X-ray diffraction (PXRD) was performed on either a Rigaku RINT 2100 (40 kV, 400 mA, using a Cu source with  $\lambda_1 = 1.540562 \text{ \AA}$  and  $\lambda_2 = 1.544398 \text{ \AA}$ ) or Bruker D4 (40 kV, 30 mA, using a Cu source with  $\lambda_1 = 1.54056 \text{ \AA}$  and  $\lambda_2 = 1.54439 \text{ \AA}$ ). A maximum range was 0-90° (2 $\theta$ ). Phase match and baseline corrections were performed on either MDI Jade, or Bruker's EVA software using the ICSD/JCPDS database. A powdered sample was flattered into an amorphous glass (Rigaku) or silicon (Bruker) holder.

### 3.1.5 X-ray photoelectron spectroscopy (XPS)

XPS is a surface-sensitive quantitative spectroscopic technique that detects only those electrons escaped from the sample into the vacuum of the instrument by irradiation with an X-ray source. Because the energy of an X-ray with particular wavelength is known (for Al K $_{\alpha}$  X-rays,  $E_{\text{photon}} = 1486.7 \text{ eV}$ ), and because the emitted electrons' kinetic energies are measured, the electron binding energy of each of the emitted electrons can be determined by using an equation that is based on the work of Ernest Rutherford (1914):

*Equation 16. Conservation of binding energy*

$$E_{\text{binding}} = E_{\text{photon}} - (E_{\text{kinetic}} + \phi)$$

Where  $E_{\text{binding}}$  is the binding energy (BE) of the electron,  $E_{\text{photon}}$  is the energy of the X-ray photons being used,  $E_{\text{kinetic}}$  is the kinetic energy of the electron as measured by the instrument and  $\phi$  is the work function dependent on both the spectrometer and the material. The work function term  $\phi$  is an adjustable instrumental correction factor that accounts for the few kinetic energies of photoelectron as it is absorbed by the instrument's detector, so it is a constant that rarely needs to be adjusted in practice.

The typical XPS spectrum is a plot of the number of electrons detected (sometimes per unit time) (y-axis, ordinate) versus the binding energy of the electrons detected (x-axis, abscissa). Each element produces a characteristic set of XPS peaks at characteristic binding energy values that directly identify each element that exists in or on the surface of the analysed material. These characteristic spectral peaks correspond to the electron configuration of the electrons within the atoms, *e.g.*, 1s, 2s, 2p, 3s, *etc.* The number of detected electrons in each of the characteristic peaks is directly linked to the amount of element within the XPS sampling volume. To generate atomic percentage values, each raw XPS signal must be corrected by dividing its signal intensity (number of electrons detected) by a 'relative sensitivity factor' (RSF), and normalised over all of the elements detected, excluding hydrogen.

Thus, XPS can measure atomic composition (%), chemical and electronic state, and bonding configuration of elements in a sample, whilst being non-destructive. Depth profiling deeper into the bulk is possible when using ion etching, but the depth is limited up to *ca.* 10 nm deep into the bulk from the surface<sup>216</sup>. Furthermore, Ultraviolet Photoelectron Spectroscopy (UPS) can be used to detect valence electrons excited by UV light, using a similar technique as XPS. Both techniques should be under Ultra High Vacuum (UHV) to make sure the very low pressures for the escaped electrons passing through a long way from the surface of the material to the detector successfully.

XPS has considerable application in characterisation of photocatalysts. For example, XPS can detect the amount of the dopants in the photocatalysts, which is helpful to optimise the atomic percentage after preparation in order to obtain the optimum dopant percent, and finally beneficial to alter the band gap and improve the photocatalytic activity<sup>217</sup>. Moreover, it is possible to find out the difference between the surface species and the bulk-bound ions through location mapping and chemical state identification by combining the XPS depth profiling and the traditional orbital labelling<sup>218</sup>. Furthermore, UPS can be used to determine the ionization potential (equivalent to the valence band energy) of the new materials by subtracting the ionization potential of the reference, which is useful to ascertain the proper conduction band and valence band levels of a photocatalysts to match the redox potentials of the photocatalytic reactions<sup>148</sup>.

In this thesis, XPS measurements were carried out on a ThermoScientific XPS K-alpha surface analysis machine using an Al source. Analysis was performed on the Thermo Advantage software. Sample was scanned 6 times at different points on the surface to eliminate point error and create an average. Specific elemental peaks were then identified, and analysed further.

### **3.1.6. Nuclear magnetic resonance (NMR) spectroscopy**

NMR spectroscopy is applied in material science as a valuable tool to obtain physical, chemical, electronic and structural information about molecules due to the chemical shift of the resonance frequencies of the nuclear spins in the sample. Peak splittings of NMR spectroscopy due to J-couplings or dipolar couplings between nuclei can provide detailed and quantitative information on the functional groups, topology, dynamics and three-dimensional structure of molecules in solution and the solid state. Since the area under an NMR peak is usually proportional to the number of spins involved, peak integrals can be used to determine composition quantitatively.

The sample is placed in a magnetic field and the NMR signal is produced by excitation of the nuclei sample with radio waves into nuclear magnetic resonance, which is detected with sensitive radio receivers. The intramolecular magnetic field around an atom in a molecule changes the resonance frequency, thus giving details of the electronic structure of a molecule and its individual functional groups. The most common types of NMR are proton, carbon-13 and nitrogen-14 NMR spectroscopy, but it is applicable to any kind of sample that contains nuclei possessing spin. As the identical functional groups with different neighboring substituents give distinguishable signals, NMR spectra are often highly predictable for different functional groups in small molecules. Preferably, the samples have to be dissolved in a solvent, because NMR analysis of solids requires a dedicated magic-angle spinning machine and may not give equally well-resolved spectra.

For this research, The NMR data were collected using a Bruker Avance 300WB equipped with a 4 mm magic-angle spinning probe for  $^{13}\text{C}$  and  $^1\text{H}$  measurements. The dipolar coupling and chemical shift anisotropy lead to a significant broadening of spectral lines. Usually 3~5 mg of sample is placed in a 5 mm tube. On doubling the sample quantity, the number of scans can be decreased 4 times in order to achieve the same level of the signal-to-noise ratio. An ACD/NMR Processor can be used for viewing or processing NMR data.

### **3.1.7 Scanning and transmission electron microscopy (SEM and TEM)**

SEM and TEM are two different techniques applied in imaging the surface structure of semiconductors. SEM is often used to capture the surface topography and composition of the sample by scanning the surface with a focused beam of electrons, especially with samples which are electrically conductive, at least at the surface, and electrically grounded to prevent the

accumulation of electrostatic charge. Metal species only need cleaning and conductive adherence to the specimen stub. Non-conducting materials are usually coating with an ultrathin layer of electrically conducting material, such as gold, platinum, iridium, and *etc.*<sup>219</sup>, deposited on the sample either by low-vacuum sputter coating or high-vacuum evaporation. The image of SEM results from interaction of the electron beam with atoms at various depths within samples. The electrons lose energy by repeated random scattering and absorption within a teardrop-shaped volume of the specimen known as the interaction volume, which usually ranges from less than 100 nm to *ca.* 5  $\mu\text{m}$  into the surface. Various types of signals are produced through the energy exchange between the electron beam and the sample, including secondary electrons (SE), reflected or back-scattered electrons (BSE), characteristic X-rays and light (cathodoluminescence) (CL), absorbed current (specimen current) and transmitted electrons, as shown in Fig. 17, each of which can be detected by specialised detectors and gives the digital image 3-dimensional appearance.

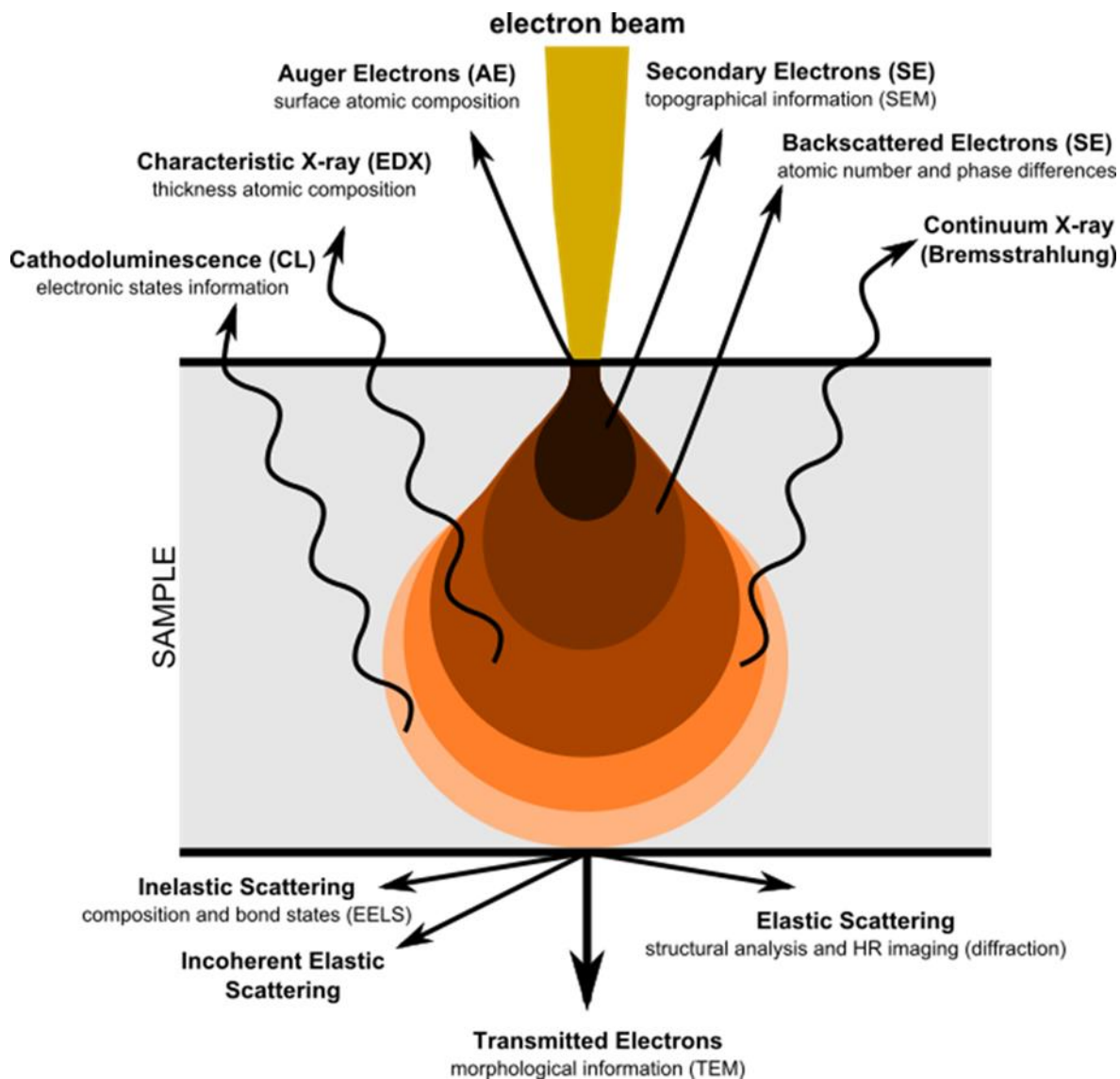
TEM forms an image by the interaction of the electrons with the sample when a beam of electrons transmits through the specimen, which is most often an ultrathin film or a suspension on a grid. TEM is capable of imaging at a significantly higher resolution than light microscopes, owing to the smaller de Broglie wavelengths of electrons, which means it can capture even as small as a single column of atoms. It is advantageous to detect nano-scale surface elements such as metallic/crystalline elements, which is challenging for SEM. Unlike SEM, TEM allows the observation of non-conductive samples, but constrain the thickness of the specimens ( $< 100\text{ nm}$ ), limited by the scattering cross-section of the atoms from which the material is comprised. By carefully selecting the orientation of the crystals, it is possible not just to determine the position of defects but also determine the type of defects present, identified by particularly strong contrast

variations produced by the distortion of the crystal plane that locally tilts the plane to the strongest diffracting angle (known as the Bragg Angle). Phase contrast of the crystal structures can be investigated by high-resolution transmission electron microscopy (HRTEM). A field emission source with the complex modulus is needed to transmit a specimen of uniform thickness, and the images are formed due to differences in phase of electron waves after the specimen interaction.

Appropriately equipping electron energy loss spectroscopy (EELS) with TEM provides information about the elemental composition and the physical and chemical properties of the specimen by detecting the energy losses of the electron beam and the energy distribution of all the inelastically scattered electrons. An electron beam with a known, narrow range of kinetic energies, may be inelastically scattered when it interacts with the atomic electrons in the specimen, which means they lose energy and their paths are slightly bent through a small angle (5~100 milliradians). Especially, the inner-shell ionization is one type of inelastic interactions and is particularly useful for detecting the elemental components of a material. The scattering angle (*i.e.*, the angle that the electron's path is bent) can give information about the dispersion relation of whatever material excitation caused by the inelastic scattering. The types of atoms, and the numbers of atoms of each type can be determined by looking at a wide range of energy losses.

Energy-dispersive X-ray spectroscopy (EDS), sometimes called EDX, is an additional feature conjugated with SEM/STEM, as it relies on an interaction of some source of X-ray excitation and a sample. The atoms are ionised by the primary electron beam leading to holes generated on the inner shells. Following the ionisation, the electrons from outer, higher-energy shells fill the holes and emit the X-rays. As the energies of the emitted X-rays are characteristic of the difference in energy between the two shells and of the atomic structure of the emitting element, EDS can

provide information of the elemental composition of the specimen. Compared to EELS, EDS is more easy to use and more sensitive to heavier elements. In photocatalysis studies, it can be used to ascertain the distribution of cocatalysts or impurities on the surface of photocatalysts.



Equation 17. Signals emitted from different parts of the interaction volume.

In this study, A JEOL JSM-7401F is used as a high resolution Field Emission Scanning Electron Microscope in which the samples are pasted on the holders. The conventional Transmission Electron

Microscopes (TEMs) were taken using a JEOL2010F, at an accelerating voltage of 200 keV. Powered samples were diluted in chloroform, sonicated to disperse particle, and then dropwise added onto a conductive copper grid.

### **3.1.8 Elemental Analysis (EA)**

EA is the most common technique to qualitatively and quantitatively determine the elemental composition and sometimes isotopic composition by analysing the combustion products: carbon dioxide, water, nitric oxide and sulphur oxide. Therefore, EA almost always refer to CHNX analysis - the analysis of the mass fractions of carbon, hydrogen, nitrogen, and heteroatoms (X) (halogens, sulphur) of a sample. Simply, a sample is burned in an oxygen rich atmosphere, and subsequently, the combustions are separated by gas chromatography, and in modern apparatus, analysed by high temperature TCD<sup>220</sup>. The masses of these combustion products are used to calculate the composition of the unknown sample. This technique is helpful to determine if a sample applied is the desired compound and confirm the purity of the compound.

In this study, Elemental Analysis (EA) was performed on a Micro Elemental Analyser (CE-400 CHN Analyser, Exeter Analytical Instruments). Accurate ( $\pm 0.1\%$ ) light percentage of carbon, nitrogen, hydrogen and trace elements were converted to atomic percentages before analysis.

### **3.2 Material performance test**

Materials photocatalytic performance test is the essential part. In this session, the gas chromatography setup, reactor, light source and efficiency calculations in the photocatalytic performance test system will be described in details.

### 3.2.1 Gas chromatography setup

The process of water redox often yields oxygen/hydrogen, and calculating the amount of each produced gas is vital. Gas chromatography is used to analyse concentration and amount of a gas in a given atmosphere, often to a great resolution. A sample of gas is injected into the head of the chromatographic column by the flow of inert, gaseous mobile phase. The column itself contains a liquid stationary phase which is absorbed onto the surface of an inert solid. The schematic diagram of a gas chromatograph is shown in Fig. 17.

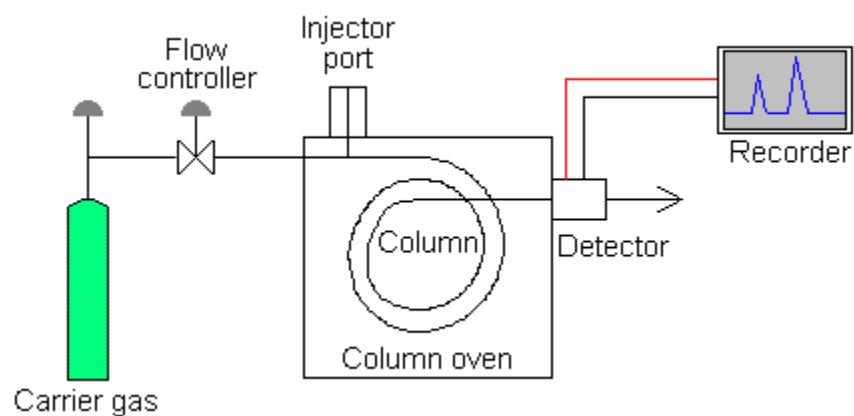


Figure 17. The Schematic diagram of a gas chromatograph.

In this experiments, a Varian 450 gas chromatograph (GC) was used to analyse the amounts of gaseous products from water redox reaction (Fig. 18), and to monitor nitrogen levels within a batch reactor. Samples were taken by using a gastight syringe (SGE® 1MDF-LL-GT 1 mL) (Fig. 19) . The GC was fitted with a TCD and molecular sieve 5A column, running with argon carrier gas (zero grade). Standard carrier gases are nitrogen, helium and argon. Argon is ideal for hydrogen and oxygen detection since it has much less thermal conductivity than the respective gases (Table 2). Helium could be used, however due to its similar thermal conductivity to

hydrogen, it would not be favourable, and also yield negative peaks, complicating the integration during analysis.

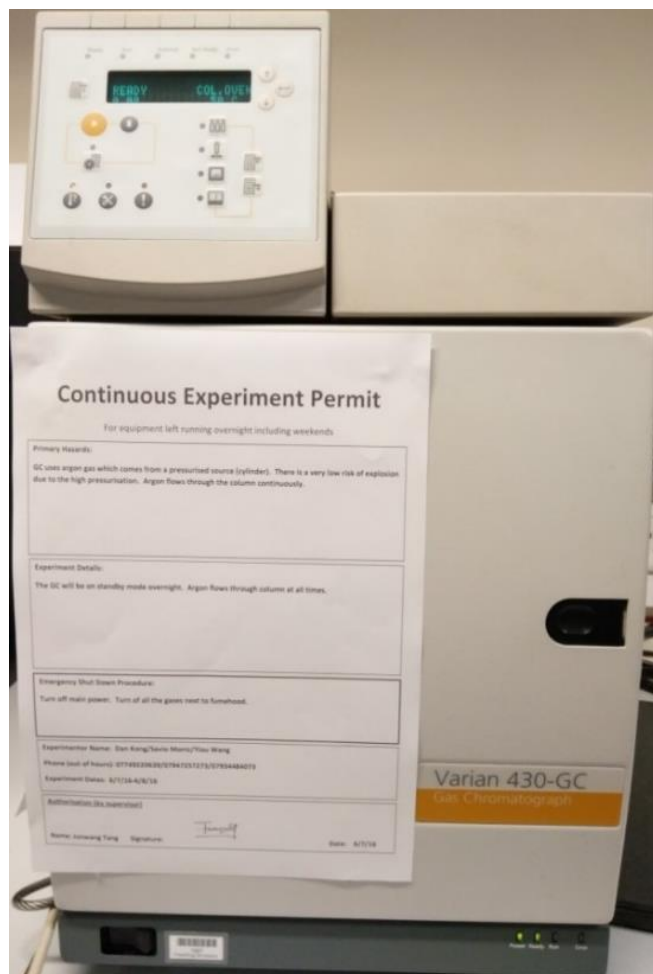


Figure 18. Photograph of the gas chromatograph system used during photocatalysis experiments.



Figure 19. Photograph of the gastight syringe used during photocatalysis experiments.

Table 2. Gases and corresponding thermal conductivity at STP<sup>221</sup>.

Gas	Thermal conductivity (Wm <sup>-1</sup> k <sup>-1</sup> )
Hydrogen	0.1805
Helium	0.1513
Nitrogen	0.0259
Oxygen	0.0266
Argon	0.0177

There are two types of analysis associated with GC's; qualitative and quantitative. Data is represented as a graph of retention time (x-axis) and detector response (y-axis) (Fig. 20); the retention time is specific to each compound (qualitative), and the detector response is dependant (with a TCD) on the thermal conductivity and amount of each element (quantitative). Chromatographic data therefore yield a spectrum of 'peaks' separated only by the time. The area under each peak represents the amount of substance present.

Before testing the products of photocatalysts, optimising the peak separation, signal/noise ratio, and baseline fluctuations is necessary for obtaining reasonable signals. Firstly, the total run time for each chromatograph should be less than 15 mins, *i.e.*, all peaks of the detectable gases should appear in a 10 ~ 15 minute window, or have a retention time (RT) less than 15 mins, considering that some products are usually recorded at either 15 or 30 minute intervals, with some even elongated to one hour<sup>222</sup>. RT of a gas in gas chromatography is influenced by the oven temperature, pressure and flow rate of carrier gas inside the column, which are usually set to 50 °C, 50 PSI and 15 mL/min in our system to enable all gases (hydrogen, oxygen and nitrogen) to come through detector in 10 minutes. Secondly, signal/noise ratio and baseline fluctuations can be optimised by adjusting flow rate and TCD filament temperature. In general, increasing the flow rate through the TCD decreases the peak width apart from shortening the RT, and also

dramatically decreases peak height/response. Therefore, a relatively low flow rate is advisable for detecting low concentrations of gas products.

After optimisation of the GC software system, a calibration curve (responses from a serie of known concentrations/amounts of standard gas) is necessary to correctly caculate the amounts of products, and is useful for deducing the reaction formula and machnism. By injecting known concentration of standard gas mixture, and then digitising the response, a graph of response area ( $y/\mu V$ ) versus amount ( $x/\mu mol$ ) can be plotted. After that, by solving the equation of aline ( $y = ax + c$ , where a and c are constants caculated from the graph curve), a amount of gas can be calculated if the response area of a similar gas is obtained from the chromatograph. The standard gas applied in this research was purchased from BOC, which comprises of 99% zero grade argon, with appropriate amounts of  $H_2$  (4000 ppm) and  $O_2$  (2000 ppm), among other gases which are possibly produced as by-products in a half reaction in the presence of charge scavenger (1000 ppm CO, 1000 ppm  $CO_2$  and 2000 ppm  $CH_4$ ).

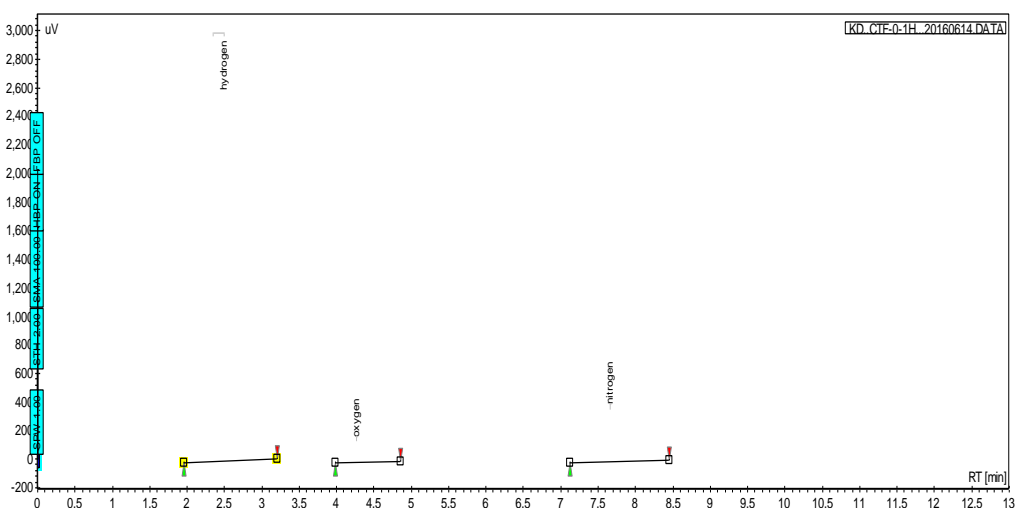


Figure 20. An example of the chromatograph. The hydrogen peak is at 2.36 min, the oxygen peak is at 4.29 min and the nitrogen peak is at 7.68 min.

Moreover, GC can be coupled with a mass spectrometer (MS), namely GC-MS (Fig. 21), which is very helpful to identify the products based on their fragmentation patterns in the complex systems. When the sample exits the chromatography column, it is passed through a transfer line into the inlet of the mass spectrometer. And then the sample is typically ionised and fragmented by an electron-impact ion source. During this process, the gas molecule is bombarded by energetic electrons continuously and ionised by losing an electron due to electrostatic repulsion. Further bombardment results in the fragmentation of the ionised molecules, which then flow into a mass analyser and then are separated according to their  $m/z$  value, or mass/charge ratio. The chromatogram of TCD detects the retention times and the response areas and the MS reveals what kind of molecules exists in the mixture by the peak positions in spectrum. Fig. 22 represents a typical mass spectrum of water molecule with the absorption peaks at appropriate  $m/z$  ratios. GC-MS is advantageous of its immediate determination of the mass of the sample and its identification of the components of incomplete separations, which is applied in this study to confirm the  $O_2$  products definitely from water by detecting  $^{18}O$  labelled oxygen products. The disadvantage of MS detectors is that the samples are tend to degrade by the fragmentation of the energetic electrons.

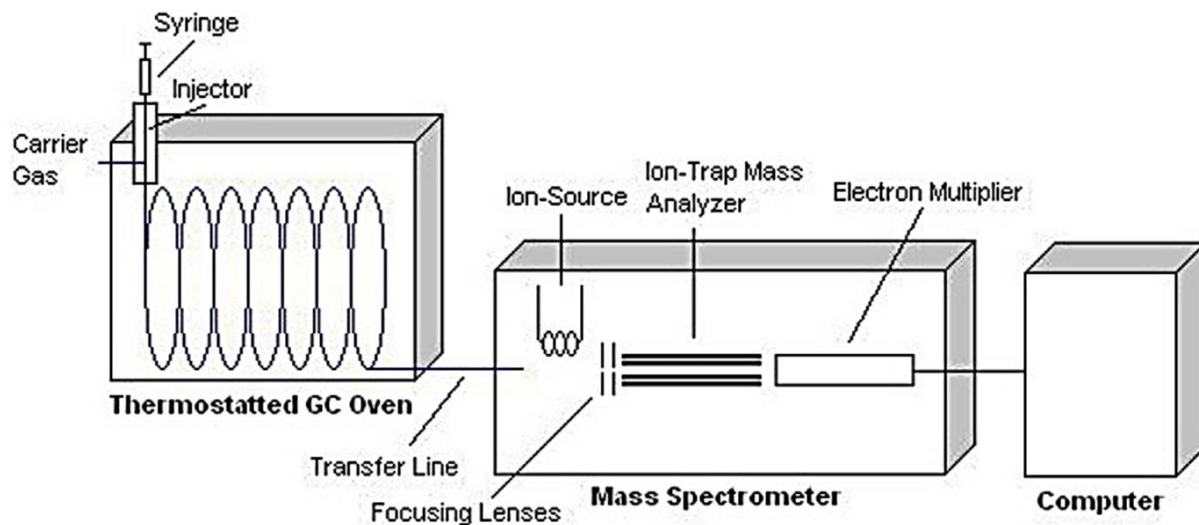


Figure 21. Schematic of the GC/MS system. The chromatograph of TCD detects the retention times and response areas, and the MS reveals the kind of molecules in the mixture by the peak positions.

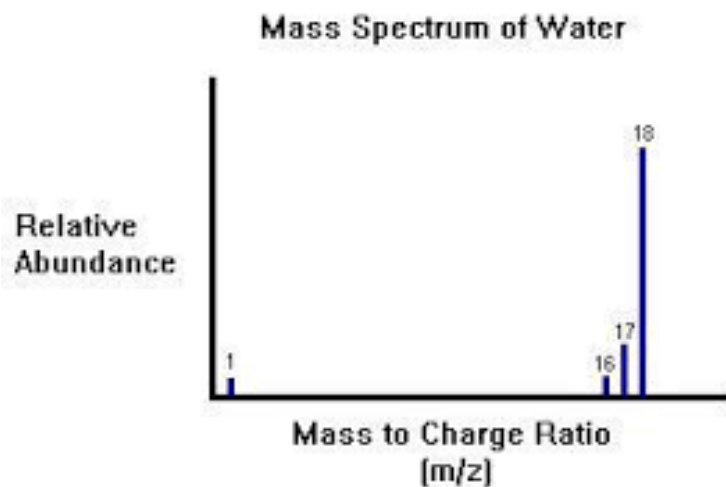


Figure 22. Mass spectrum of water.

### 3.2.2 Particle suspension reactors

A borosilicate cylindrical glass reactor was designed and then handmade by Labglass Ltd (4.5 cm radius, 11.5 cm height) as shown in Fig. 23. The total volume was 730 cm<sup>3</sup>, including headspace

(calculated by water displacement). The vessel was fitted with a flat high purity borosilicate side window, which was slightly bigger than the beam of light source (40cm  $\phi$  reactor window, 33 cm  $\phi$  beam). High purity borosilicate is suitable for a photocatalytic reactions as the low impurity content (such as iron) allows both UV and visible wavelength of light pass through without any absorption.

The reactor was also fitted with two side ports (fitted with GL18 aperture caps and silicon septa) for purging and gas sampling. The top of the system was a PTFE screw thread aperture cap, with a detachable transparent borosilicate window. The reactor sealing mechanism was originally a 0.5mm depth silicon ring which fitted between the window and the top PTFE aperture cap.



*Figure 23. Borosilicate reactor for water redox batch reactions. Light is irradiated on the side window and two side outlets are used for purging and taking the gas products.*

### 3.2.3 Light source

One 300 W xenon (Xe) lamp (Newport 66485-300XF-R1) was purchased from Newport Spectra to act as artificial light sources as shown in Fig. 24. Xe lamps have a spectral profile akin to that of the solar spectrum, with intensity less than  $20 \text{ mWm}^{-2}\text{nm}^{-1}$  at  $250 < \lambda < 800 \text{ nm}$ . A 300 W Xe lamp was used for oxygen, hydrogen production and water splitting. A 150 W Xe lamp was utilised for the photocatalytic efficiency measurements, and the lower intensity of the 150 W Xe lamp could also prevent from the damage of the band pass filters, which absorbed substantial amounts of light at other wavelengths, up to 90%.

The power from the lamp was calculated using a Silicon photodiode detector (190-1100nm), with built in attenuator, connected to a handheld digital power meter (both purchased from Newport Spectra). Various band pass filters were used, *e.g.* 365 nm, 420 nm, 500 nm, 600 nm and 800 nm, supplied by Comar Optics, enabling the selective use of either full arc or visible light irradiation. These filters had a quoted centre wavelength and the width of all the pass-bands was 10 nm, for example, the filter of 420 nm could only pass the light of wavelength between 415 and 425 nm.

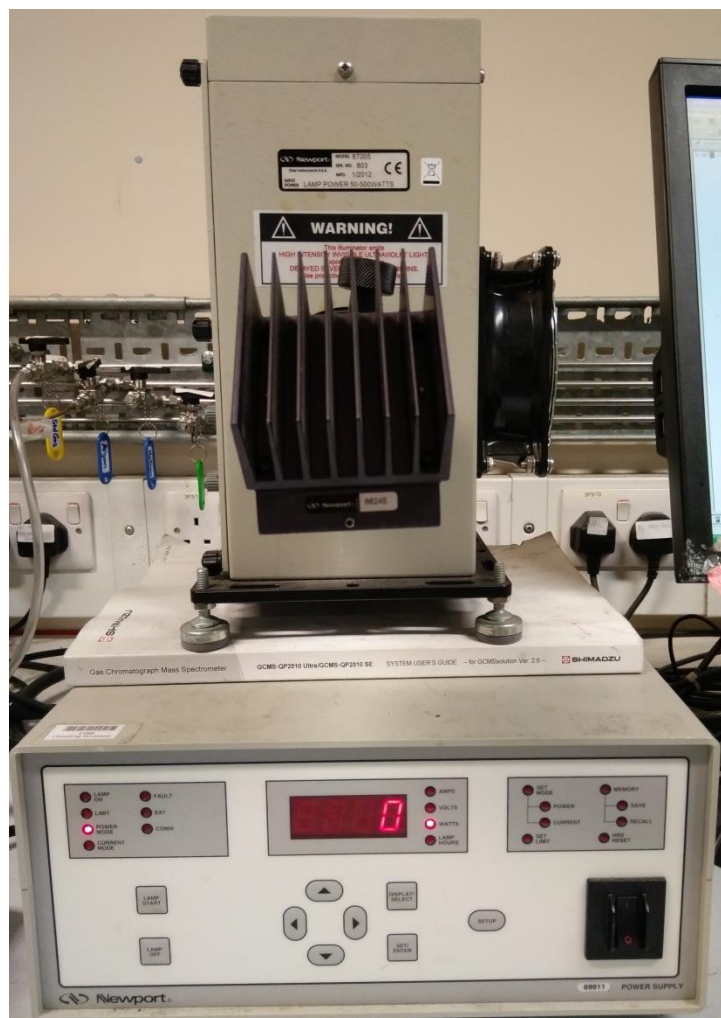


Figure 24. The lamp system is used to supply the irradiation light.

### 3.2.4 Efficiency calculations

The efficiency of photocatalytic water splitting can be evaluated by many methods and equations<sup>18</sup>. In this section, three most frequently used equations will be described, and the application conditions of these equations will also be illustrated.

In common, the production rate of hydrogen or oxygen is given with the unit of micromole per hour, per gram of the photocatalyst, namely  $\mu\text{mol}\cdot(\text{hg})^{-1}$ , which is calculated by the gas amount

deduced from GC data, the reaction time and the amount of photocatalysts. However, this gas evolution rate is incomparable if the reaction conditions of the experiments are different, since the light source and the reactor size also influence the evolution rate. Thus, the quantum yield (QY) is important to evaluate the efficiency of photocatalytic system by calculating the ratio of the number of charged carriers used for H<sub>2</sub>/O<sub>2</sub> production to the number of photons of a given light source shining on the reactor. Here, the number of photons of a given light source shining on the reactor can be measured by a thermopile or silicon detector/photodiode. In theory, the real amount of photons absorbed by a photocatalyst in a suspension system is hard to be obtained, which is smaller than the amount of photons of the lamp irradiating on the reactor due to light scattering and transmission effects. Thus, the corresponding quantum yield is an apparent quantum yield (AQY) (Equation.18), which is expected to be smaller than the real QY. In the AQY equation, the number of charge carriers collected by the photocatalysts is calculated based on the amount of evolved hydrogen or oxygen and the number of photons of a given energy shining on the reactor calculated by the illumination intensity and area.

*Equation 18. Apparent Quantum Yield*

$$AQY(\%) = \frac{\text{number of charge carriers used for hydrogen or oxygen production}}{\text{number of photons of a given light source shining on the reactor}} \times 100$$

A more accurate measurement of the number of photons incident on the photocatalyst surface can be executed by subtracting the flux of photons measured from the back of the reactor, from that measured in front of the reactor. In this case, the QY is termed 'internal quantum yield' (IQY), which means the quantum yield of the photons of the reactor absorbed, which is more closed to real QY than AQY.

In chemical fields, turnover number (TON) is applied for clarifying whether the products are truly catalysed or not. Successfully used in homogeneous catalysis (TON = moles of desired charge carriers used for the production/moles of catalysts), the TON has some minor modifications applied in a heterogeneous system (Equation. 19). Commonly, the moles of active sites on the photocatalysts are defined as the moles of the cocatalysts coated on the surface of the photocatalysts. Sometimes, the moles of active sites can be very roughly approximated to the moles of the molecules in the photocatalyst, which significantly underestimates the actual TON, due to that only the surface molecules of the photocatalyst can act as the active sites for the reduction/oxidation reaction<sup>223</sup>.

*Equation 19. Turnover Number*

$$TON = \frac{\text{moles of desired charge carriers used for the production}}{\text{moles of active sites on photocatalysts}}$$

Solar-To-Hydrogen conversion efficiency (STH%, Equation 20) is different from QY and TON, which is usually used for evaluation of solar cells. In a particle suspension system, STH% only considers output energy as H<sub>2</sub> and O<sub>2</sub>, and is only applied to overall water splitting reactions, such as a Z-scheme overall water splitting. This is because the redox mediators in Z-scheme overall water splitting (such as Fe<sup>2+/3+</sup> and I-/IO<sub>3</sub><sup>-</sup>) are not exhausted/consumed, and therefore Z-scheme systems can be evaluated by STH%. Nevertheless, in the half reaction, the scavenger for H<sub>2</sub>/O<sub>2</sub> production is consumed, and the output energy of the process is not solely as H<sub>2</sub>/O<sub>2</sub>. For example, when the methanol works as the hole scavenger in the water reduction reaction, the reformation of methanol will consume the energy of solar light and is considered as one way to output energy.

Equation 20. *STH%*

$$STH(\%) = \frac{\text{Output energy as } H_2 \text{ and } O_2}{\text{Energy of incident solar light}} \times 100$$

## 4 Chapter 4

### Modified OCT for water oxidation across UV to full visible spectrum

As the rate determined step in water splitting, water oxidation was paid particular attention in the project. This chapter details the oxygenated covalent triazine framework OCT for water oxidation.

Due to that solar-driven water splitting is highly desirable for clean hydrogen fuel production, numerous efforts have been made on hydrogen production, especially by means of stable and efficient photocatalysts of main group elements, *e.g.* carbon, nitrogen and oxygen. However, carbon-based photocatalysts have met with limited success for rate-determining water oxidation due to the extremely slow “four-hole” chemistry. Coupling computational design and controlled molecular synthesis, this chapter will demonstrate that an efficient strategy to change bandgap and band position of the covalent triazine 2-D photocatalyst. The synthesised oxygenated OCT is remarkably active for oxygen production at a wide operation window from UV, visible, and even to NIR (up to 800 nm), neatly matching the solar spectrum with an unprecedented external quantum efficiency even at 600 nm and 800 nm. Moreover, it remains active for H<sub>2</sub> production. DFT calculations show that oxygen incorporation not only narrows the band gap but also causes appropriate band-edge shifts, due to the formation of C=O moiety in the structure. In the end, a controlled small amount of oxygen in the ionothermal reaction was found to be a promising, novel and facile way of achieving such oxygen incorporation. This discovery is a significant step towards both scientific understanding and practical development of metal-free photocatalysts for cost-effective water oxidation and hydrogen generation over a large spectral window.

## 4.1 Introduction

Photocatalytic hydrogen production directly from water allows the conversion of solar energy into renewable and clean chemical energy and thus provides a potential solution to energy security and CO<sub>2</sub> emission reduction<sup>19, 207, 224</sup>. There have been numerous studies on semiconductor photocatalysts for either hydrogen or oxygen evolution half reaction over the past decades<sup>3, 225-230</sup>, which is the key for both photoelectrochemical waters splitting and Z-scheme water splitting that can simultaneously produce specially separated H<sub>2</sub> and O<sub>2</sub> gas. However the majority of these photocatalysts are inorganic materials.<sup>227, 229</sup> It is only in the last decade that metal-free photocatalysts have been developed, including graphite oxide<sup>224</sup>, g-C<sub>3</sub>N<sub>4</sub><sup>8, 231</sup> and conjugated polymers<sup>181, 232</sup>. The latter ones usually show excellent photocatalytic performance for hydrogen production, but are rather poor or moderate for water oxidation (or oxygen generation) due to either a too large band gap and/or inappropriate band edges, especially not efficient at the strongest solar insolation range from 400 to 700 nm<sup>207, 224</sup>. The oxygen evolution process involves both 4e/4H<sup>+</sup> electrochemistry and O=O bond formation. As such it is much more challenging than proton reduction to hydrogen and is the rate determining step in water splitting<sup>22, 181</sup>. Currently, a few metal oxides (*e.g.* Ag<sub>3</sub>PO<sub>4</sub>, WO<sub>3</sub> and BiVO<sub>4</sub>) are reported to oxidise water under visible light as mentioned in the chapter 2, albeit with a relatively narrow operation window (from UV up to 560 nm), which does not match well with the solar spectrum and thus limits their efficiency<sup>149, 233-235</sup>. Unmodified organic photocatalysts usually show negligible activity for water oxidation, typically due to high lying valence bands that are too close to the water oxidation potential, *e.g.* g-C<sub>3</sub>N<sub>4</sub>.<sup>11, 231</sup> Band gap engineering to modify the optical properties of organic photocatalysts has been experimentally and theoretically proposed, *e.g.* via addition of co-monomers<sup>236</sup>, addition of sulphur<sup>237</sup>, or anionic doping<sup>238</sup>. However, such band gap

engineering has only been demonstrated for graphitic carbon nitride ( $g\text{-C}_3\text{N}_4$ )<sup>239-240</sup>, of which the majority narrows the band gap by raising the Valence Band Edge (VBE) so that it is too close to the water oxidation potential to drive water oxidation. It has so far been proved that it is challenging to engineer the band gap of organic photocatalysts by the way of controllable shifting conduction band (CB) positions to enhance the much harder oxygen evolution reaction (with kinetics five orders of magnitude slower)<sup>22</sup>. Very recently, Wang et al were successful to prepare a series of CTP organic photocatalysts, with CTP-2 presenting a visible absorption to 530 nm with a *ca.*  $3 \mu\text{mol h}^{-1}$  oxygen evolution rate under full arc irradiation<sup>241</sup>. Moreover, it is still challenging to demonstrate an organic photocatalyst possessing visible light activity of oxygen evolution comparable to the best inorganic oxygen evolution photocatalysts, *e.g.*  $\text{BiVO}_4$ . The present study employs an efficient strategy to enable the band gap narrowing primarily by shifting down the conduction band edge (CBE) of a wide bandgap polymer photocatalyst by oxygenation, not only maintaining the strong oxidation potential but also enhancing visible light absorption to IR region<sup>242</sup>, as such it would be an ideal photocatalyst in a Z-Scheme system for complete water splitting<sup>243-244</sup>.

Recently, a planar organic material, covalent triazine framework (CTF-1), has being shown to possess promising structural and chemical properties, with a large surface area, of *circa*  $500\sim 2500 \text{ m}^2/\text{g}$ <sup>183-185, 242</sup>. This material is composed of two molecular units, benzene and triazine, in contrast to the single molecular unit of  $g\text{-C}_3\text{N}_4$ . Theoretical work demonstrated that this is a semiconductor, with band edges straddling both the oxidation and reduction potentials for water splitting<sup>208</sup>. Experimentally the onset for light absorption is 2.94 eV due to a very negative CB, light absorption mainly occurs under UV irradiation<sup>245</sup>. More importantly, band positions of CTF-1 are easy to be

functionalised through synthesis process (*e.g.* by doping), potentially improving the optical absorption and the photocatalytic performance.

By simulations collaborated with Xiaoyu Han in Chemistry Department of UCL, it is identified that OCT obtains the modified or disrupted triazine units, which in turn alters optical absorption properties and band gap levels. Therefore, the OCT is investigated in this chapter.

## 4.2 Methodology

### 4.1.1 Synthesis techniques

OCT was synthesised by mixing 1,4-dicyanobenzene and zinc chloride with ratio 1:1 in a glove box. Mixed powders were transferred into pyrex ampoules, dried in the oven at 70 °C for one hour and then the ampoules were evacuated. Then a gas mixture of different oxygen/nitrogen ratios was introduced, and finally the ampoules were sealed. The reaction scheme is illustrated in Fig. 25. The ampoule was heated in a tube furnace at 400 °C for 40 hours. After heating, the products were ground, washed in distilled water and hydrochloric acid solution, and then further washed in deionised water. Molten  $\text{ZnCl}_2$  at 400 °C fulfils all the prerequisites to obtain crystalline porous polytriazines. First, nitriles show a good solubility in this ionic melt owing to strong Lewis acid-base interactions, and all the monomers described here form clear solutions in this salt melt. Second,  $\text{ZnCl}_2$  is a good catalyst for the trimerization reaction, which seems to be sufficiently reversible at this temperature.  $\text{BiVO}_4$  was synthesised using a method described in the previous study<sup>43</sup>.

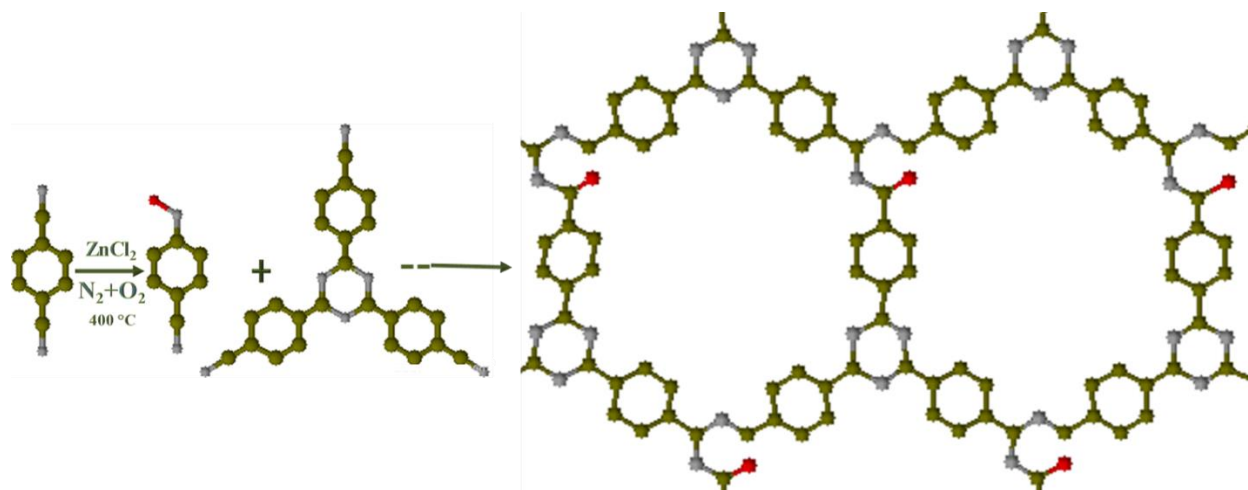


Figure 25. Reaction Mechanism of OCT starting from 1,4-dicyanobenzene to the extended 2D OCT. Red dots are oxygen atoms, olive-green ones are carbon atoms and grey ones are nitrogen atoms.

#### 4.1.2 General characterization

The Solid State Nuclear Magnetic Resonance (NMR) data were collected using a Bruker Avance 300WB equipped with a 4-mm magic-angle spinning probe for  $^{13}\text{C}$  and  $^1\text{H}$  measurements. Powder X-Ray Diffraction (PXRD) measurements were taken by a Bruker D4 diffractometer at 40 kV and 40 mA with Ni-filtered  $\text{Cu K}\alpha$  irradiation ( $\lambda_1 = 1.540562 \text{ \AA}$ ,  $\lambda_2 = 1.544398 \text{ \AA}$ ). X-ray photoelectron spectroscopy (XPS) was taken on a ThermoScientific XPS K-alpha surface analysis machine using an Al source. The Fourier Transform Infrared (FTIR) spectra were recorded on a Perkin-Elmer 1605 FT-IR spectrometer. The Brunauer-Emmett-Teller (BET) surface area measurement was performed on Micromeritics® Tristar 3000 with  $\text{N}_2$  carrier gas. Annular dark field scanning transmission electron microscopy (ADF-STEM) combined with electron energy loss spectroscopy (EELS) by JEOL ARM-200F was operated at 80 kV for EELS. Elemental analysis was carried out by Elemental Analyser, Model 1108 (Carlo-Erba, Milan, Italy) with PC based data system, Eager 200 for Windows™ and a Sartorius Ultra Micro Balance, 4504MP8. UV-vis reflectance spectra

were recorded at room temperature by a Shimadzu UV-Vis 2550 spectrophotometer, which were converted by the Kubelka-Mulk transformation to obtain the absorption spectra.

#### 4.1.3 Photocatalytic activity evolution

For oxygen and hydrogen evolution, reactions were performed separately in a custom Pyrex® batch reactor cell. For the case of H<sub>2</sub> production, 100 mg photocatalyst was mixed with aqueous solution containing triethanolamine and 3wt%Pt (H<sub>2</sub>PtCl<sub>6</sub>). The reactor was sealed and then purged with argon to remove all air in the reactor before reaction. Hydrogen was produced under full-arc irradiation using a 300W Xe lamp (*Newport 66485-300XF-R1*). Oxygen evolution was processed in deionised water with 10 mg photocatalyst (OCT or BiVO<sub>4</sub>) and 1g AgNO<sub>3</sub>. The other procedure was the same as hydrogen evolution. A 420 nm long pass filter was used for removing UV radiation and 365, 400, 420, 500, 600 and 800 nm monochromatic light filters for quantum efficiency measurement where necessary. All the gas was analysed by gas chromatography (*Varian 430-GC, TCD, argon carrier gas 99.999%*). The quantum efficiency ( $\Phi$ ) was calculated by the equation mentioned in chapter 3.2.4 :  $AQY = \frac{4 \times \text{the number of evolved } O_2 \text{ molecules}}{\text{the number of incident photons}} \times 100\%$ . The incident photons were calculated by the equation:  $I = hcR(\lambda)/\lambda$ , based on light intensity measured by a Newport power meter. In a direct-transition semiconductor material, the absorption coefficient  $\alpha$  is correlated to the optical bandgap by the equation:  $(ah\nu)^2 = A(h\nu - E_g)$ , where  $h$  is Planck's constant;  $\nu$  is the frequency of the incident photo;  $A$  is a constant that depends on the mobility of the electrons and holes in the material;  $E_g$  is the optical bandgap. Hence, the optical bandgap of OCT can be determined by Tuac's plot, namely, the linear part of the  $(ah\nu)^2$  curve is extrapolated toward the energy  $h\nu$  axis at  $(ah\nu)^2=0$ .

#### 4.1.4 Computational simulations

Oxygen interactions with covalent triazine frameworks, specifically OCT, were investigated using periodic Density Functional Theory (DFT), using the VASP code<sup>246</sup>, which was carried out by Xiaoyu Han at UCL Chemistry Department. A plane wave cutoff of 520 eV was selected, with the Projector Augmented Wave methods used to treat the core electrons<sup>247</sup>. The PBE functional was used for structure optimization, thermodynamic calculation, and electronic structure analysis<sup>248</sup>. Van der Waals interactions were included via the usage of the DFT-D2 method of Grimme<sup>249</sup>. All atoms were fully relaxed until the change in force upon ionic displacement was less than 0.01 eV/Å, with the change in energies no greater than  $10^{-5}$  eV. OCT crystals were generated using an AA stacking motif. The lattice parameters of CT were obtained by generating energy-volume data, with lattice parameters as 14.57 Å, which is in line with previous calculations and experimental values<sup>183, 185, 208</sup>.

Oxygen-dopant thermodynamics were determined using a (2×2) single sheet supercell, with a Monkhorst-Pack k-point mesh of (5×5×1) found to be sufficient in order to produce well converged energies and forces. Spin-polarisation was used in all calculations. A vacuum spacing of 20 Å was used. The single sheet structure was also used to accurately align Kohn-Sham (KS) eigenvalues for the pure and doped supercells. As a large vacuum spacing was used in the simulations, the planar averaged electrostatic potential converged to a constant value far from the surface. These converged values may be taken as the reference level with which the Kohn-Sham (KS) eigenvalues are aligned<sup>250</sup>. For the band alignment of the CTF-1 and OCTs, the Fermi levels were determined by the calculations of each work function, where vacuum is set to zero.

## 4.2 Results and discussion

### 4.2.1 General strategy and structural analysis of OCT

Firstly, the three possible oxygenated products applied in the calculations and compared with undoped CTF-1 (Fig. 26a and 26b) are introduced to explain the general strategy and structural analysis of OCTs. For ideal CTF-1 (Fig. 26d), the triazine unit forms from condensation of 1,4-dicyanobenzene (Fig. 26a) with molten zinc chloride in vacuum, following the nucleophile reaction mechanism. Three dicyanobenzenes coordinate to form triazines. The prediction (Fig. 26b and 26c) was derived from simple tuning on the end of precursor, 1,4-dicyanobenzene, and preserved the same formation mechanism of the CTF-1. In structure OCT(i),  $O_2$  attacks the nitrile group, replacing nitrogen by oxygen ( $O_N$ ). In structure OCT(ii), the  $C=O$  bond is created by  $O_2$  attacking the nitrile group in the first step, and then remains unattacked but emit NO in the second step. In structure OCT(iii), one oxygen atom bounds to the tail of nitrile group directly, and then form single C-O-N linker in the triazine ring. Here denotes the structure of pure triazine ring and those with oxygen containing structures as CTF-1, OCT(i), OCT(ii) and OCT(iii) in Fig. 26d, 26e, 26f and 26g, respectively, with the supercells shown in Fig. 27. During the synthesis, oxygen may be used for functionalising the end groups of the molecules, resulting the modified triazine and thus modified optical properties. To clarify, oxygen will disrupt the formation of some triazine molecules, forming ketone or nitrous groups in the final materials. The most likely structure, OCT(ii), is discussed later.

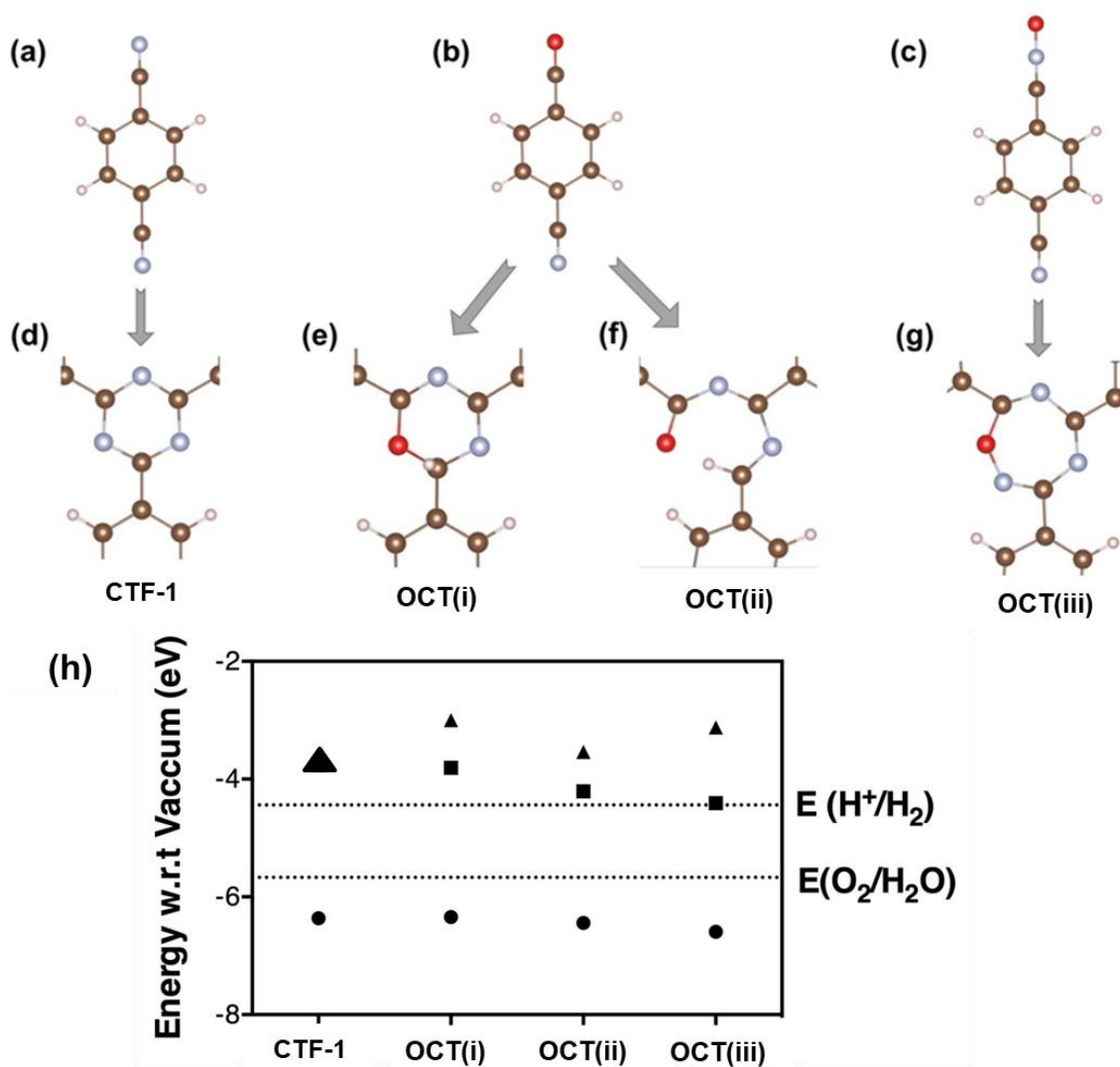


Figure 26. Schematic of formation process of pure CTF-1 (a and d), OCT(i) (b and e), OCT(ii) (b and f) and OCT(iii) (c and g) structures. . Carbon is represented by brown sphere, nitrogen grey, hydrogen light pink, and oxygen red. (h) The band alignments of CTF-1 and proposed OCT structures. The dots represent the VBEs and the squares and triangles represent the unoccupied defect states and CBEs, respectively. The dash lines are the  $H^+/H_2$  (up) and  $O_2/H_2O$  (down) redox levels. All the energy is calculated with reference to the vacuum level.

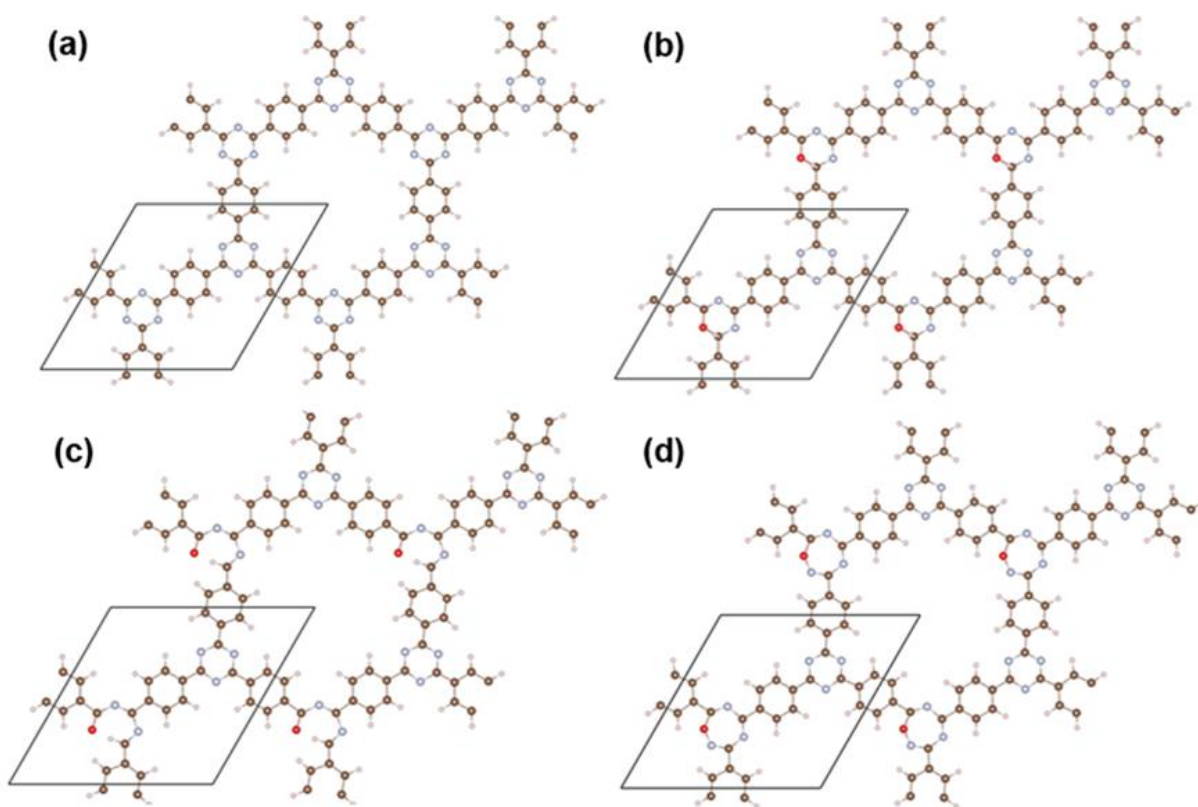


Figure 27. The periodic structures of pure CTF-1 (a), OCT(i) (b), OCT(ii) (c) and OCT(iii) (d). The solid lines represent the unit cell.

OCT was fabricated by co-polymerizing monomers of 1,4-dicyanobenzene with zinc chloride in a 1:1 molar ratio in oxygen containing condition, as shown in Fig. 25. After synthesis, a black crystalline material was observed. The XRD analysis shows several intense reflection peaks, namely (100), (110), (200) and (001) in Fig. 28. This indicates that crystalline triazine-based frameworks have been formed<sup>207</sup>. The large diffraction peak at  $2\theta = 26.4^\circ$ , assigned to the (001) peak, corresponds to an interlayer distance of 3.4 Å. Compared with the ideal CTF-1 in previous study<sup>184</sup>, the OCT shares the similar level of crystallinity with the ideal CTF-1 but a shift of the (001) peak from  $26.1^\circ$  to  $26.4^\circ$ . It suggested the stacking distance is slightly reduced due to the doped oxygen atom which is smaller than the substituted nitrogen atom in the same position.

Moreover, from the calculated VBM/CBM (valence band maximum/ conduction band minimum) spatial distribution (Fig. 29), the oxygen substitution on the opened triazine units further induced charge delocalisation, which can contribute to the van der Waals bonding additionally, and then enhancing interlayer integration by reducing the interlayer spacing.

Fig. 30 shows further structural characterisation from FTIR, which clearly confirmed the existence of triazine units and C=O bonds in the OCT in the following details. The peaks at 1020 and 796  $\text{cm}^{-1}$  match well with the C=C bending of benzene units<sup>251-252</sup>, and the C-H in-plane bending vibrations of the benzene rings<sup>252</sup>, respectively. The characteristic bonds for the triazine unit were found at 1508  $\text{cm}^{-1}$  (C-N stretching mode)<sup>185, 253</sup> and 1354  $\text{cm}^{-1}$  (in-plane ring stretching vibrations)<sup>253-254</sup>, confirming the successful formation of triazine rings in these experiments. The peak at 1412  $\text{cm}^{-1}$  corresponds to the absorption by the benzene ring that also forms the basic framework, which proves the existence of the aromatic hydrocarbon<sup>255</sup>. The peaks at 1730 and 1688  $\text{cm}^{-1}$  represents the C=O bond, indicating the presence of oxygen in the polymer<sup>256-257</sup>. The peaks at 2230 and 2340  $\text{cm}^{-1}$  contribute to the conjugated C $\equiv$ N bonds, due to the remaining triazine ring terminals<sup>258-259</sup>.

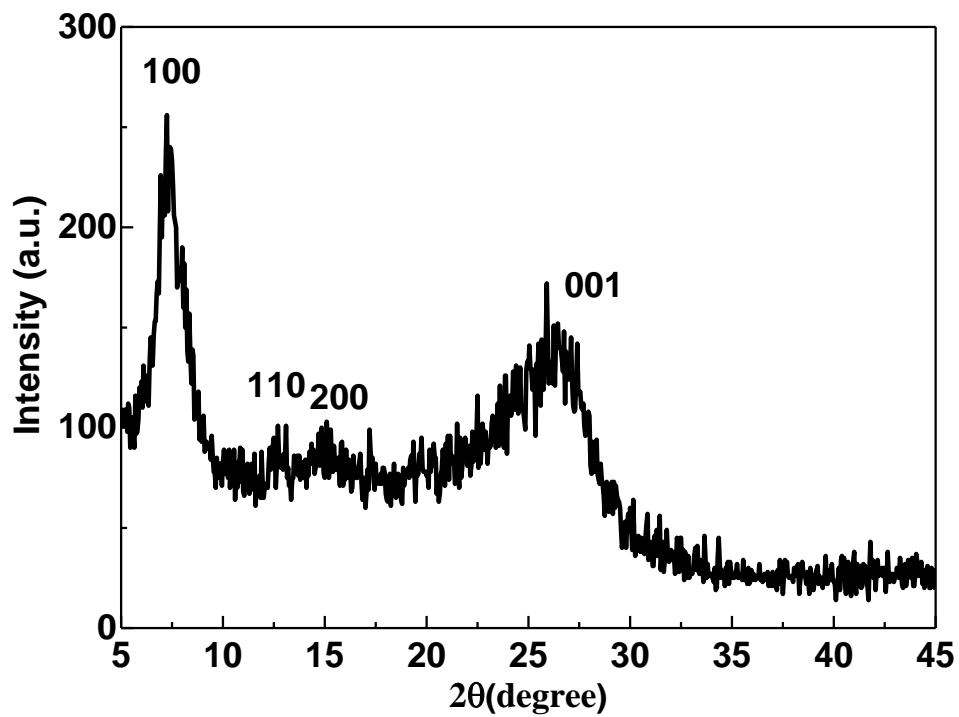


Figure 28. Powder XRD spectra of 6.68 at% OCT. The peaks (100), (110), (200) and (001) indicates that crystalline triazine-based frameworks have been formed.

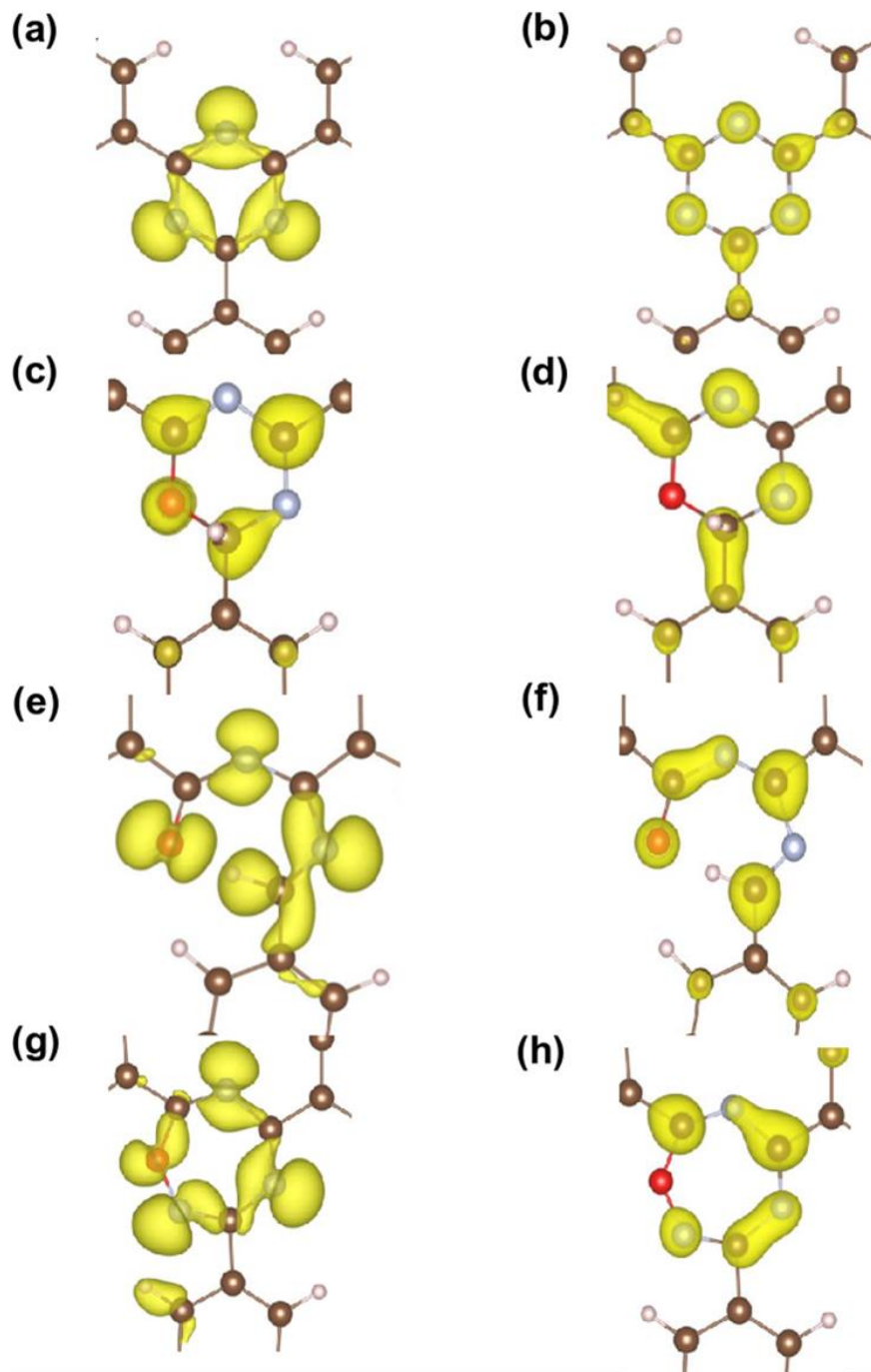


Figure 29. The Spatial distribution of the valence band maximum (VBM) (a, c, e, g) and the conduction band minimum (CBM) (b, d, f, h) of the structure pure CTF-1, OCT(i), OCT(ii) and OCT(iii), respectively. All the isosurfaces were set to  $0.005 e/a_0^3$ , where  $a_0$  is the Bohr radii.

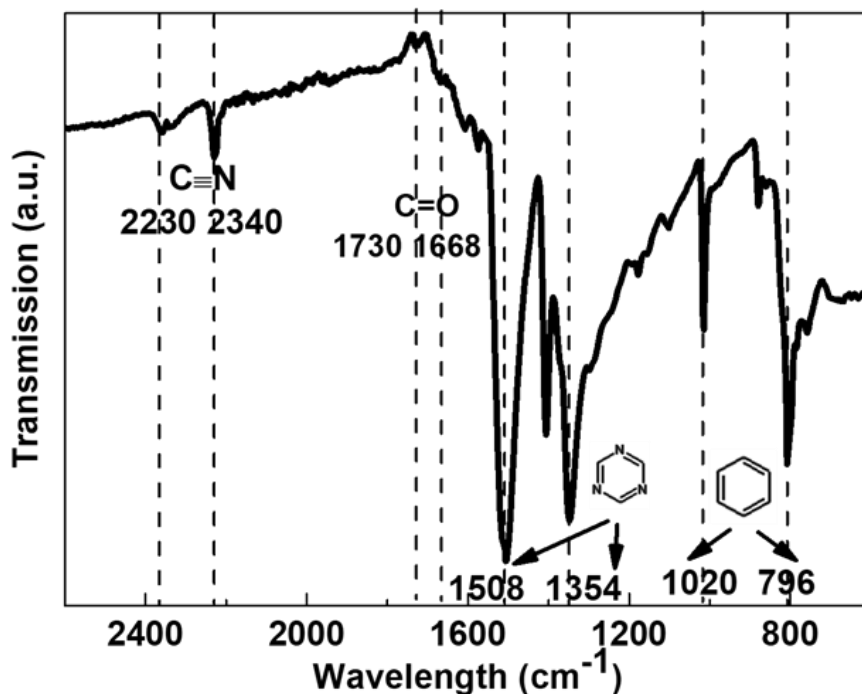


Figure 30. FTIR spectroscopy of 6.68 at% OCT. The peaks at 796 and 1020  $\text{cm}^{-1}$  match well with the C-H in-plane bending vibrations of the benzene rings, and the C=C bending of benzene units, respectively. The characteristic bonds for the triazine unit were found at 1508  $\text{cm}^{-1}$  (C-N stretching mode) and 1354  $\text{cm}^{-1}$  (in-plane ring stretching vibrations), confirming the successful formation of triazine rings in these experiments.

Further structural analysis performed by <sup>13</sup>C cross-polarization magic angle spinning (CP-MAS) solid-state NMR (ssNMR) spectroscopy (Fig. 31a) shows that the OCT has strong peaks at 170, 139, 129 and 116 ppm. The peak at 170 ppm was assigned to the symmetric carbon C1 in the central triazine ring<sup>167</sup>, while the peaks at 139 and 129 ppm were identified as the two separate carbon atoms of the benzene ring (C2 and C3), respectively. The small peak at 116 ppm was assigned to terminal nitrile<sup>207, 260</sup>. The C=O band signal is at 174ppm, dominated by the symmetric

carbon C1 signal and overlapping with peak 170 ppm. The elemental composition analysis was made by XPS in Fig. 31b. The presence of oxygen is detected with no ZnCl<sub>2</sub> residue left in the samples. Detailed analysis of the OCT C1s and O1s signal profiles (Fig. 32) reveals C=O peaks at both 288.0 eV in C1s XPS spectra and 533.0 eV in O1s XPS spectra. This agrees with the FTIR spectra that show carbon-oxygen double bonds. EELS measurements were further taken from numerous positions in thin sections of the sample, which indicates the presence of oxygen in Fig.33. In order to obtain a higher signal-to-noise C, N and O K-edge EELS, I averaged three EELS measurements taken in different regions of sample, shown in Fig. 33d, where the ADF-STEM image of line profiles across the edge of sample were taken. The reason to collect data from the thin edge of sample is to make sure the beam pass through the samples and the outlet signal can be collected. Fig. 33a, b and c show the C, N and O K-edge EELS signal respectively from the line in Fig. 33d. Analysis of C and N K-edge EELS shows that the system is practically exclusively composed of sp<sup>2</sup> hybridised carbon and nitrogen atoms, as indicated by the presence of the 1s→π\* transition for both elements. The carbon-K ionization edge and nitrogen-K ionization edge show identical near edge structures indicating a similar threefold coordination and electronic environment of carbon and nitrogen in the synthesised material<sup>261</sup>. The first peak of O K-edge EELS spectrum at 532 eV is assigned to O<sub>C=O</sub> 1s→π\*<sup>262</sup> in Fig. 33c, the second peak at 538 eV is attributed to O<sub>C=O</sub> 1s→3p according to the EELS study of liquid acetone<sup>261, 263</sup>, which strongly indicates the presence of C=O structure in the materials. Elemental Analysis (EA) shows that the precise molar ratio of C to N is around 4.5, as detailed in Table 3, which is closed to the theoretical value of 4, for the pure CTF-1<sup>184</sup>. The 6.68 at% oxygen gradient into the sample may be due to initial rapid nucleation and seed formation of CTF-1 with insufficient oxygen, and then slow growth/polymerisation occurring allowing the incorporation of relatively high levels of oxygen. The sample has a large BET surface area of 388.7 m<sup>2</sup>/g with a pore size of 0.212 cm<sup>3</sup>/g, similar to

other values obtained experimentally<sup>185</sup>. Above all, oxygen doped covalent triazine materials were synthesised successfully by the creation of C=O bonds in the structure (structure OCT(ii)), which can play a key role in optical, electronic and photocatalytic properties as discussed in the following.

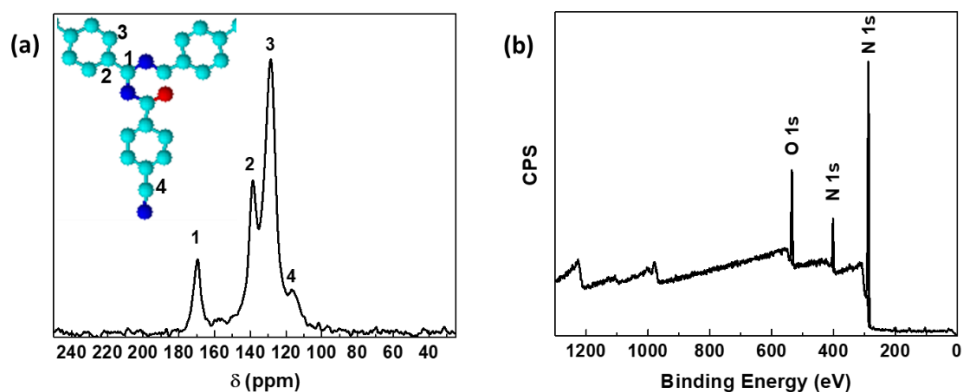


Figure 31. (a) <sup>13</sup>C cross-polarization magic angle spinning solid-state NMR and (b) XPS survey spectrum after etching to 150 nm thickness of the 6.68 at% OCT. The light blue dots are carbon atoms, the dark blue ones are nitrogen atoms, and the red one is oxygen atom.

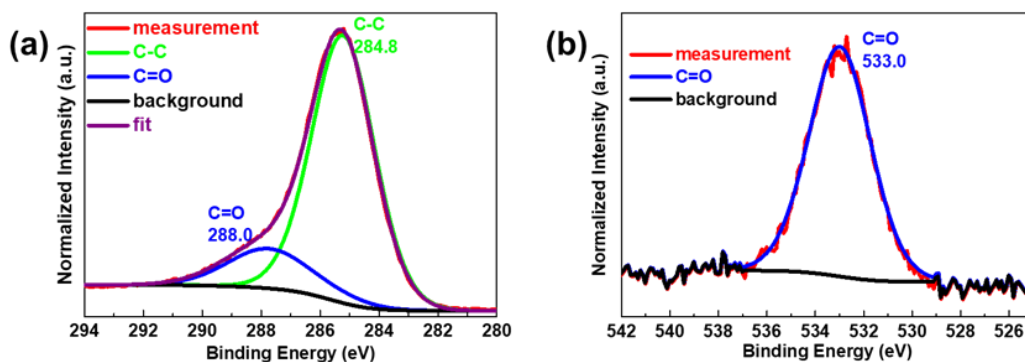


Figure 32. The C1s (a) and O1s (b) XPS spectra for the 6.68 at% OCT. (Charge referenced to adventitious C1s peak at 284.8 eV).

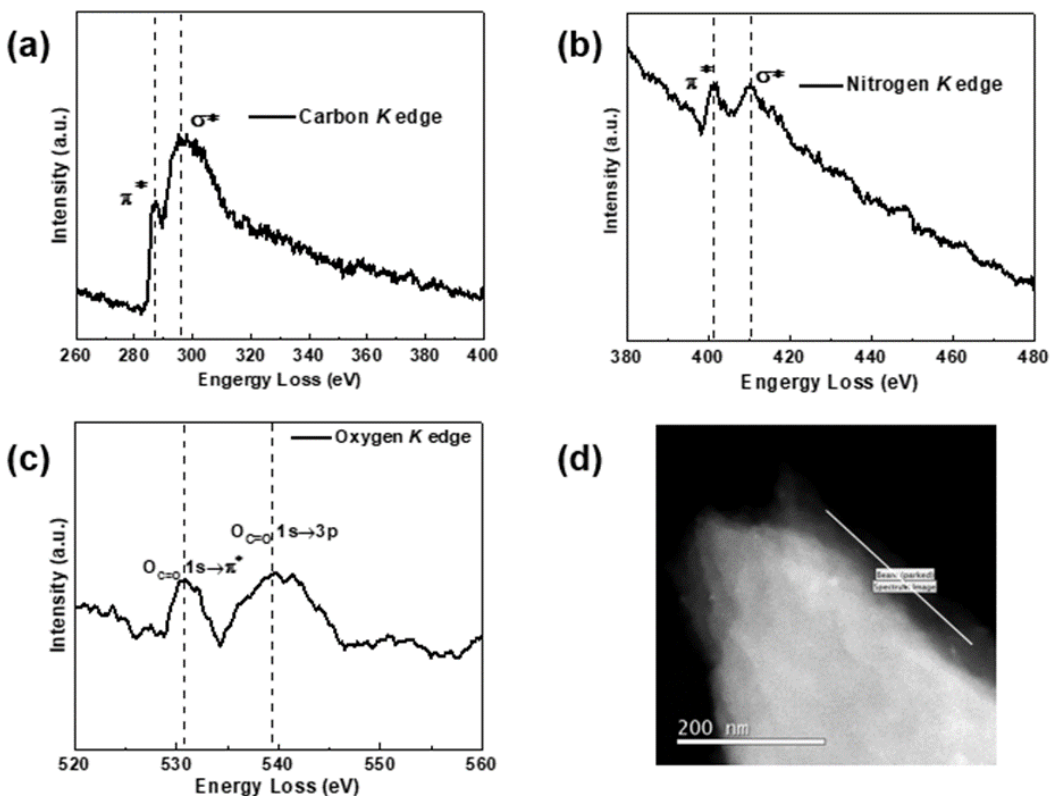


Figure 33. Carbon(a), nitrogen(b) and oxygen(c) K-edge region of the electron energy loss spectroscopy (EELS) from averaging three different spectra taken from the intensity line profiles from the region in ADF-STEM image (d) of 6.68 at% OCT.

Table 3. Elemental analysis of different ratio OCTs and the corresponding mole ratio of O<sub>2</sub>/1,4-dicyanobenzene during the synthesis.

Mol %	Carbon	Nitrogen	Hydrogen	Oxygen	C/N ratio	mole ratio of O <sub>2</sub> /1,4-dicyanobenzene during the synthesis
3.97% 0-CT	63.53	14.49	18.01	3.97	4.4	10%
4.51% 0-CT	63.02	14.41	18.06	4.51	4.4	20%
5.48% 0-CT	62.84	13.75	17.93	5.48	4.6	30%
6.68% 0-CT	61.46	13.72	18.14	6.68	4.5	40%
7.71% 0-CT	62.06	12.25	17.98	7.71	5.1	50%

#### 4.2.2 Photocatalytic and optical properties of 6.68 at% OCT

The photocatalytic activity of the 6.68 at% OCT was determined in the presence of sacrificial reagents under full arc and visible irradiation in Fig. 34. Without cocatalysts, the OCT shows near linear oxygen evolution from aqueous solution with an initial rate of  $10.24 \mu\text{mol h}^{-1}$  (Fig. 34a). Remarkably, the photocatalytic activity for oxygen production under visible light ( $\lambda > 420 \text{ nm}$ ) is very close to that under full-arc, distinguished from the water oxidation photocatalysts reported so far, where visible-light driven activity is always much smaller than full-arc driven activity. I also investigated the ability of the OCT to produce hydrogen, with triethanolamine as an electron donor and Pt as a cocatalyst. The OCT produces hydrogen from water at an average rate of *ca.*  $13 \mu\text{mol h}^{-1}$  under full-arc irradiation (Fig. 34b). Under visible light, hydrogen is produced at *ca.*  $0.5 \mu\text{mol h}^{-1}$ . This suggests that there are likely at least two low energy accessible unoccupied states of OCT, one significantly more positive than the other. The more positive unoccupied state is unable to provide enough driving force for the proton reduction, hindering hydrogen production under visible light illumination as shown in Fig. 34b. Experimental measurement obtained from the UV-vis absorption data (Fig. 35a) determined two optical band gaps with separation 1.6 eV and 2.8 eV. Under full-arc irradiation, the electrons are excited from the VBE to the unoccupied defect state and CBE, enabling both efficient  $\text{O}_2$  and  $\text{H}_2$  productions. Under visible light irradiation, electrons are excited from the VBE only to the unoccupied defect state, so the rate of oxygen generation is maintained but the rate of hydrogen production is relatively slow, due to the reduced driving force for the hydrogen evolution.

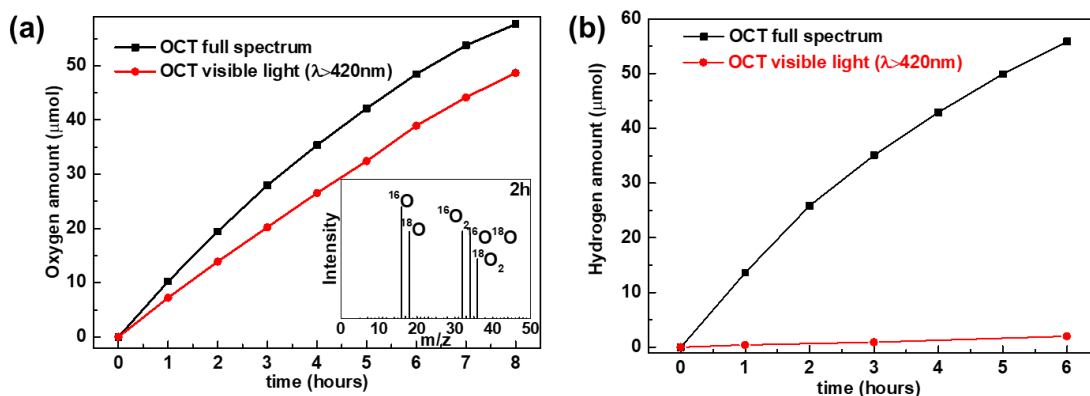


Figure 34. Time courses of 6.68 at% OCT for oxygen (a) and hydrogen (b) production from water under full-arc irradiation and visible light illumination ( $\lambda > 420 \text{ nm}$ ) in the presence of relevant scavengers.

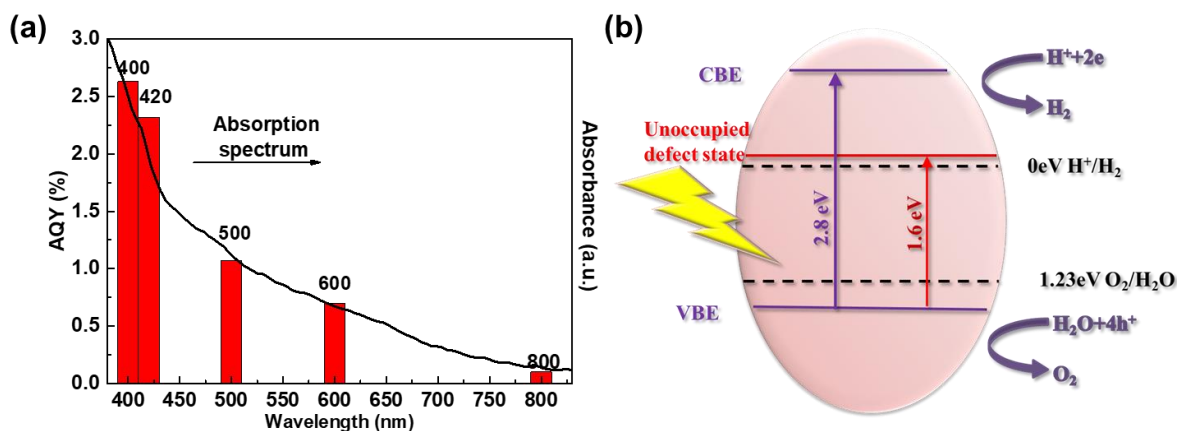


Figure 35. (a) AQY for  $\text{O}_2$  generation at 400, 420, 500, 600 and 800 nm (left-hand axis) with optical absorption spectrum plotted (right-hand side) and (b) band positions and the pathways for water redox of 6.68 at% OCT, where the CBE is the original conduction band in the unmodified CTF-1 and the unoccupied defect state is the lowered CB in the OCT.

One benchmark water oxidation photocatalyst, the tetragonal and monoclinic  $\text{BiVO}_4$ , was compared to evaluate the efficiency for oxygen generation of the OCT.  $\text{BiVO}_4$  has been reported

to efficiently oxidise water under visible light irradiation<sup>43, 264-265</sup>. As it is impossible to calculate the molar amount of OCT due to the unknown molecular weight of polymeric material, the same weight amount (1 g) of BiVO<sub>4</sub> photocatalysts as OCT was used in the water oxidation reaction. In addition, the electron scavengers, *e.g.* Ag<sup>+</sup> in this project, are a key factor in separating of holes from electrons and obtaining long-lived holes, which significantly influences the efficiency of O<sub>2</sub> production<sup>22</sup>, so the same amount of AgNO<sub>3</sub> was applied in the benchmarking protocol. Thus, this benchmarking protocol ensures the fair, relevant, quantitative comparisons of photocatalytic water oxidation performance of OCT and BiVO<sub>4</sub>. From the observation of Fig. 36, it is found that the OCT is as efficient as BiVO<sub>4</sub> (8.29 μmol h<sup>-1</sup> when a 420-nm cut-off filter was used). Furthermore, the OCT is still efficient when BiVO<sub>4</sub> does not work, at wavelengths longer than 600 nm, consistent with their optical absorption. Fig. 35a shows the AQY for oxygen production, which is more reliable as an indicator of photocatalyst efficiency. Notably, the OCT has a very wide operation window, with an AQY of 2.6% at 400 nm, 1.1% at 500 nm, and even 0.2% at wavelengths as long as 800 nm. Such a long wavelength response goes far beyond any inorganic and organic photocatalysts reported so far for oxygen evolution. In addition, the correlation between UV-vis absorption spectrum and AQY suggest that water oxidation is driven by light.

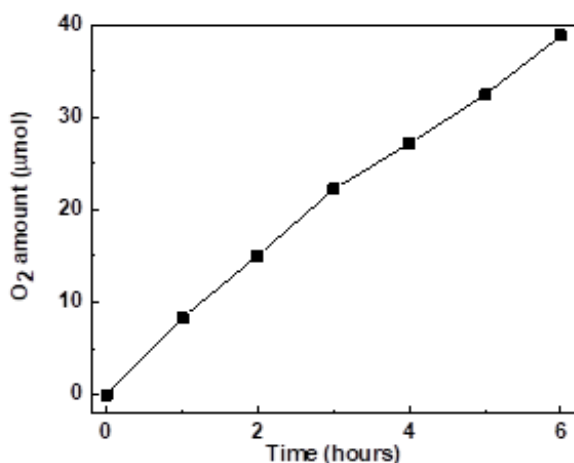


Figure 36. O<sub>2</sub> evolution of 0.1 g BiVO<sub>4</sub> under visible light ( $\lambda > 420$  nm) in the presence of the electron scavenger of 1 g AgNO<sub>3</sub>.

Next, it is assessed that the stability of the samples by running a three-cycle photocatalytic test and performing structural analysis before and after water oxidation. The reaction of O<sub>2</sub> evolution was run for a total 24 h within intermittent evacuation every 8 h under both full arc and visible light irradiation (Fig. 37a). Continuous O<sub>2</sub> is produced but with the noticeable decrease due to the deposition of metallic silver on the catalyst surface when using Ag<sup>+</sup> as an electron scavenger, blocking light absorption and obstructing active sites<sup>8, 266</sup>. On the other hand, as shown in Fig. 37b, the reaction of H<sub>2</sub> evolution was run for a total of 18 h with intermittent evacuation every 6 h under both full arc and visible light irradiation ( $\lambda > 420$  nm). The amount of H<sub>2</sub> evolution is almost the same at the end of every cycle, which means the stability of 6.68 at% OCT during the reaction. Whereas, the structure of photocatalysts remains stable after reaction, as confirmed by the FTIR and ssNMR spectra taken before and after water oxidation in Fig. 38. Both demonstrate the stability of the polymer after photocatalytic reaction.

It is further verified that the detected O<sub>2</sub> was indeed generated by water oxidation. Firstly, the total amount of O<sub>2</sub> obtained after 24 h was *ca.* 135.2 μmol of O<sub>2</sub>, or 270.4 μmol of oxygen atoms as shown in Fig. 37a. This is more than four times of the amount of oxygen atoms (63.3 μmol) contained in the 6.68 at% OCT sample drawn from the elemental analysis in Table 3, proving that the oxygen gas was produced from water rather than deoxygenation of the polymer. In addition, isotopic measurement showed that the photocatalytic oxygen evolution in the <sup>18</sup>O-labelled water generates a strong <sup>18</sup>O<sub>2</sub> peak after reaction for 2 h reaction, as noted in the GC-MS spectra in Fig. 39, further confirming that the oxygen production is originally from the water.

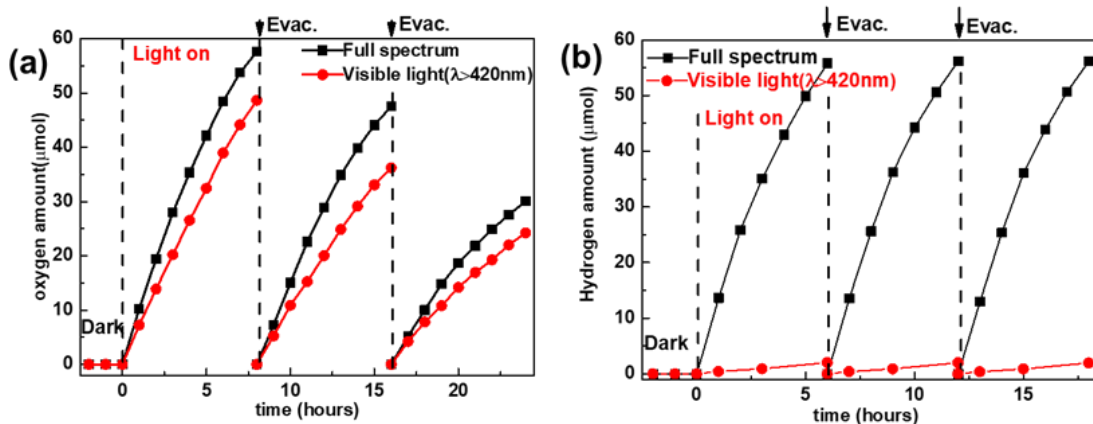


Figure 37. The typical time courses of (a) O<sub>2</sub> production from water containing 1 g AgNO<sub>3</sub> as a hole scavenger and (b) H<sub>2</sub> production from water containing 10 vol% TEOA as an electron donor and 3 wt% Pt (H<sub>2</sub>PtCl<sub>6</sub>) as a cocatalyst, under full arc and visible light (of wavelength longer than 420 nm) by 6.68 at% OCT. The reaction of O<sub>2</sub> evolution was run for 24 h, with evacuation every 8 h (dashed line). The reaction of H<sub>2</sub> evolution was run for 18 h, with evacuation every 6 h (dashed line).

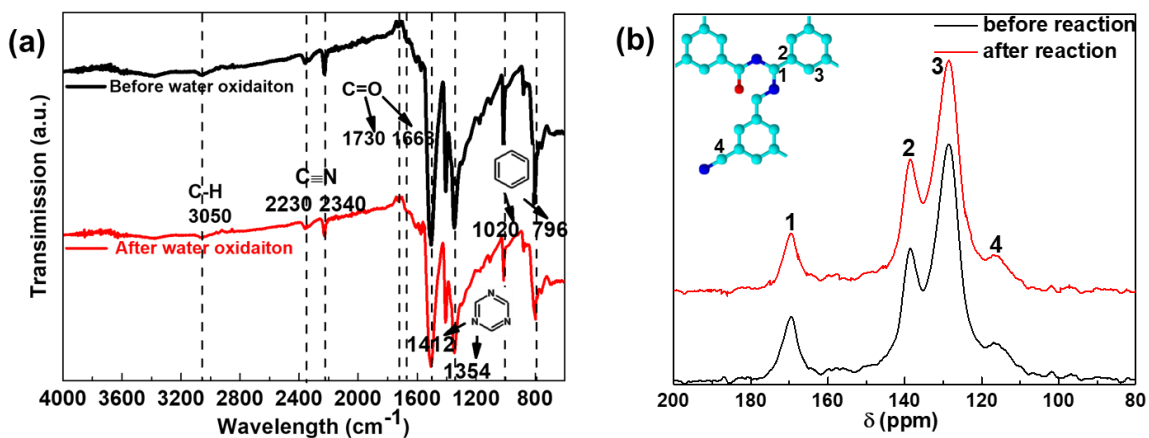


Figure 38. FTIR spectra(a) and <sup>13</sup>C cross-polarization magic angle spinning ssNMR spectra(b) of 6.68 at% OCT before and after water oxidation reaction. The light blue dots are carbon atoms, the dark blue ones are nitrogen atoms, and the red one is oxygen atom.

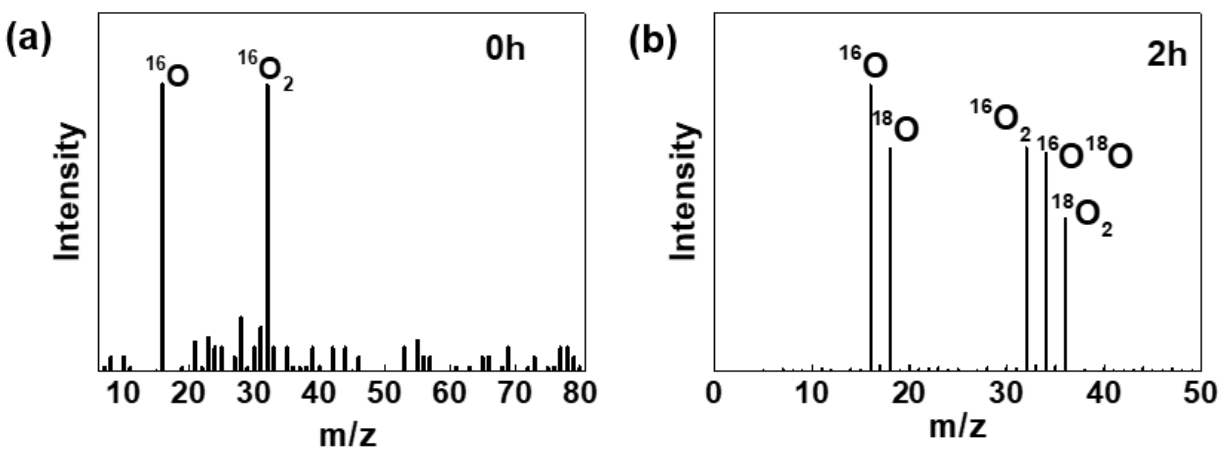


Figure 39. Gas Chromatography mass spectra of oxygen obtained under full arc irradiation in the 95% <sup>18</sup>O-labelled-water photocatalytic system at reaction time points of (a) 0 h and (b) 2 h.

### 4.2.3 Discussion of prospective structure optical properties

Density functional theory (DFT) study was taken into consideration based on the formation process, see Fig. 26, and probed the electronic structures and optical properties of several prospective modified structures.

To compare the pure CTF-1 and the OCTs, the reaction energy was calculated according to the following equation:  $E_f = E_{CT/OCTs} - 2E_{precursor\ 0} - E_{precursor} + \Delta E_H$ , where the  $E_{CT/OCTs}$  is the total energy of the systems of CTF-1 or OCTs. The  $E_{precursor\ 0}$  represents the total energy of 1, 4-dicyanobenzene molecule and  $E_{precursor}$  is the energy of the proposed precursors shown in Fig. 26 b and c, respectively. The  $\Delta E_H$  is the adjustment energy to balance the equation and was calculated by half of the energy of  $H_2$ . The reaction energy of each structure is listed in Table 4. From the thermodynamic point of view, all the reactions are exothermic; so, all the three structures could be produced in the final compounds. Structures OCT(i) and OCT(iii) conserve the framework, while OCT(ii) disrupts the triazine unit that links benzenes, hindering complete crystallization of the OCT and resulting in crystal disorder as observed in XRD, Fig. 28.

Table 4. The reaction energy of each structure of pure CTF-1 and OCTs.

Structure	Formation Energy (eV/atom)
CTF-1	-0.138
OCT(i)	-0.148
OCT(ii)	-0.099
OCT(iii)	-0.163

The oxygenation not only disturbs the formation of the triazine ring, but more importantly changes the electronic distribution on VBM and CBM, as shown in Fig. 40. For the pure CTF-1

(Fig. 40(a and b)), the nitrogen atoms contribute to both VBM and CBM, respectively by electrons from  $p_x$  and  $p_y$  orbitals and from  $p_z$  orbitals. The oxygen doping dramatically tunes the configuration of the band configurations. For the OCT(i), both carbon and oxygen donate  $p_z$  electrons to the VBM. For OCT(ii) and OCT(iii), the VBM is from electrons over a wider area, especially in the carbonyl group. Moreover, the oxygen does not contribute to the CBM in OCT(i) and OCT(iii), but that does partially to the CBM from the  $p_z$  orbital in OCT(ii). Overall, partially distorted triazine units due to oxygenation show relatively high delocalisation of electron density (Fig. 29), implying that photogenerated charges are more readily to diffuse through the OCT to react with other species than through the pure CTF-1. Thus, oxygen incorporation stimulates the mobility of the charged carriers and inhibits the recombination of electrons and holes.

I next compared the density of states (DOS) of CTF-1 and OCTs in Fig. 40. The band gap of the pure CT is 2.6 eV, and OCT(i) shows a slight reduction in band gap, to 2.54 eV, whereas the other structures display significantly redshifts in absorption by 0.37 eV (OCT(ii)) and 0.42 eV (OCT(iii)), respectively. The unoccupied defect states result from the formation of the oxygen-containing functional groups, albeit with significant delocalisation arising from the significant aromaticity of the benzene and triazine components of the CTF-1. As shown in Fig. 26h, oxygenation of the polymer dramatically reduces the overpotential for  $H_2$  production under visible light irradiation, but almost retains a relatively stable VBE, not affecting  $O_2$  production. Among them in Fig. 26h, the OCT(ii) demonstrates the narrowest band gap, most benefit the visible optical absorption, but the unoccupied defect state is too closed to the potential of water reduction to produce  $H_2$  under visible light irradiation, thus efficient hydrogen production only occurs under full arc irradiation. Furthermore, OCT(ii) is the only structure containing the C=O bonding, which is consistent with

the experimental structure characterization results and further confirms that OCT(ii) is the most promising structure matching all the characterization and simulation results.

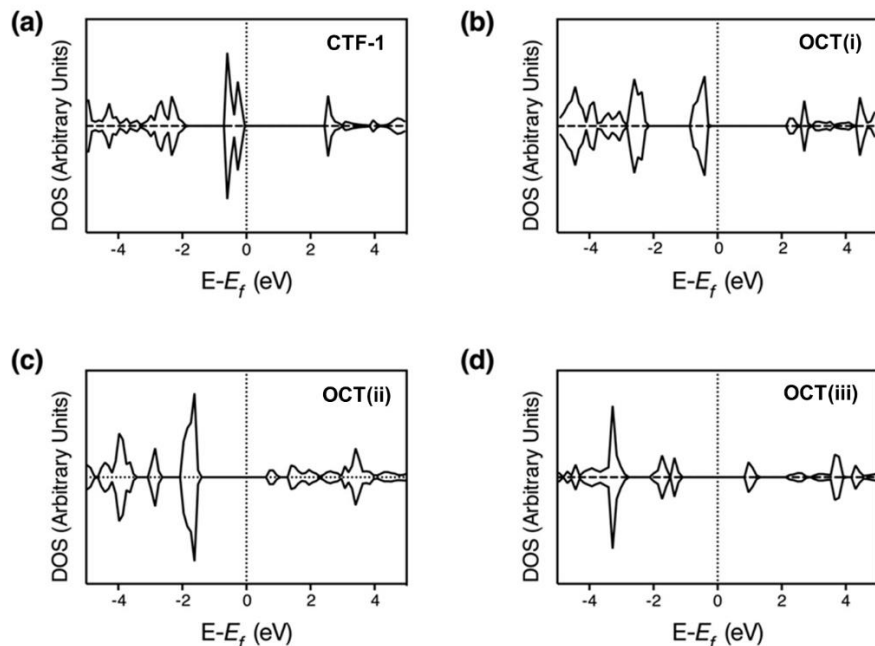


Figure 40. The density of states (DOS) of the structure for pure CTF-1 (a), OCT(i) (b), OCT(ii) (c) and OCT(iii) (d). The Fermi levels were adjusted to zero.

#### 4.2.4 Effect of oxygen content on water oxidation and optical and electrical properties

Furthermore, I explored the effect of oxygen content in the materials on their water oxidation performance. Five samples with different levels of oxygen doping were synthesised and the detailed elemental ratios are shown in Table 3. The C/N ratios of all polymers are around 4.5, close to the theoretical value of 4 for the pure CT. The slightly higher ratio is believed to be mainly due to oxygen doping and more benzene ring terminals or edges. The higher the level of oxygen doped in the framework, the narrower the band gap, up to 1.6 eV when an oxygen content being 6.68 at% (Fig. 41b). Moreover, the effect of the level of doped oxygen on the photocatalytic

performance and the band gap converted from UV-vis absorption has been further investigated experimentally, shown in the Fig. 41. The results show that the amount of photocatalytic oxygen evolution increases as the oxygen doping level increases to a peak at the oxygen-doping level of 6.68 at%, of the initial rate of 10.24  $\mu\text{mol}$ . Afterwards, the amount of produced oxygen drops as the oxygen doping level increases to 7.71%. The trend of this experimental performance is in good agreement with the changes of calculated the band positions and the band gap of the OCT polymers, as shown in Fig. 42. Compared to the pure CT, the unoccupied defect state of OCT shifts down greatly, and the VB relatively remains, thus narrowing the band gap. Above all, doping oxygen into covalent triazine framework synthesised by a controlled polymerization method realised readily band gap Engineering. The UV-vis absorption spectra of different oxygen-incorporated CT polymers show the increase in the level of doped oxygen, leading to a long wavelength absorption value,  $\lambda_{max}$ , due to a narrower band gap at a higher level of doped-oxygen in the CT, as predicted theoretically. With further increase of the oxygen doping level, as indicated by the XPS spectra in Fig. 43, the extra oxygen tends to form C-O/C-OH bonds, rather than the C=O bond. This indicates that the C=O bond is more effective to tune the band gap, and more importantly, acts as active site for water oxidation.

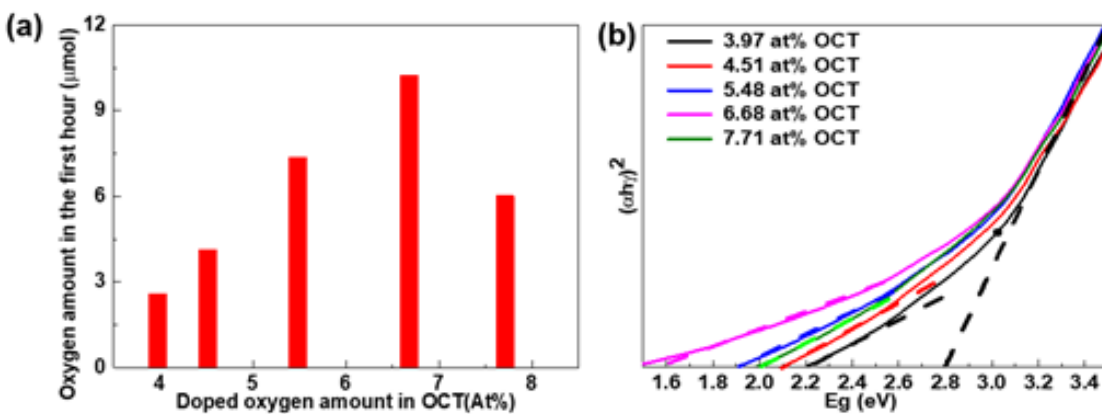


Figure 41. Oxygen evolution amount for different amount of oxygen doped in OCT (a) and the corresponding Tauc Plots calculated based on the UV-vis spectra(b).

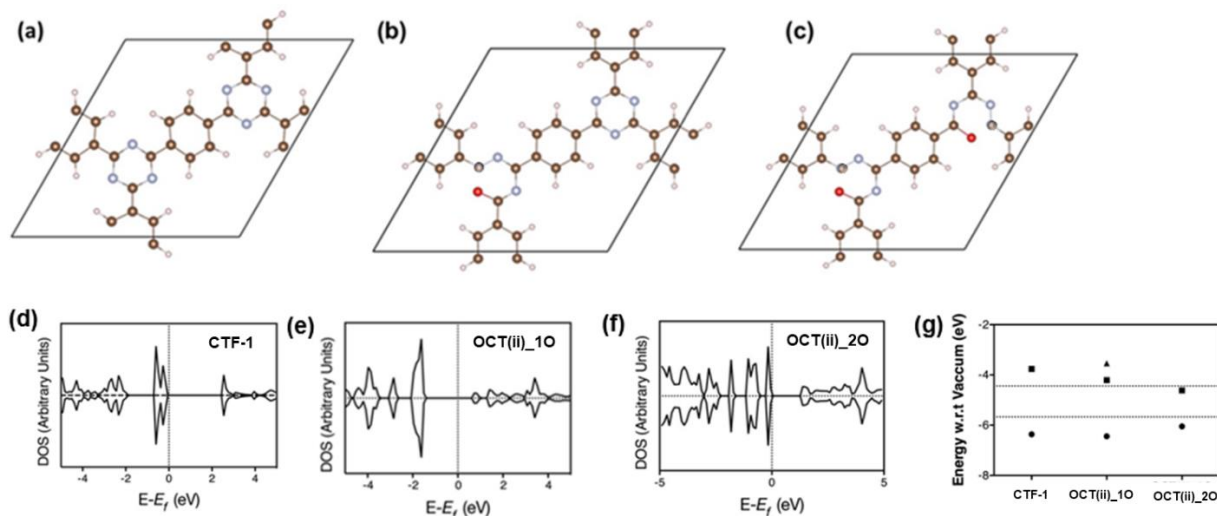
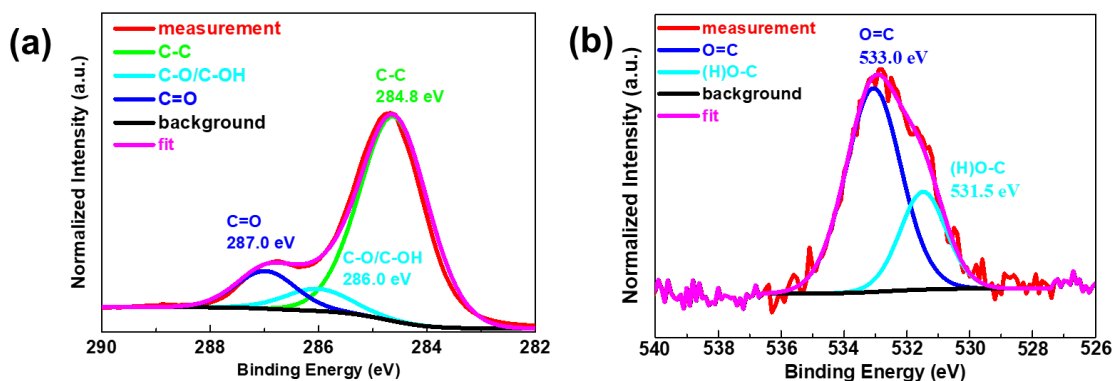


Figure 42. The equilibrium structures and its density of states for pure CTF-1 (a and d), 3.33 at% OCT(ii) (b and e) and 6.68 at% OCT(ii) (c and f), respectively and the band alignment calculations in PBE level of OCT(ii) for different oxygen doping levels (g). The bottom ones (solid circles) are the position of the VBs and the solid squares and triangle represent the CBs and the unoccupied defect state.



*Figure 43. (a) C1s and (b) O1s XPS spectra for the 7.71 at% OCT. (Charge referenced to adventitious C1s peak at 284.8 eV).*

### **4.3 Conclusions**

In conclusion, an oxygen-doped covalent triazine (OCT) material was successfully synthesised by polymerization of 1,4-dicyanobenzene in controlled gas mixtures of oxygen and nitrogen. Under full-arc irradiation, the new OCT photocatalyst shows both oxygen and hydrogen evolutions from water in the presence of separate scavengers and demonstrates oxygen evolution longer than a day.

For the first time, water oxidation proceeds from UV up to 800 nm irradiation, consistent with the UV-vis absorption spectrum, with an AQY of 2.3% at 420 nm, 1.1% at 500 nm, closed to 1% even at 600 nm. The visible light absorption is attributed to a significant reduction in the gap, caused by disruption of the triazine structural unit and the formation of the effective C=O moiety. This moiety has a very significant effect on the band gap engineering, creating the unoccupied defect states, which benefits the water oxidation under the visible light irradiation.

It is demonstrated, an organic water oxidation photocatalyst that has an exceptionally wide window of operation, up to 800 nm for both H<sub>2</sub> and O<sub>2</sub> production in the presence of relevant sacrificial reagent. Overall, these findings demonstrate a strong potential for the development of low-cost and environmental-friendly photocatalysts for effective solar driven water splitting. However, this modified polymer photocatalysts still show moderate activity under visible light. A more efficient polymer photocatalyst will be developed next.

## 5 Chapter 5

### **New CTF-0 for both visible light-driven efficient hydrogen and oxygen generation from water**

As mentioned before that covalent triazine frameworks (CTFs), which was firstly synthesised successful as crosslinked porous polymers with two-dimensional molecular structures a few years ago, have very recently become appealing harvesters for photocatalytic water splitting, owing to their adjustable band gap and facile processing. Herein, two different synthesis ways of a novel photocatalyst covalent triazine framework CTF-0 was investigated, which was then tested as a superior photocatalyst for enhanced photocatalytic H<sub>2</sub> and O<sub>2</sub> evolution under visible light irradiation. The CTF-0-M<sub>2</sub> produced by microwave method shows much higher photocatalytic activity of hydrogen evolution (up to 701 μmol/h) than the CTF-0-I produced by conventional ionothermal trimerization method under identical photocatalytic conditions. This can be attributed to the narrowed band gap, the most negative conduction band and the rapid photogenerated charge separation and transformation. Whereas, CTF-0-I initially produces *ca.* 6 times higher oxygen evolution than CTF-0-M<sub>2</sub> under the same experimental condition, due to the large driving force of water oxidation and the large number of active sites. The findings therefore suggest that, varying the experimental conditions of synthesizing CTF-0 modulates their ordered interlayer structure and bandgap positions, thus further optimizing their optical and redox properties, resulting in an enhanced performance for photocatalytic hydrogen and oxygen evolution, which has been further proved by the theoretical modelling and PEC results.

## 5.1 Introduction

Storage solar energy into chemical fuels by artificial photosynthesis is an environmentally friendly way for production of clean and sustainable energy, prohibiting the environment pollution by reducing the greenhouse gas emission from fossil fuels<sup>267</sup>. Specifically, visible-light driven water splitting into O<sub>2</sub> and H<sub>2</sub> by photocatalysts has a promising potential to realise the application of solar-to-chemical energy conversion in practice<sup>240</sup>. For overall water splitting (OWS), single semiconductor photocatalysts has been reported to successfully and simultaneously generate hydrogen and oxygen from water under light illumination in a suspension system<sup>51, 268-269</sup>. However, the highest quantum efficiency of single photocatalyst for OWS has been reported about 2.5 % at 420-440 nm on (Ga<sub>1-x</sub>Zn<sub>x</sub>)(N<sub>1-x</sub>O<sub>x</sub>)<sup>270</sup>, which is much lower than that of a Z-scheme OWS system, *e.g.* the SrTiO<sub>3</sub>:La, Rh/ Au/BiVO<sub>4</sub>:Mo photocatalyst sheet, which exhibited an apparent quantum efficiency of 33% at 419 nm<sup>271</sup>. The major reason is likely that the Z-scheme system dramatically alleviates unexpected while inevitable back reaction on single photocatalysts and expands the light absorption by using narrow band gap semiconductors that are even deficient in terms of either the CBM level (that is, the CBM is more positive than the H<sup>+</sup>/H<sub>2</sub> potential) or the VBM level (that is, the VBM is more negative than the O<sub>2</sub>/H<sub>2</sub>O potential). Thus, only certain oxides and (oxy)nitrides can be used as single photocatalysts for OWS, while many other types of semiconductors can potentially be used in the Z-scheme system<sup>272</sup>. Furthermore, photoelectrochemical (PEC) water splitting also demonstrate a high solar-to-hydrogen efficiency, such as ~3.3% for pH neutral overall water splitting by double-band GaN:Mg/InGaN:Mg nanosheet photochemical diodes<sup>273</sup>. Equally important, for the safety reason, *in-situ* separation H<sub>2</sub> and O<sub>2</sub> is preferable<sup>243</sup>, which can be achieved in either PEC or Z-scheme system economically. The requisite of both PEC and Z-scheme system is efficiency

photocatalysts for half reaction (either water reduction or oxidation reaction). Therefore, many studies concentrate on the discovery of efficient photocatalysts for either half reactions.

In the Chapter 4, I investigated the CTF-1 and modified CTF-1 for water splitting, which show some attractive properties while AQY is not satisfactory. In this work, novel conjugated, crystalline CTF-0s using 1,3,5-tricyanobenzene (TCB) as a precursor under both microwave-assisted and ionothermal conditions were synthesised. The correlation between the structure and photocatalytic activity will be thoroughly investigated and discussed in this Chapter.

## **5.2 Methodology**

### **5.2.1 Chemicals**

1,3,5-tricyanobenzene was purchased from OTAVA Ltd.. Trifluoromethanesulfonic acid (TFMS) was purchased from Sigma-Aldrich. Zinc Chloride was purchased from Alfa Aesar. They were used as received.

### **5.2.2 Synthesis of CTF-0-I**

CTF-0-I was synthesised from 1 g (6.5 mmol) of 1, 3, 5-tricyanobenzene and 0.9 g (6.5 mmol) of  $ZnCl_2$  in a glass ampule. The ampule was evacuated and then flame-sealed and placed into a furnace for heat treatment at 400 °C and 40 h. The light-yellow solid was obtained after breaking the cool ampule and then ground thoroughly. The powder was dispersed in the water and then kept stirring for 12 h at 90 °C after sonicated. 0.1 M HCl was added in the water and the solution was stirred for another 12 h at 90 °C. The sample was finally washed successively with water, acetone, and ethanol, and then dried in the vacuum oven at 120 °C for 12 h.

### 5.2.3 Synthesis of CTF-0-Ms

CTF-0-M<sub>1</sub>, CTF-0-M<sub>2</sub> and CTF-0-M<sub>3</sub> were synthesised by 1 g of 1, 3, 5-dicyanobenzene (13 mmol) and 1.5 mL, 2 mL and 2.5 mL (6.9 mmol, 17.9 mmol and 22.4 mmol) of TFMS as a catalyst and solvent. The mixed chemicals were moved into a 10 mL glass reaction vessel (CEM, Discover and Explorer SP Vessels) with a magnetic stirrer and the vessel was covered. And the vessel was immediately placed into a CEM microwave and worked for 30 min with the power of 300 W. In the first minute, the solution started boiling and pale-yellow solid precipitates were formed gradually and finally the precipitates after 30 min microwave heating were collected and washed by ammonia solution to remove the acid, and then washed with ethanol, acetone and water subsequently. Finally, the products were obtained as powders after drying in the vacuum oven at 180 °C for 12 h.

### 5.2.4 Characterization

Powder X-ray Diffractograms (PXRD) of the as-prepared samples were taken by a Bruker D4 Diffractometer with Ni-filtered Cu K<sub>α</sub> irradiation ( $\lambda_1=1.540562\text{\AA}$ ,  $\lambda_2=1.544398\text{\AA}$ ). The Brunauer-Emmett-Teller (BET) surface area measurement was performed on Micromeritics® Tristar 3000 with N<sub>2</sub> carrier gas. Solid-state Nuclear Magnetic Resonance (ssNMR) spectra were carried out on a Bruker Advance 300WB spectrometer running with a 4mm magic-angle spinning probe for <sup>13</sup>C and <sup>1</sup>H measurements. Fourier transform infrared spectra (FTIR) were performed on a Perkin-Elmer 1605 FT-IR spectrometer in the wavelength range from 400-4000 cm<sup>-1</sup> with a resolution of 0.5 cm<sup>-1</sup>. UV-visible reflectance spectroscopy was conducted using a Shimadzu UV-Vis 2550 spectrophotometer fitted with barium sulphate as a referent. Photoluminescence (PL) spectroscopy measurements were performed on a Renishaw spectrograph system based on use

of Kayser™ notch filters with a sensitive CCD detector coupled to a microscope for point-by-point analyses, using a 325-nm excitation laser and a wavenumber range of 100-2000 cm<sup>-1</sup>. X-ray photoelectron spectra (XPS) was performed using a ThermoScientific XPS K-alpha surface analysis machine using an Al source. Analysis was performed using CasaXPS.

### 5.2.5 Theoretical Calculations

To understand the electron characters of the investigated compounds CTF-0, the Density Functional Theory (DFT) was used by the VASP code<sup>246</sup>. A plane wave cutoff of 520 eV was selected, with the Projector Augmented Wave methods used to treat the core electrons<sup>247</sup>. The PBE functional was used for structure optimization, thermodynamic calculation, and electronic structure analysis<sup>248</sup>. Van der Waals interactions were included via the usage of the DFT-D2 method of Grimme<sup>249</sup>. All atoms were fully relaxed until the change in force upon ionic displacement was less than 0.01 eV/Å, with the change in energies no greater than 10<sup>-5</sup> eV. CTF-0 crystals were generated using an AA stacking motif. CTF-0 thermodynamics were determined using a (2×2) single sheet supercell, with a Monkhorst-Pack k-point mesh of (5×5×1) found to be sufficient in order to produce well converged energies and forces. Spin-polarisation was used in all calculations. The single sheet structure was also used to accurately align Kohn-Sham (KS) eigenvalues for the pure and doped supercells. As a large vacuum spacing was used in the simulations, the planar averaged electrostatic potential converged to a constant value far from the surface. These converged values may be taken as the reference level with which the Kohn-Sham (KS) eigenvalues are aligned.<sup>250</sup> For the band alignment of the CTF-0, the Fermi level were determined by the calculations of each work function, where vacuum is set to zero.

### 5.2.6 Photocatalytic measurements

Oxygen and hydrogen evolution performances were carried out separately in a custom Pyrex® batch reactor cell under the irradiation of a 300 W Xe lamp (*TrusTech PLS-SXE 300/300UV*). A reaction cell under the full-arc irradiation was used for hydrogen evolution, containing 100 mg of solid catalysts loaded with 3 wt% Pt and 230 ml of H<sub>2</sub>O mixed with 10 vol% triethanolamine while for the oxygen evolution containing 100 mg of solid catalysts and 1 g of AgNO<sub>3</sub> dissolved in the 230 ml H<sub>2</sub>O. Before the reaction, the reactor was sealed and then argon was purged into it to remove all the air. To measure the photocatalytic efficiency under the visible light irradiation, a 420-nm long pass filter was installed in front of the lamp to remove UV light. 365, 420, 500, 600 and 800 nm bandpass light filters was used for quantum efficiency measurement. All the product gas was analysed by gas chromatography (*Varian 430-GC, TCD, argon carrier gas 99.999%*). The apparent quantum efficiency ( $\Phi$ ) was calculated by the equation:  $\Phi = (N \times O/n) \times 100$ , where N, O and n were equivalent to the numbers of charge carriers for one molecular gas, evolved gas molecules and number of the incident photons, respectively. The number of incident photons was calculated by the equation:  $n = I\lambda/hc$ , where the light intensity I was measured by a Newport power meter. The turnover number (TON) was calculated after seven cycles by using the following formula: TON = moles of H<sub>2</sub> molecules generated / moles of active sites (herein platinum on the photocatalysts).

### 5.2.7 Photoelectrochemical Measurements

The photoelectrochemical properties were investigated in a conventional three-electrode cell using an electrochemical analyser (IVIUM Technologies). CTF-0 films were prepared as followings: FTO glass was washed sequentially with distilled water, ethanol and acetone in an

ultrasonic cleaner for 30 min. Then, 5 mg CTF-0 grounded powders were mixed with 750  $\mu\text{L}$  distilled water, 250  $\mu\text{L}$  2-propanol and 10  $\mu\text{L}$  Nafion in an ultrasonic cleaner for 30 min and then the slurry was coated onto 2 cm  $\times$  2 cm FTO by spin coater. After drying overnight in a hot plate at 250  $^{\circ}\text{C}$ , the electrodes were sintered at 400  $^{\circ}\text{C}$  for 30 min to improve adhesion. The prepared films, a Pt net and Ag/AgCl (saturated KCl) were used as the working, counter and reference electrodes, respectively. Sunlight was simulated with a 150 W xenon lamp (Newport) and AM 1.5 filter (Newport). The light intensity was tuned using a calibrated crystalline silicon solar cell, equivalent to global AM 1.5 illumination at 100  $\text{mW}/\text{cm}^2$ . The photocurrent of samples was measured in 0.1 M  $\text{Na}_2\text{SO}_4$  aqueous solution (pH=6.5). Samples were illuminated from the back side (FTO substrate) and the mask-off irradiated area was 2  $\text{cm}^2$ . Mott-Schottky curves were measured at a certain DC potential range with an AC amplitude of 5 mV and a frequency of 0.5 kHz, 1 kHz and 2 kHz under dark condition. Electrochemical impedance spectra (EIS) were measured with 0.0 V bias versus AgCl/Ag.

## 5.3 Results and Discussion

### 5.3.1 General Characterisations

To certify the successful polymerization of triazine rings and characterise their structure of the new CTF polymers, the prepared samples were characterised by PXRD, nitrogen sorption measurements, solid-state  $^{13}\text{C}$  NMR spectroscopy, and FTIR spectroscopy.

XRD measurements of samples in Fig.44 shows that all the samples are at least partially crystalline, while the intensity and the width of the peaks can be influenced by the synthesis temperatures and the reaction concentration of the acid. There are two distinct peaks at  $\sim 15^{\circ}$  and  $\sim 25.5^{\circ}$  in XRD patterns of all the samples. The low-angle peak at  $\sim 15^{\circ}$  can be attributed to the in-

plane reflection (100) of three hexagonal unit cells built by the bridge structure between the respective aromatic units and the triazine-linkers as shown in Fig.44, while the broad peak at  $\sim 25.5^\circ$  can be interpreted as the interlayer spacing (001) with vertical stacked sheets of 3.42 Å. One can see that CTF-0-M<sub>2</sub> has the highest ordered interlayered structure among all samples. Therefore, the morphology of CTF-0-M<sub>2</sub> was observed by TEM as shown in Fig. 45. Clearly, the lattice space of *ca.* 0.34 nm for the multilayer structure of CTF-0-M<sub>2</sub> was measured from the TEM contrast intensity profile and the Fast Fourier Transforms (FFT) in Fig.45, which is corresponding to the result of the (001) peak shown in the PXRD spectra. Obviously, the materials prepared by the higher temperature treatment have the higher peaks of in-plane reflection (100) than the interlayer reflection (001). However, the samples prepared by the microwave method at the room temperature obtain the higher intensities of the interlayer reflection than the in-plane reflection. The enhanced crystallised structure between interlayers of CTF-0-Ms can correspond to the relatively higher energy provided by the microwave in a certain period than the ionothermal method. In contrast, the low angle (100) peak of CTF-0-I is increased in intensity compared to CTF-0-Ms, which points to the long enough reaction time (40 h) under the high temperature (400) facilitating the reorganization of monomers in planes. Thus, the higher temperature induces more in-plate crystallisation. The polymers prepared by the microwave method show an order of degree of crystallinity CTF-0-M<sub>2</sub> > CTF-0-M<sub>1</sub> > CTF-0-M<sub>3</sub> likely due to lower or higher concentration of the TFMS catalyst which either reduce or destroy the crystallinity, respectively. In other words, the nearly 1:1 ratio of the reactant and catalyst produces the highest degree of crystallinity of the CTF polymer.

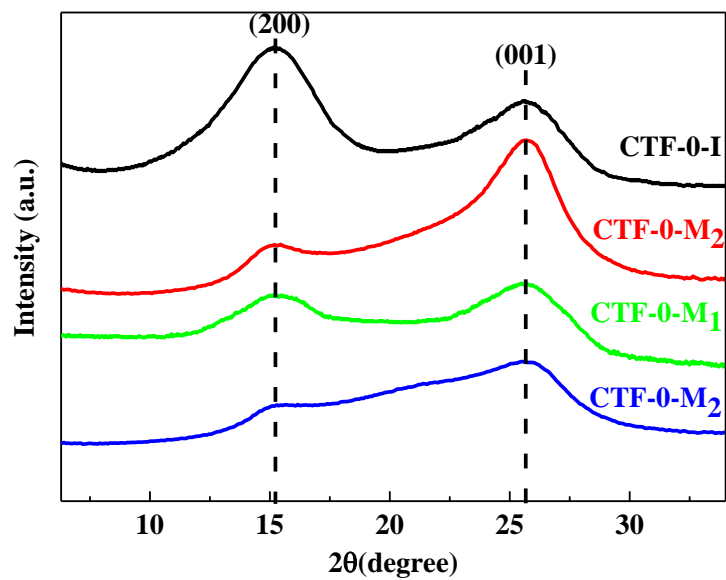


Figure 44. PXRD patterns of CTF-0-I prepared by the ionothermal method, and CTF-0-M<sub>1</sub>, CTF-0-M<sub>2</sub> and CTF-0-M<sub>3</sub> prepared by the microwave method.

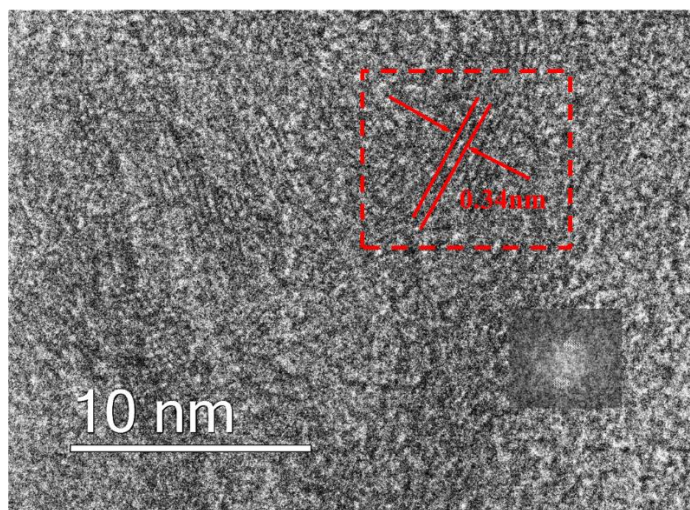


Figure 45. Transmission electron microscopy (TEM) image of CTF-0-M<sub>2</sub>.

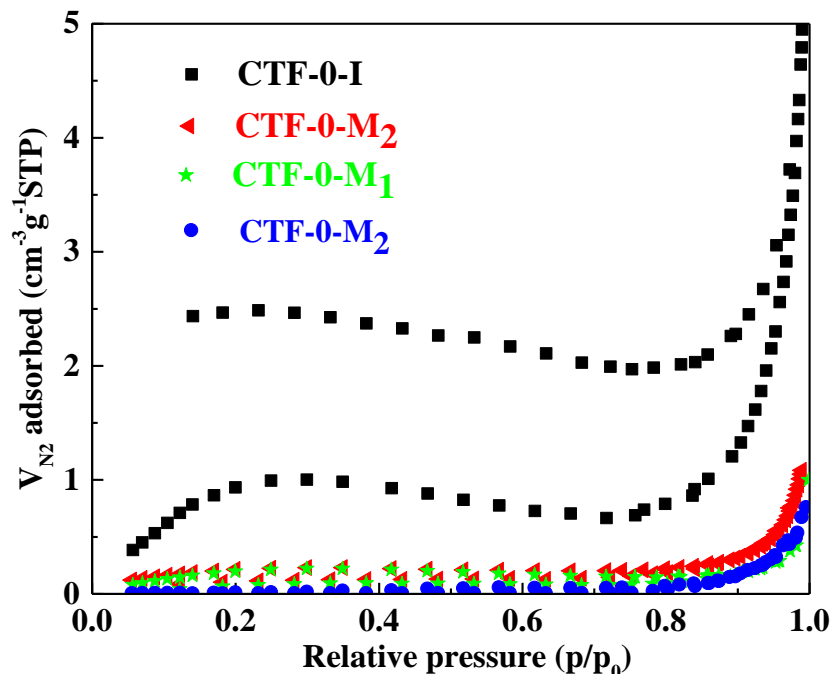


Figure 46. Nitrogen sorption measurements of CTF-0-I prepared by the ionothermal method, and CTF-0-M<sub>1</sub>, CTF-0-M<sub>2</sub> and CTF-0-M<sub>3</sub> prepared by the microwave method.

The porosity of the resulting CTFs was studied by N<sub>2</sub> sorption experiments at 77 K (Fig. 46), which can influence the surface reactions in the photocatalytic water splitting. All the samples (CTF-0-Ms) synthesised by the microwave method show very low, nearly 0.1 m<sup>2</sup>·g<sup>-1</sup> of N<sub>2</sub> accessible surface area, as the pore entrances are too narrow to allow the uptake of a probe with a radius of 1.82 (N<sub>2</sub>). The CTF-0-I shows a comparably loose organic network with apparent BET surface of 5.13 m<sup>2</sup>·g<sup>-1</sup>, which is reasonable, as the higher temperature in the ionothermal treatment induced the production of a small amount of gas during the synthesis, creating small pores in the surface of the sample. This result is in line with the previous report, in which the higher temperature during the polymerization can give rise to the higher surface area<sup>183</sup>, which is beneficial for providing more active sites.

The ssNMR measurements (Fig. 47) of the CTF-0s materials certifies the conjugated triazine rings synthesised successfully, which shows three distinct peaks which can be assigned to the carbon atoms in the triazine rings (169 ppm) and two distinguishable carbons in the bridging benzene rings (138 and 117 ppm). No peaks of residual cyano groups (110 ppm) can be detected in the spectrum<sup>183</sup>. At the first glance, it is seen that the intensity of the peak at 169 ppm for CTF-0-M<sub>2</sub> is highest, CTF-0-M<sub>1</sub> middle and CTF-0-M<sub>3</sub> lowest. While less (CTF-0-M<sub>1</sub>) or more catalyst (CTF-0-M<sub>3</sub>) would either limit polymerisation or decompose the polymer, leading to a weaker peak at 117 ppm, consistent with XRD analysis. The elemental composition of all the samples are analysed by XPS spectra shown in Fig. 48 and the elemental analysis (EA) in Table 5, which confirms only carbon, nitrogen and hydrogen exist, excluding other impurities in the photocatalysts. As the XPS is a surface sensitive technique, EA measurements are used to further certify the elemental compositions. The C: H: N ratio of CTF-0-M<sub>2</sub> is 71.4: 2.0: 26.3, which is mostly closed the theoretical ratio of 70:6: 2.0: 27.4, then CTF-0-M<sub>1</sub>, and last CTF-0-M<sub>3</sub>. Less catalyst or more catalyst induces more carbon in the final samples. For CTF-0-I, the higher synthesised temperature further increases the carbon to the highest amount among all samples<sup>183</sup>.

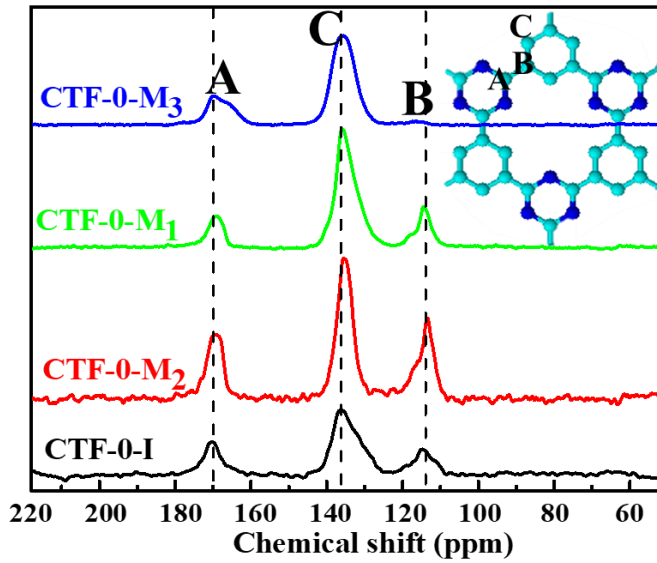


Figure 47. Solid-state  $^{13}\text{C}$  NMR spectra of CTF-0-I prepared by the ionothermal method, and CTF-0-M<sub>1</sub>, CTF-0-M<sub>2</sub> and CTF-0-M<sub>3</sub> prepared by the microwave method.

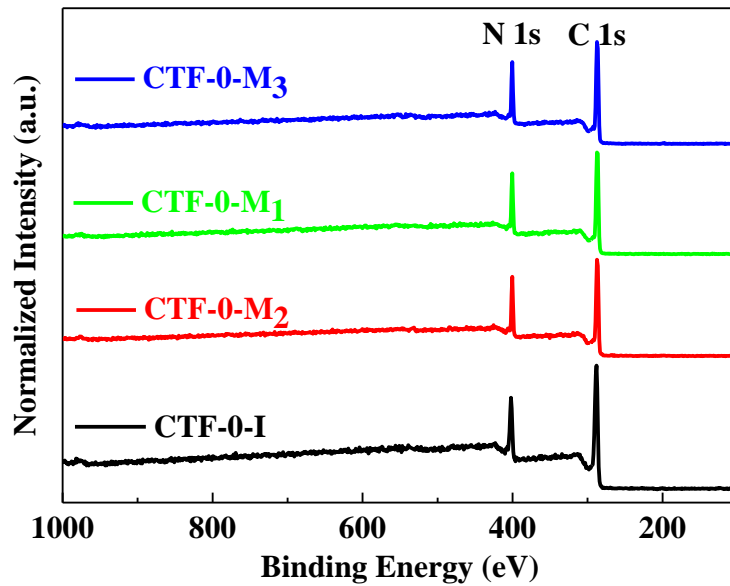


Figure 48. XPS survey spectra of CTF-0-I, CTF-0-M<sub>1</sub>, CTF-0-M<sub>2</sub> and CTF-0-M<sub>3</sub>.

Table 5. Elemental analysis data of the polymers CTF-0-I, CTF-0-M<sub>1</sub>, CTF-0-M<sub>2</sub> and CTF-0-M<sub>3</sub>.

Polymer	Acid catalyst	TCB	Experimental %			Theory %		
			C	H	N	C	H	N
CTF-0-I	0.9 g	1 g	76.8	2.5	20.0	70.6	2.0	27.4
CTF-0-M <sub>2</sub>	2 mL	1 g	71.4	2.0	26.3	70.6	2.0	27.4
CTF-0-M <sub>1</sub>	1.5 mL	1 g	72.1	2.1	25.3	70.6	2.0	27.4
CTF-0-M <sub>3</sub>	2.5 mL	1 g	72.3	2.2	24.8	70.6	2.0	27.4

Moreover, the FTIR spectra (Fig. 49) represents the existence of the intense carbonitrile band at 1308 and 1519 cm<sup>-1</sup>, indicating successful trimerization reaction, and a very small peak at 2244 cm<sup>-1</sup> also points to the increasing formation of triazine rings<sup>183</sup>. Peak at 1308 cm<sup>-1</sup> in the FTIR spectroscopy also indicates an order of the degree of polymerisation, CTF-0-M<sub>2</sub> > CTF-0-M<sub>1</sub> ~ CTF-0-I > CTF-0-M<sub>3</sub>. Based on the above measurements, I can conclude that covalent triazine frameworks CTF-0 have been successfully synthesised by both the ionothermal method and microwave method while the order of the degree of crystallinity follows CTF-0-M<sub>2</sub> > CTF-0-M<sub>1</sub> ~ CTF-0-I > CTF-0-M<sub>3</sub>. In addition, CTF-0-I has the largest surface area and highest amount of impurity carbon.

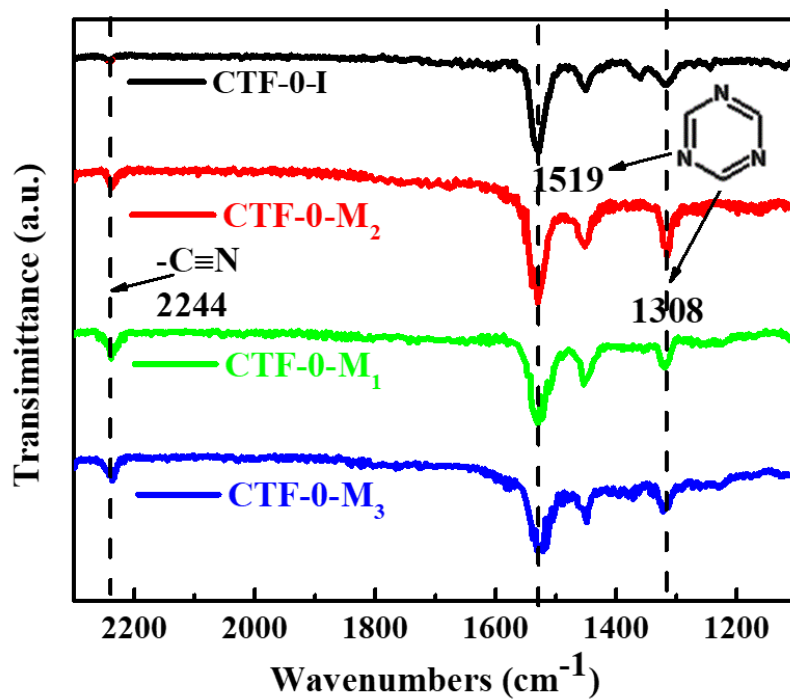


Figure 49. FTIR spectra of CTF-0-I prepared by the ionothermal method, and CTF-0-M<sub>1</sub>, CTF-0-M<sub>2</sub> and CTF-0-M<sub>3</sub> prepared by the microwave method.

### 5.3.2 Optical properties and the proposed band gap structure diagram

To further investigate optical properties and derive their band gap structure, photoluminescence spectra, UV/vis diffuse reflectance spectroscopy and valence-band XPS spectra were observed.

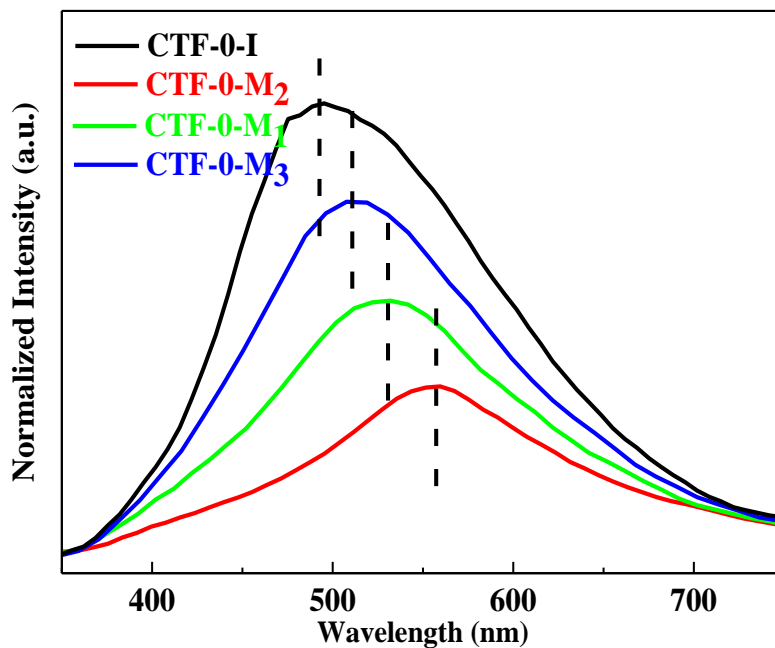


Figure 50. Photoluminescence spectrum of CTF-0-I, CTF-0-M<sub>1</sub>, CTF-0-M<sub>2</sub> and CTF-0-M<sub>3</sub>.

Photoluminescence spectra of the re-prepared polymers were recorded at solid state with 325 nm light excitation at room temperature shown in Fig. 50. The emission maxima are red-shifted from CTF-0-I to CTF-0-M<sub>2</sub>, as well as the PL intensities follow the trend of CTF-0-I > CTF-0-M<sub>3</sub> > CTF-0-M<sub>1</sub> > CTF-0-M<sub>2</sub>. Notably, this result is consistent with the increasing trend of the nitrogen elemental ratio in the elemental analysis, which suggests the increasing covalent triazine rings. Therefore, it is believed that the PL emission induced by the localised electronic transition in the triazine rings should play a critical role in the photoluminescence<sup>274-275</sup>. Such PL emission is believed to be affected by the ordered structure and carbon impurity with the smallest PL intensity on CTF-0-M<sub>2</sub> due to the least carbonisation impurities and the best ordered structure. This PL emission is related to the charge recombination, which is a crucial factor in the photocatalytic reaction<sup>276-277</sup>. In addition, the highest intensity of PL spectrum of CTF-0-I likely

results from highest amount of carbon impurities and the peaks shift is related to the charge states in the four polymers.

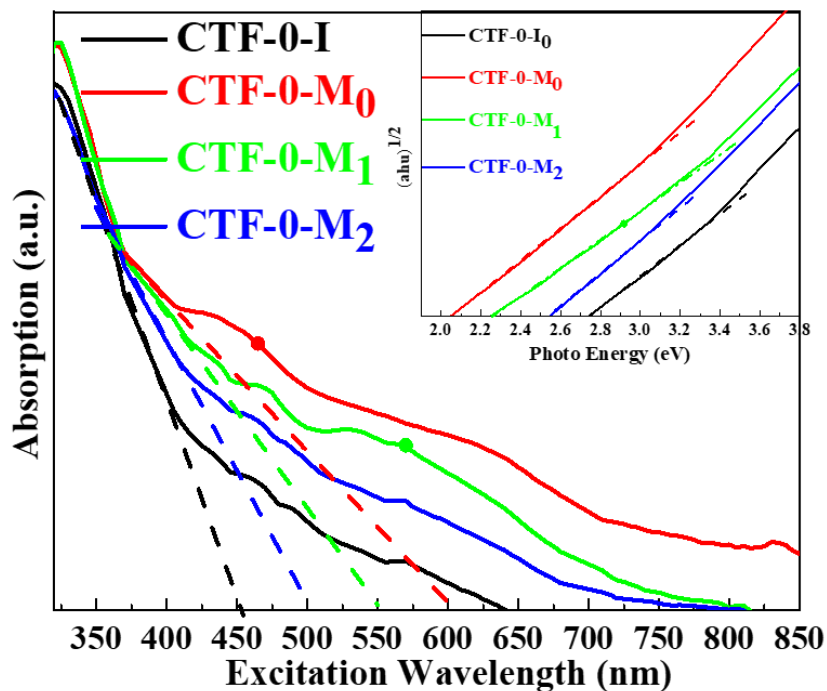


Figure 51. UV/Vis absorption spectra and optical energy band gap estimated by the method proposed by Wood and Tauc<sup>278</sup> of CTF-0-I, CTF-0-M<sub>1</sub>, CTF-0-M<sub>2</sub> and CTF-0-M<sub>3</sub>.

The absorbance spectroscopy (Fig.51) reveals that the absorption edge for CTF-0-I, CTF-0-M<sub>2</sub>, CTF-0-M<sub>1</sub> and CTF-0-M<sub>3</sub> are located at around 450, 600, 550 and 500 nm respectively, which is consistent with the trend of the PL emission maxima of these samples shown in Fig. 50. In addition, the materials CTF-0-Ms prepared by the microwave method show enhanced the absorption intensity in the visible region compared to the CTF-0-I, favouring photogenerated electron formation under visible light irradiation. Among all the samples, CTF-0-M<sub>2</sub> shows the

most red-shift absorption, which is due to the ordered structure as proved by the XRD, NMR and FTIR. Based on the Kubelka-Munk function, their band gaps are calculated to be 2.76, 2.07, 2.25 and 2.48 eV respectively. To estimate the relative positions of their CBM and VBM, the position of the VBM of these polymers were also measured by valence band XPS (Fig. 52). For CTF-0-M<sub>2</sub>, the VBM negatively shifts toward the vacuum level compared to CTF-0-I. Correspondingly, the value of the energy difference between the CTF-0-M<sub>2</sub> and CTF-0-I peaks is 0.81 eV, and the differences for CTF-0-M<sub>1</sub> and CTF-0-M<sub>3</sub> when compared with CTF-0-I are 0.58 eV and 0.08 eV, respectively. Furthermore, the flat band positions of all the materials are derived from the extrapolation of Mott-Schottky plots at different frequencies shown in Fig. 53. They are determined to be -0.58, -0.65, -0.70 and -0.38 eV vs. Ag/AgCl for CTF-0-I, CTF-0-M<sub>1</sub>, CTF-0-M<sub>2</sub>, and CTF-0-M<sub>3</sub>, respectively. Given the band gap obtained from UV/vis spectra and the flat band positions, the valence bands of them should be located at 2.18, 1.60, 1.37 and 2.10 eV, respectively, as shown in Fig. 54, which are consistent with the trend of the valence band measurement by XPS. Apparently, the ordered surface shifts the valence band of CTF-0-M<sub>2</sub> upward. Correspondingly, CTF-0-M<sub>2</sub> shows the lowest driving force for water oxidation reaction, then CTF-0-M<sub>1</sub>, next CTF-0-M<sub>3</sub>, while CTF-0-I has the strongest over potential for oxidation reaction.

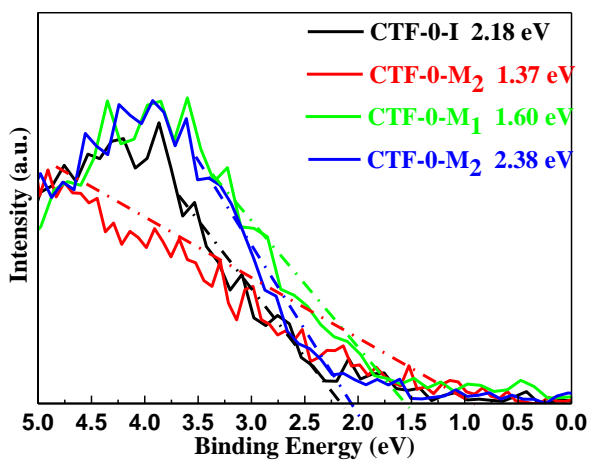


Figure 52. Valence-band XPS spectra of CTF-0-I, CTF-0-M<sub>1</sub>, CTF-0-M<sub>2</sub> and CTF-0-M<sub>3</sub>.

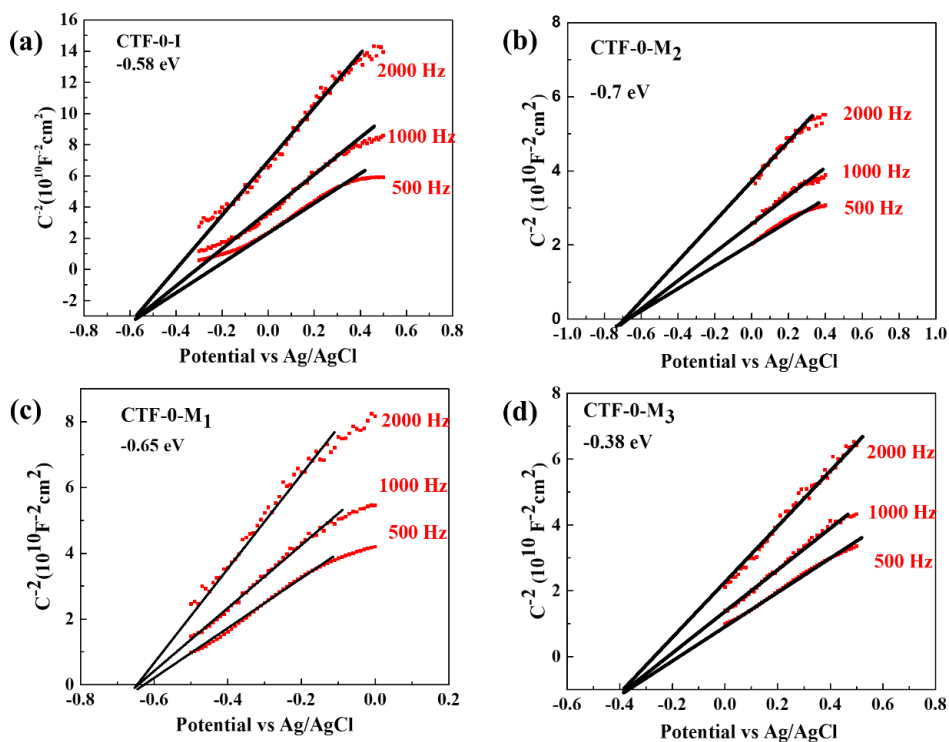


Figure 53. Mott-Schottky plots of the CTF-0-I (a), CTF-0-M<sub>2</sub> (b), CTF-0-M<sub>1</sub> (c) and CTF-0-M<sub>3</sub> (d) electrode in 0.1 M Na<sub>2</sub>SO<sub>4</sub> at 2k, 1k and 0.5k Hz under the dark condition.

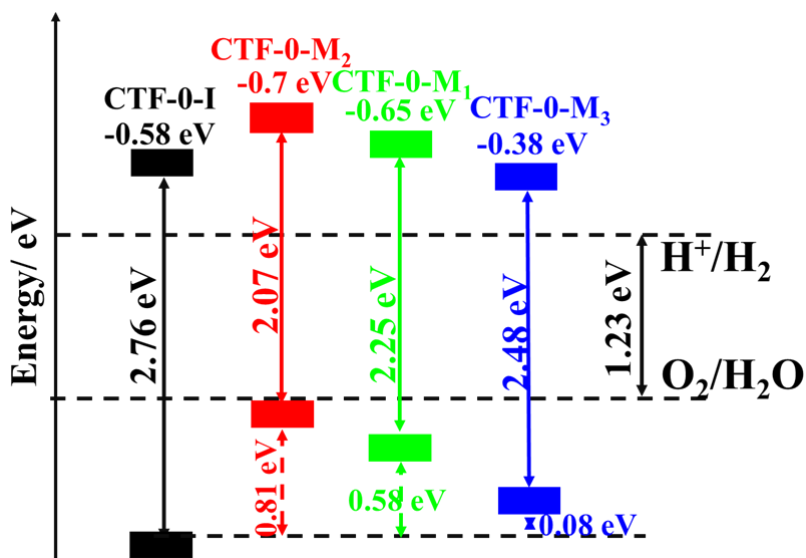


Figure 54. Band structure diagram of CTF-0-I, CTF-0-M<sub>1</sub>, CTF-0-M<sub>2</sub> and CTF-0-M<sub>3</sub>.

Combined with the results from optical measurements, a schematic illustration of band structure of these materials is shown in Fig. 54. It should be noted that CBM position of CTF-0-M<sub>2</sub> is the highest, while the VBM position of CTF-0-I is the lowest. The change of the VBM position can be attributed to the interlayer coupling of valence electrons<sup>208</sup>, which will be explained in details in the below calculation discussion. Generally, the photocatalytic efficiency is affected by the energy level of electron/holes. The larger the difference between the CBM and the H<sup>+</sup>/H<sub>2</sub> potential (or the VBM and the O<sub>2</sub>/H<sub>2</sub>O potential), the higher the reduction (oxidizing) power. Therefore, CTF-0-M<sub>2</sub> and CTF-0-I indicate the strongest reducing and oxidizing capability, respectively. Whereas, CTF-0-M<sub>2</sub> is not favourable for water oxidation due to that its VBM is very close to the water oxidation potential, which could not provide enough driving force for oxygen production.

### 5.3.3 Photocatalytic performance and stability

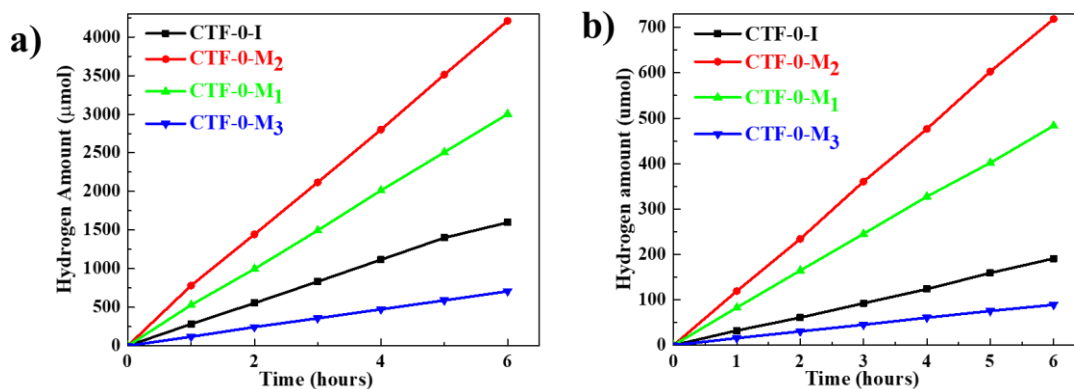


Figure 55. The time course of the H<sub>2</sub> production for CTF-0-I and CTF-0-Ms polymers under (a) full arc and (b) under visible light irradiation ( $\lambda > 420$  nm).

Following the successful preparation of the predicted materials and their structural and optical characterization, their photocatalytic hydrogen and oxygen evolution performance were tested shown in Fig. 55 and 56. The performance of all polymers for H<sub>2</sub> production was investigated with 3 wt% Pt as a cocatalyst and TEOA as a sacrificial electron donor. It is noted that the H<sub>2</sub> evolution rate measured here on CTF-0-M<sub>2</sub> is the highest among these polymers, up to 701 μmol/h (Fig. 55a), which is six times more than CTF-0-M<sub>3</sub>, the lowest one of 116 μmol/h. CTF-0-M<sub>2</sub> is also very active under visible light irradiation, reaching at 103 μmol/h (Fig. 55b), which is around seven times more than CTF-0-M<sub>3</sub> of 15 μmol/h. The turnover number, in terms of reacted electrons relative to the amount of Pt loaded on the surface of the sample, reaches 726 after running the experiment 6 h, indicating that the reaction occurs catalytically.

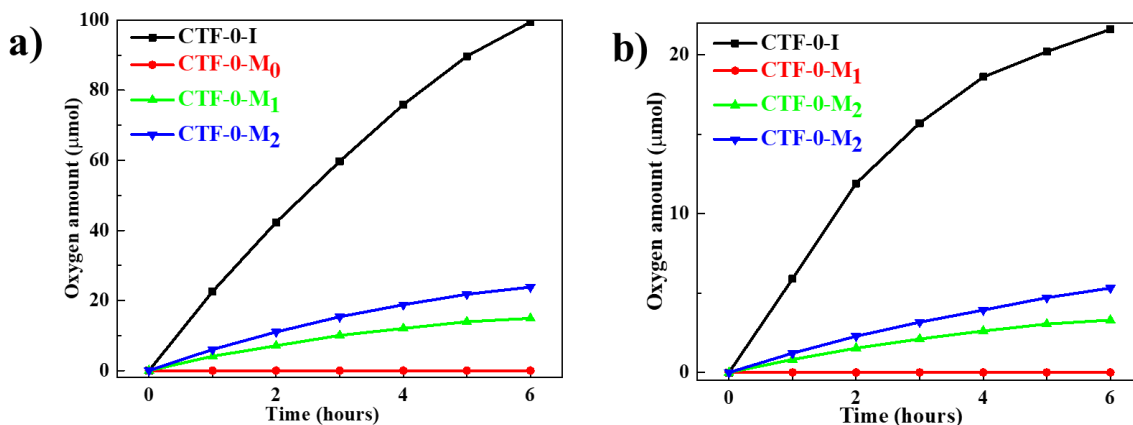


Figure 56. The time course of the O<sub>2</sub> evolution production for CTF-0-I and CTF-0-Ms polymers under (a) full arc and (b) under visible light irradiation ( $\lambda > 420$  nm).

On the other side, the activity of these polymers for O<sub>2</sub> production was measured without cocatalysts but in the presence of AgNO<sub>3</sub> as sacrificial electron scavenger. CTF-0-I shows the best performance on O<sub>2</sub> evolution both under full arc and visible light irradiation (22.6 and 5.9 μmol in the first hour respectively in Fig. 56a and d), which is six times more than CTF-0-M<sub>2</sub> of the lowest rate of 4.1 and 0.8 μmol in the first hour under full arc and visible light irradiation respectively. The photocatalytic activity for water reduction and oxidation could be well correlated to the band positions as shown in Fig. 54. Deeper the VBM, higher the water oxidation rates and more negative the CBM, higher the water reduction rates. The relatively large surface area of 5.13 m<sup>2</sup>/g of CTF-0-I versus 0.1 m<sup>2</sup>/g for CTF-0-Ms also favours its photocatalytic efficiency as providing more active sites, while there is no oxygen generated on CTF-0-M<sub>2</sub> under the same reaction condition due to its VBM too closed to the water oxidation potential.

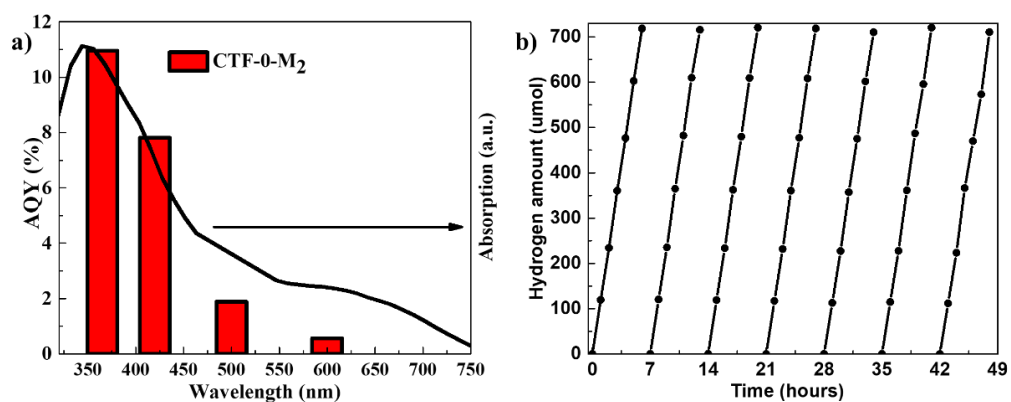


Figure 57. (a) Apparent quantum yield (AQY) for  $H_2$  production and (b) stability test of CTF-0- $M_2$  at atmospheric pressure under nearly one sun irradiation conditions. The seven cycles were under ambient conditions ( $\lambda > 420$  nm irradiation).

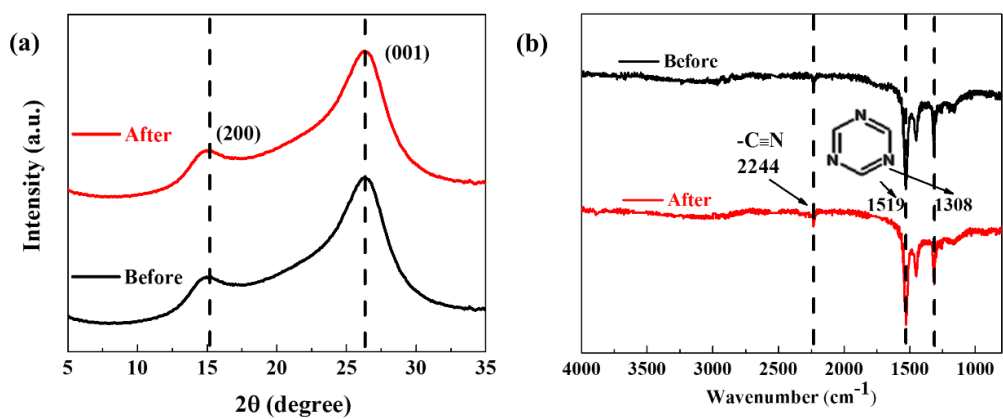


Figure 58. XRD patterns (a) and FTIR spectra (b) of CTF-0- $M_2$  before and after photocatalyst reaction.

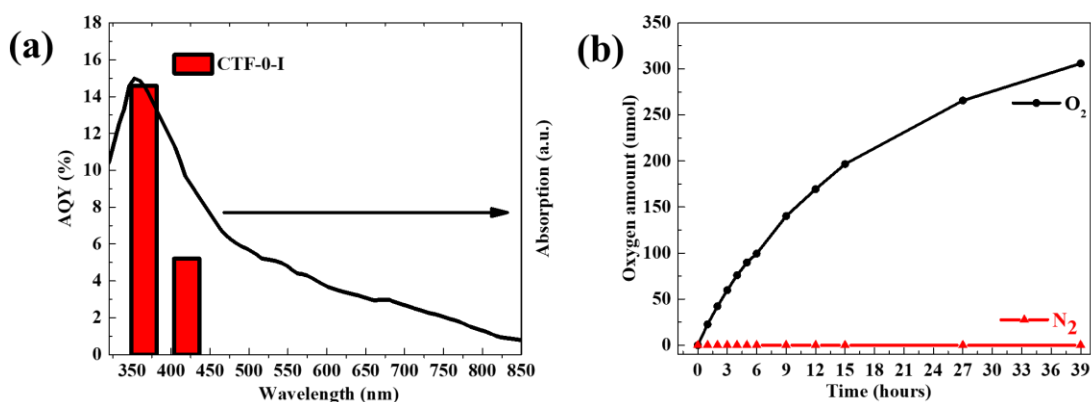


Figure 59. (a) Apparent quantum yield (AQY) for O<sub>2</sub> production and (b) stability test of CTF-0-I at atmospheric pressure under ambient conditions.

To further prove that the reaction is driven by light absorption, the AQY of H<sub>2</sub> generation of CTF-0-M<sub>2</sub> was examined with band-pass filters of different wavelengths. After seven runs, the reproducible AQY of CTF-0-M<sub>2</sub> is 11.0% at 365 nm and 7.8% at 420 nm. At 500 nm, the AQY of 2.0% is achieved and H<sub>2</sub> can also be produced even at 600 nm (Fig. 57a). Continuous H<sub>2</sub> evolution with no noticeable deactivation of the CTF-0-M<sub>2</sub> is clearly observed for nearly 50 hours as shown in Fig. 57b. Totally, around 4900 μmol H<sub>2</sub> is produced during these seven cycles, leading to an extremely high turnover number (TON) of 726 over platinum cocatalysts. The XRD patterns and FTIR spectra of the 50-h run CTF-0-M<sub>2</sub> are similar to those of the fresh sample shown in Fig. 58, indicating that the chemical structure of the photocatalyst remains unchanged after photocatalytic reactions. Interestingly, the AQY of O<sub>2</sub> evolution of CTF-0-I shows 14.6% at 365 nm and 5.0% at 420 nm (Fig. 59a). As shown in Fig. 59b, it is clear that CTF-0-I is capable of producing O<sub>2</sub> continuously over 39 h, obtaining 305.9 μmol totally even without any modification. It should be also noted that N<sub>2</sub> evolution could not be detected in the case of CTF-0-I shown in Fig. 59b, indicating relatively good stability of this material. The rate of O<sub>2</sub> evolution decreases during

the reaction as a result of the deposition of metallic silver on the surface of CTF-0-I to shield incident light and turn the sample black. There is no noticeable difference in the XRD and FTIR spectra of the sample before and after reaction shown in Fig. 60, except for a diffraction at *ca.* 38° after the reaction in XRD pattern (Fig. 60a) attributed to metallic Ag. The XPS spectra of CTF-0-I before and after the reaction (Fig. 61) is also consistent with the observation of the Ag deposition generated by the Ag<sup>+</sup> reduction, which is a typical behaviour in the photocatalytic water oxidation when using Ag<sup>+</sup> as an electron scavenger<sup>264, 279-280</sup>. These results indicate excellent stability of the CTF-0-M<sub>2</sub> and CTF-0-I for photocatalytic water reduction and oxidation, respectively.

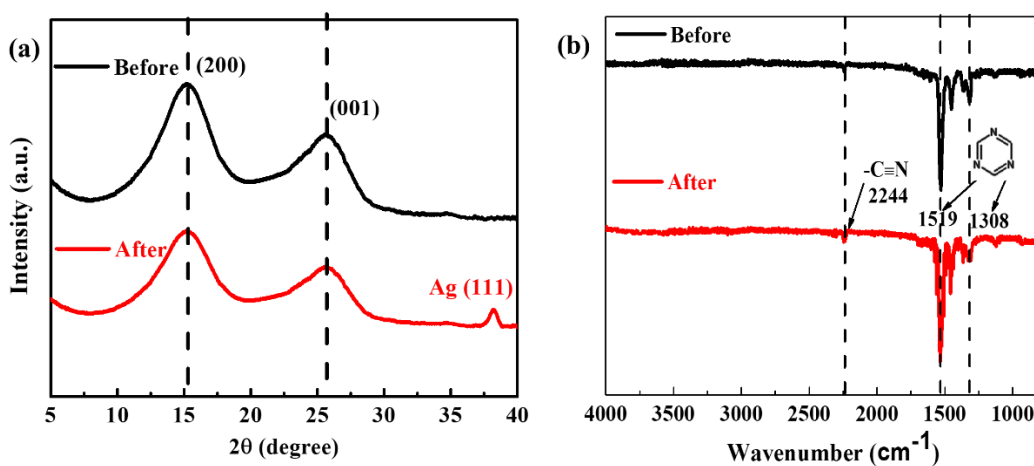


Figure 60. XRD patterns (a) and FTIR spectra (b) of CTF-0-I before and after photocatalyst reaction.

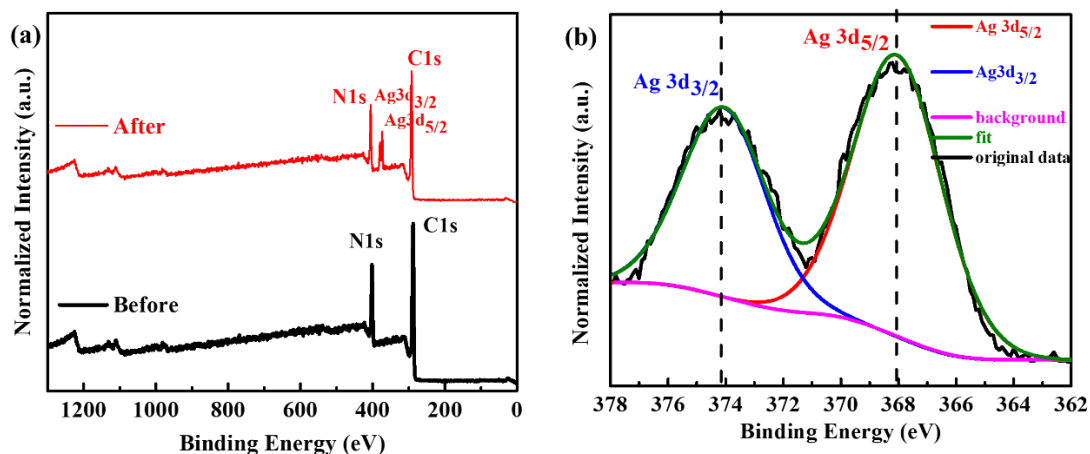


Figure 61. XPS survey spectra of CTF-0-I before and after photocatalyst reaction (a) and Ag 3d XPS spectra of CTF-0-I after photocatalytic reaction. Charge referenced to adventitious C1s peak at 284.8eV.

### 5.3.4 Understanding the electronic characteristics and the photocatalytic kinetics

To further understand the effects of triazine ring and benzene ring on the electronic characters of the framework, the charge distributions based on the optimised structure of the cluster model CTF-0 were investigated by density functional theory calculations in collaboration with Xiaoyu Han in Chemistry Department UCL. The CBM is contributed by triazine acceptor unites and the hydrocarbon portion of the benzene units shown in Fig. 62a. The electrons from  $p_x$  and  $p_y$  orbitals of both nitrogen and carbon atoms in the triazine ring and partial carbon atoms in the benzene rings preferentially determine the CBM. On the other side, the VBM is only concentrated over the triazine donors, which is localised by the electrons from  $p_z$  orbitals of nitrogen atoms shown in Fig. 62c. The energy level diagram of the single sheet CTF-0 is shown in Figure 62b. The simulated CBM and VBM of CTF-0 lie at -3.65 and -6.22 eV (vs. vacuum) respectively. Compared with the redox potential of water reduction (-4.44 eV vs. Vacuum) and oxidation (-5.67 eV vs. Vacuum), it

has enough driving force for both hydrogen and oxygen generation. Obviously, the VBM is more feasibly influenced by the concentration of nitrogen in the sample. The N content is 20.0%, 26.3%, 25.3% and 24.8% for CTF-0-I, CTF-0-M<sub>2</sub>, CTF-0-M<sub>1</sub> and CTF-0-M<sub>3</sub> respectively in Table 5. Hence, I speculate that the proposed VBM shown in Fig. 54 shift down as the N content decreases, leading to the larger band gap based on the smaller change of the CBM. Generally speaking, the photocatalytic efficiency depends on the numbers of electrons/holes having higher potential than the water reduction/oxidation potential. The larger difference, the higher the reducing/oxidizing power. Therefore, the downwards shift of absolute VBM from CTF-0-M<sub>2</sub> to CTF-0-I indicates the oxidizing capability is strengthened, which is more favourable for oxygen production. At the same time, the decrease of nitrogen content results in the significant widening of the band gap and thus restrain the capability to reduce water into H<sub>2</sub>. All this is in good agreement with the experimental findings.

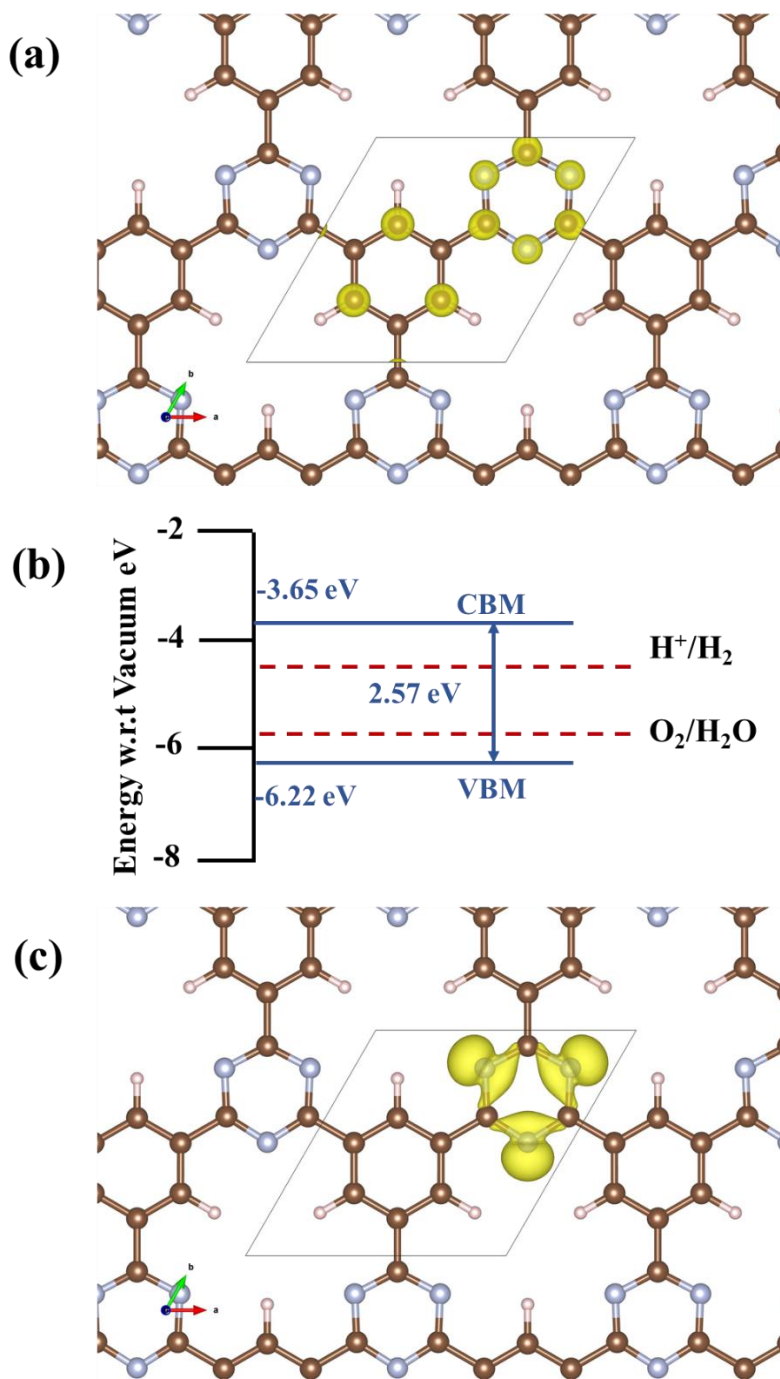


Figure 62. The Spatial distribution of the CBM (a) and the VBM (c), and the band alignments (b) of CTF-0 estimated by DFT calculations. All the energy is calculated with reference to the vacuum level. Carbon, nitrogen and hydrogen in the structural models are shown as brown, baby blue and pale pink spheres, respectively.

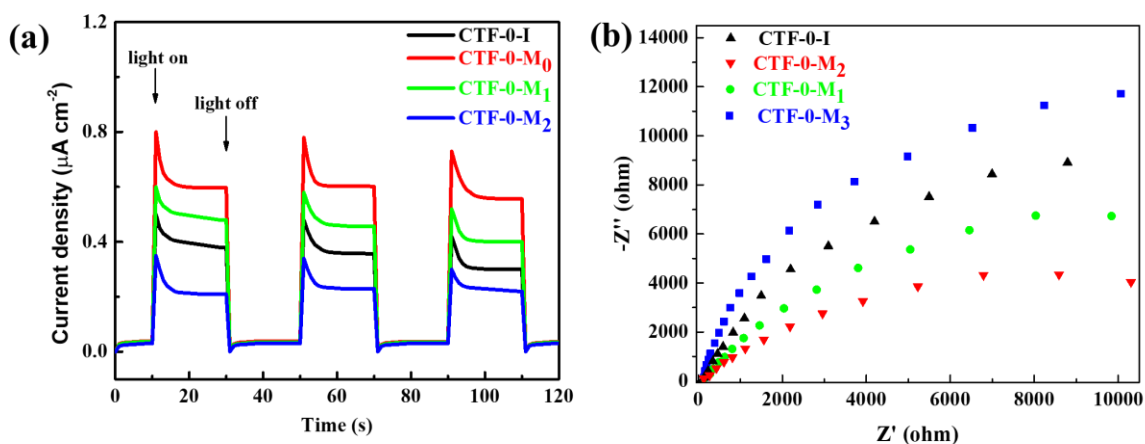


Figure 63. The periodic on/off photocurrent response (a) and Nyquist plots (b) of CTF-0-I, CTF-0-M<sub>1</sub>, CTF-0-M<sub>2</sub> and CTF-0-M<sub>3</sub> electrodes in 0.1 M Na<sub>2</sub>SO<sub>4</sub> with 0 V bias versus Ag/AgCl.

To uncover the kinetics of the photocatalysis in the CTF-0s, the photocurrent responses and electrochemical impedance spectroscopy (EIS) of CTF-0-I, CTF-0-M<sub>1</sub>, CTF-0-M<sub>2</sub> and CTF-0-M<sub>3</sub> were explored by an electrochemical analyser (IVIUM Technologies). Fig. 63a shows the photocurrent curve generated by the electrodes for several on-off cycles of irradiation. The photocurrent goes down to zero rapidly once the light turns off while the photocurrent will return to a steady value when the light turns on again, which is repeatable, indicating the high photostability of the samples. The CTF-0-M<sub>2</sub> photoelectrode shows the highest photocurrent intensity over other photoelectrodes, indicating that the high-polymerised interlayer structure of CTF-0-M<sub>2</sub> can efficiently suppress charge recombination by improving the interlayer charge transfer under visible light irradiation. And the photocurrents follow the order: CTF-0-M<sub>2</sub> > CTF-0-M<sub>1</sub> > CTF-0-I > CTF-0-M<sub>3</sub>, which is in good agreement with the photocatalytic performance for hydrogen generation. The charge transfer resistance was investigated by EIS. Fig. 63b reveals that the Nyquist plots arc radius of CTF-0-M<sub>2</sub> is much smaller than other samples, suggesting the

lower electric charge transfer resistance and the faster interlayer photoinduced electron transfer. This trend is consistent with the photocurrent results. Above all, the CTF-0-M<sub>2</sub> showed the highest photocatalytic activity of water reduction than other samples, probably because of the narrowest band gap and most negative CBM, as well as the most efficient transport of the photoinduced electrons in the ordered-interlayer structure. These interesting results from two polymers indicate a potential Z-scheme for water splitting, which will be a future work.

### 5.3 Conclusions

In summary, polymeric covalent triazine frameworks as a tunable and non-metal photocatalysts were synthesised by microwave and ionothermal methods, where the triazine units can be controlled by the precursor concentration and the preparation method. The higher amount of nitrogen or triazine unites results into more negative VBM, or the higher amount of benzene unites, the lower VBM position, proved by the modelling results as the triazine unites dominate the VB.

The covalent triazine framework CTF-0-M<sub>2</sub> produced by the microwave method with the best ordered interlayer structure and the highest amount of triazine unites shows the best photocatalytic hydrogen evolution under both UV/vis and visible light irradiation, resulting into 7.8% AQY at 420 nm and 2.0% at 500 nm. The superior performance is ascribed to the narrowest bandgap, efficient interlayer charge transfer and most negative CBM.

CTF-0-I synthesised by ionothermal method with the highest amount of benzene units exhibits the best photocatalytic water oxidation performance under the same light irradiation condition, resulting into 14.6% AQY at 365 nm and 5.0% at 420 nm, which is due to the deepest VBM and the relatively large surface area. Thus, both efficient half reaction photocatalysts have been

obtained. These triazine moieties in principle can be readily tuned to further study their application in the overall water splitting using a Z-scheme pathway and explore the mechanism of the water oxidation and reduction to enhance their light harvesting ability.

Compared with the results achieved in the chapter 4, one can find for water oxidation, CTF-0-M<sub>2</sub> is the best polymer with a AQY of 7.8% at 420 nm and for H<sub>2</sub> production, CTF-0-I is the best with a AQY of 5.0% at 420 nm for O<sub>2</sub> production. This is due to the relatively narrow bandgap, efficient interlayer charge transfer and suitable bandgap positions.

## 6 Chapter 6

### Overall water splitting on the selected CTF-0 polymers

Solar-driven water splitting into simultaneous H<sub>2</sub> and O<sub>2</sub> production using photocatalysts is an ideal pathway to supply the clean, storable, and renewable source of energy to tackle the global challenge of energy and environmental issue in the future. Although, many inorganic semiconductor photocatalysts have been explored for this purpose, the photocatalytic activities of several kinds of organic materials are intriguing due to their tailorable structure, electronic properties, and diverse synthetic modularity. In particular, covalent triazine frameworks were proved by me and others to be a new family of photocatalysts for water splitting in the presence of sacrificial reagents, based on their activity in half reactions observed in the Chapter 4 and 5. While the use of covalent triazine frameworks in overall water splitting in the absence of sacrificial agents have been much less reported. To achieve such potential, I will decorate different cocatalysts on the surface of the covalent triazine framework CTF-0, which can effectively increase the photocatalytic activity and adjust the ratio of H<sub>2</sub> and O<sub>2</sub> production from pure water by increasing light absorption ability, the separation and transfer of photogenerated charged carriers, as well as enhancing the stability of the photocatalysts.

#### 6.1 Introduction

Photocatalytic water splitting into H<sub>2</sub> and O<sub>2</sub> is a highly promising pathway towards clean and renewable energy supply of the future<sup>148, 281</sup>. The ultimate goal to this end is to develop an efficient, low cost and stable photocatalyst available for overall water splitting under visible light irradiation without using sacrificial agents and external bias<sup>282</sup>. However, it still remains

challenging to find a single photocatalyst material (one-step system) which processes (I) a sufficiently narrow bandgap ( $< 3$  eV) to harness visible photons, (II) suitable band-edge potentials for overall water splitting (*i.e.*, simultaneous production of  $H_2$  and  $O_2$ ), (III) a high level of stability against photocorrosion and (iv) relatively low cost<sup>64</sup>. In this regard, various inorganic semiconductors have been explored for overall water splitting, with few successful cases, but it is possible when composed with other materials, such as  $h/\text{Cr}_2\text{O}_3$ -modified  $\text{Ta}_3\text{N}_5/\text{KTaO}_3$  and  $(\text{Ga}_{1-x}\text{Zn}_x)(\text{N}_{1-x}\text{O}_x)$ , which also indicate the significance of cocatalysts<sup>33, 283</sup>. Recently, conjugated polymers, particularly covalent carbon nitride ( $\text{C}_3\text{N}_4$ ) semiconductors, have been rapidly developed as a new type of photocatalyst for solar energy utilization, while the majority have been found to be active for  $H_2$  production in the presence of sacrificial reagents<sup>43, 127, 164, 284-286</sup>. Interestingly, it is found very recently that the selective creation of both  $H_2$  and  $O_2$  cocatalysts  $\text{PtO}_x$  as surface active sites on  $g\text{-C}_3\text{N}_4$  conjugated polymers via photodeposition could trigger the splitting of water into  $H_2$  and  $O_2$  gases in a stoichiometric ratio of 2:1 simultaneously, without using any sacrificial reagents<sup>287</sup>.

Another group of covalent triazine frameworks (CTFs) were recently reported for half reaction of water splitting in the presence of relevant sacrificial reagents<sup>208, 288-289</sup>, indicating that such CTFs could be good candidates for pure water splitting. However, to achieve this potential is rather challenging. As discussed in Chapter 5, CTF-0s showed activity for both the production of  $H_2$  and  $O_2$  in the presence of sacrificial reagents and is the best photocatalyst for water oxidation among all the polymer photocatalysts samples<sup>208</sup>. The oxygen evolution process is more challenging than proton reduction to hydrogen, due to both  $4e/4H^+$  electrochemistry and  $\text{O}=\text{O}$  bond formation, which is the rate determining step in water splitting.<sup>22, 181</sup> Taking into account these and the performance of CTF-0 synthesised by the ionothermal method for water oxidation, it was chosen

as a single photocatalyst for the overall water splitting with loading cocatalysts Pt and  $\text{CoO}_x$ . To the best of the knowledge, such one-step overall water splitting by CTF-0 photocatalysts without any sacrificial agent has not been reported so far.

## **6.2 Methodology**

### **6.6.1 Materials and Synthesis of samples**

The materials and synthesis process of CTF-0 samples was same as described in Chapter 5.2.1 and 5.2.2, by the ionothermal method.

### **6.2.2 Characterizations**

The Fourier transform infrared (FTIR) spectra were recorded on a Perkin-Elmer 1605 FT-IR spectrometer in the wavelength range from 400-4000  $\text{cm}^{-1}$  with a resolution of 0.5  $\text{cm}^{-1}$ . UV-Vis reflectance spectroscopy was performed on a Shimadzu UV-Vis 2550 spectrophotometer fitted with barium sulphate as a referent. The X-ray photoelectron spectroscopy (XPS) data were obtained using a ThermoScientific XPS K-alpha surface analysis machine using an Al source. Analysis was performed using Casa XPS. Transmission electron microscopy (TEM) and energy dispersive X-ray spectroscopy (EDX) were performed on a JEOL 100k eV system.

### **6.2.3 Cocatalysts depositions**

The Co cocatalyst was loaded on the photocatalyst surface by wet impregnation method. In a typical synthesis, an aqueous suspension of CTF-0 was first prepared by dispersing 200 mg CTF-0 into 50 mL deionised water with sonication and was then transferred into oil bath at 70 °C. Then 7 mg  $\text{Co}(\text{NO}_3)_2$  was added into the CTF-0 aqueous dispersion and kept stirring for 18 h to form

homogeneous solution. The mixture was then dried by evaporation and thermal treated in muffle furnace at 350 °C for 1 h.

The Pt cocatalysts was loaded on the photocatalysts surface by in-situ photo-deposition method. Firstly, 100 mg photocatalyst powder was dispersed in deionised water (100 mL) contained 10% vol (10 mL) MeOH and 5% vol (5 mL) TEOA as the sacrificial agent. A certain amount of  $\text{H}_2\text{PtCl}_6$  (3 wt%, based on Pt atoms) was added into the solution. After 2-hour irradiation under 300 W lamp, the photocatalyst was filtered and washed with deionised water several times. Then the photocatalyst was dried at 60°C for 4 hours.

For preparing Pt/ $\text{CoO}_x$ @CTF-0, the procedure was to decorate  $\text{CoO}_x$  on the surface of CTF-0 as described above, and then load Pt on the  $\text{CoO}_x$ @CTF-0 by photodeposition method as illustrated above.

#### 6.2.4 Photocatalytic activity tests

The reactions were carried out in a Quartz top-irradiation reactor cell under the irradiation of a 300 W Xe lamp (*TrusTech PLS-SXE 300/300UV*). The hydrogen production was performed by dispersing 10 mg of photocatalyst powder in pure water (20 mL) contained 10% vol (2 mL) TEOA as the sacrificial agent. The oxygen production was performed by dispersing 10 mg of photocatalyst powder in pure water (20 mL) contained 0.01 M  $\text{AgNO}_3$  as the sacrificial agent. The overall water splitting was carried out by dispersing 10 mg of photocatalyst powder in pure water (20 mL). The reaction solution was evacuated 15 mins to completely remove the air prior to full spectrum irradiation. The temperature of reaction solution was at room temperature using a cooling water bath during the reaction. All the gas productions were analysed by gas chromatography (*Varian 430-GC, TCD, argon carrier gas 99.999%*).

### 6.2.5 Photoelectrochemical measurements

Measurements were performed on a photoelectrochemical analyser (IVIUM Technologies) with a standard three-electrode cell using a Ag/AgCl electrode (3 M KCl) and a Pt plate as a reference electrode and counter electrode, respectively. The working electrode was prepared as follows: 5 mg of sample was grounded and dissolved in 750  $\mu\text{L}$  distilled water, 250  $\mu\text{L}$  2-propanol and 10  $\mu\text{L}$  Nafion under sonication for 1 h to get a slurry and then the slurry was cautiously spread onto 2 cm  $\times$  2 cm FTO by a spin coater. After drying overnight on a hot plate at 250  $^{\circ}\text{C}$ , the electrodes were sintered at 400  $^{\circ}\text{C}$  for 30 min to improve adhesion. Sunlight was simulated on the working electrode with a 150 W xenon lamp (Newport) and AM 1.5 filter (Newport). The light intensity was calibrated using a calibrated crystalline silicon solar cell, equivalent to a global AM 1.5 illumination at 100 mW/cm<sup>2</sup>. Samples were illuminated from the back side (FTO substrate) and the mask-off irradiated area was 0.5 cm<sup>2</sup>. Electrochemical impedance spectra (EIS) were measured with 0.0 V bias versus AgCl/Ag.

## 6.3 Results and discussion

### 6.3.1 Structural characterizations

Both X-ray diffractograms and solid state <sup>13</sup>C NMR spectra of pure CTF-0 and cocatalysts loaded samples shown the typical pattern of CTF-0 as presented in Fig. 64 and Fig. 65. Two distinct peaks at 15 $^{\circ}$  and 26 $^{\circ}$  could be distinguished in the XRD spectra in Fig. 64, indicating some degree of extended order of the sample, while the intensity and width of the peaks could be influenced by the monomer/ZnCl<sub>2</sub> ratio and reaction time and temperature<sup>183</sup>. Even these peaks were too broad

to give a conclusive picture on the atomistic structure of CTF-0, the low-angle peak could be interpreted as the in-plane reflection (100) and the diffraction peak at  $\sim 26^\circ$  could be attributed to an inter-layer spacing between stacked sheets of 3.35 Å. There are some small peaks at  $19^\circ$ ,  $32^\circ$ ,  $37^\circ$  and  $39^\circ$  in the Pt/CoO<sub>x</sub>@CTF-0 sample, which do not exist in the CTF-0 sample and can be indexed to cobalt oxide particles<sup>290</sup>. The <sup>13</sup>C CP-MAS ssNMR (Fig. 65) illustrate the trimerization of the precursors was almost complete (the subsequent FTIR shows tiny residue of cyano species). The reason is that besides the three expected peaks at  $\delta = 170, 136, 114$  ppm ascribed to the three sp<sup>2</sup> carbons of the ideal CTF-0 frameworks, no obvious peaks of residual cyano groups were perceived at 110 ppm in the spectrum of both samples. Furthermore, only one peak at -121 ppm in both <sup>15</sup>N ssNMR spectra was observed in Fig. 66, which is assigned to the triazine moiety<sup>291</sup>, proving the stability of the materials before and after cocatalysts decoration. The FTIR spectra in Fig. 67 show the vibrational fingerprint of the triazine rings at 1308 and 1519 cm<sup>-1</sup>. The small peak of CTF-0 at 2244 cm<sup>-1</sup> belongs to the cyano groups, which has the similar height after decorating the cocatalysts on the photocatalysts. In a short summary, all these characterizations illustrate the chemical structures of the frameworks keep stable after cocatalysts decoration.

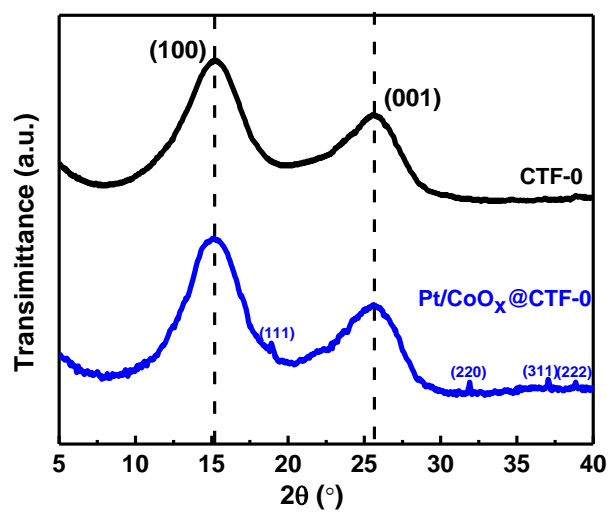


Figure 64. XRD patterns of CTF-0 and Pt/CoO<sub>x</sub>@CTF-0.

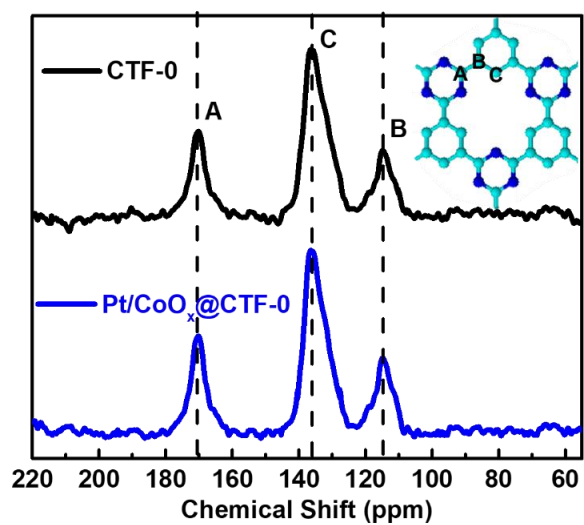


Figure 65. <sup>13</sup>C CP-MAS ssNMR spectra of CTF-0 and Pt/CoO<sub>x</sub>@CTF-0.

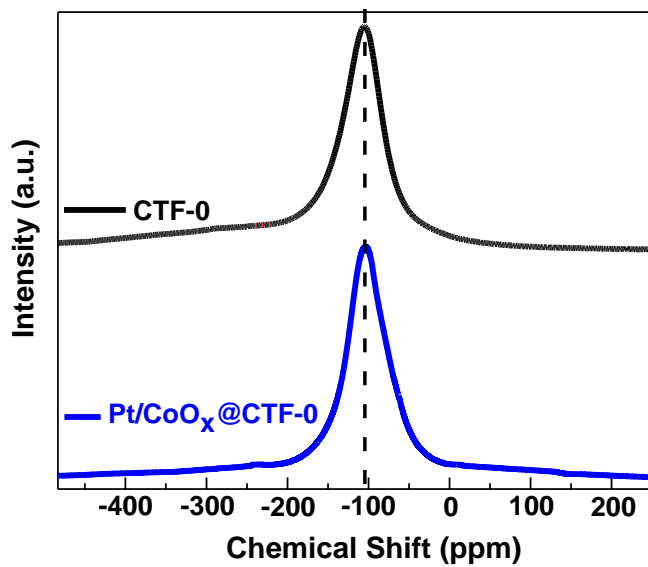


Figure 66.  $^{15}\text{N}$  CP-MAS ssNMR spectra of CTF-0 and Pt/CoO<sub>x</sub>@CTF-0.

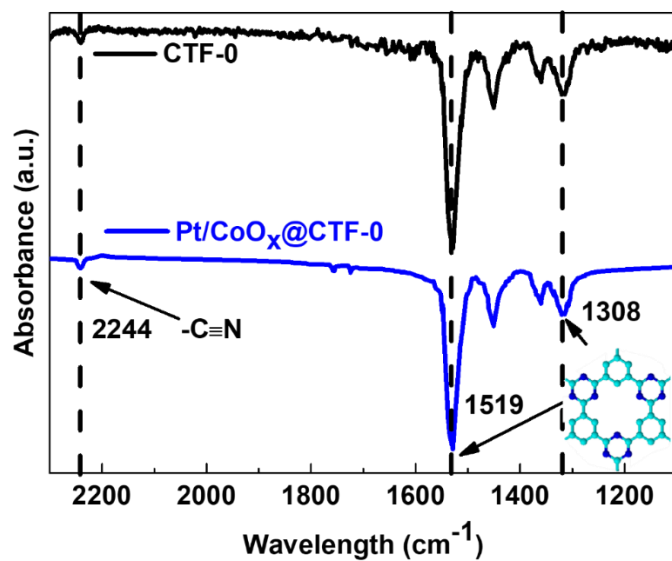


Figure 67. FTIR spectra of CTF-0 and Pt/CoO<sub>x</sub>@CTF-0.

To further examine the existence of the cocatalysts on the surface of the photocatalysts, XPS measurements were conducted. Obviously, the XPS survey of the CTF-0 samples only shows the peaks of C1s and N1s in Fig. 68, while the sample of Pt/CoO<sub>x</sub>@CTF-0s also have the peaks of Co 2p and Pt 4f, which locate at around 790 and 70 eV, respectively. A small amount of oxygen was also detected from the survey spectra, which was from the cocatalysts cobalt oxide. For the cocatalysts CoO<sub>x</sub>, the high-resolution XPS spectrum of Co 2p shows two major peaks with binding energies of 779.5 and 794.8 eV, corresponding to Co 2p<sub>3/2</sub> and Co 2p<sub>1/2</sub>, respectively (Fig. 69). The energy difference between the Co 2p<sub>3/2</sub> and Co 2p<sub>1/2</sub> splitting is around 15 eV, which indicates the existence of Co<sup>2+</sup> and Co<sup>3+</sup> and likely corresponds to the existence of Co<sub>3</sub>O<sub>4</sub><sup>292-293</sup>. The two small peaks at 784.9 and 800.2 eV are typical Co<sup>2+</sup> shakeup satellite peaks of Co<sub>3</sub>O<sub>4</sub>. Correspondingly, the deconvoluted XPS spectra for O 1s display two types of contributions for oxygen species in Fig. 70. The one peak at 529.7 eV is dominant and is corresponding to the cobalt oxides, and the other one at 531.1 eV indicates the presence of -OH species on the surfaces of cobalt oxide cocatalysts.<sup>293</sup> To investigate the electronic structures of Pt, the Pt 4f XPS spectra were measured in Fig. 71. The Pt 4f peak can be deconvoluted into two pairs of doublets. The deconvoluted peaks at 71.3 and 74.7 eV are ascribed to the 4f<sub>7/2</sub> and 4f<sub>5/2</sub> peaks of Pt<sup>0</sup>, respectively.<sup>294-295</sup> Similarly, the set of peaks at 72.7 and 76.1 eV are assigned to the 4f<sub>7/2</sub> and 4f<sub>5/2</sub> peaks of Pt<sup>2+</sup> (PtO or Pt(OH)<sub>2</sub>), respectively. A comparison of the relative areas of the integrated intensity of the Pt<sup>0</sup> and Pt<sup>2+</sup> peaks in Fig. 71 (the area ratio is 2.2:1) indicates that most of the Pt exists as Pt<sup>0</sup> in the cocatalysts, which will help H<sub>2</sub> evolution in the following overall water splitting. Moreover, TEM observation was carried out and shown in Fig. 72 to investigate the architecture of the cocatalysts on the surface of samples. It can be seen that the cocatalyst particles are homogeneously dispersed on the photocatalysts. The high resolution TEM image shows clear lattice fringes in the sample (Fig. 72b). The lattice spacing of Pt is 0.22 nm, corresponding to d(111)

value of fcc Pt<sup>296</sup>, and the lattice spacing of Co<sub>3</sub>O<sub>4</sub> is 0.24 and 0.20 nm, ascribed to (222) and (400) crystal planes of cubic Co<sub>3</sub>O<sub>4</sub><sup>297</sup>. Moreover, elemental mapping images also suggest that the Co and Pt atoms were uniformly dispersed on the surface of the CTF-0, as shown in Fig. 73. The TEM analyses together with the XPS results indicate the Pt and Co<sub>3</sub>O<sub>4</sub> particles were decorated on the surface of CTF-0 successfully. In kinetical theory, CTF-0 takes a role as a catalyst during the synthesis of Pt and Co<sub>3</sub>O<sub>4</sub> particles, which can significantly decrease the activation energy of both Pt and Co<sub>3</sub>O<sub>4</sub> generation reaction<sup>298</sup> as described in Fig. 74. Thus, most of the Pt and Co<sub>3</sub>O<sub>4</sub> particles will be produced on the interface between aqueous water and CTF-0, enhancing the adherence of Pt and Co<sub>3</sub>O<sub>4</sub> to the surface of CTF-0 during the synthesis. Thus, it is successful to load the Pt and Co<sub>3</sub>O<sub>4</sub> on the surface of CTF-0, consistent with the results of experimental characterisations discussed above.

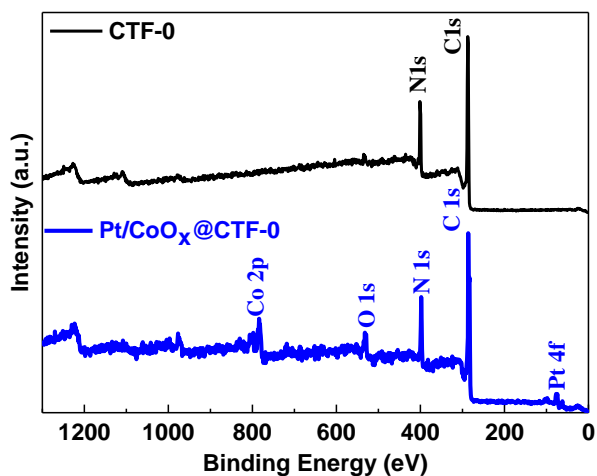


Figure 68. The XPS survey spectra of CTF-0 and Pt/CoO<sub>x</sub>@CTF-0.

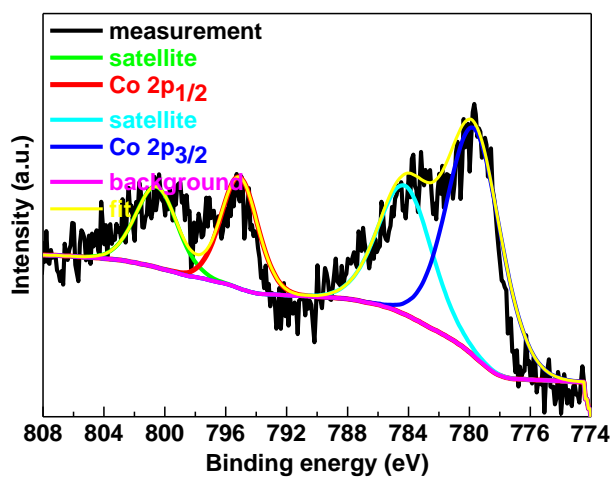


Figure 69. The Co 2p XPS spectra of Pt/CoO<sub>x</sub>@CTF-0.

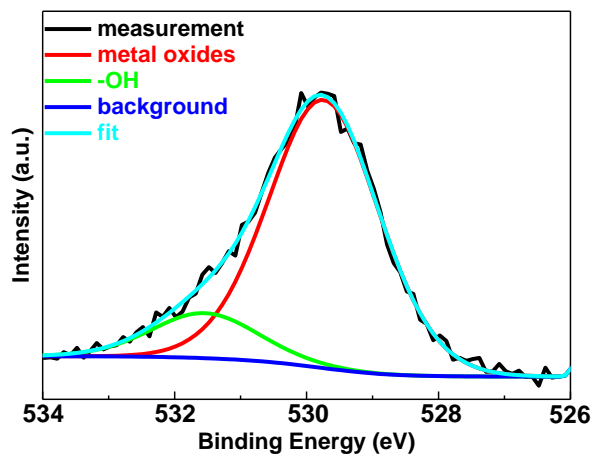


Figure 70. The O 1s XPS spectra of Pt/CoO<sub>x</sub>@CTF-0.

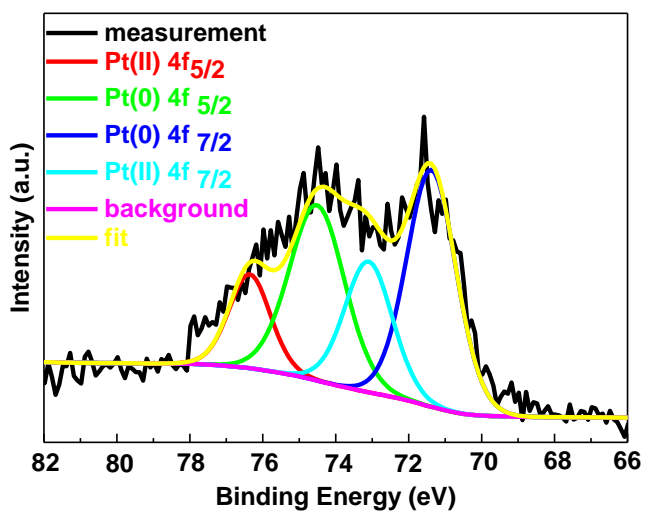


Figure 71. The Pt 4f XPS spectra of Pt/CoO<sub>x</sub>@CTF-0.

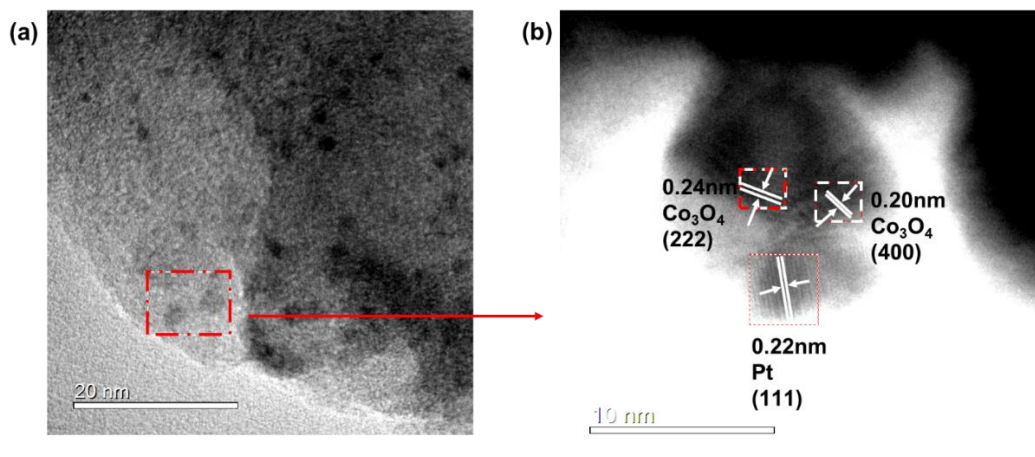


Figure 72. TEM (a) and HRTEM (b) images of Pt/CoO<sub>x</sub>@CTF-0.

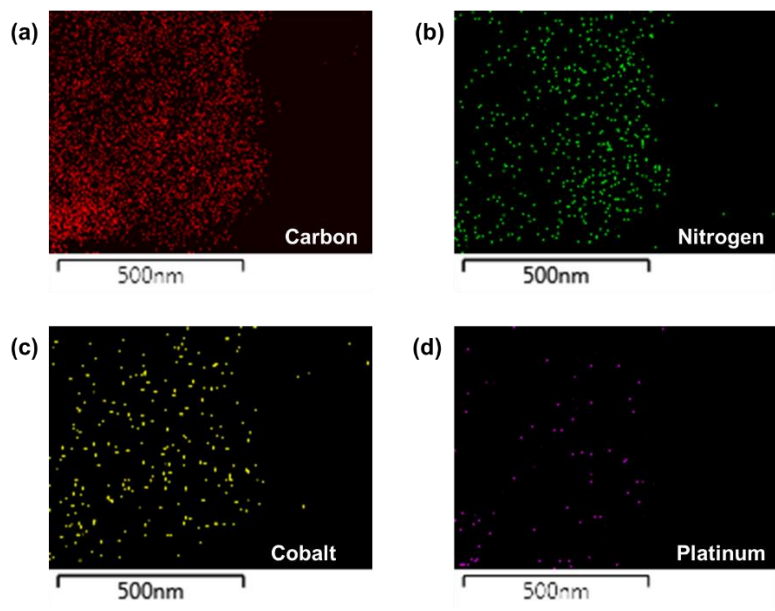


Figure 73. Elemental mapping images (a-d) of Pt/CoOx@CTF-0.

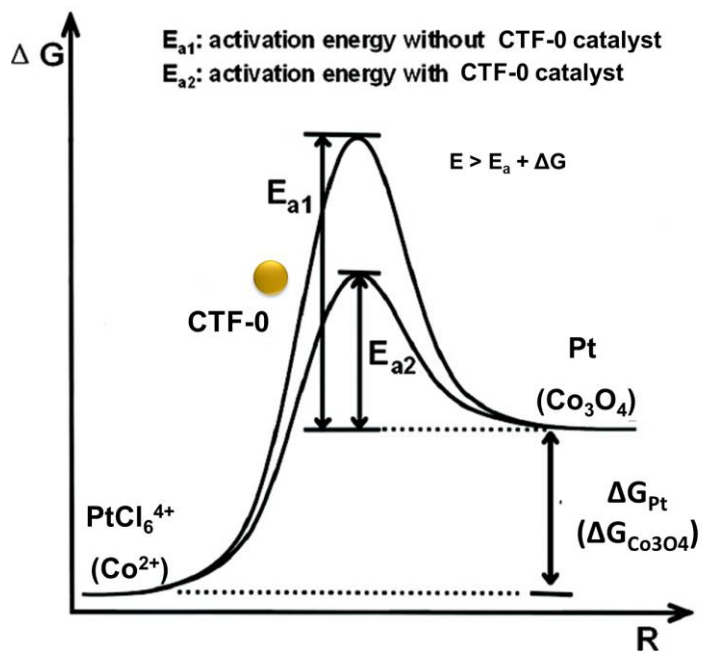


Figure 74. Schematic description of the role of CTF-0 catalyst in Pt and  $\text{Co}_3\text{O}_4$  generations, separately.  $E_{a1}$  and  $E_{a2}$  are the activation energy without and with CTF-0 catalysts in the reaction, respectively.  $\Delta G$  is the standard free energy for the reaction,  $E$  is the minimum energy required for Pt or  $\text{Co}_3\text{O}_4$  generation. CTF-0 catalysts can largely decrease the activation energy of the Pt and  $\text{Co}_3\text{O}_4$  generation, separately.

### 6.3.2 Photocatalytic activity

The half reactions of overall water splitting for H<sub>2</sub> and O<sub>2</sub> evolution were first tested and are shown in Fig. 75a and b, respectively. For comparison, pure CTF-0 was served as a reference. Obviously, CTF-0 could produce H<sub>2</sub> of 2262 μmol/(gh) with Pt as cocatalysts stably in the presence of TEOA as the sacrificial agent, extremely higher than that without Pt under full arc irradiation (Fig. 75a). On the other side, Co<sub>3</sub>O<sub>4</sub> decorated CTF-0 can produce the highest amount of O<sub>2</sub>, namely 365 μmol/g in the first hour, twice higher than pure CTF-0. Therefore, the decoration of both Pt and CoO<sub>x</sub> on CTF-0 has been explored to realise the overall water splitting into H<sub>2</sub> and O<sub>2</sub> and the results are shown in Fig. 75c and d. The pure CTF-0 (blank) sample exhibits no detectable activity toward overall water splitting. However, hydrogen and oxygen gases were detected when co-deposited Pt and Co<sub>3</sub>O<sub>4</sub> on the CTF-0 surface. This result demonstrates that the loading of cocatalysts is a critical step to induce the pure water splitting reaction. The stoichiometric ratio of hydrogen and oxygen equal to 2:1 was only achieved when 6 wt% or higher amount of Co<sub>3</sub>O<sub>4</sub> was loaded on the surface of the photocatalysts, indicating water oxidation is more challenging. Note that the oxygen evolution rate is slower than the theoretical value if hydrogen evolution rate is used as the reference. At the same time, nitrogen gas was also detected, when the loaded amount of Co<sub>3</sub>O<sub>4</sub> on the surface of the photocatalysts was smaller than the ideal amount of 6 wt%. This is reasonable as N<sub>2</sub> evolution was sometimes observed in photocatalytic reactions with nitrogen-containing photocatalysts, due to the decomposition of photocatalysts by the photogenerated holes<sup>299</sup>. However, the oxidative decomposition of a photocatalyst itself can be suppressed if enough oxidation catalytic active sites are provided by suitable cocatalysts, namely Co<sub>3</sub>O<sub>4</sub> in this research, which efficiently promoted the consumption of photogenerated holes by the oxidation of water into O<sub>2</sub>. Therefore, a typical time course of the simultaneous

evolution of H<sub>2</sub> and O<sub>2</sub> for the overall water splitting with 3 wt% Pt and 6 wt% Co<sub>3</sub>O<sub>4</sub> deposited CTF-0 without any sacrificial agent was showed in Fig. 75d. H<sub>2</sub> and O<sub>2</sub> evolution are observed only after turning on the light, confirming a photoactive response. The both gas evolutions show constant rates with an expected molar ratio of 2:1 for H<sub>2</sub>/O<sub>2</sub>. Moreover, the photocatalytic activity displays no noticeable reduce in a 18 h reaction, and the FTIR spectra of Pt/Co<sub>3</sub>O<sub>4</sub>@CTF-0 before and after the photocatalysis during the prolonged operation remain unchanged as shown in Fig. 76. All the above confirm the stability of the photocatalysts. These results suggest that the suitable amount of Pt and Co species on the surface of CTF-0 is of crucial significance for the photocatalytic overall water splitting.

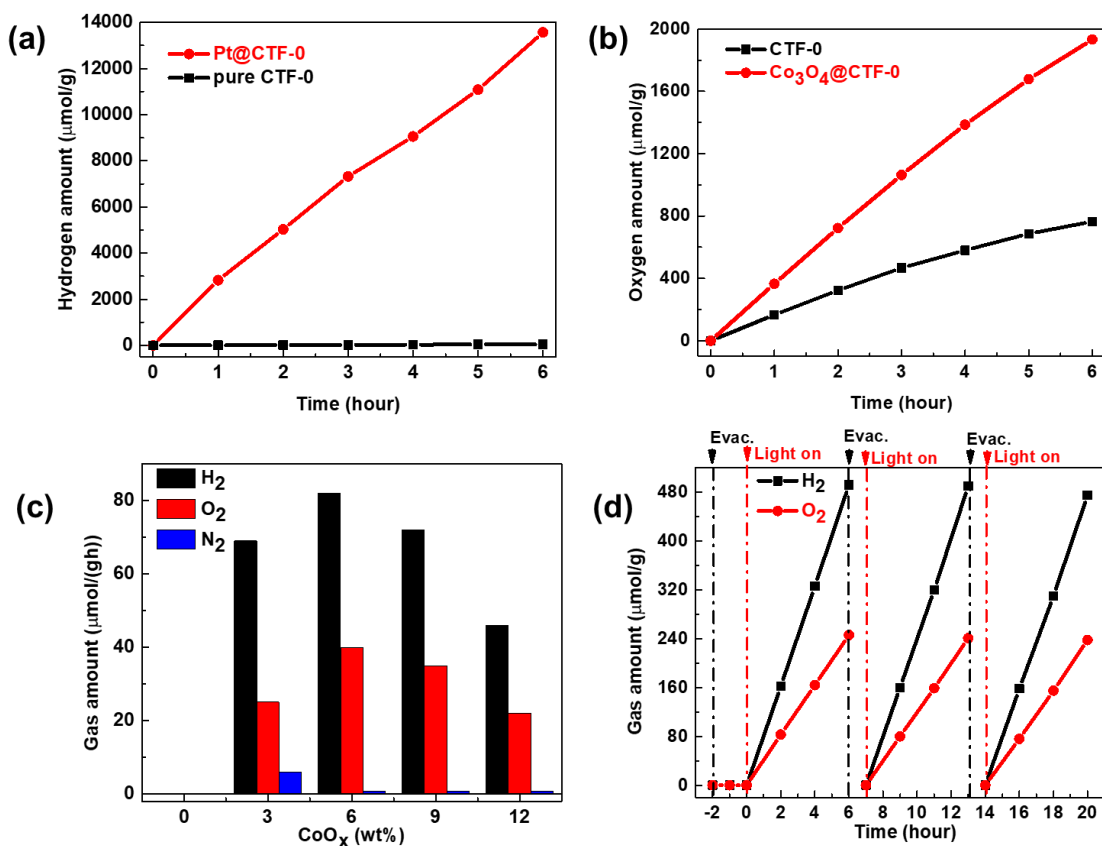


Figure 75. (a)  $H_2$  half reaction of pure and Pt-deposited CTF-0 with TEOA as the sacrificial agent, (b)  $O_2$  half reaction of pure,  $Co_3O_4$ -deposited CTF-0 with  $AgNO_3$  as the sacrificial agent, (c) Photocatalytic overall water splitting of different amounts of Co-loaded on CTF-0 with 3 wt% Pt as co-catalyst except for the blank one, (d) Cyclic runs of  $H_2$  and  $O_2$  production from pure water by 6 wt%  $Co_3O_4$  and 3 wt% Pt-deposited CTF-0. All the experiments were under full arc irradiation of a 300 W Xe lamp.

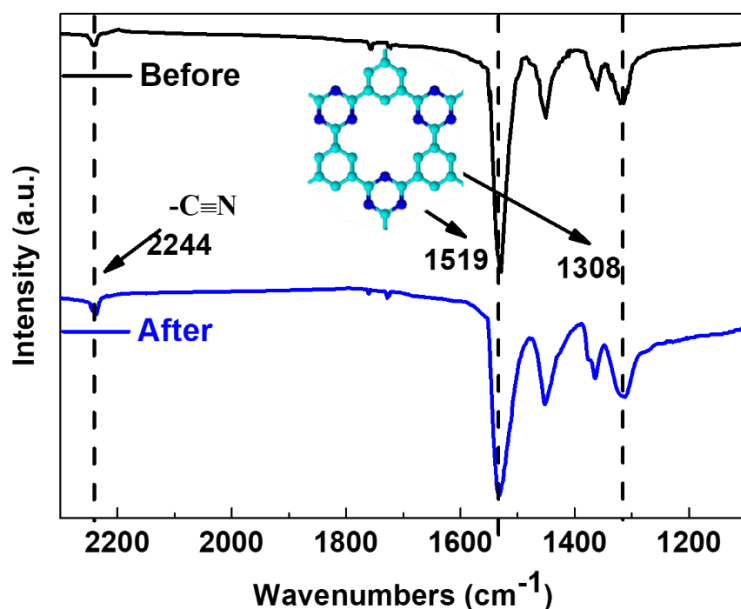
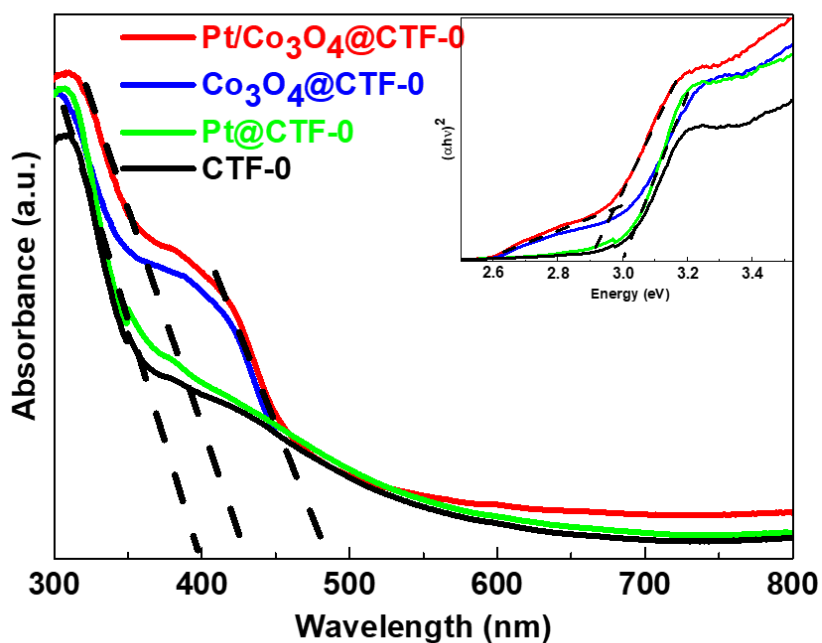


Figure 76. The FTIR spectra of Pt/ $Co_3O_4$ @CTF-0 before and after photocatalytic reaction.

### 6.3.3 Mechanism discussion

Efficient optical absorption and photocharge separation is of great importance for the photocatalytic reaction. As expected, the optical absorption is significantly increased on Pt/ $Co_3O_4$ @CTF-0, confirmed by the UV-vis diffuse reflectance measurements in Fig. 77. In the UV-vis spectra, the typical band edge of the CTF-0 photocatalyst is observed at around 400 nm. Correspondingly, the band gap of CTF-0 is calculated as 3.0 eV, observed from the Tauc plots of

the UV-vis absorption data. After coupling with Pt particles in Pt@CTF-0, the absorption edge has no discernible change, indicating that introduction of Pt cocatalysts does not affect the band structure. However, after loading cobalt oxide cocatalysts in  $\text{Co}_3\text{O}_4$ @CTF-0, there is an additional absorption edge at 480 nm, and the corresponding band gap is 2.6 eV. For the absorption edge at 480 nm, the absorption ( $\lambda < 500$  nm) were referred to ligand-metal charge transfer events  $\text{O}(-\text{II}) \rightarrow \text{Co}(\text{II})^{300}$ . As a result of decoration of both Pt and  $\text{Co}_3\text{O}_4$  on the surface of CTF-0, the UV-vis light absorption shows two sharp absorption edges at 420 and 480 nm and the corresponding band gaps were 2.9 and 2.6 eV. So, the two-bandgap absorption should be attributed to band gap absorption of CTF-0 and  $\text{Co}_3\text{O}_4$ . However, the absorption of  $\text{Co}_3\text{O}_4$  does not contribute to water splitting as no activity under visible light observed. Thus, the decoration of cocatalysts somewhat enhanced the absorption in the UV-vis range.



*Figure 77. Diffuse reflectance UV-vis absorption spectra and Tauc plots (right top side corner) of CTF-0, Pt@CTF-0, Co<sub>3</sub>O<sub>4</sub>@CTF-0 and Pt/Co<sub>3</sub>O<sub>4</sub>@CTF-0.*

For investigation of the transfer of photoexcited electron-hole pairs, photoelectrochemical analysis was performed on the CTF-0 and Pt/Co<sub>3</sub>O<sub>4</sub>@CTF-0 excited by the simulated solar light. The impedance arc radiuses of Pt/Co<sub>3</sub>O<sub>4</sub>@CTF-0 is much smaller than pure CTF-0 (Fig. 78a), indicating the better electrical conductivity, would facilitate the migration of the photoexcited carriers, and therefore, enhancing the photocatalytic efficiency. As pointed out in Fig. 78b, the transient photocurrent responses of the samples are still reproducible and stable during several on-off cycles of regular irradiation of the simulated solar light. The Pt/Co<sub>3</sub>O<sub>4</sub>@CTF-0 exhibits a higher photocurrent than the pure CTF-0, which indicates the more efficient separation and transmission of the photogenerated carriers. In the light of the above results and analyses, a schematic illustration of the reaction mechanism on the Pt/Co<sub>3</sub>O<sub>4</sub>@CTF-0 was proposed in Fig. 78c. Firstly, the electrons are excited from the valence band (VB) of CTF-0 to the respective conduction band (CB) under full arc irradiation. Secondly, the generated electrons and holes transfer to the Pt and Co<sub>3</sub>O<sub>4</sub> cocatalysts, which can catalyse proton reduction ( $4e^- + 4H^+ \rightarrow 2H_2$ ) and water oxidation ( $2H_2O + 4h^+ \rightarrow O_2 + 4H^+$ ) for the overall water splitting, respectively. At this point, decorating cocatalysts on CTF-0 can increase the charge carrier separation and transfer, and thus significantly improve the photocatalytic activity of the overall water splitting.

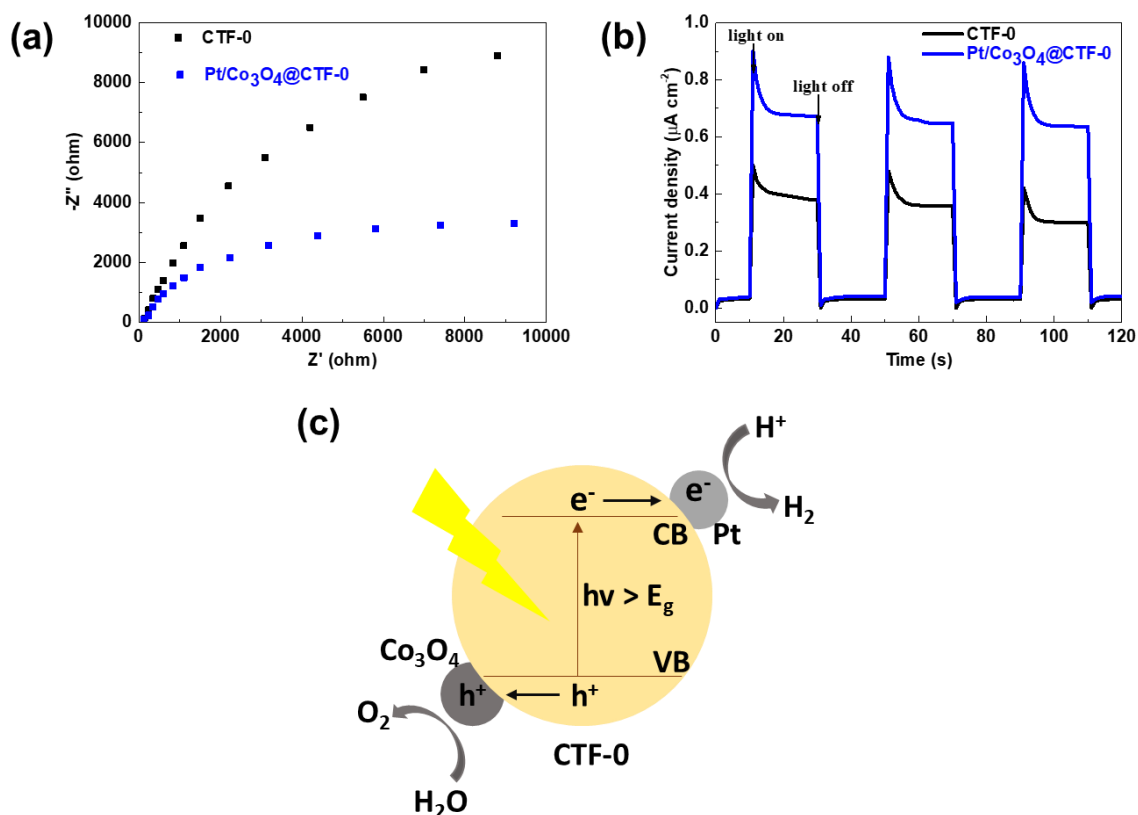


Figure 78. Electrochemical impedance spectroscopy Nyquist plots (a), transient photocurrent response (b) of CTF-0 and Pt/Co<sub>3</sub>O<sub>4</sub>@CTF-0, and proposed schematic of the photocatalytic overall water splitting reaction mechanism on Pt/Co<sub>3</sub>O<sub>4</sub>@CTF-0 (c)

## 6.4 Conclusion

In summary, it is demonstrated, for the first time, that photocatalytic one-step overall water splitting over a single CTF-0 photocatalyst has been achieved by loading both Pt and Co<sub>3</sub>O<sub>4</sub> as cocatalysts. The photocatalytic activity of cocatalyst-modified CTF-0 is improved greatly in each half reaction of water splitting. A hydrogen production rate of 2262  $\mu\text{mol}/(\text{gh})$  and an initial oxygen evolution amount 365  $\mu\text{mol}/\text{g}$  were achieved in the water reduction and oxidation reaction, respectively. The stoichiometric ratio of  $H_2 / O_2 = 2:1$  was obtained by adjusting the

amount of  $\text{Co}_3\text{O}_4$  and Pt cocatalysts, and the optimum is 6 wt%  $\text{Co}_3\text{O}_4$  and 3 wt% Pt, leading to 82  $\mu\text{mol}/(\text{gh})$   $\text{H}_2$  and 40  $\mu\text{mol}/(\text{gh})$   $\text{O}_2$  produced in 18 hours, corresponding to a turn-over number of 958 over Pt and 593 over  $\text{Co}_3\text{O}_4$ . Based on the light absorption and photoelectrochemical measurements, it is found that loading both Pt and  $\text{Co}_3\text{O}_4$  is essential for the overall water splitting of CTF-0, which boosts the light absorption, offers more active sites, and accelerates the transfer of photogenerated charges. The one-step approach of water splitting on CTF-0 provides new insight into the artificial photocatalysis and represent a promising route for further practical applications.

## 7 Overall conclusions

In summary, a successful photocatalytic system for pure water splitting needs to satisfy at least three requirements as illustrated in Chapter 2.1. In this system, the photocatalyst should have a suitable thermodynamic potential for water splitting, a sufficiently narrow band gap to harvest visible photons, and stability against photocorrosion. Because of these stringent requirements, the number of reliable and reproducible photocatalysts suitable for water splitting is quite limited, including inorganic and organic materials summarised in Chapter 2.3. In the water splitting system, there are many factors influencing the reduction or oxidation performance of photocatalysts in the suspension system, such as the solution pH, crystal structure, crystallinity, surface area, cocatalysts, sacrificial reagents and redox mediators.

Among the organic materials, CTFs are a unique class of polymers that inherently combine  $\pi$  conjugation with porosity. To discover the strategy for efficient and low cost photocatalytic materials development, CTFs were selected to provide a powerful means for tuning the band gap, surface area and reaction centers. Based on that, I have developed a new crystalline triazine-based OCT, which is the first polymer photocatalyst to show photocatalytic oxygen evolution from UV light to the near infrared light irradiation in the presence of the hole scavenger  $\text{AgNO}_3$ , resulting into an AQY of 2.6% at 400 nm, 1.1% at 500 nm, 0.7% at 600 nm and even 0.2% at wavelengths as long as 800 nm. The enhanced activity under visible light irradiation is attributed to a significant reduction in the bandgap, caused by doping the oxygen atoms in the triazine structural units. The oxygen doping results into a more negative shift on the CBE of OCT, reducing the driving force for  $\text{H}_2$  production under visible light. As a result, The OCT produces hydrogen from water at an average rate of  $100 \mu\text{mol} \cdot (\text{gh})^{-1}$  under full-arc irradiation. Whereas,

under visible light, hydrogen is produced at  $5 \mu\text{mol} \cdot (\text{gh})^{-1}$ . Furthermore, the effect of oxygen content in the materials on their water oxidation performance was also explored. The higher the level of oxygen doped in the framework, the narrower the band gap, it is up to 1.6 eV when an oxygen content being 6.68 at%. Moreover, the effect of the level of doped oxygen on the photocatalytic performance and the band gap has been further investigated experimentally. The results show that the amount of photocatalytic oxygen evolution increases as the oxygen doping level increases to a peak at the oxygen-doping level of 6.68 at%, with the initial rate of  $10.24 \mu\text{mol/h}$  (10 mg photocatalysts). Afterwards, the amount of produced oxygen drops as the oxygen doping level increases to 7.71%.

Then the focus of the thesis is directed towards the efficient photocatalytic water oxidation and reduction using CTF-0 photocatalysts. Two methods were applied for the synthesis of CTF-0. It is found that CTF-0-M<sub>2</sub> synthesised by the microwave method has the highest activity of photocatalytic hydrogen evolution under both UV and visible light irradiation, resulting into 7.8% AQY at 420 nm and 2% at 500 nm, much better than OCT polymer. The reason for the highest efficiency may be due to the narrowest bandgap, efficient interlayer charge transfer and most negative CBM. On the other side, CTF-0-I prepared by the ionothermal method exhibits the best photocatalytic performance for oxygen evolution under the same light irradiation condition, leading to 14.6% AQY at 365 nm and 5.0% at 420 nm, which is due to the deepest VBM and the relatively large surface area.

To further understand the effects of triazine ring and benzene ring on the electronic characters of the framework, the charge distribution of ideal cluster model of CTF-0 was investigated by density functional theory calculations. The CBM is contributed by triazine acceptor unites and the hydrocarbon potion in the benzene rings, while the VBM is only concentrated over the triazine

donors, which means the VBM is more feasibly influenced by the concentration of nitrogen atoms in the sample. Based on the Elemental Analysis results, CTF-0-I had the lowest concentration of nitrogen, which results into the most negative VBM, largely increasing the oxidizing driving force for water splitting, which, therefore, is more favourable for oxygen production. On the other hand, photoelectrochemical measurements was applied to reveal the kinetics of photocatalysis in the CTF-0s. As a result, CTF-0-M<sub>2</sub> photoelectrode shows the highest photocurrent intensity and the smallest Nyquist plots arc radius over other photoelectrodes, indicating the interlayer charge transfer was largely improved and the charge recombination was efficiently prevented, which might bring to the highest photocatalytic activity of water reduction. Thus, both efficient half reaction photocatalysts have been achieved.

Due to the progress made in the previous two chapters, the feasibility of realising overall water splitting on CTF-0 by loading efficient and functional cocatalysts was then assessed. After loading Pt as cocatalysts by the photodeposition method, CTF-0 could produce H<sub>2</sub> of 2262 μmol/(gh) stably in the presence of TEOA as the sacrificial agent, while there was no activity of CTF-0 without cocatalysts under the same condition. On the other side, Co<sub>3</sub>O<sub>4</sub> decorated CTF-0 could produce O<sub>2</sub> of 365 μmol/g in the first hour, twice higher than pure CTF-0. Therefore, decorating both Pt and Co<sub>3</sub>O<sub>4</sub> on CTF-0 was evaluated to realise the overall water splitting into H<sub>2</sub> and O<sub>2</sub>. The stoichiometric ratio of hydrogen and oxygen equal to 2:1 was only achieved with 82 μmol/(gh) hydrogen evolution and 40 μmol/(gh) oxygen evolution when 6 wt% of Co<sub>3</sub>O<sub>4</sub> and 3 wt% Pt was loaded on the surface of photocatalysts. Based on the investigations of light absorption and photoelectrochemical measurements, it was found that loading both Pt and Co<sub>3</sub>O<sub>4</sub> could offers more active sites and accelerates the transfer of photogenerated charge carriers. The one-step overall water splitting system gives a new insight and platform into the artificial photocatalysis.

## 8 Future Work

Although the thesis achieved the main goals set up at the beginning, further investigations are still required in this field to fundamentally understand the mechanism of the photocatalysis on the covalent triazine based frameworks. This project can be viewed as a platform, for the follow up exploration of highly efficient photocatalysts for advanced energy-related applications.

For example, a better understanding on the underlying mechanisms of photocatalytic activity enhancement by different covalent triazine frameworks is a challenging but crucial for designing novel and highly photoactive triazine-based photocatalysts. To clarify the mechanism of photocatalytic reaction, all aspects in the synthesis-structure-property relationship will need to be better explored. In this regards, the mechanisms can be analysed through the utilisation of single-layer covalent triazine framework sheets in the future. Moreover, investigations by Transient Absorption Spectroscopy (TAS) have previously provided to be a powerful tool to understand the rate limiting steps in other photocatalysts such as  $\text{TiO}_2$ <sup>22</sup>,  $\text{Fe}_2\text{O}_3$ <sup>131</sup> and  $\text{BiVO}_4$ <sup>301</sup>. This technique could be applied in examining the kinetics of photogenerated charge carriers in covalent triazine frameworks, which would illustrate a way to further improve the efficiency for the photocatalysts, e.g. by tailoring the reaction condition or precursors and loading cocatalysts.

Pure overall water splitting systems were shown in Chapter 6, and CTF-0 was realised to be a functional photocatalyst for both water oxidation and reduction. Despite the high quantum efficiency was demonstrated in sacrificial systems in chapter 5, the photocatalytic efficiency of the overall water splitting on the single photocatalysts was low, with 82  $\mu\text{mol}/(\text{gh})$   $\text{H}_2$  and 40  $\mu\text{mol}/(\text{gh})$   $\text{O}_2$  produced stably for 18 hours under full arc but no activity under visible light irradiation. Therefore, further study would be required to optimise this novel system. One route

would be to load alternative cocatalysts with proper structure, possibly monitoring cocatalysts structure using TEM and SEM images. Alternatively, it would be feasible to use covalent triazine framework to build a Z-scheme system with other photocatalysts. As mentioned in Chapter 5, CTF-0-M<sub>2</sub> and CTF-0-I have the highest activities for hydrogen and oxygen evolution, respectively. Combining these two materials in a Z-scheme system would be worthy exploring, and thus, excavating the suitable redox mediators and solution pH value would be the crucial step in the complex system. Alternatively, it would also be possible to couple CTF-0-M<sub>2</sub> or CTF-0-I with another photocatalyst in the Z-scheme system for efficient water splitting. Furthermore, the surface and interface design of cocatalysts is also of great importance to the charge transfer in photocatalysis when multiple components are involved in the photocatalytic system<sup>302</sup>. Therefore, the interface control on the location of Pt and Co<sub>3</sub>O<sub>4</sub> cocatalysts on the surface of photocatalysts homogeneously by the surface reagents could also be a route to largely improve the photocatalytic performance of the overall water splitting.

Finally, the device exploration of covalent triazine frameworks is also important for continuous H<sub>2</sub> fuel production from water by photocatalysis, which has been little studied.

## 9. Bibliography

1. Shafiee, S.; Topal, E., When will fossil fuel reserves be diminished? *Energy Policy* **2009**, *37* (1), 181-189.
2. Hildingsson, R.; Johansson, B., Governing low-carbon energy transitions in sustainable ways: Potential synergies and conflicts between climate and environmental policy objectives. *Energy Policy* **2016**, *88*, 245-252.
3. Moniz, S. J. A.; Shevlin, S. A.; Martin, D. J.; Guo, Z.-X.; Tang, J., Visible-light driven heterojunction photocatalysts for water splitting - a critical review. *Energy & Environmental Science* **2015**, *8* (3), 731-759.
4. Li, K.; An, X.; Park, K. H.; Khraisheh, M.; Tang, J., A critical review of CO<sub>2</sub> photoconversion: Catalysts and reactors. *Catalysis Today* **2014**, *224*, 3-12.
5. Fujishima, A.; Honda, K., Electrochemical Photolysis of Water at a Semiconductor Electrode. *Nature* **1972**, *238* (5358), 37-38.
6. Padhi, D. K.; Parida, K., Facile fabrication of [small alpha]-FeOOH nanorod/RGO composite: a robust photocatalyst for reduction of Cr(vi) under visible light irradiation. *Journal of Materials Chemistry A* **2014**, *2* (26), 10300-10312.
7. Zhou, H.; Ding, L.; Fan, T.; Ding, J.; Zhang, D.; Guo, Q., Leaf-inspired hierarchical porous CdS/Au/N-TiO<sub>2</sub> heterostructures for visible light photocatalytic hydrogen evolution. *Applied Catalysis B: Environmental* **2014**, *147*, 221-228.

8. Wang, X.; Maeda, K.; Thomas, A.; Takanabe, K.; Xin, G.; Carlsson, J. M.; Domen, K.; Antonietti, M., A metal-free polymeric photocatalyst for hydrogen production from water under visible light. *Nat Mater* **2009**, *8* (1), 76-80.
9. Tong, H.; Ouyang, S.; Bi, Y.; Umezawa, N.; Oshikiri, M.; Ye, J., Nano-photocatalytic Materials: Possibilities and Challenges. *Advanced Materials* **2012**, *24* (2), 229-251.
10. Wang, Y.; Wang, Q.; Zhan, X.; Wang, F.; Safdar, M.; He, J., Visible light driven type II heterostructures and their enhanced photocatalysis properties: a review. *Nanoscale* **2013**, *5* (18), 8326-8339.
11. Zuo, F.; Wang, L.; Wu, T.; Zhang, Z.; Borchardt, D.; Feng, P., Self-Doped Ti<sup>3+</sup> Enhanced Photocatalyst for Hydrogen Production under Visible Light. *Journal of the American Chemical Society* **2010**, *132* (34), 11856-11857.
12. Asahi, R.; Morikawa, T.; Ohwaki, T.; Aoki, K.; Taga, Y., Visible-Light Photocatalysis in Nitrogen-Doped Titanium Oxides. *Science* **2001**, *293* (5528), 269-271.
13. Bao, N.; Shen, L.; Takata, T.; Domen, K., Self-Templated Synthesis of Nanoporous CdS Nanostructures for Highly Efficient Photocatalytic Hydrogen Production under Visible Light. *Chemistry of Materials* **2008**, *20* (1), 110-117.
14. Zhang, X.; Xie, X.; Wang, H.; Zhang, J.; Pan, B.; Xie, Y., Enhanced Photoresponsive Ultrathin Graphitic-Phase C<sub>3</sub>N<sub>4</sub> Nanosheets for Bioimaging. *Journal of the American Chemical Society* **2013**, *135* (1), 18-21.
15. Su, D. S.; Zhang, J.; Frank, B.; Thomas, A.; Wang, X.; Paraknowitsch, J.; Schlögl, R., Metal-Free Heterogeneous Catalysis for Sustainable Chemistry. *ChemSusChem* **2010**, *3* (2), 169-180.

16. Esiner, S.; Willems, R. E. M.; Furlan, A.; Li, W.; Wienk, M. M.; Janssen, R. A. J., Photoelectrochemical water splitting in an organic artificial leaf. *Journal of Materials Chemistry A* **2015**, *3* (47), 23936-23945.
17. Goettmann, F.; Fischer, A.; Antonietti, M.; Thomas, A., Chemical Synthesis of Mesoporous Carbon Nitrides Using Hard Templates and Their Use as a Metal-Free Catalyst for Friedel-Crafts Reaction of Benzene. *Angewandte Chemie International Edition* **2006**, *45* (27), 4467-4471.
18. Kudo, A.; Miseki, Y., Heterogeneous photocatalyst materials for water splitting. *Chemical Society Reviews* **2009**, *38* (1), 253-278.
19. Chen, X.; Shen, S.; Guo, L.; Mao, S. S., Semiconductor-based Photocatalytic Hydrogen Generation. *Chemical Reviews* **2010**, *110* (11), 6503-6570.
20. Kudo, A.; Sekizawa, M., Photocatalytic H<sub>2</sub> evolution under visible light irradiation on Ni-doped ZnS photocatalyst. *Chemical Communications* **2000**, (15), 1371-1372.
21. Liu, M.; You, W.; Lei, Z.; Zhou, G.; Yang, J.; Wu, G.; Ma, G.; Luan, G.; Takata, T.; Hara, M.; Domen, K.; Li, C., Water reduction and oxidation on Pt-Ru/Y<sub>2</sub>Ta<sub>2</sub>O<sub>5</sub>N<sub>2</sub> catalyst under visible light irradiation. *Chemical Communications* **2004**, (19), 2192-2193.
22. Tang, J.; Durrant, J. R.; Klug, D. R., Mechanism of Photocatalytic Water Splitting in TiO<sub>2</sub>. Reaction of Water with Photoholes, Importance of Charge Carrier Dynamics, and Evidence for Four-Hole Chemistry. *Journal of the American Chemical Society* **2008**, *130* (42), 13885-13891.
23. Kubacka, A.; Fernández-García, M.; Colón, G., Advanced Nanoarchitectures for Solar Photocatalytic Applications. *Chemical Reviews* **2012**, *112* (3), 1555-1614.
24. Pesci, F. M.; Wang, G.; Klug, D. R.; Li, Y.; Cowan, A. J., Efficient Suppression of Electron-Hole Recombination in Oxygen-Deficient Hydrogen-Treated TiO<sub>2</sub> Nanowires for

Photoelectrochemical Water Splitting. *The Journal of Physical Chemistry. C, Nanomaterials and Interfaces* **2013**, 117 (48), 25837-25844.

25. Reza Gholipour, M.; Dinh, C.-T.; Beland, F.; Do, T.-O., Nanocomposite heterojunctions as sunlight-driven photocatalysts for hydrogen production from water splitting. *Nanoscale* **2015**, 7 (18), 8187-8208.

26. Ahmad, H.; Kamarudin, S. K.; Minggu, L. J.; Kassim, M., Hydrogen from photo-catalytic water splitting process: A review. *Renewable and Sustainable Energy Reviews* **2015**, 43, 599-610.

27. Primo, A.; Corma, A.; Garcia, H., Titania supported gold nanoparticles as photocatalyst. *Physical Chemistry Chemical Physics* **2011**, 13 (3), 886-910.

28. Qi, K.; Cheng, B.; Yu, J.; Ho, W., A review on TiO<sub>2</sub>-based Z-scheme photocatalysts. *Chinese Journal of Catalysis* **2017**, 38 (12), 1936-1955.

29. Martin, D. J., *Investigation into high efficiency visible light photocatalysts for water reduction and oxidation*. Springer: 2015.

30. Handoko, A. D.; Li, K.; Tang, J., Recent progress in artificial photosynthesis: CO<sub>2</sub> photoreduction to valuable chemicals in a heterogeneous system. *Current Opinion in Chemical Engineering* **2013**, 2 (2), 200-206.

31. Xu, H.; Wang, W.; Zhu, W., Shape evolution and size-controllable synthesis of Cu<sub>2</sub>O octahedra and their morphology-dependent photocatalytic properties. *The Journal of Physical Chemistry B* **2006**, 110 (28), 13829-13834.

32. Pan, L.; Zou, J.-J.; Wang, S.; Liu, X.-Y.; Zhang, X.; Wang, L., Morphology Evolution of TiO<sub>2</sub> Facets and Vital Influences on Photocatalytic Activity. *ACS Applied Materials & Interfaces* **2012**, 4 (3), 1650-1655.

33. Kato, H.; Asakura, K.; Kudo, A., Highly Efficient Water Splitting into H<sub>2</sub> and O<sub>2</sub> over Lanthanum-Doped NaTaO<sub>3</sub> Photocatalysts with High Crystallinity and Surface Nanostructure. *Journal of the American Chemical Society* **2003**, *125* (10), 3082-3089.
34. Hu, Y.-S.; Kleiman-Shwarsstein, A.; Forman, A. J.; Hazen, D.; Park, J.-N.; McFarland, E. W., Pt-Doped  $\alpha$ -Fe<sub>2</sub>O<sub>3</sub> Thin Films Active for Photoelectrochemical Water Splitting. *Chemistry of Materials* **2008**, *20* (12), 3803-3805.
35. Sato, J.; Saito, N.; Yamada, Y.; Maeda, K.; Takata, T.; Kondo, J. N.; Hara, M.; Kobayashi, H.; Domen, K.; Inoue, Y., RuO<sub>2</sub>-Loaded  $\beta$ -Ge<sub>3</sub>N<sub>4</sub> as a Non-Oxide Photocatalyst for Overall Water Splitting. *Journal of the American Chemical Society* **2005**, *127* (12), 4150-4151.
36. Maeda, K.; Lu, D.; Domen, K., Direct Water Splitting into Hydrogen and Oxygen under Visible Light by using Modified TaON Photocatalysts with d<sup>0</sup> Electronic Configuration. *Chemistry – A European Journal* **2013**, *19* (16), 4986-4991.
37. Kato, H.; Sasaki, Y.; Shirakura, N.; Kudo, A., Synthesis of highly active rhodium-doped SrTiO<sub>3</sub> powders in Z-scheme systems for visible-light-driven photocatalytic overall water splitting. *Journal of Materials Chemistry A* **2013**, *1* (39), 12327-12333.
38. Maeda, K.; Lu, D.; Domen, K., Solar-Driven Z-scheme Water Splitting Using Modified BaZrO<sub>3</sub>-BaTaO<sub>2</sub>N Solid Solutions as Photocatalysts. *ACS Catalysis* **2013**, *3* (5), 1026-1033.
39. Niishiro, R.; Tanaka, S.; Kudo, A., Hydrothermal-synthesized SrTiO<sub>3</sub> photocatalyst codoped with rhodium and antimony with visible-light response for sacrificial H<sub>2</sub> and O<sub>2</sub> evolution and application to overall water splitting. *Applied Catalysis B: Environmental* **2014**, *150-151*, 187-196.

40. Kawashima, K.; Hojamberdiev, M.; Wagata, H.; Yubuta, K.; Vequizo, J. J. M.; Yamakata, A.; Oishi, S.; Domen, K.; Teshima, K., NH<sub>3</sub>-Assisted Flux-Mediated Direct Growth of LaTiO<sub>2</sub>N Crystallites for Visible-Light-Induced Water Splitting. *The Journal of Physical Chemistry C* **2015**, *119* (28), 15896-15904.
41. Hisatomi, T.; Katayama, C.; Moriya, Y.; Minegishi, T.; Katayama, M.; Nishiyama, H.; Yamada, T.; Domen, K., Photocatalytic oxygen evolution using BaNbO<sub>2</sub>N modified with cobalt oxide under photoexcitation up to 740 nm. *Energy & Environmental Science* **2013**, *6* (12), 3595-3599.
42. Ma, S. S. K.; Hisatomi, T.; Maeda, K.; Moriya, Y.; Domen, K., Enhanced Water Oxidation on Ta<sub>3</sub>N<sub>5</sub> Photocatalysts by Modification with Alkaline Metal Salts. *Journal of the American Chemical Society* **2012**, *134* (49), 19993-19996.
43. Martin, D. J.; Reardon, P. J. T.; Moniz, S. J. A.; Tang, J., Visible Light-Driven Pure Water Splitting by a Nature-Inspired Organic Semiconductor-Based System. *Journal of the American Chemical Society* **2014**, *136* (36), 12568-12571.
44. Li, X.; Bi, W.; Zhang, L.; Tao, S.; Chu, W.; Zhang, Q.; Luo, Y.; Wu, C.; Xie, Y., Single-Atom Pt as Co-Catalyst for Enhanced Photocatalytic H<sub>2</sub> Evolution. *Advanced Materials* **2016**, *28* (12), 2427-2431.
45. Yang, X.-F.; Wang, A.; Qiao, B.; Li, J.; Liu, J.; Zhang, T., Single-Atom Catalysts: A New Frontier in Heterogeneous Catalysis. *Accounts of Chemical Research* **2013**, *46* (8), 1740-1748.
46. Xing, J.; Chen, J. F.; Li, Y. H.; Yuan, W. T.; Zhou, Y.; Zheng, L. R.; Wang, H. F.; Hu, P.; Wang, Y.; Zhao, H. J.; Wang, Y.; Yang, H. G., Stable Isolated Metal Atoms as Active Sites for Photocatalytic Hydrogen Evolution. *Chemistry – A European Journal* **2014**, *20* (8), 2138-2144.

47. Yin, P.; Yao, T.; Wu, Y.; Zheng, L.; Lin, Y.; Liu, W.; Ju, H.; Zhu, J.; Hong, X.; Deng, Z.; Zhou, G.; Wei, S.; Li, Y., Single Cobalt Atoms with Precise N-Coordination as Superior Oxygen Reduction Reaction Catalysts. *Angewandte Chemie International Edition* **2016**, *55* (36), 10800-10805.
48. Fei, H.; Dong, J.; Arellano-Jiménez, M. J.; Ye, G.; Dong Kim, N.; Samuel, E. L. G.; Peng, Z.; Zhu, Z.; Qin, F.; Bao, J.; Yacaman, M. J.; Ajayan, P. M.; Chen, D.; Tour, J. M., Atomic cobalt on nitrogen-doped graphene for hydrogen generation. *Nature Communications* **2015**, *6*, 8668.
49. Cheng, N.; Stambula, S.; Wang, D.; Banis, M. N.; Liu, J.; Riese, A.; Xiao, B.; Li, R.; Sham, T.-K.; Liu, L.-M.; Botton, G. A.; Sun, X., Platinum single-atom and cluster catalysis of the hydrogen evolution reaction. *Nature Communications* **2016**, *7*, 13638.
50. Abe, R.; Sayama, K.; Sugihara, H., Development of New Photocatalytic Water Splitting into H<sub>2</sub> and O<sub>2</sub> using Two Different Semiconductor Photocatalysts and a Shuttle Redox Mediator IO<sup>3-</sup>/I<sup>-</sup>. *The Journal of Physical Chemistry B* **2005**, *109* (33), 16052-16061.
51. Maeda, K.; Takata, T.; Hara, M.; Saito, N.; Inoue, Y.; Kobayashi, H.; Domen, K., GaN:ZnO Solid Solution as a Photocatalyst for Visible-Light-Driven Overall Water Splitting. *Journal of the American Chemical Society* **2005**, *127* (23), 8286-8287.
52. Chen, X.; Liu, L.; Yu, P. Y.; Mao, S. S., Increasing Solar Absorption for Photocatalysis with Black Hydrogenated Titanium Dioxide Nanocrystals. *Science* **2011**, *331* (6018), 746-750.
53. Tijare, S. N.; Joshi, M. V.; Padole, P. S.; Mangrulkar, P. A.; Rayalu, S. S.; Labhsetwar, N. K., Photocatalytic hydrogen generation through water splitting on nano-crystalline LaFeO<sub>3</sub> perovskite. *International Journal of Hydrogen Energy* **2012**, *37* (13), 10451-10456.
54. Maeda, K.; Sahara, G.; Eguchi, M.; Ishitani, O., Hybrids of a Ruthenium(II) Polypyridyl Complex and a Metal Oxide Nanosheet for Dye-Sensitized Hydrogen Evolution with Visible

Light: Effects of the Energy Structure on Photocatalytic Activity. *ACS Catalysis* **2015**, 5 (3), 1700-1707.

55. Zhang, W.; Hong, J.; Zheng, J.; Huang, Z.; Zhou, J.; Xu, R., Nickel-Thiolate Complex Catalyst Assembled in One Step in Water for Solar H<sub>2</sub> Production. *Journal of the American Chemical Society* **2011**, 133 (51), 20680-20683.

56. Tsuji, I.; Kato, H.; Kudo, A., Photocatalytic Hydrogen Evolution on ZnS-CuInS<sub>2</sub>-AgInS<sub>2</sub> Solid Solution Photocatalysts with Wide Visible Light Absorption Bands. *Chemistry of Materials* **2006**, 18 (7), 1969-1975.

57. Jang, J. S.; Hwang, D. W.; Lee, J. S., CdS-AgGaS<sub>2</sub> photocatalytic diodes for hydrogen production from aqueous Na<sub>2</sub>S/Na<sub>2</sub>SO<sub>3</sub> electrolyte solution under visible light ( $\lambda \geq 420$  nm). *Catalysis Today* **2007**, 120 (2), 174-181.

58. Xu, X.; Randorn, C.; Efstathiou, P.; Irvine, J. T. S., A red metallic oxide photocatalyst. *Nat Mater* **2012**, 11 (7), 595-598.

59. Frame, F. A.; Townsend, T. K.; Chamousis, R. L.; Sabio, E. M.; Dittrich, T.; Browning, N. D.; Osterloh, F. E., Photocatalytic Water Oxidation with Nonsensitized IrO<sub>2</sub> Nanocrystals under Visible and UV Light. *Journal of the American Chemical Society* **2011**, 133 (19), 7264-7267.

60. Wang, B.; Shen, S.; Guo, L., SrTiO<sub>3</sub> single crystals enclosed with high-indexed {0 2 3} facets and {0 0 1} facets for photocatalytic hydrogen and oxygen evolution. *Applied Catalysis B: Environmental* **2015**, 166-167, 320-326.

61. Li, R.; Han, H.; Zhang, F.; Wang, D.; Li, C., Highly efficient photocatalysts constructed by rational assembly of dual-cocatalysts separately on different facets of BiVO<sub>4</sub>. *Energy & Environmental Science* **2014**, 7 (4), 1369-1376.

62. Tsuji, K.; Tomita, O.; Higashi, M.; Abe, R., Manganese - Substituted Polyoxometalate as an Effective Shuttle Redox Mediator in Z - Scheme Water Splitting under Visible Light. *ChemSusChem* **2016**, 9 (16), 2201-2208.
63. Zhou, P.; Yu, J.; Jaroniec, M., All-Solid-State Z-Scheme Photocatalytic Systems. *Advanced Materials* **2014**, 26 (29), 4920-4935.
64. Maeda, K., Photocatalytic water splitting using semiconductor particles: History and recent developments. *Journal of Photochemistry and Photobiology C: Photochemistry Reviews* **2011**, 12 (4), 237-268.
65. Ran, J.; Zhang, J.; Yu, J.; Jaroniec, M.; Qiao, S. Z., Earth-abundant cocatalysts for semiconductor-based photocatalytic water splitting. *Chemical Society Reviews* **2014**, 43 (22), 7787-7812.
66. Zhang, J.; Zhou, P.; Liu, J.; Yu, J., New understanding of the difference of photocatalytic activity among anatase, rutile and brookite TiO<sub>2</sub>. *Physical Chemistry Chemical Physics* **2014**, 16 (38), 20382-20386.
67. Khan, S. U. M.; Al-Shahry, M.; Ingler, W. B., Efficient Photochemical Water Splitting by a Chemically Modified n-TiO<sub>2</sub>. *Science* **2002**, 297 (5590), 2243-2245.
68. Liu, B.; Liu, L.-M.; Lang, X.-F.; Wang, H.-Y.; Lou, X. W.; Aydil, E. S., Doping high-surface-area mesoporous TiO<sub>2</sub> microspheres with carbonate for visible light hydrogen production. *Energy & Environmental Science* **2014**, 7 (8), 2592-2597.
69. Nelson, B. P.; Candal, R.; Corn, R. M.; Anderson, M. A., Control of Surface and  $\zeta$  Potentials on Nanoporous TiO<sub>2</sub> Films by Potential-Determining and Specifically Adsorbed Ions. *Langmuir* **2000**, 16 (15), 6094-6101.

70. Fonseca de Lima, J.; Harunsani, M. H.; Martin, D. J.; Kong, D.; Dunne, P. W.; Gianolio, D.; Kashtiban, R. J.; Sloan, J.; Serra, O. A.; Tang, J.; Walton, R. I., Control of chemical state of cerium in doped anatase TiO<sub>2</sub> by solvothermal synthesis and its application in photocatalytic water reduction. *Journal of Materials Chemistry A* **2015**, 3 (18), 9890-9898.
71. Yu, H.; Zhao, Y.; Zhou, C.; Shang, L.; Peng, Y.; Cao, Y.; Wu, L.-Z.; Tung, C.-H.; Zhang, T., Carbon quantum dots/TiO<sub>2</sub> composites for efficient photocatalytic hydrogen evolution. *Journal of Materials Chemistry A* **2014**, 2 (10), 3344-3351.
72. Schneider, J.; Matsuoka, M.; Takeuchi, M.; Zhang, J.; Horiuchi, Y.; Anpo, M.; Bahnemann, D. W., Understanding TiO<sub>2</sub> Photocatalysis: Mechanisms and Materials. *Chemical Reviews* **2014**, 114 (19), 9919-9986.
73. Mori, K.; Miura, Y.; Shironita, S.; Yamashita, H., New Route for the Preparation of Pd and PdAu Nanoparticles Using Photoexcited Ti-Containing Zeolite as an Efficient Support Material and Investigation of Their Catalytic Properties. *Langmuir* **2009**, 25 (18), 11180-11187.
74. Murakami, M.; Hong, D.; Suenobu, T.; Yamaguchi, S.; Ogura, T.; Fukuzumi, S., Catalytic Mechanism of Water Oxidation with Single-Site Ruthenium-Heteropolytungstate Complexes. *Journal of the American Chemical Society* **2011**, 133 (30), 11605-11613.
75. Concepcion, J. J.; Tsai, M.-K.; Muckerman, J. T.; Meyer, T. J., Mechanism of Water Oxidation by Single-Site Ruthenium Complex Catalysts. *Journal of the American Chemical Society* **2010**, 132 (5), 1545-1557.
76. Cao, Y.; Chen, S.; Luo, Q.; Yan, H.; Lin, Y.; Liu, W.; Cao, L.; Lu, J.; Yang, J.; Yao, T.; Wei, S., Atomic-Level Insight into Optimizing the Hydrogen Evolution Pathway over a Co1-N4 Single-Site Photocatalyst. *Angewandte Chemie International Edition* **2017**, 56 (40), 12191-12196.

77. Ma, B.; Guan, P.-Y.; Li, Q.-Y.; Zhang, M.; Zang, S.-Q., MOF-Derived Flower-like MoS<sub>2</sub>@TiO<sub>2</sub> Nanohybrids with Enhanced Activity for Hydrogen Evolution. *ACS Applied Materials & Interfaces* **2016**, *8* (40), 26794-26800.
78. Gomathi Devi, L.; Kavitha, R., A review on plasmonic metal TiO<sub>2</sub> composite for generation, trapping, storing and dynamic vectorial transfer of photogenerated electrons across the Schottky junction in a photocatalytic system. *Applied Surface Science* **2016**, *360*, 601-622.
79. Lakshminarasimhan, N.; Kim, W.; Choi, W., Effect of the Agglomerated State on the Photocatalytic Hydrogen Production with in Situ Agglomeration of Colloidal TiO<sub>2</sub> Nanoparticles. *The Journal of Physical Chemistry C* **2008**, *112* (51), 20451-20457.
80. Kandiel, T. A.; Dillert, R.; Robben, L.; Bahnemann, D. W., Photonic efficiency and mechanism of photocatalytic molecular hydrogen production over platinized titanium dioxide from aqueous methanol solutions. *Catalysis Today* **2011**, *161* (1), 196-201.
81. Kho, Y. K.; Iwase, A.; Teoh, W. Y.; Mädler, L.; Kudo, A.; Amal, R., Photocatalytic H<sub>2</sub> Evolution over TiO<sub>2</sub> Nanoparticles. The Synergistic Effect of Anatase and Rutile. *The Journal of Physical Chemistry C* **2010**, *114* (6), 2821-2829.
82. Luo, B.; Song, R.; Jing, D., Particle aggregation behavior during photocatalytic ethanol reforming reaction and its correlation with the activity of H<sub>2</sub> production. *Colloids and Surfaces A: Physicochemical and Engineering Aspects* **2017**, *535*, 114-120.
83. Wang, C.-y.; Böttcher, C.; Bahnemann, D. W.; Dohrmann, J. K., A comparative study of nanometer sized Fe(iii)-doped TiO<sub>2</sub> photocatalysts: synthesis, characterization and activity. *Journal of Materials Chemistry* **2003**, *13* (9), 2322-2329.

84. Abe, R.; Higashi, M.; Domen, K., Facile Fabrication of an Efficient Oxynitride TaON Photoanode for Overall Water Splitting into H<sub>2</sub> and O<sub>2</sub> under Visible Light Irradiation. *Journal of the American Chemical Society* **2010**, *132* (34), 11828-11829.
85. Zhang, G.; Liu, G.; Wang, L.; Irvine, J. T. S., Inorganic perovskite photocatalysts for solar energy utilization. *Chemical Society Reviews* **2016**, *45* (21), 5951-5984.
86. Peña, M. A.; Fierro, J. L. G., Chemical Structures and Performance of Perovskite Oxides. *Chemical Reviews* **2001**, *101* (7), 1981-2018.
87. Mu, L.; Zhao, Y.; Li, A.; Wang, S.; Wang, Z.; Yang, J.; Wang, Y.; Liu, T.; Chen, R.; Zhu, J.; Fan, F.; Li, R.; Li, C., Enhancing charge separation on high symmetry SrTiO<sub>3</sub> exposed with anisotropic facets for photocatalytic water splitting. *Energy & Environmental Science* **2016**.
88. Takata, T.; Furumi, Y.; Shinohara, K.; Tanaka, A.; Hara, M.; Kondo, J. N.; Domen, K., Photocatalytic Decomposition of Water on Spontaneously Hydrated Layered Perovskites. *Chemistry of Materials* **1997**, *9* (5), 1063-1064.
89. G. Kim, H.; W. Hwang, D.; Kim, J.; G. Kim, Y.; S. Lee, J., Highly donor-doped (110) layered perovskite materials as novel photocatalysts for overall water splitting. *Chemical Communications* **1999**, (12), 1077-1078.
90. Kim, H. G.; Hwang, D. W.; Bae, S. W.; Jung, J. H.; Lee, J. S., Photocatalytic Water Splitting over La<sub>2</sub>Ti<sub>2</sub>O<sub>7</sub> Synthesized by the Polymerizable Complex Method. *Catalysis Letters* **2003**, *91* (3), 193-198.
91. Yuliaty, L.; Yang, J.-H.; Wang, X.; Maeda, K.; Takata, T.; Antonietti, M.; Domen, K., Highly active tantalum(v) nitride nanoparticles prepared from a mesoporous carbon nitride template for

photocatalytic hydrogen evolution under visible light irradiation. *Journal of Materials Chemistry* **2010**, *20* (21), 4295-4298.

92. Kubota, J.; Domen, K., Photocatalytic Water Splitting Using Oxynitride and Nitride Semiconductor Powders for Production of Solar Hydrogen. **2013**, *22* (2), 57-62.

93. Sasaki, R.; Maeda, K.; Kako, Y.; Domen, K., Preparation of calcium tantalum oxynitride from layered oxide precursors to improve photocatalytic activity for hydrogen evolution under visible light. *Applied Catalysis B: Environmental* **2012**, *128*, 72-76.

94. Ida, S.; Okamoto, Y.; Matsuka, M.; Hagiwara, H.; Ishihara, T., Preparation of Tantalum-Based Oxynitride Nanosheets by Exfoliation of a Layered Oxynitride,  $\text{CsCa}_2\text{Ta}_3\text{O}_{10-x}\text{N}_y$ , and Their Photocatalytic Activity. *Journal of the American Chemical Society* **2012**, *134* (38), 15773-15782.

95. Siritanaratkul, B.; Maeda, K.; Hisatomi, T.; Domen, K., Synthesis and Photocatalytic Activity of Perovskite Niobium Oxynitrides with Wide Visible-Light Absorption Bands. **2011**, *4* (1), 74-78.

96. Fuertes, A., Synthesis and properties of functional oxynitrides – from photocatalysts to CMR materials. *Dalton Transactions* **2010**, *39* (26), 5942-5948.

97. Takata, T.; Hitoki, G.; Kondo, J. N.; Hara, M.; Kobayashi, H.; Domen, K., Visible-light-driven photocatalytic behavior of tantalum-oxynitride and nitride. *Research on Chemical Intermediates* **2007**, *33* (1), 13-25.

98. Lee, Y.; Terashima, H.; Shimodaira, Y.; Teramura, K.; Hara, M.; Kobayashi, H.; Domen, K.; Yashima, M., Zinc Germanium Oxynitride as a Photocatalyst for Overall Water Splitting under Visible Light. *The Journal of Physical Chemistry C* **2007**, *111* (2), 1042-1048.

99. Fang, C. M.; Orhan, E.; de Wijs, G. A.; Hintzen, H. T.; de Groot, R. A.; Marchand, R.; Saillard, J. Y.; de With, G., The electronic structure of tantalum (oxy)nitrides TaON and TaN. *Journal of Materials Chemistry* **2001**, *11* (4), 1248-1252.
100. Hara, M.; Hitoki, G.; Takata, T.; Kondo, J. N.; Kobayashi, H.; Domen, K., TaON and Ta<sub>3</sub>N<sub>5</sub> as new visible light driven photocatalysts. *Catalysis Today* **2003**, *78* (1-4), 555-560.
101. Ahmed, M.; Xinxin, G., A review of metal oxynitrides for photocatalysis. *Inorganic Chemistry Frontiers* **2016**, *3* (5), 578-590.
102. Kasahara, A.; Nukumizu, K.; Takata, T.; Kondo, J. N.; Hara, M.; Kobayashi, H.; Domen, K., LaTiO<sub>2</sub>N as a Visible-Light ( $\leq 600$  nm)-Driven Photocatalyst (2). *The Journal of Physical Chemistry B* **2003**, *107* (3), 791-797.
103. Hisatomi, T.; Katayama, C.; Teramura, K.; Takata, T.; Moriya, Y.; Minegishi, T.; Katayama, M.; Nishiyama, H.; Yamada, T.; Domen, K., The Effects of Preparation Conditions for a BaNbO<sub>2</sub>N Photocatalyst on Its Physical Properties. **2014**, *7* (7), 2016-2021.
104. Kamat, P. V., Meeting the Clean Energy Demand: Nanostructure Architectures for Solar Energy Conversion. *The Journal of Physical Chemistry C* **2007**, *111* (7), 2834-2860.
105. Zong, X.; Yan, H.; Wu, G.; Ma, G.; Wen, F.; Wang, L.; Li, C., Enhancement of Photocatalytic H<sub>2</sub> Evolution on CdS by Loading MoS<sub>2</sub> as Cocatalyst under Visible Light Irradiation. *Journal of the American Chemical Society* **2008**, *130* (23), 7176-7177.
106. Wang, H.; Chen, W.; Zhang, J.; Huang, C.; Mao, L., Nickel nanoparticles modified CdS – A potential photocatalyst for hydrogen production through water splitting under visible light irradiation. *International Journal of Hydrogen Energy* **2015**, *40* (1), 340-345.

107. Meissner, D.; Memming, R.; Kastening, B., Photoelectrochemistry of cadmium sulfide. 1. Reanalysis of photocorrosion and flat-band potential. *The Journal of Physical Chemistry* **1988**, *92* (12), 3476-3483.
108. Eevans, J. E.; Springer, K. W.; Zhang, J. Z., Femtosecond studies of interparticle electron transfer in a coupled CdS-TiO<sub>2</sub> colloidal system. **1994**, *101* (7), 6222-6225.
109. Reber, J. F.; Rusek, M., Photochemical hydrogen production with platinized suspensions of cadmium sulfide and cadmium zinc sulfide modified by silver sulfide. *The Journal of Physical Chemistry* **1986**, *90* (5), 824-834.
110. Darwent, J. R., H<sub>2</sub> production photosensitized by aqueous semiconductor dispersions. *Journal of the Chemical Society, Faraday Transactions 2: Molecular and Chemical Physics* **1981**, *77* (9), 1703-1709.
111. Mills, A.; Porter, G., Photosensitised dissociation of water using dispersed suspensions of n-type semiconductors. *Journal of the Chemical Society, Faraday Transactions 1: Physical Chemistry in Condensed Phases* **1982**, *78* (12), 3659-3669.
112. Hirai, T.; Shiojiri, S.; Komasaawa, I., Preparation of Metal Sulfide Composite Ultrafine Particles in Reverse Micellar Systems and Their Photocatalytic Property. *JOURNAL OF CHEMICAL ENGINEERING OF JAPAN* **1994**, *27* (5), 590-597.
113. Fujii, H.; Ohtaki, M.; Eguchi, K.; Arai, H., Preparation and photocatalytic activities of a semiconductor composite of CdS embedded in a TiO<sub>2</sub> gel as a stable oxide semiconducting matrix. *Journal of Molecular Catalysis A: Chemical* **1998**, *129* (1), 61-68.

114. Xing, C.; Zhang, Y.; Yan, W.; Guo, L., Band structure-controlled solid solution of Cd<sub>1-x</sub>Zn<sub>x</sub>S photocatalyst for hydrogen production by water splitting. *International Journal of Hydrogen Energy* **2006**, *31* (14), 2018-2024.
115. Kambe, S.; Fujii, M.; Kawai, T.; Kawai, S.; Nakahara, F., Photocatalytic hydrogen production with Cd(S, Se) solid solution particles: Determining factors for the highly efficient photocatalyst. *Chemical Physics Letters* **1984**, *109* (1), 105-109.
116. Sathish, M.; Viswanathan, B.; Viswanath, R. P., Alternate synthetic strategy for the preparation of CdS nanoparticles and its exploitation for water splitting. *International Journal of Hydrogen Energy* **2006**, *31* (7), 891-898.
117. Arai, T.; Sato, Y.; Shinoda, K.; Jeyadevan, B.; Tohji, K., Stratified Materials Synthesized in the Liquid Phase. In *Morphology Control of Materials and Nanoparticles*, Springer: 2004; pp 65-84.
118. Savinov, E. N.; Gruzdkov, Y. A.; Parmon, V. N., Suspensions of semiconductors with microheterojunctions – A new type of highly efficient photocatalyst for dihydrogen production from solution of hydrogen sulfide and sulfide ions. *International Journal of Hydrogen Energy* **1989**, *14* (1), 1-9.
119. Zhukovskiy, M.; Tongying, P.; Yashan, H.; Wang, Y.; Kuno, M., Efficient Photocatalytic Hydrogen Generation from Ni Nanoparticle Decorated CdS Nanosheets. *ACS Catalysis* **2015**, *5* (11), 6615-6623.
120. Reber, J. F.; Meier, K., Photochemical production of hydrogen with zinc sulfide suspensions. *The Journal of Physical Chemistry* **1984**, *88* (24), 5903-5913.

121. Tsuji, I.; Kato, H.; Kudo, A., Visible-Light-Induced H<sub>2</sub> Evolution from an Aqueous Solution Containing Sulfide and Sulfite over a ZnS–CuInS<sub>2</sub>–AgInS<sub>2</sub> Solid-Solution Photocatalyst. **2005**, *44* (23), 3565-3568.
122. Tsuji, I.; Kato, H.; Kobayashi, H.; Kudo, A., Photocatalytic H<sub>2</sub> Evolution Reaction from Aqueous Solutions over Band Structure-Controlled (AgIn)<sub>x</sub>Zn<sub>2(1-x)</sub>S<sub>2</sub> Solid Solution Photocatalysts with Visible-Light Response and Their Surface Nanostructures. *Journal of the American Chemical Society* **2004**, *126* (41), 13406-13413.
123. Sobczynski, A.; Yildiz, A.; Bard, A. J.; Campion, A.; Fox, M. A.; Mallouk, T.; Webber, S. E.; White, J. M., Tungsten disulfide: a novel hydrogen evolution catalyst for water decomposition. *The Journal of Physical Chemistry* **1988**, *92* (8), 2311-2315.
124. Bessekhoud, Y.; Mohammedi, M.; Trari, M., Hydrogen photoproduction from hydrogen sulfide on Bi<sub>2</sub>S<sub>3</sub> catalyst. *Solar Energy Materials and Solar Cells* **2002**, *73* (3), 339-350.
125. Cao, S.; Wang, C.-J.; Fu, W.-F.; Chen, Y., Metal Phosphides as Co-Catalysts for Photocatalytic and Photoelectrocatalytic Water Splitting. **2017**, *10* (22), 4306-4323.
126. Sun, Z.; Zheng, H.; Li, J.; Du, P., Extraordinarily efficient photocatalytic hydrogen evolution in water using semiconductor nanorods integrated with crystalline Ni<sub>2</sub>P cocatalysts. *Energy & Environmental Science* **2015**, *8* (9), 2668-2676.
127. Wang, X.; Maeda, K.; Thomas, A.; Takanabe, K.; Xin, G.; Carlsson, J. M.; Domen, K.; Antonietti, M., A metal-free polymeric photocatalyst for hydrogen production from water under visible light. *Nature Materials* **2008**, *8*, 76.
128. Khaselev, O.; Turner, J. A., A Monolithic Photovoltaic-Photoelectrochemical Device for Hydrogen Production via Water Splitting. **1998**, *280* (5362), 425-427.

129. Grätzel, M., Photoelectrochemical cells. *Nature* **2001**, *414*, 338.
130. Kanan, M. W.; Nocera, D. G., In Situ Formation of an Oxygen-Evolving Catalyst in Neutral Water Containing Phosphate and  $\text{Co}^{2+}$ . **2008**, *321* (5892), 1072-1075.
131. Pendlebury, S. R.; Barroso, M.; Cowan, A. J.; Sivula, K.; Tang, J.; Grätzel, M.; Klug, D.; Durrant, J. R., Dynamics of photogenerated holes in nanocrystalline  $\alpha\text{-Fe}_2\text{O}_3$  electrodes for water oxidation probed by transient absorption spectroscopy. *Chemical Communications* **2011**, *47* (2), 716-718.
132. Tang, J.; Cowan, A. J.; Durrant, J. R.; Klug, D. R., Mechanism of  $\text{O}_2$  Production from Water Splitting: Nature of Charge Carriers in Nitrogen Doped Nanocrystalline  $\text{TiO}_2$  Films and Factors Limiting  $\text{O}_2$  Production. *The Journal of Physical Chemistry C* **2011**, *115* (7), 3143-3150.
133. Ma, S. S. K.; Maeda, K.; Abe, R.; Domen, K., Visible-light-driven nonsacrificial water oxidation over tungsten trioxide powder modified with two different cocatalysts. *Energy & Environmental Science* **2012**, *5* (8), 8390-8397.
134. Kudo, A.; Ueda, K.; Kato, H.; Mikami, I., Photocatalytic  $\text{O}_2$  evolution under visible light irradiation on  $\text{BiVO}_4$  in aqueous  $\text{AgNO}_3$  solution. *Catalysis Letters* **1998**, *53* (3), 229-230.
135. Li, R.; Zhang, F.; Wang, D.; Yang, J.; Li, M.; Zhu, J.; Zhou, X.; Han, H.; Li, C., Spatial separation of photogenerated electrons and holes among {010} and {110} crystal facets of  $\text{BiVO}_4$ . *Nat Commun* **2013**, *4*, 1432.
136. Yi, Z.; Ye, J.; Kikugawa, N.; Kako, T.; Ouyang, S.; Stuart-Williams, H.; Yang, H.; Cao, J.; Luo, W.; Li, Z.; Liu, Y.; Withers, R. L., An orthophosphate semiconductor with photooxidation properties under visible-light irradiation. *Nature Materials* **2010**, *9*, 559.

137. Wang, H.; Bai, Y.; Yang, J.; Lang, X.; Li, J.; Guo, L., A Facile Way to Rejuvenate  $\text{Ag}_3\text{PO}_4$  as a Recyclable Highly Efficient Photocatalyst. **2012**, *18* (18), 5524-5529.
138. Martin, D. J.; Umezawa, N.; Chen, X.; Ye, J.; Tang, J., Facet engineered  $\text{Ag}_3\text{PO}_4$  for efficient water photooxidation. *Energy & Environmental Science* **2013**, *6* (11), 3380-3386.
139. Zhang, S.; Zhang, S.; Song, L., Super-high activity of  $\text{Bi}^{3+}$  doped  $\text{Ag}_3\text{PO}_4$  and enhanced photocatalytic mechanism. *Applied Catalysis B: Environmental* **2014**, *152-153*, 129-139.
140. Yan, T.; Zhang, H.; Liu, Y.; Guan, W.; Long, J.; Li, W.; You, J., Fabrication of robust  $\text{M}/\text{Ag}_3\text{PO}_4$  (M = Pt, Pd, Au) Schottky-type heterostructures for improved visible-light photocatalysis. *RSC Advances* **2014**, *4* (70), 37220-37230.
141. Yu, H.; Cao, G.; Chen, F.; Wang, X.; Yu, J.; Lei, M., Enhanced photocatalytic performance of  $\text{Ag}_3\text{PO}_4$  by simultaneous loading of Ag nanoparticles and Fe(III) cocatalyst. *Applied Catalysis B: Environmental* **2014**, *160-161*, 658-665.
142. Chen, X.; Dai, Y.; Wang, X., Methods and mechanism for improvement of photocatalytic activity and stability of  $\text{Ag}_3\text{PO}_4$ : A review. *Journal of Alloys and Compounds* **2015**, *649*, 910-932.
143. Yao, W.; Zhang, B.; Huang, C.; Ma, C.; Song, X.; Xu, Q., Synthesis and characterization of high efficiency and stable  $\text{Ag}_3\text{PO}_4/\text{TiO}_2$  visible light photocatalyst for the degradation of methylene blue and rhodamine B solutions. *Journal of Materials Chemistry* **2012**, *22* (9), 4050-4055.
144. Yaghi, O.; Li, H. J. J. o. t. A. C. S., Hydrothermal synthesis of a metal-organic framework containing large rectangular channels. **1995**, *117* (41), 10401-10402.
145. Toyao, T.; Saito, M.; Horiuchi, Y.; Mochizuki, K.; Iwata, M.; Higashimura, H.; Matsuoka, M., Efficient hydrogen production and photocatalytic reduction of nitrobenzene over a visible-

light-responsive metal-organic framework photocatalyst. *Catalysis Science & Technology* **2013**, *3* (8), 2092-2097.

146. He, J.; Wang, J.; Chen, Y.; Zhang, J.; Duan, D.; Wang, Y.; Yan, Z., A dye-sensitized Pt@UiO-66(Zr) metal-organic framework for visible-light photocatalytic hydrogen production. *Chemical Communications* **2014**, *50* (53), 7063-7066.

147. Fateeva, A.; Chater, P. A.; Ireland, C. P.; Tahir, A. A.; Khimyak, Y. Z.; Wiper, P. V.; Darwent, J. R.; Rosseinsky, M. J., A Water-Stable Porphyrin-Based Metal-Organic Framework Active for Visible-Light Photocatalysis. **2012**, *51* (30), 7440-7444.

148. Liu, J.; Liu, Y.; Liu, N.; Han, Y.; Zhang, X.; Huang, H.; Lifshitz, Y.; Lee, S.-T.; Zhong, J.; Kang, Z., Metal-free efficient photocatalyst for stable visible water splitting via a two-electron pathway. **2015**, *347* (6225), 970-974.

149. Wang, Q.; Hisatomi, T.; Jia, Q.; Tokudome, H.; Zhong, M.; Wang, C.; Pan, Z.; Takata, T.; Nakabayashi, M.; Shibata, N.; Li, Y.; Sharp, I. D.; Kudo, A.; Yamada, T.; Domen, K., Scalable water splitting on particulate photocatalyst sheets with a solar-to-hydrogen energy conversion efficiency exceeding 1%. *Nat Mater* **2016**, *15* (6), 611-615.

150. Xia, X.; Deng, N.; Cui, G.; Xie, J.; Shi, X.; Zhao, Y.; Wang, Q.; Wang, W.; Tang, B., NIR light induced H<sub>2</sub> evolution by a metal-free photocatalyst. *Chemical Communications* **2015**, *51* (54), 10899-10902.

151. Woods, C. R.; Britnell, L.; Eckmann, A.; Ma, R. S.; Lu, J. C.; Guo, H. M.; Lin, X.; Yu, G. L.; Cao, Y.; Gorbachev, R. V.; Kretinin, A. V.; Park, J.; Ponomarenko, L. A.; Katsnelson, M. I.; Gornostyrev, Y. N.; Watanabe, K.; Taniguchi, T.; Casiraghi, C.; Gao, H. J.; Geim, A. K.; Novoselov,

K. S., Commensurate–incommensurate transition in graphene on hexagonal boron nitride. *Nature Physics* **2014**, *10*, 451.

152. Yeh, T.-F.; Syu, J.-M.; Cheng, C.; Chang, T.-H.; Teng, H., Graphite Oxide as a Photocatalyst for Hydrogen Production from Water. **2010**, *20* (14), 2255-2262.

153. Yeh, T.-F.; Chen, S.-J.; Yeh, C.-S.; Teng, H., Tuning the Electronic Structure of Graphite Oxide through Ammonia Treatment for Photocatalytic Generation of H<sub>2</sub> and O<sub>2</sub> from Water Splitting. *The Journal of Physical Chemistry C* **2013**, *117* (13), 6516-6524.

154. Yeh, T.-F.; Teng, C.-Y.; Chen, S.-J.; Teng, H., Nitrogen-Doped Graphene Oxide Quantum Dots as Photocatalysts for Overall Water-Splitting under Visible Light Illumination. **2014**, *26* (20), 3297-3303.

155. Rani, P.; Jindal, V. K., Designing band gap of graphene by B and N dopant atoms. *RSC Advances* **2013**, *3* (3), 802-812.

156. Latorre-Sánchez, M.; Primo, A.; García, H., P-Doped Graphene Obtained by Pyrolysis of Modified Alginate as a Photocatalyst for Hydrogen Generation from Water–Methanol Mixtures. **2013**, *52* (45), 11813-11816.

157. Ballesteros-Garrido, R.; Baldoví, H. G.; Latorre-Sanchez, M.; Alvaro, M.; Garcia, H., Photocatalytic hydrogen generation from water-methanol mixtures using halogenated reconstituted graphenes. *Journal of Materials Chemistry A* **2013**, *1* (38), 11728-11734.

158. Feng, X.; Ding, X.; Jiang, D., Covalent organic frameworks. *Chemical Society Reviews* **2012**, *41* (18), 6010-6022.

159. Côté, A. P.; Benin, A. I.; Ockwig, N. W.; O'Keeffe, M.; Matzger, A. J.; Yaghi, O. M., Porous, Crystalline, Covalent Organic Frameworks. **2005**, *310* (5751), 1166-1170.

160. El-Kaderi, H. M.; Hunt, J. R.; Mendoza-Cortés, J. L.; Côté, A. P.; Taylor, R. E.; O'Keeffe, M.; Yaghi, O. M., Designed Synthesis of 3D Covalent Organic Frameworks. **2007**, *316* (5822), 268-272.
161. Ding, S.-Y.; Wang, W., Covalent organic frameworks (COFs): from design to applications. *Chemical Society Reviews* **2013**, *42* (2), 548-568.
162. Côté, A. P.; El-Kaderi, H. M.; Furukawa, H.; Hunt, J. R.; Yaghi, O. M., Reticular Synthesis of Microporous and Mesoporous 2D Covalent Organic Frameworks. *Journal of the American Chemical Society* **2007**, *129* (43), 12914-12915.
163. Gutzler, R.; Perepichka, D. F.,  $\pi$ -Electron Conjugation in Two Dimensions. *Journal of the American Chemical Society* **2013**, *135* (44), 16585-16594.
164. Sprick, R. S.; Jiang, J.-X.; Bonillo, B.; Ren, S.; Ratvijitvech, T.; Guiglion, P.; Zwijnenburg, M. A.; Adams, D. J.; Cooper, A. I., Tunable Organic Photocatalysts for Visible-Light-Driven Hydrogen Evolution. *Journal of the American Chemical Society* **2015**, *137* (9), 3265-3270.
165. Vyas, V. S.; Haase, F.; Stegbauer, L.; Savasci, G.; Podjaski, F.; Ochsenfeld, C.; Lotsch, B. V., A tunable azine covalent organic framework platform for visible light-induced hydrogen generation. *Nature Communications* **2015**, *6*, 8508.
166. Stegbauer, L.; Schwinghammer, K.; Lotsch, B. V., A hydrazone-based covalent organic framework for photocatalytic hydrogen production. *Chemical Science* **2014**, *5* (7), 2789-2793.
167. Vyas, V. S.; Haase, F.; Stegbauer, L.; Savasci, G.; Podjaski, F.; Ochsenfeld, C.; Lotsch, B. V., A tunable azine covalent organic framework platform for visible light-induced hydrogen generation. *Nat Commun* **2015**, *6*.

168. Thote, J.; Aiyappa, H. B.; Deshpande, A.; Díaz Díaz, D.; Kurungot, S.; Banerjee, R., A Covalent Organic Framework–Cadmium Sulfide Hybrid as a Prototype Photocatalyst for Visible-Light-Driven Hydrogen Production. *2014*, *20* (48), 15961-15965.
169. Li, L.; Yu, Y.; Ye, G. J.; Ge, Q.; Ou, X.; Wu, H.; Feng, D.; Chen, X. H.; Zhang, Y., Black phosphorus field-effect transistors. *Nature Nanotechnology* **2014**, *9*, 372.
170. Morita, A. J. A. P. A., Semiconducting black phosphorus. **1986**, *39* (4), 227-242.
171. Wang, X.; Jones, A. M.; Seyler, K. L.; Tran, V.; Jia, Y.; Zhao, H.; Wang, H.; Yang, L.; Xu, X.; Xia, F., Highly anisotropic and robust excitons in monolayer black phosphorus. *Nature Nanotechnology* **2015**, *10*, 517.
172. Wu, J.; Mao, N.; Xie, L.; Xu, H.; Zhang, J., Identifying the Crystalline Orientation of Black Phosphorus Using Angle-Resolved Polarized Raman Spectroscopy. **2015**, *54* (8), 2366-2369.
173. Xia, F.; Wang, H.; Xiao, D.; Dubey, M.; Ramasubramaniam, A., Two-dimensional material nanophotonics. *Nature Photonics* **2014**, *8*, 899.
174. Low, J.; Cao, S.; Yu, J.; Wageh, S., Two-dimensional layered composite photocatalysts. *Chemical Communications* **2014**, *50* (74), 10768-10777.
175. Wang, H.; Yang, X.; Shao, W.; Chen, S.; Xie, J.; Zhang, X.; Wang, J.; Xie, Y., Ultrathin Black Phosphorus Nanosheets for Efficient Singlet Oxygen Generation. *Journal of the American Chemical Society* **2015**, *137* (35), 11376-11382.
176. Lu, W.; Nan, H.; Hong, J.; Chen, Y.; Zhu, C.; Liang, Z.; Ma, X.; Ni, Z.; Jin, C.; Zhang, Z. J. N. R., Plasma-assisted fabrication of monolayer phosphorene and its Raman characterization. **2014**, *7* (6), 853-859.

177. Tsyurupa, M. P.; Davankov, V. A., Hypercrosslinked polymers: basic principle of preparing the new class of polymeric materials. *Reactive and Functional Polymers* **2002**, 53 (2), 193-203.
178. McKeown, N. B.; Budd, P. M., Polymers of intrinsic microporosity (PIMs): organic materials for membrane separations, heterogeneous catalysis and hydrogen storage. *Chemical Society Reviews* **2006**, 35 (8), 675-683.
179. Park, J. H.; Ko, K. C.; Park, N.; Shin, H.-W.; Kim, E.; Kang, N.; Hong Ko, J.; Lee, S. M.; Kim, H. J.; Ahn, T. K.; Lee, J. Y.; Son, S. U., Microporous organic nanorods with electronic push-pull skeletons for visible light-induced hydrogen evolution from water. *Journal of Materials Chemistry A* **2014**, 2 (21), 7656-7661.
180. Sprick, R. S.; Bonillo, B.; Clowes, R.; Guiglion, P.; Brownbill, N. J.; Slater, B. J.; Blanc, F.; Zwijnenburg, M. A.; Adams, D. J.; Cooper, A. I., Visible - Light - Driven Hydrogen Evolution Using Planarized Conjugated Polymer Photocatalysts. *Angewandte Chemie International Edition* **2016**, 55 (5), 1792-1796.
181. Sprick, R. S.; Bonillo, B.; Clowes, R.; Guiglion, P.; Brownbill, N. J.; Slater, B. J.; Blanc, F.; Zwijnenburg, M. A.; Adams, D. J.; Cooper, A. I., Visible-Light-Driven Hydrogen Evolution Using Planarized Conjugated Polymer Photocatalysts. *Angewandte Chemie International Edition* **2016**, 55 (5), 1792-1796.
182. Park, J. H.; Ko, K. C.; Park, N.; Shin, H.-W.; Kim, E.; Kang, N.; Hong Ko, J.; Lee, S. M.; Kim, H. J.; Ahn, T. K.; Lee, J. Y.; Son, S. U., Microporous organic nanorods with electronic push-pull skeletons for visible light-induced hydrogen evolution from water. *Journal of Materials Chemistry A* **2014**, 2 (21), 7656-7661.

183. Katekomol, P.; Roeser, J.; Bojdys, M.; Weber, J.; Thomas, A., Covalent Triazine Frameworks Prepared from 1,3,5-Tricyanobenzene. *Chemistry of Materials* **2013**, *25* (9), 1542-1548.
184. Kuhn, P.; Antonietti, M.; Thomas, A., Porous, Covalent Triazine-Based Frameworks Prepared by Ionothermal Synthesis. *Angewandte Chemie International Edition* **2008**, *47* (18), 3450-3453.
185. Bojdys, M. J.; Jeromenok, J.; Thomas, A.; Antonietti, M., Rational Extension of the Family of Layered, Covalent, Triazine-Based Frameworks with Regular Porosity. *Advanced Materials* **2010**, *22* (19), 2202-2205.
186. Kuhn, P.; Forget, A.; Su, D.; Thomas, A.; Antonietti, M., From Microporous Regular Frameworks to Mesoporous Materials with Ultrahigh Surface Area: Dynamic Reorganization of Porous Polymer Networks. *Journal of the American Chemical Society* **2008**, *130* (40), 13333-13337.
187. Kuhn, P.; Forget, A.; Hartmann, J.; Thomas, A.; Antonietti, M., Template-Free Tuning of Nanopores in Carbonaceous Polymers through Ionothermal Synthesis. *Advanced Materials* **2009**, *21* (8), 897-901.
188. Kuhn, P.; Thomas, A.; Antonietti, M., Toward Tailorable Porous Organic Polymer Networks: A High-Temperature Dynamic Polymerization Scheme Based on Aromatic Nitriles. *Macromolecules* **2009**, *42* (1), 319-326.
189. Ren, S.; Bojdys, M. J.; Dawson, R.; Laybourn, A.; Khimyak, Y. Z.; Adams, D. J.; Cooper, A. I., Porous, Fluorescent, Covalent Triazine-Based Frameworks Via Room-Temperature and Microwave-Assisted Synthesis. *Advanced Materials* **2012**, *24* (17), 2357-2361.
190. Hug, S. Covalent triazine frameworks. Imu, 2014.

191. Bhunia, A.; Vasylyeva, V.; Janiak, C., From a supramolecular tetranitrile to a porous covalent triazine-based framework with high gas uptake capacities. *Chemical Communications* **2013**, *49* (38), 3961-3963.
192. Bhunia, A.; Boldog, I.; Moller, A.; Janiak, C., Highly stable nanoporous covalent triazine-based frameworks with an adamantane core for carbon dioxide sorption and separation. *Journal of Materials Chemistry A* **2013**, *1* (47), 14990-14999.
193. Zhang, W.; Li, C.; Yuan, Y.-P.; Qiu, L.-G.; Xie, A.-J.; Shen, Y.-H.; Zhu, J.-F., Highly energy- and time-efficient synthesis of porous triazine-based framework: microwave-enhanced ionothermal polymerization and hydrogen uptake. *Journal of Materials Chemistry* **2010**, *20* (31), 6413-6415.
194. Wang, W.; Ren, H.; Sun, F.; Cai, K.; Ma, H.; Du, J.; Zhao, H.; Zhu, G., Synthesis of porous aromatic framework with tuning porosity via ionothermal reaction. *Dalton Transactions* **2012**, *41* (14), 3933-3936.
195. Liu, X.; Li, H.; Zhang, Y.; Xu, B.; A, S.; Xia, H.; Mu, Y., Enhanced carbon dioxide uptake by metalloporphyrin-based microporous covalent triazine framework. *Polymer Chemistry* **2013**, *4* (8), 2445-2448.
196. Zhao, Y.; Yao, K. X.; Teng, B.; Zhang, T.; Han, Y., A perfluorinated covalent triazine-based framework for highly selective and water-tolerant CO<sub>2</sub> capture. *Energy & Environmental Science* **2013**, *6* (12), 3684-3692.
197. Kuhn, P.; Kruger, K.; Thomas, A.; Antonietti, M., "Everything is surface": tunable polymer organic frameworks with ultrahigh dye sorption capacity. *Chemical Communications* **2008**, (44), 5815-5817.

198. Wang, T.; Kailasam, K.; Xiao, P.; Chen, G.; Chen, L.; Wang, L.; Li, J.; Zhu, J., Adsorption removal of organic dyes on covalent triazine framework (CTF). *Microporous and Mesoporous Materials* **2014**, *187*, 63-70.
199. Liu, J.; Chen, H.; Zheng, S.; Xu, Z., Adsorption of 4,4'-(Propane-2,2-diyl)diphenol from Aqueous Solution by a Covalent Triazine-Based Framework. *Journal of Chemical & Engineering Data* **2013**, *58* (12), 3557-3562.
200. Chan-Thaw, C. E.; Villa, A.; Katekomol, P.; Su, D.; Thomas, A.; Prati, L., Covalent Triazine Framework as Catalytic Support for Liquid Phase Reaction. *Nano Letters* **2010**, *10* (2), 537-541.
201. Chan-Thaw, C. E.; Villa, A.; Prati, L.; Thomas, A., Triazine-Based Polymers as Nanostructured Supports for the Liquid-Phase Oxidation of Alcohols. *Chemistry – A European Journal* **2011**, *17* (3), 1052-1057.
202. Periana, R. A.; Taube, D. J.; Gamble, S.; Taube, H.; Satoh, T.; Fujii, H., Platinum Catalysts for the High-Yield Oxidation of Methane to a Methanol Derivative. *Science* **1998**, *280* (5363), 560-564.
203. Hao, L.; Luo, B.; Li, X.; Jin, M.; Fang, Y.; Tang, Z.; Jia, Y.; Liang, M.; Thomas, A.; Yang, J.; Zhi, L., Terephthalonitrile-derived nitrogen-rich networks for high performance supercapacitors. *Energy & Environmental Science* **2012**, *5* (12), 9747-9751.
204. Sakaushi, K.; Hosono, E.; Nickerl, G.; Gemming, T.; Zhou, H.; Kaskel, S.; Eckert, J., Aromatic porous-honeycomb electrodes for a sodium-organic energy storage device. *Nat Commun* **2013**, *4*, 1485.
205. Butchosa, C.; McDonald, T. O.; Cooper, A. I.; Adams, D. J.; Zwijnenburg, M. A., Shining a Light on s-Triazine-Based Polymers. *The Journal of Physical Chemistry C* **2014**, *118* (8), 4314-4324.

206. Bi, J.; Fang, W.; Li, L.; Wang, J.; Liang, S.; He, Y.; Liu, M.; Wu, L., Covalent Triazine-Based Frameworks as Visible Light Photocatalysts for the Splitting of Water. *Macromolecular Rapid Communications* **2015**, n/a-n/a.
207. Schwinghammer, K.; Hug, S.; Mesch, M. B.; Senker, J.; Lotsch, B. V., Phenyl-Triazine Oligomers for Light-Driven Hydrogen Evolution. *Energy & Environmental Science* **2015**.
208. Jiang, X.; Wang, P.; Zhao, J., 2D covalent triazine framework: a new class of organic photocatalyst for water splitting. *Journal of Materials Chemistry A* **2015**, 3 (15), 7750-7758.
209. Tauc, J., Optical properties and electronic structure of amorphous Ge and Si. *Materials Research Bulletin* **1968**, 3 (1), 37-46.
210. Tsunekawa, S.; Sahara, R.; Kawazoe, Y.; Kasuya, A., Origin of the Blue Shift in Ultraviolet Absorption Spectra of Nanocrystalline CeO<sub>2-x</sub> Particles. *Materials Transactions, JIM* **2000**, 41 (8), 1104-1107.
211. Hind, A. R.; Bhargava, S. K.; McKinnon, A., At the solid/liquid interface: FTIR/ATR – the tool of choice. *Advances in Colloid and Interface Science* **2001**, 93 (1), 91-114.
212. Ausili, A.; Sánchez, M.; Gómez-Fernández, J. C. J. B. S.; Imaging, Attenuated total reflectance infrared spectroscopy: A powerful method for the simultaneous study of structure and spatial orientation of lipids and membrane proteins. **2015**, 4 (2), 159-170.
213. Mirabella, F. M., *Internal reflection spectroscopy: theory and applications*. CRC Press: 1992; Vol. 15.
214. Yu, J.; Kudo, A., Effects of Structural Variation on the Photocatalytic Performance of Hydrothermally Synthesized BiVO<sub>4</sub>. **2006**, 16 (16), 2163-2169.

215. Bueno-Ferrer, C.; Parres-Esclapez, S.; Lozano-Castelló, D.; Bueno-López, A., Relationship between surface area and crystal size of pure and doped cerium oxides. *Journal of Rare Earths* **2010**, 28 (5), 647-653.
216. Muilenberg, G. J. P.-E. C., Handbook of X-ray photoelectron spectroscopy. **1979**, 64.
217. Asahi, R.; Morikawa, T.; Ohwaki, T.; Aoki, K.; Taga, Y., Visible-Light Photocatalysis in Nitrogen-Doped Titanium Oxides. **2001**, 293 (5528), 269-271.
218. Paracchino, A.; Laporte, V.; Sivula, K.; Grätzel, M.; Thimsen, E., Highly active oxide photocathode for photoelectrochemical water reduction. *Nature Materials* **2011**, 10, 456.
219. Suzuki, E., High-resolution scanning electron microscopy of immunogold-labelled cells by the use of thin plasma coating of osmium. **2002**, 208 (3), 153-157.
220. Pavia, D. L.; Lampman, G. M.; Kriz, G. S.; Vyvyan, J. A., *Introduction to spectroscopy*. Cengage Learning: 2008.
221. Tseederberg, N. V. C., R. D., *Thermal conductivity of gases and liquids*. MIT press Cambridge, Massachusetts: 1965.
222. Kong, D.; Zheng, Y.; Kobielski, M.; Wang, Y.; Bai, Z.; Macyk, W.; Wang, X.; Tang, J., Recent advances in visible light-driven water oxidation and reduction in suspension systems. *Materials Today* **2018**.
223. Serpone, N.; Terzian, R.; Lawless, D.; Kennepohl, P.; Sauvé, G., On the usage of turnover numbers and quantum yields in heterogeneous photocatalysis. *Journal of Photochemistry and Photobiology A: Chemistry* **1993**, 73 (1), 11-16.

224. Xie, G.; Zhang, K.; Guo, B.; Liu, Q.; Fang, L.; Gong, J. R., Graphene-Based Materials for Hydrogen Generation from Light-Driven Water Splitting. *Advanced Materials* **2013**, *25* (28), 3820-3839.
225. Muhich, C. L.; Ehrhart, B. D.; Al-Shankiti, I.; Ward, B. J.; Musgrave, C. B.; Weimer, A. W., A review and perspective of efficient hydrogen generation via solar thermal water splitting. *Wiley Interdisciplinary Reviews: Energy and Environment* **2015**, n/a-n/a.
226. Hisatomi, T.; Kubota, J.; Domen, K., Recent advances in semiconductors for photocatalytic and photoelectrochemical water splitting. *Chemical Society Reviews* **2014**, *43* (22), 7520-7535.
227. Osterloh, F. E., Inorganic nanostructures for photoelectrochemical and photocatalytic water splitting. *Chemical Society Reviews* **2013**, *42* (6), 2294-2320.
228. Tachibana, Y.; Vayssieres, L.; Durrant, J. R., Artificial photosynthesis for solar water-splitting. *Nat Photon* **2012**, *6* (8), 511-518.
229. Zhuang, H. L.; Hennig, R. G., Single-Layer Group-III Monochalcogenide Photocatalysts for Water Splitting. *Chemistry of Materials* **2013**, *25* (15), 3232-3238.
230. Jiang, C.; Moniz, S. J. A.; Khraisheh, M.; Tang, J., Earth-Abundant Oxygen Evolution Catalysts Coupled onto ZnO Nanowire Arrays for Efficient Photoelectrochemical Water Cleavage. *Chemistry – A European Journal* **2014**, *20* (40), 12954-12961.
231. Martin, D. J.; Qiu, K.; Shevlin, S. A.; Handoko, A. D.; Chen, X.; Guo, Z.; Tang, J., Highly Efficient Photocatalytic H<sub>2</sub> Evolution from Water using Visible Light and Structure-Controlled Graphitic Carbon Nitride. *Angewandte Chemie International Edition* **2014**, *53* (35), 9240-9245.

232. Wang, K.; Yang, L.-M.; Wang, X.; Guo, L.; Cheng, G.; Zhang, C.; Jin, S.; Tan, B.; Cooper, A., Covalent Triazine Frameworks via a Low-Temperature Polycondensation Approach. *Angewandte Chemie International Edition* **2017**, *56* (45), 14149-14153.
233. Yi, Z.; Ye, J.; Kikugawa, N.; Kako, T.; Ouyang, S.; Stuart-Williams, H.; Yang, H.; Cao, J.; Luo, W.; Li, Z.; Liu, Y.; Withers, R. L., An orthophosphate semiconductor with photooxidation properties under visible-light irradiation. *Nat Mater* **2010**, *9* (7), 559-564.
234. Li, Y.; Zhu, J.; Chu, H.; Wei, J.; Liu, F.; Lv, M.; Tang, J.; Zhang, B.; Yao, J.; Huo, Z.; Hu, L.; Dai, S., BiVO<sub>4</sub> semiconductor sensitized solar cells. *Science China Chemistry* **2015**, *58* (9), 1489-1493.
235. Martin, D. J.; Liu, G.; Moniz, S. J. A.; Bi, Y.; Beale, A. M.; Ye, J.; Tang, J., Efficient visible driven photocatalyst, silver phosphate: performance, understanding and perspective. *Chemical Society Reviews* **2015**, *44* (21), 7808-7828.
236. Zhang, J. S.; Zhang, G. G.; Chen, X. F.; Lin, S.; Mohlmann, L.; Dolega, G.; Lipner, G.; Antonietti, M.; Blechert, S.; Wang, X. C., Co-Monomer Control of Carbon Nitride Semiconductors to Optimize Hydrogen Evolution with Visible Light. *Angewandte Chemie-International Edition* **2012**, *51* (13), 3183-3187.
237. Zhang, J. S.; Sun, J. H.; Maeda, K.; Domen, K.; Liu, P.; Antonietti, M.; Fu, X. Z.; Wang, X. C., Sulfur-mediated synthesis of carbon nitride: Band-gap engineering and improved functions for photocatalysis. *Energy & Environmental Science* **2011**, *4* (3), 675-678.
238. Shevlin, S. A.; Guo, Z. X., Anionic Dopants for Improved Optical Absorption and Enhanced Photocatalytic Hydrogen Production in Graphitic Carbon Nitride. *Chemistry of Materials* **2016**, *28* (20), 7250-7256.

239. Liu, J.; Liu, Y.; Liu, N. Y.; Han, Y. Z.; Zhang, X.; Huang, H.; Lifshitz, Y.; Lee, S. T.; Zhong, J.; Kang, Z. H., Metal-free efficient photocatalyst for stable visible water splitting via a two-electron pathway. *Science* **2015**, *347* (6225), 970-974.
240. Wang, Y.; Bayazit, M. K.; Moniz, S. J. A.; Ruan, Q.; Lau, C. C.; Martsinovich, N.; Tang, J., Linker-controlled polymeric photocatalyst for highly efficient hydrogen evolution from water. *Energy & Environmental Science* **2017**, *10* (7), 1643-1651.
241. Lan, Z. A.; Fang, Y.; Zhang, Y.; Wang, X., Photocatalytic Oxygen Evolution from Functional Triazine - Based Polymers with Tunable Band Structures. *Angewandte Chemie International Edition* **2018**, *57* (2), 470-474.
242. Wang, P.; Jiang, X.; Zhao, J., Bottom-up design of 2D organic photocatalysts for visible-light driven hydrogen evolution. *Journal of Physics: Condensed Matter* **2015**, *28* (3), 034004.
243. Wang, Y.; Suzuki, H.; Xie, J.; Tomita, O.; Martin, D. J.; Higashi, M.; Kong, D.; Abe, R.; Tang, J., Mimicking Natural Photosynthesis: Solar to Renewable H<sub>2</sub> Fuel Synthesis by Z-Scheme Water Splitting Systems. *Chemical Reviews* **2018**, *118* (10), 5201-5241.
244. Kong, D.; Zheng, Y.; Kobielski, M.; Wang, Y.; Bai, Z.; Macyk, W.; Wang, X.; Tang, J., Recent advances in visible light-driven water oxidation and reduction in suspension systems. *Materials Today* **2018**, *04* (009).
245. Bi, J.; Fang, W.; Li, L.; Wang, J.; Liang, S.; He, Y.; Liu, M.; Wu, L., Covalent Triazine-Based Frameworks as Visible Light Photocatalysts for the Splitting of Water. *Macromolecular Rapid Communications* **2015**, *36*(20), 1799-1805.
246. Kresse, G.; Furthmüller, J., Efficient iterative schemes for ab initio total-energy calculations using a plane-wave basis set. *Physical Review B* **1996**, *54* (16), 11169-11186.

247. Blöchl, P. E., Projector augmented-wave method. *Physical Review B* **1994**, 50 (24), 17953-17979.
248. Perdew, J. P.; Burke, K.; Ernzerhof, M., Generalized Gradient Approximation Made Simple. *Physical Review Letters* **1996**, 77 (18), 3865-3868.
249. Grimme, S., Semiempirical GGA-type density functional constructed with a long-range dispersion correction. *Journal of Computational Chemistry* **2006**, 27 (15), 1787-1799.
250. Walsh, A.; Catlow, C. R. A., Structure, stability and work functions of the low index surfaces of pure indium oxide and Sn-doped indium oxide (ITO) from density functional theory. *Journal of Materials Chemistry* **2010**, 20 (46), 10438-10444.
251. Struijk, C. B.; Beerthuis, R. K.; Pabon, H. J. J.; van Dorp, D. A., Specificity in the enzymic conversion of polyunsaturated fatty acids into prostaglandins. *Recueil des Travaux Chimiques des Pays-Bas* **1966**, 85 (12), 1233-1250.
252. Gattrell, M.; Kirk, D., A Fourier Transform Infrared Spectroscopy Study of the Passive Film Produced during Aqueous Acidic Phenol Electro - oxidation. *Journal of The Electrochemical Society* **1992**, 139 (10), 2736-2744.
253. Manecke, V. G.; Wöhrle, D., Synthese und halbleitereigenschaften einiger komplexe und der aus ihnen hergestellten polymeren. Teil 2. Polymere mit phthalocyaninartiger und triazinartiger stuktur. *Die Makromolekulare Chemie* **1968**, 120 (1), 176-191.
254. Liebl, M. R.; Senker, J., Microporous Functionalized Triazine-Based Polyimides with High CO<sub>2</sub> Capture Capacity. *Chemistry of Materials* **2013**, 25 (6), 970-980.

255. Wu, W.-C.; Liao, L.-F.; Lien, C.-F.; Lin, J.-L., FTIR study of adsorption, thermal reactions and photochemistry of benzene on powdered TiO<sub>2</sub>. *Physical Chemistry Chemical Physics* **2001**, 3 (19), 4456-4461.
256. Liu, B. H.; Dou, L. T.; He, F.; Yang, J.; Li, Z. P., A cobalt coordination compound with indole acetic acid for fabrication of a high performance cathode catalyst in fuel cells. *RSC Advances* **2016**, 6 (23), 19025-19033.
257. Murtada, A. T.; Shree, R. S.; Vida, A. D., Biodegradable PLGA85/15 nanoparticles as a delivery vehicle for Chlamydia trachomatis recombinant MOMP-187 peptide. *Nanotechnology* **2012**, 23 (32), 325101.
258. Larkin, P., *Infrared and Raman spectroscopy: principles and spectral interpretation*. Elsevier: 2017.
259. Nakamoto, K.; Nakamoto, K., *Infrared and Raman spectra of inorganic and coordination compounds*. Wiley: 1977.
260. Hug, S.; Mesch, M. B.; Oh, H.; Popp, N.; Hirscher, M.; Senker, J.; Lotsch, B. V., A fluorene based covalent triazine framework with high CO<sub>2</sub> and H<sub>2</sub> capture and storage capacities. *Journal of Materials Chemistry A* **2014**, 2 (16), 5928-5936.
261. Thomas, A.; Fischer, A.; Goettmann, F.; Antonietti, M.; Muller, J.-O.; Schlogl, R.; Carlsson, J. M., Graphitic carbon nitride materials: variation of structure and morphology and their use as metal-free catalysts. *Journal of Materials Chemistry* **2008**, 18 (41), 4893-4908.
262. Muller, D. A.; Sorsch, T.; Moccio, S.; Baumann, F.; Evans-Lutterodt, K.; Timp, G., The electronic structure at the atomic scale of ultrathin gate oxides. *Nature* **1999**, 399 (6738), 758-761.

263. Robin, M. B.; Ishii, I.; McLaren, R.; Hitchcock, A. P., Fluorination effects on the inner-shell spectra of unsaturated molecules. *Journal of Electron Spectroscopy and Related Phenomena* **1988**, *47*, 53-92.
264. Kudo, A.; Omori, K.; Kato, H., A Novel Aqueous Process for Preparation of Crystal Form-Controlled and Highly Crystalline BiVO<sub>4</sub> Powder from Layered Vanadates at Room Temperature and Its Photocatalytic and Photophysical Properties. *Journal of the American Chemical Society* **1999**, *121* (49), 11459-11467.
265. Kim, T. W.; Choi, K.-S., Nanoporous BiVO<sub>4</sub> Photoanodes with Dual-Layer Oxygen Evolution Catalysts for Solar Water Splitting. **2014**, *343* (6174), 990-994.
266. Ishikawa, A.; Takata, T.; Kondo, J. N.; Hara, M.; Kobayashi, H.; Domen, K., Oxysulfide Sm<sub>2</sub>Ti<sub>2</sub>S<sub>2</sub>O<sub>5</sub> as a Stable Photocatalyst for Water Oxidation and Reduction under Visible Light Irradiation ( $\lambda \leq 650$  nm). *Journal of the American Chemical Society* **2002**, *124* (45), 13547-13553.
267. Chi, J.; Yu, H., Water electrolysis based on renewable energy for hydrogen production. *Chinese Journal of Catalysis* **2018**, *39* (3), 390-394.
268. Xiang, W.; Qian, X.; Mingrun, L.; Shuai, S.; Xiuli, W.; Yaochuan, W.; Zhaochi, F.; Jingying, S.; Hongxian, H.; Can, L., Photocatalytic Overall Water Splitting Promoted by an  $\alpha$ - $\beta$  phase Junction on Ga<sub>2</sub>O<sub>3</sub>. *Angewandte Chemie* **2012**, *124* (52), 13266-13269.
269. Kong, D.; Zheng, Y.; Kobielski, M.; Wang, Y.; Bai, Z.; Macyk, W.; Wang, X.; Tang, J., Recent advances in visible light-driven water oxidation and reduction in suspension systems. *Materials Today* DOI:<https://doi.org/10.1016/j.mattod.2018.04.009>.
270. Maeda, K.; Teramura, K.; Lu, D.; Takata, T.; Saito, N.; Inoue, Y.; Domen, K., Photocatalyst releasing hydrogen from water. *Nature* **2006**, *440*, 295.

271. Wang, Q.; Hisatomi, T.; Jia, Q.; Tokudome, H.; Zhong, M.; Wang, C.; Pan, Z.; Takata, T.; Nakabayashi, M.; Shibata, N.; Li, Y.; Sharp, I. D.; Kudo, A.; Yamada, T.; Domen, K., Scalable water splitting on particulate photocatalyst sheets with a solar-to-hydrogen energy conversion efficiency exceeding 1%. *Nature Materials* **2016**, *15*, 611.
272. Chen, S.; Takata, T.; Domen, K., Particulate photocatalysts for overall water splitting. *Nature Reviews Materials* **2017**, *2*, 17050.
273. Chowdhury, F. A.; Trudeau, M. L.; Guo, H.; Mi, Z., A photochemical diode artificial photosynthesis system for unassisted high efficiency overall pure water splitting. *Nature Communications* **2018**, *9* (1), 1707.
274. Zhou, Z.; Shen, Y.; Li, Y.; Liu, A.; Liu, S.; Zhang, Y., Chemical Cleavage of Layered Carbon Nitride with Enhanced Photoluminescent Performances and Photoconduction. *ACS Nano* **2015**, *9* (12), 12480-12487.
275. Zhiping, S.; Tianran, L.; Lihua, L.; Sen, L.; Fengfu, F.; Xinchun, W.; Liangqia, G., Invisible Security Ink Based on Water - Soluble Graphitic Carbon Nitride Quantum Dots. *Angewandte Chemie International Edition* **2016**, *55* (8), 2773-2777.
276. Zhang, Z.; Long, J.; Yang, L.; Chen, W.; Dai, W.; Fu, X.; Wang, X., Organic semiconductor for artificial photosynthesis: water splitting into hydrogen by a bioinspired C<sub>3</sub>N<sub>3</sub>S<sub>3</sub> polymer under visible light irradiation. *Chemical Science* **2011**, *2* (9), 1826-1830.
277. Liqiang, J.; Yichun, Q.; Baiqi, W.; Shudan, L.; Baojiang, J.; Libin, Y.; Wei, F.; Honggang, F.; Jiazhong, S., Review of photoluminescence performance of nano-sized semiconductor materials and its relationships with photocatalytic activity. *Solar Energy Materials and Solar Cells* **2006**, *90* (12), 1773-1787.

278. Tauc, J.; Abeles (Eds), F., Optical Properties of Solids. *North-Holland, Amsterdam* **1970**.
279. Kazuhiko, M.; Koki, I.; Yuki, T.; Daling, L.; Miharuru, E., Modification of Wide-Band-Gap Oxide Semiconductors with Cobalt Hydroxide Nanoclusters for Visible-Light Water Oxidation. *Angewandte Chemie* **2016**, *128* (29), 8449-8453.
280. Maeda, K.; Higashi, M.; Siritanaratkul, B.; Abe, R.; Domen, K., SrNbO<sub>2</sub>N as a Water-Splitting Photoanode with a Wide Visible-Light Absorption Band. *Journal of the American Chemical Society* **2011**, *133* (32), 12334-12337.
281. Fabian, D. M.; Hu, S.; Singh, N.; Houle, F. A.; Hisatomi, T.; Domen, K.; Osterloh, F. E.; Ardo, S., Particle suspension reactors and materials for solar-driven water splitting. *Energy & Environmental Science* **2015**, *8* (10), 2825-2850.
282. Suntivich, J.; May, K. J.; Gasteiger, H. A.; Goodenough, J. B.; Shao-Horn, Y., A Perovskite Oxide Optimized for Oxygen Evolution Catalysis from Molecular Orbital Principles. **2011**, *334* (6061), 1383-1385.
283. Maeda, K.; Higashi, M.; Lu, D.; Abe, R.; Domen, K., Efficient Nonsacrificial Water Splitting through Two-Step Photoexcitation by Visible Light using a Modified Oxynitride as a Hydrogen Evolution Photocatalyst. *Journal of the American Chemical Society* **2010**, *132* (16), 5858-5868.
284. Yang, C.; Ma, B. C.; Zhang, L.; Lin, S.; Ghasimi, S.; Landfester, K.; Zhang, K. A. I.; Wang, X., Molecular Engineering of Conjugated Polybenzothiadiazoles for Enhanced Hydrogen Production by Photosynthesis. **2016**, *55* (32), 9202-9206.
285. Liu, G.; Niu, P.; Sun, C.; Smith, S. C.; Chen, Z.; Lu, G. Q.; Cheng, H.-M., Unique Electronic Structure Induced High Photoreactivity of Sulfur-Doped Graphitic C<sub>3</sub>N<sub>4</sub>. *Journal of the American Chemical Society* **2010**, *132* (33), 11642-11648.

286. Ran, J.; Ma, T. Y.; Gao, G.; Du, X.-W.; Qiao, S. Z., Porous P-doped graphitic carbon nitride nanosheets for synergistically enhanced visible-light photocatalytic H<sub>2</sub> production. *Energy & Environmental Science* **2015**, *8* (12), 3708-3717.
287. Zhang, G.; Lan, Z.-A.; Lin, L.; Lin, S.; Wang, X., Overall water splitting by Pt/g-C<sub>3</sub>N<sub>4</sub> photocatalysts without using sacrificial agents. *Chemical Science* **2016**, *7* (5), 3062-3066.
288. Bi, J.; Fang, W.; Li, L.; Wang, J.; Liang, S.; He, Y.; Liu, M.; Wu, L., Covalent Triazine-Based Frameworks as Visible Light Photocatalysts for the Splitting of Water. **2015**, *36* (20), 1799-1805.
289. Li, L.; Fang, W.; Zhang, P.; Bi, J.; He, Y.; Wang, J.; Su, W., Sulfur-doped covalent triazine-based frameworks for enhanced photocatalytic hydrogen evolution from water under visible light. *Journal of Materials Chemistry A* **2016**, *4* (32), 12402-12406.
290. Chen, X.; Cheng, J. P.; Shou, Q. L.; Liu, F.; Zhang, X. B., Effect of calcination temperature on the porous structure of cobalt oxide micro-flowers. *CrystEngComm* **2012**, *14* (4), 1271-1276.
291. Hug, S.; Tauchert, M. E.; Li, S.; Pachmayr, U. E.; Lotsch, B. V., A functional triazine framework based on N-heterocyclic building blocks. *Journal of Materials Chemistry* **2012**, *22* (28), 13956-13964.
292. Yang, J.; Liu, H.; Martens, W. N.; Frost, R. L., Synthesis and Characterization of Cobalt Hydroxide, Cobalt Oxyhydroxide, and Cobalt Oxide Nanodiscs. *The Journal of Physical Chemistry C* **2010**, *114* (1), 111-119.
293. Salunkhe, R. R.; Tang, J.; Kamachi, Y.; Nakato, T.; Kim, J. H.; Yamauchi, Y., Asymmetric Supercapacitors Using 3D Nanoporous Carbon and Cobalt Oxide Electrodes Synthesized from a Single Metal-Organic Framework. *ACS Nano* **2015**, *9* (6), 6288-6296.

294. Matin, M. A.; Lee, E.; Kim, H.; Yoon, W.-S.; Kwon, Y.-U., Rational syntheses of core-shell Fe@(PtRu) nanoparticle electrocatalysts for the methanol oxidation reaction with complete suppression of CO-poisoning and highly enhanced activity. *Journal of Materials Chemistry A* **2015**, 3 (33), 17154-17164.
295. Xu, H.; Ding, L.-X.; Liang, C.-L.; Tong, Y.-X.; Li, G.-R., High-performance polypyrrole functionalized PtPd electrocatalysts based on PtPd/PPy/PtPd three-layered nanotube arrays for the electrooxidation of small organic molecules. *Npg Asia Materials* **2013**, 5, e69.
296. Wu, P.; Lv, H.; Peng, T.; He, D.; Mu, S., Nano Conductive Ceramic Wedged Graphene Composites as Highly Efficient Metal Supports for Oxygen Reduction. *Scientific Reports* **2014**, 4, 3968.
297. Sadasivan, S.; Bellabarba, R. M.; Tooze, R. P., Size dependent reduction-oxidation-reduction behaviour of cobalt oxide nanocrystals. *Nanoscale* **2013**, 5 (22), 11139-11146.
298. Yang, J.; Wang, D.; Han, H.; Li, C., Roles of Cocatalysts in Photocatalysis and Photoelectrocatalysis. *Accounts of Chemical Research* **2013**, 46 (8), 1900-1909.
299. Maeda, K.; Wang, X.; Nishihara, Y.; Lu, D.; Antonietti, M.; Domen, K., Photocatalytic Activities of Graphitic Carbon Nitride Powder for Water Reduction and Oxidation under Visible Light. *The Journal of Physical Chemistry C* **2009**, 113 (12), 4940-4947.
300. Barreca, D.; Massignan, C.; Daolio, S.; Fabrizio, M.; Piccirillo, C.; Armelao, L.; Tondello, E., Composition and Microstructure of Cobalt Oxide Thin Films Obtained from a Novel Cobalt(II) Precursor by Chemical Vapor Deposition. *Chemistry of Materials* **2001**, 13 (2), 588-593.

301. Ma, Y.; Pendlebury, S. R.; Reynal, A.; Le Formal, F.; Durrant, J. R., Dynamics of photogenerated holes in undoped BiVO<sub>4</sub> photoanodes for solar water oxidation. *Chemical Science* **2014**, 5 (8), 2964-2973.
302. Bai, S.; Yin, W.; Wang, L.; Li, Z.; Xiong, Y., Surface and interface design in cocatalysts for photocatalytic water splitting and CO<sub>2</sub> reduction. *RSC Advances* **2016**, 6 (62), 57446-57463.